UNIVERSITAT AUTÒNOMA DE BARCELONA

POSTGRADUATE SCHOOL

PHYSICS DEPARTMENT

P h D T H E S I S

to obtain the title of

PhD of Science

of the Universitat Autonòma de Barcelona

Specialty : MATERIALS SCIENCE AND TECHNOLOGY

Presented by

Jose Manuel Caicedo Roque

Magneto-Optical Spectroscopy of Complex Systems: Magnetic Oxides and Photonic Crystals

Thesis Advisor: Gervasi Herranz Casabona

Thesis Advisor: Josep Fontcuberta Griñó

prepared at the Institut de Ciència de Materials de Barcelona (ICMAB) ,
Consejo Superior de Investigaciones Científicas (CSIC)

defended on:

2012

Contents

List of Figures

Part I

General

0.1 Acknowledgements

I would like to express my gratitude to my supervisors, Dr. Gervasi Herranz Casabona and Prof. Josep Fontcuberta Griñó whose expertise, understanding, and patience, added considerably to my Ph-D Thesis experience. I appreciate their vast knowledge and skill in many areas, and their assistance in writing reports (i.e., grant proposals, scholarship applications and this Thesis), which have on occasion made me "as a motorcycle" . I would like to thank the members of the jury for reading this Thesis. Special acknowledgements for the Dr. Sarah M. Thompson who advice me during my inter-ship in the University of York.

I want to thanks Oana Pascu who work tirelessly to help me to finish this thesis. A very special thanks goes out to Dr. David Hrabovsky, without his motivation and encouragement I would not have considered a Ph-D Thesis in magnetooptics research. Dr. Michael Foester is the one colleague who truly made a difference in all this time. I must also acknowledge Dr. Florencio Sanchez and Anna Roig for their suggestions and for all their help. Appreciation also goes out to Nico Dix, for technical support and revolutionary experimental ideas. I would also like to thank the administration staff for all of their documents and letters and legal technical assistance throughout my Ph-D Thesis program. Thanks to Rebeca, Montse, Maria, Pietat, Vicentini and to the administration staff for all the instances in which their assistance helped me along the way. Thanks also goes out to those who provided me with legal advice at times of critical need; Maria Trinidad Palomera Laforga. I would also like to thank my friends in the magnetic group, particularly Franco Rigato, Xavi Marti, Ignasi Fina, Romais Bachelet, Murali, Kanamadi, Diego, Ondrej Vlasie and David Pesquera for our philosophical debates, exchanges of knowledge, skills, and venting of frustration during my graduate program, which helped to enrich the experience. How to forget the lunch people; Philosopher, thinker, physicist,Catalan, poet and madman Jaume Roqueta, Manrressa son: Bernat Bosso, Andreas, Marc, Roberto, Julianne,Pablaza and many other who went through the ICMAB during these 4 years. I would also like to thank my family for the support they provided me through my entire life and in particular, I must acknowledge my brother Totin and my best friends James and Diego, without whose help, encouragement and editing assistance, I would not have finished this Thesis.

I recognize that this research would not have been possible without the financial assistance of FPI-CSIC-MICINN (Formación de Profesorado Investigador-Consejo Superior de Investigaciones Cientificas) Grant reference BES-2007-1499 belong to project MAT2005-05656-C04-01, and the technical and academic support of the Department of Magnetism and Magnetic Materials at the ICMAB (Instituto de Ciencia de Materiales de Barcelona),

Special acknowledgements for the Photonic Crystal Group under advise of Prof. Ceferino Lopez at the Instituto de Ciencia de Materiales de Madrid (ICMM). This collaboration was done under the context of Proyecto Intramural de Fronteras (PIF-CSIC)-"Hacia una nueva generación de de cristales fotónicos sintonizables". We also acknowledge the collaboration with the Dr. Alvaro Blanco at the Instituto de Ciencia de Materiales de Madrid (ICMM-CSIC) for the preparation of opal crystals and optical characterization.

I warmly acknowledge discussions on the subject with Antonio García Martín and Gaspar Armelles (CNM-CSIC). I acknowledge partial financial support from the CSIC CRIMAFOT (PIF 08-016), the Spanish Government (CONSOLIDER-Nanoselect-CSD2007-00041 and NanoLight.es- CSD20070046, MAT2008-06761-C03, MAT2009-08024, MAT2009-06885-E, MAT2009-07841, the Generalitat de Catalunya (2009SGR-376, 2009SGR-203), the Comunidad de Madrid S-0505/ESP-0200, and the EC FP7 NoE Nanophotonics4Energy-248855, and the CNRS-CSIC PICS under Grant No. PICS2008FR1, and the DFG under Grant No. FOR520, RR, SKA and IVS gratefully acknowledge financial support from the Science Foundation of Ireland, SFI, under contract no. 00/PI.1/C042. is acknowledged. I would like to express my gratitude to both persons and agencies.

0.2 Abstract

The history of magnetooptics goes back to the mid-nineteenth century, when Michael Faraday discovered in 1845 that a block of glass subjected to a magnetic field became optically active [1]: when a plane-polarized light passed trough glass in a direction parallel to applied field, the plane of polarization was rotated. Subsequently, magnetooptical effects were also observed in reflection by the Scottish physicist John Kerr in 1888 [2]. He observed that when plane-polarized light is reflected at normal incidence from the polished pole of an electromagnet, it became elliptically polarized with the major axis of the ellipse rotated with respect to the plane of polarization of the incident beam. The simplicity of the magnetooptic approach has helped to exploit it widely as a standard characterization of the magnetic properties of materials. Magnetooptic characterization embraces different techniques, including in-situ real-time growth monitoring of magnetic multilayers, vectorial magnetometry or magnetic domain imaging. Beyond its application as a characterization tool, magnetooptics has an interest by their own as a functional property. The last decades have witnessed the development of different applications in data storage and optical communications. Thus, strategies are sought to either enhance the magnetooptic signal or to tailor the magnetooptical spectral responses. This Thesis is focused on the analysis of the modification of the magnetooptic spectral responses either by intrinsic changes of the electronic properties of materials, or by exploiting geometric resonances induced by structuring the matter and enhance the magnetooptical responses.

We note that the magnetooptical activity is intimately connected to the electronic structure of the magnetooptical medium and, therefore, the magnetooptical response is strongly dependent on the wavelength (λ) of the incident light. Transitions between electronic states induced by light are usually located within the optical range, i.e. from infrared to ultraviolet, with typical energies of $(1 - 5eV)$. Therefore, the magnetooptical spectral response is closely determined by the electronic structure of the medium. Notwithstanding, the spectral response may be modified when the electronic structure is perturbed by, e.g., metal-insulator transitions, where some systems may undergo dramatic changes of their electronic properties. Strongly correlated electronic systems are suitable candidates to analyze such phenomena: we have analyzed these effects in magnetic oxides, including several manganites and magnetite. The former exhibit a variety of physical properties, such as colossal magneto-resistance and electron-phonon coupling controlled by doping level, which are notably attractive for both basic research and technology. In magnetite the presence of a metal to insulator transition (Verwey transition), across which the conductivity abruptly decreases, is also an attractive scenario to analyze the

effect on optical properties. The extreme sensitivity to external magnetic fields of these metal-to-insulator transitions is revealed by the so-called magnetorefractive effect. This phenomenon, although intensively studied in the far- and mid-infrared, has been little explored in the visible. In this Thesis, we have found that, while the magneto-refractive effect in the infrared is associated essentially to the response of delocalized carriers to magnetic fields, in the visible is due to changes of the electronic structure and, more specifically, to the modulation of polaron conductivity with magnetic fields.

A further modification of the magnetooptical response is by nano-structuring the medium, so that we can exploit the phenomenon of diffraction and geometrical resonances rather than electronic ones, to alter deeply the magnetooptical properties. An example of such systems are the magnetophotonic crystals in which the strong photon confinement in the vicinity of the photonic band gap results in a large enhancement of linear and nonlinear magnetooptical responses of the media. With this in view, we have studied the magnetooptical spectral response of three-dimensional photonic crystals infiltrated with magnetic nanoparticles.

The work presented in this Thesis has had two main objectives: (i) **The study of the magneto-transport in ferromagnetic oxide thin films by magnetooptical methods**. We have tackled this issue by using the magnetooptic spectral dependence to analyze the electronic transport at high frequencies from ultraviolet down to the far infra red. This frequency range probes the optical responses from the low-frequency range (free electron-like behavior) up to high-frequency (bound electron-like behavior). The role of electron-lattice coupling is analyzed by the magnetooptical characterization of mixed valence manganites of different chemical compositions. (ii) **Magnetooptical enhancement induced by photonic band-edge effects.** A magnetooptical characterization of magneto-photonic crystals has been carried out in order to study a photonic-induced magnetooptical enhancement for wavelengths around the band gap abortions edges.

To accomplish these objectives, we designed and built up a magnetooptical experimental set-up to analyze the spectral response in different configurations: Faraday (transmission) and Kerr (reflection) rotation and ellipticity and magnetic circular dichroism.

0.3 Outline

The Thesis contains a first part divided into three chapters in which basic magnetooptical concepts and experimental details are introduced. Subsequently, the experimental results are discussed in the following four chapters contained into the second part. A first chapter named "Basic concepts" introduces the reader into the fundamentals of magnetooptics. The second chapter named "Metal insulator transitions" presents basic properties of ferromagnetic manganites and magnetite. The chapter named "Experimental" describes the experimental set-ups and methodologies used in this Thesis. The second part ("Results") shows a detailed magnetooptical study of ferromagnetic manganites and magnetite from ultraviolet (UV) to far infra red(far-IR). The influence of electron-phonon coupling in these spectra was analyzed by measuring manganites with different chemical compositions and different electron-lattice interactions. A connection between a strong magnetotrefractive effect, magnetoresistance and electron-lattice interaction is established through an extensive analysis of different magnetic oxides, including manganites and magnetite.

We also tackle a different kinds of materials by magnetooptical tools. The magnetophotonic crystal concept is introduced as a periodically ordered system. In order to compare and discriminate the intrinsic material magnetooptical response from the photonic ones, a random (not ordered) systems are studied in the "Colloidal dispersion" chapter, furthermore, we show the potential of magnetooptical spectroscopy to analyze extremely diluted magnetic liquid dispersions of nanoparticles. In the chapter "Magneto-photonic crystals" we present a physical description of the mechanisms underlying the interaction between light and media with a periodic modulation of the permittivity, i.e., photonic crystals. In particular, we analyze how the spectral magnetooptical response of magnetic systems is altered by photonic effects by measuring the spectra of magneto-photonic crystals. In particular, we discuss the enhancement of the magnetooptical signal around the edges of the magneto-photonic band gap.

Finally we included a complete set of appendix as complementary information, including exhaustive description of the designed and built up the magnetooptical experimental set-up to analyze the spectral response in different configurations: Faraday (transmission) and Kerr (reflection) rotation and ellipticity and magnetic circular dichroism. The Thesis closes with a brief summary of the main conclusions and perspectives.

CHAPTER 1

Basic concepts

1.1 Light-matter interaction

Magnetooptics results from the interaction of polarized light with a magnetic material. In the following, we make a brief description of the light polarization in order to define concepts and conventions used in following sections. The polarization of light is a vectorial property of the electromagnetic waves. The electric field $E(z,t)$ can be chosen to define the state of the light polarization of a wave propagating in the z direction by a complex function:

$$E(z,t) = Re\{E_0 e^{i(\omega t - kz)}\} \tag{1.1}$$

Where E_0 is the amplitude of the electric field, ω is the angular frequency and k is the wavevector. In a monochromatic light, the electric field changes harmonically with time, so that at a given point z, the field E traces an ellipse on the xy plane. The polarization ellipse is described by the azimuth angle θ and by the ellipticity angle ϵ (Figure 1.1). As we will see below, the magnetooptical activity results from a very small conversion -which is proportional to the magnetization of the magnetic medium- between orthogonal components of the polarization, that gives way to an induced rotation and ellipticity.

In order to describe the magnetooptical effects let us to introduce the dielectric permittivity tensor [3]. We start with the Maxwell equations:

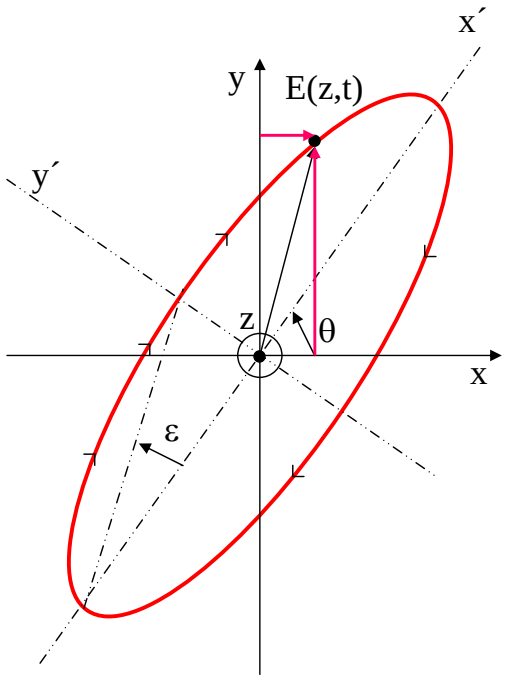

Figure 1.1: *Elliptical polarization*

$$\nabla \cdot E = 4\pi\rho \tag{1.2}$$

$$\nabla \cdot B = 0 \tag{1.3}$$

$$\nabla \times E = -\frac{1}{c}\frac{\partial B}{\partial t} \tag{1.4}$$

$$\nabla \times B = \frac{4\pi}{c}j + \frac{1}{c}\frac{\partial E}{\partial t} \tag{1.5}$$

where E is the electric field, B the magnetic induction, and ρ and j are the charge and current densities, respectively, which are related by the continuity equation:

$$\frac{\partial \rho}{\partial t} + \nabla \cdot j = 0 \tag{1.6}$$

In a materials description the polarization (P) and magnetization (M) are usually used, instead of ρ and j, where:

$$\rho = -\nabla \cdot P \tag{1.7}$$

$$j = \frac{\partial P}{\partial t} + c\nabla \times M$$

Using the materials equations:

$$B = H + 4\pi M \tag{1.8}$$
$$D = E + 4\pi P$$

The Maxwell equations for a magnetic medium can be rewritten as:

$$\nabla \cdot D = 0 \tag{1.9}$$
$$\nabla \cdot B = 0 \tag{1.10}$$
$$\nabla \times E = -\frac{1}{c}\frac{\partial B}{\partial t} \tag{1.11}$$
$$\nabla \times H = \frac{1}{c}\frac{\partial D}{\partial t} \tag{1.12}$$

Here it is assumed that the vectors P and E, as well as M and H, are linearly connected. These vectors are related by means of the materials equation, which are derived on the basis of certain microscopy concepts of the electronic and atomic structure of the medium:

$$P_i(\omega) = \hat{\alpha}_{ij}(\omega)E_j(\omega) \tag{1.13}$$
$$M_i(\omega) = \hat{\chi}_{ij}(\omega)H_j(\omega) \tag{1.14}$$

where $\hat{\alpha}_{ij}(\omega)$ and $\hat{\chi}_{ij}(\omega)$ are the tensors of the electric and magnetic susceptibilities; the fields E and D, as well as B and H, are related via the expressions:

$$D_i = \hat{\epsilon}_{ij}(\omega)E_j(\omega) \tag{1.15}$$
$$B_i = \hat{\mu}_{ij}(\omega)H_j(\omega) \tag{1.16}$$

where $\hat{\epsilon}_{ij}(\omega)$ and $\hat{\mu}_{ij}(\omega)$ are respectively the electric permittivity and magnetic permeability tensors of the medium. The current density $j_i(\omega)$ in terms of conductivity $\hat{\sigma}_{ij}(\omega, k)$ is given by:

$$j_i(\omega) = \sigma_{ij}(\omega)E_j(\omega) \tag{1.17}$$

and the the D vector is given by:

$$D_i(\omega) = \hat{\epsilon}_{ij}E_j(\omega) \tag{1.18}$$

where:

$$\hat{\epsilon}_{ij}(\omega) = \delta_{ij} - \frac{i4\pi\hat{\sigma}_{ij}(\omega)}{\omega} \tag{1.19}$$

At optical frequencies, the magnetic permeability is $\mu \approx 1$, and only the permittivity tensor is relevant for the light-matter interaction. The general form of $\hat{\epsilon}_{ij}$ for a magnetized medium with negligible losses is given by:

$$\hat{\epsilon}_{ij} = \begin{pmatrix} \epsilon'_{xx} & \epsilon'_{xy} + ig''_z & \epsilon'_{xz} - ig''_y \\ \epsilon'_{xy} - ig''_z & \epsilon'_{yy} & \epsilon'_{yz} + ig''_x \\ \epsilon'_{xz} + ig''_y & \epsilon'_{yz} - ig''_x & \epsilon'_{zz} \end{pmatrix} \tag{1.20}$$

Whereas the real components of $\tilde{\epsilon}_{ij}$ have to be even function of the magnetic field, the off-diagonal components -which are at the origin of magnetooptic effects- contain the gyration components ig''_i which are odd function of the magnetic field. The complex components of $\tilde{\epsilon}_{ij}$ are, thus, not only a function of the light frequency, but also of the magnetization M, and generally can be expanded in terms of the magnetization components:

$$\hat{\epsilon}_{ij} = \epsilon^0_{ij} + K_{ijk}M_k + G_{ijkl}M_kM_l + \ldots = \epsilon^0_{ij} + \epsilon^1_{ij} + \epsilon^2_{ij} + \ldots \tag{1.21}$$

Where, ϵ^0_{ij} are the permittivity components without magnetization in the crystal ($M = 0$), K_{ijk} are components of third rank linear magnetooptical tensor describing linear dependence on the magnetization and G_{ijkl} are the components of fourth rank quadratic magneto optical tensor describing quadratic dependence on the magnetization. Usually, the linear terms are predominant, but as we will see in chapter 4, second-order terms may be remarkable at some frequencies for certain materials.

The magnetooptical effects generally depend on both diagonal and off-diagonal elements of the dielectric tensor in a rather complicated way. In the the simplest case of an optically isotropic ferromagnet, with the z-axis directed along the magnetization M, the $\tilde{\epsilon}_{ij}$ can be represented as a sum of symmetric and anti-symmetric tensors, as follows:

$$\tilde{\epsilon}_{ij} = \begin{pmatrix} \epsilon'_{xx} & 0 & 0 \\ 0 & \epsilon'_{yy} & 0 \\ 0 & 0 & \epsilon'_{zz} \end{pmatrix} + \begin{pmatrix} 0 & +ig''_z & 0 \\ -ig''_z & 0 & 0 \\ 0 & 0 & 0 \end{pmatrix} \tag{1.22}$$

The second term in the equation 1.22 describes the gyrotropic effects connected to magnetic birefringence/dichroism. For instance, it can be demonstrated that in a medium of length L described by 1.22, the complex rotation for the transmitted light (Faraday

configuration) is given by $\theta + i\epsilon \approx \frac{\varepsilon_{xy}}{\sqrt{\varepsilon_{xx}}} \frac{\omega L}{2c} tan\phi$, where c is the velocity of light and ϕ is the angle of refraction [4]. Thus, we see that the off-diagonal components of the permittivity tensor must be nonzero to have magnetooptical activity. At a microscopic level, the magnetooptical effects are associated to spin-orbit interaction and they are usually small because of itś relativistic origin [3].

1.2 Magnetooptical effects

The basic magnetooptical phenomena can be classified according to the relative orientation between the wave vector of the light radiation κ and the magnetic field H. Two basic geometries are distinguished when light is transmitted through the medium:

- (i) Faraday geometry: the light travels along the field direction ($\vec{\kappa} \parallel H$)

- (ii) Voigt or Cotton-Mouton geometry: the light travels perpendicular to the field direction ($\vec{\kappa} \perp H$).

When an electromagnetic wave propagates unperturbed through a medium it is in an eigen-mode propagation state. In Faraday geometry, the eigen-modes are left- and right-circularly polarized light, and in Voigt geometry the eigen-modes are linearly polarized light (with polarizations perpendicular and parallel to the field H direction, respectively). In magnetooptical phenomena, the symmetry is broken by the presence of a magnetic field, which induces an asymmetry of the propagation of the eigen-modes. For instance, in Faraday geometry, *left-* and *right-* circularly polarized light propagate differently. The different propagation of the eigen-modes can be explained by the effects of birefringence and dichroism. Birefringence occurs when the two light eigen-modes (for instance, *left-* and *right-* circularly polarized light in Faraday geometry) propagate with different velocities. Dichroism occurs when the two eigen-modes are absorbed differently by the magnetic medium, i.e., the absorption coefficients for two orthogonal polarizations are different. Dichroism is related to the difference between the absorption of the circularly polarized components $\kappa_+ - \kappa_-$ in the case of the Faraday geometry (so-called magnetic circular dichroism MCD), and in the Voigt geometry it is determined from the difference between the absorption of the components polarized parallel and perpendicular $\kappa_{\parallel H} - \kappa_{\perp H}$ to the magnetic field (the magnetic linear dichroism MLD). Figure 1.2 shows both geometries.

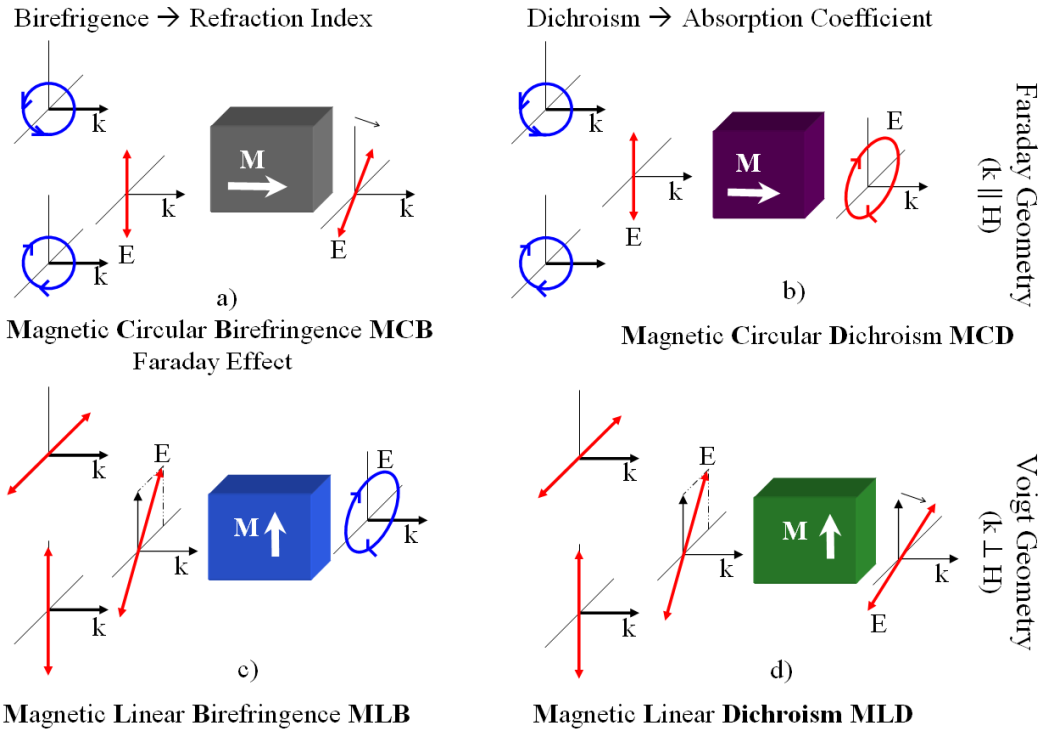

Figure 1.2: *The magnetooptical effects depending on the geometry: magnetic circular birefringence a), magnetic circular dichroism b), magnetic linear birefringence c), and magnetic linear dichroism d)*

When working in reflection (Kerr effects) the polarization state is defined with respect to the plane of incidence. Two orthogonal linear polarizations are used as a basis: a linear polarization "s", where the polarization is perpendicular to the plane of incidence, and a linear polarization "p", where the polarization is parallel to plane of incidence. Let us consider a well defined linear polarization ($s-$ or $p-$) incident on the magnetic medium. After reflection on the magnetic surface, an orthogonal polarization appears as a consequence of the magnetooptical activity. Thus, we will have both $s-$ and $p-$ components. In order to describe the polarization state of the light in Cartesian coordinates the Jones vector is defined as:

$$R = \begin{pmatrix} E_s \\ E_p \end{pmatrix} \tag{1.23}$$

Where E_s and E_p represent the components of the polarization (i.e. ., $s-$ and $p-$ polarized components of light). The total intensity is defined as:

$$I = JJ^* = \left(E_s E_s^* + E_p E_p^*\right) = \left(|E_s|^2 + |E_p|^2\right) \tag{1.24}$$

The effect of an arbitrary optical system on reflected light can be described by a matrix of four reflection coefficients given by:

$$R = \begin{pmatrix} r_{ss} & r_{ps} \\ r_{sp} & r_{pp} \end{pmatrix} \tag{1.25}$$

where the diagonal elements r_{ss} and r_{pp} describe the changes of amplitude and phase for a given polarization. The off-diagonal elements r_{sp} and r_{ps} reflect the conversion between polarizations, which takes place after the interaction with the magnetic medium. The individual coefficients are defined as the ratio between reflected and incident electromagnetic waves as follows (see figure 1.3):

$$r_{ss} = \frac{E_s^r}{E_s^i};\ r_{pp} = \frac{E_p^r}{E_p^i};\ r_{sp} = \frac{E_s^r}{E_p^i};\ r_{ps} = \frac{E_p^r}{E_s^i}; \tag{1.26}$$

The Kerr rotation $(\theta_{ks}; \theta_{kp})$ and ellipticity $(\epsilon_{ks}; \epsilon_{kp}\ )$ for $s-$ and $p-$ incident polarized light are given by :

$$\theta_{ks} + i\epsilon_{ks} = \frac{r_{sp}}{r_{ss}}; \qquad \theta_{kp} + i\epsilon_{kp} = -\frac{r_{ps}}{r_{pp}}; \tag{1.27}$$

Note that all these magnetooptical effects arise as a partial conversion from incident $s-$ polarized light into $p-$ polarization and, viceversa, of incident $p-$ polarization into $s-$ polarization.

1.3 Kerr effect Geometries

In reflection three main magnetooptical geometries can be identified: polar, longitudinal, and transverse. They are classified according to the relative orientation of the wave vector of the light $\vec{\kappa}$ and the magnetization vector M. Using these three different configurations we can obtain the three perpendicular components of the magnetization. In the polar geometry we are sensitive to the out-of-plane magnetization component M_p, whereas in longitudinal and transverse geometries we are sensitive to in-plane components M_l, M_t, see figure 1.3. Choosing adequately the geometry allows the determination of each component.

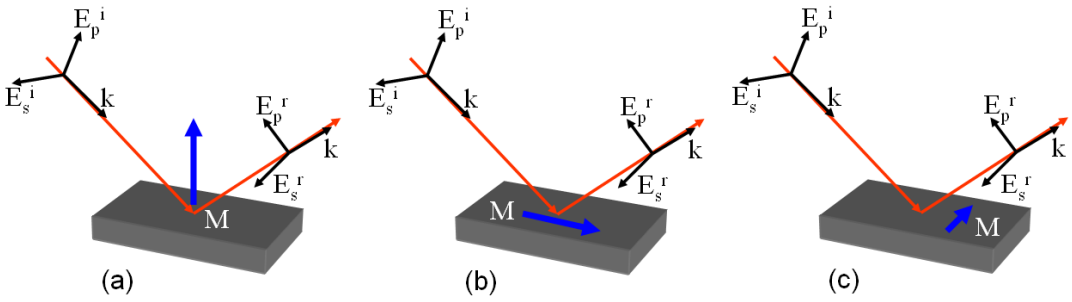

Figure 1.3: *Kerr effect geometries. Polar (a), Longitudinal (b), Tranverse (c)*

1.3.1 Polar

The polar Kerr geometry is performed at near-normal incidence and the magnetic field is applied perpendicular to the sample surface, and it is sensitive to the out of-plane magnetization (M_p) (see figure 1.3a). The most important advantage of the normal incidence geometry is the disappearance of the longitudinal and transverse Kerr effects, because the projection of the wavevector $\vec{\kappa}$ on the in-plane magnetization components M_l, M_p vanishes whereas it is maximal on the out of-plane magnetization component M_p. Oblique incidence is also possible for the measurement of the polar magnetization component but some mixing of the longitudinal Kerr effect may occur in this case.

1.3.2 Longitudinal

The geometry of the longitudinal Kerr effect is shown in the figure 1.3b. This geometry configuration is sensitive to the in-plane magnetization contained in the plane of incidence. In the longitudinal configuration the magnetooptical magnitudes i.e., the Kerr rotation and ellipticity θ_k, ϵ_k are proportional to M_l. The longitudinal Kerr effect can be thought as a projection of wavevector $\vec{\kappa}$ on the in-plane magnetization component M_l, so that there is a dependence on the angle of incidence. The maximum effect is usually in the range between $60° - 90°$ with respect to the normal to the surface of the sample. Therefore high incidence angles are usually used and the magnetic field is applied parallel to the sample surface. The main disadvantage is that there may be some mixing of polar Kerr effect (if a polar magnetization component exists), which is commonly stronger than the longitudinal one.

1.3.3 Transverse

The geometry of the transverse Kerr effect is depicted in the figure 1.3c. Transverse magnetooptical Kerr effects are observed when the magnetization vector is oriented perpendicularly to the plane of incidence and this is revealed as a change of intensity and phase of the p-linearly polarized light reflected by the magnetized medium. In this case the projection of light wavevector $\vec{\kappa}$ on the magnetization direction is zero. Unlike longitudinal and polar configurations (which detect the field-induced rotation and ellipticity), the transverse effect is detected as a change with the magnetic field of the intensity of the p-polarized light (proportional to the change of the reflection coefficient r_{pp} with the magnetic field). The most important advantages of this configuration are the insensitivity to the polar and longitudinal magnetization components.

1.4 Magnetorefractive effect

Whereas nonzero off-diagonal terms of the permittivity are required for the magnetooptical activity, a magnetic field can induce also changes restricted to the diagonal components, giving way to a magnetorefractive effect (MRE). While magnetooptics is directly connected to the relativistic spin-orbit interaction and its effects are small [3], in the infrared the MRE can provide quite large changes with field -up to 10 -20%- in reflection and transmission [5–14].

The MRE is defined as the change of the refractive index $\tilde{n}$ due to changes in the magnetic structure of the medium [15]. In order to get some phenomenological understanding of the MRE, let us consider the complex refractive index $\tilde{n} = n + i\kappa$, where n and κ are the refractive index and absorption coefficients, respectively. For an electromagnetic wave of frequency ω propagating in a medium with refractive index $\tilde{n}$, optical dielectric constant $\tilde{\epsilon}$ and conductivity $\tilde{\sigma}$, the following expression holds:

$$\tilde{n} = \sqrt{\tilde{\epsilon}} = \sqrt{1 + i\frac{4\pi\tilde{\sigma}}{\omega}} \tag{1.28}$$

where it was assumed that the magnetic permeability is $\mu = 1$ at the frequency ω. That means that strong changes of the conductivity should drive significant changes of the optical properties (such as optical transmission and reflectance) through the modification of the refractive index. The magnetorefractive effect has been studied extensively in the far- and mid-infrared in different systems, including granular alloys, nanocomposites,

single crystals, thin films and photonic crystals [9, 10, 12–14, 16–18, 18–28], but these effects have been much less investigated in the visible range of wavelengths [1]. In chapters 4-6 we describe our results on the analysis of the magnetorefractive effect by carrying out a spectroscopy of the complex transverse Kerr effect in a variety of magnetic oxides showing a prominent metal-insulator transition: colossal magnetoresistance thin films, viz. $La_{0.7}Ca_{0.3}MnO_3, La_{0.7}Sr_{0.3}MnO_3, (Pr_{0.4}La_{0.6})_{0.7}\,MnO_3$, and magnetite. Probing the metal-insulator transitions with the transverse magnetooptic signal we are able to discriminate between the magnetooptical response from the MRE, and relate the latter with the magneto-transport at optical frequencies.

[1] In this Thesis we use the term magnetorefractive effect in a broad sense to go beyond the high-frequency response of the magnetoresistance. Therefore, the concept considered here also includes different mechanisms of magnetoreflection/magnetotransmission related to field-induced changes of the electronic structure, such as field-modulated interband transitions or the influence of the magnetic field on polaron conduction and Jahn-Teller interactions.

CHAPTER 2

Metal insulator transitions in magnetic oxides

2.1 Overview

The analysis of metal-insulator transitions is one of most studied topics in solid state physics. These transitions are usually accompanied by huge resistivity changes that, for particular cases, can be of several orders of magnitude [29]. In addition, for temperatures close to the metal insulator transitions, some magnetic materials display a strong magnetic dependence of the transport properties. In these cases, a spin-dependent magneto-transport appears as a change of electric resistance upon varying external magnetic field. Most of the efforts have been focused, almost entirely on static (d.c) and low frequency (infra-red) behavior which are dominated by free electrons (Drude contribution). However huge resistivity changes are observed in the optical response as well [30] giving way to a sizeable magneto-refractive effect.

Optical spectroscopy can reveal invaluable information closely related to intra-band transitions and localized electronic states. Especially important are the transitions driven by correlation effects associated with both the $electron - electron$ and $electron - phonon$ interactions. The colossal magneto-resistance (CMR) manganites afford an interesting playground to test the magnetotransport at optical frequencies. Manganites are electron-correlated systems in which the spin, lattice and orbital degrees of freedom are interweaved and give way to dramatic changes of the resistivity with the magnetic field [31]. Near the metal-insulator transition, the transport in manganites is dominated by Jahn-Teller polarons with energy scales of the eV, and thus can be probed by visible wavelengths. Since Jahn-Teller distortions are strongly affected by both temperature and magnetic

fields, we expect a strong changes in the magneto-transport tested at visible frequencies in a narrow window of temperatures around the Curie temperature. Other classical example is the Verwey transition in magnetite for which, unlike manganites, the resistivity jump across the transition is not related to any magnetic transition. Although originally purely electronic effects were postulated to drive the Verwey transition, recent works also point to a fundamental role of electron-phonon coupling [32]. The first objective of this Thesis has been devoted to analyze the magnetooptical spectral response for temperatures around the metal-insulator transition of several magnetic oxides, including some manganites and magnetite.

2.2 Manganites

The manganites exhibit a variety of properties, such as ferroelectricity and colossal magnetoresistance (CMR), which makes them appealing to study both in terms of basic research and from a technological viewpoint. The research in this field has been driven by a desire to understand and exploit the large negative magnetoresistance effects which appear near and below the Curie temperature of these materials [33]. Although a full literature review of manganites is out of the scope of this Thesis, several references are mentioned. A detailed review about metal-insulator transitions was published by Imada *et al.* [29] in 1998, followed by Coey *et al.* [33] in 1999 who reviewed different aspects of manganite physics, including the nature of the electronic ground states, the effects of pressure and temperature, the mechanisms for the electronic transport and the physics of polarons. Subsequently, in 2001 Dagotto *et al.* [34] reported a extensive review about phase separation in CMR, and around this year Salamon and Jaime [35] reviewed the progress made at that time, the concept of double exchange in particular, and pointed out the elements that have led to a massive resurgence of interest in these materials. Finally, a year later Edwards [36] published a review about electron-phonon coupling in the manganites.

The laboratory of magnetic materials and functional oxides led by Prof. Josep Fontcuberta, has investigated manganites for more than 10 years. From this activity many publications [37–54]) and several thesis have been published in this period, in particular we cite Bibes [55], Herranz [56], Infante [57] and Marti [58].

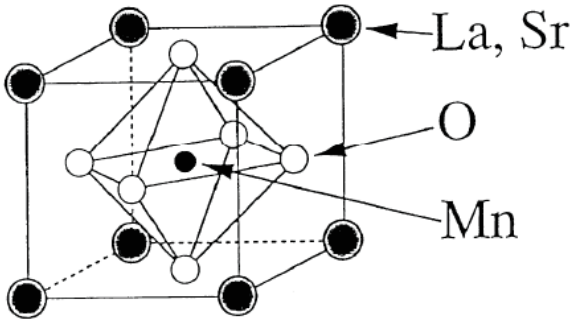

Figure 2.1: *The basic perovskite structure. Taken from [33]*

2.2.1 Basic properties of manganites

The manganite perovskites can be regarded as solid solutions between end members such as $AMnO_3$ and $BMnO_3$, where usually $A = La, Bi, Nd...$ and $B = Ca, Sr, Ba....$ Formal valence states can be assigned to $A^{+3}Mn^{+3}O^{-2}_{+3}$ and $B^{+2}Mn^{+4}O^{-2}_{+3}$, leading to mixed-valence compounds such as $(A^{+3}_{1-x}B^{+2}_{x})(Mn^{+3}_{1-x}Mn^{+4}_{x})O_3$ with the relative fraction of Mn^{+3} and Mn^{+4} being controlled by x. The nominal electronic configurations of the Mn^{+3} and Mn^{+4} are $3d^4$ and $3d^3$ respectively. The basic structure is shown in the figure 2.1.

The structure is characterized by the wide range of cations that can occupy the A site in the perovskite structure, which may be set at the body-centre or the cube corner (2.1). A good way to regard the structure is as a cubic close-packed array formed of O^{2-} anions and large A cations, with the small B cations in the octahedral interstitial sites. The oxygen octahedron surrounding the B site cation splits the energy levels of a $3d$ ion such as Mn^{3+}, i.e., the crystal field induced by the oxygen ions in the perovskite structure splits the $3d$ levels into a low energy t_{2g} triplet and a high energy e_g doublet, producing a further braking of orbital degeneracy.

We select some of our measurements in order to illustrate some properties. The figure 2.2 shows the magnetic and d.c. transport basic properties of a typical $La_{0.3}Ca_{0.7}MnO_3$ (LCMO) manganite. An inspection of figure 2.2a immediately reveals that the magnetization of the LCMO films displays a magnetic transition from paramagnetic to ferromagnetic as the temperature decreases, with a transition temperature (Curie temperature) around $T_C \approx 268K$. The inset in the figure 2.2a shows a ferromagnetic hysteresis loop measured at $10K$. The magnetic transition can be observed in the d.c. transport properties as well (2.2b). The temperature dependence of the resistivity measured at magnetic fields $H = 0kOe$ as $H = 90kOe$ is shown in the figure 2.2b. The magnetotransport character-

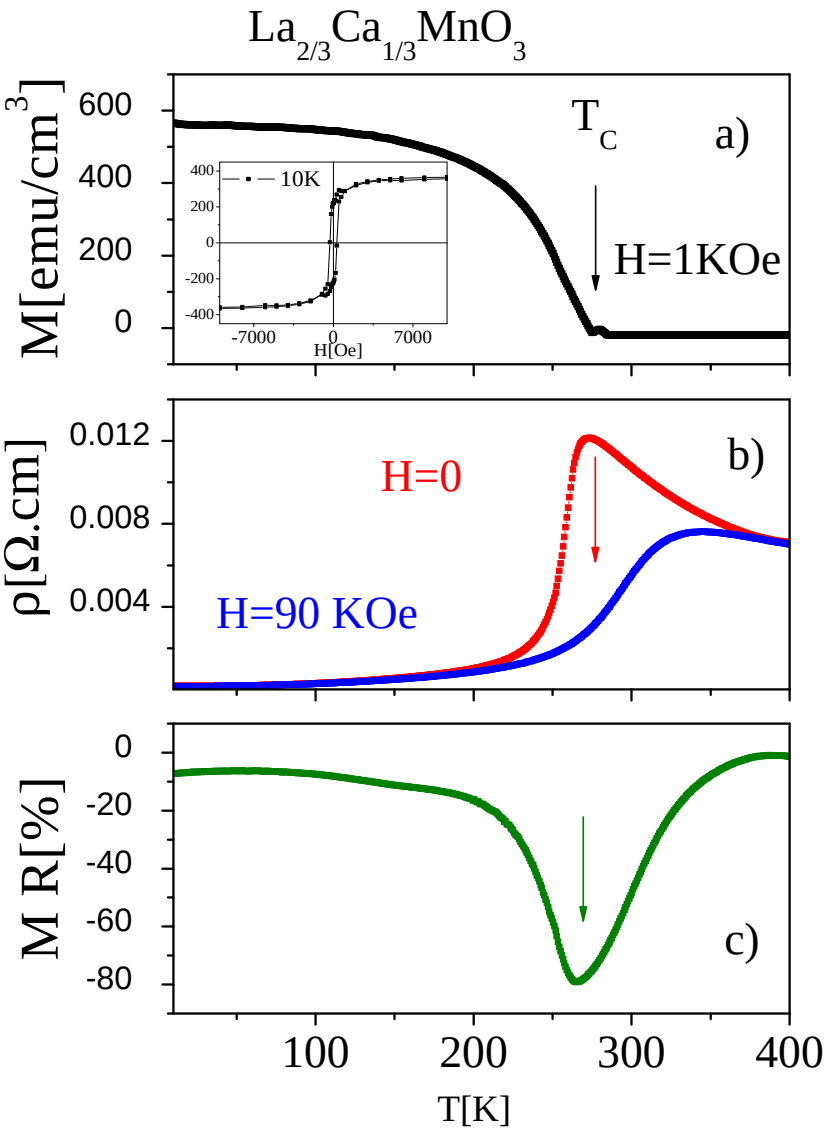

Figure 2.2: *Magnetic and d.c. transport basic properties on LCMO. Magnetization temperature dependence a), Magnetization field dependence (inset), zero field cool (red curve) and field cool (blue curve) resistance b), magnetoresistance c)*

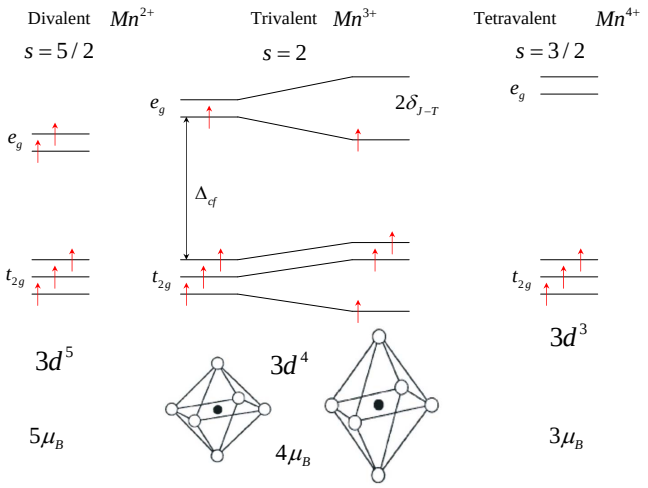

Figure 2.3: *Manganese ions electronic structure. After to [34]*

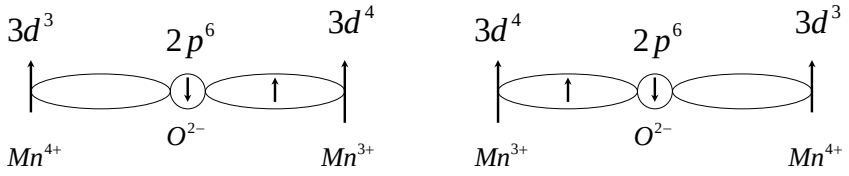

Figure 2.4: *Schematic diagram of the double-exchange mechanism. After to [33]*

ization reveals a clear metal insulator transition (MIT) closely related to the magnetic properties. Indeed, the application of a magnetic field leads to a large suppression of the resistance resulting in a colossal magnetoresistance, typical of such type of systems. Finally, the negative magnetoresistance defined as $MR(\%) = (\rho(H) - \rho(0))/\rho(0)$ is shown in the figure 2.2c. The MR shows a peak around T_C.

Electronic features in manganites

There seems to be a consensus in the literature about the fundamental mechanisms explaining the transport and optical properties in manganites. viz.

- Strong *Hund's rule exchange coupling*: the $A_{1-x}B_xMnO_3$ system contains $(4-x)Mn-d$ electrons, three of which occupy the t_{2g} levels, d_{xy}, d_{yz}, d_{zx} providing a strong localized core spin of $S_c = 3/2$, while the remaining $(1-x)$ electron occupies the e_g level, with its spin oriented parallel to the core spin due to a large Hund's rule exchange coupling (J_H) in the system (see figure 2.3).

  Starting from the insulating antiferromagnetic $AMnO_3$ end member where electrons

are localized on the atomic orbitals, Zener [59, 60] showed how the system should gradually become ferromagnetic upon hole doping (introduction of Mn^{+4}), see figure 2.4. He considered the problem of the exchange between Mn^{+3} and Mn^{+4} ions via an oxygen ion and introduced the concept of simultaneous transfer of an electron from the Mn^{+3} to the oxygen and from the oxygen to the neighbouring Mn^{+4}. Such a transfer was called double exchange. In the case of magnetic atoms, the configurations $Mn^{3+} - O^{2-} - Mn^{4+}$ and $Mn^{4+} - O^{2-} - Mn^{3+}$ are degenerate if the spins of the two d shells are parallel, and the lowest energy of the system at low temperature corresponds to parallel alignment of the spins of the two adjacent cations. The resulting hopping of the *spin-polarized* e_g electrons between Mn^{+3} and Mn^{+4} sites largely accounts for dramatically *colossal magnetoresistance* behaviour observed in $A_{1-x}B_xMnO_3$ system.

- *Jahn-Teller distortion*: A distortion of the oxygen octahedron lowers the symmetry of the cubic crystal field in such a way that the centre of gravity of the t_{2g} levels and the centre of gravity of the e_g levels is unchanged. There is therefore nothing to be gained by Mn^{2+} or Mn^{4+} from such a distortion, but Mn^3 can lower its energy in proportion to the distortion, and the corresponding penalty in elastic energy will scale as the distortion squared, hence we have the marked tendency of d^4 ions to distort their octahedral environment in order to lower their energy (see figure 2.3). Many references have shown that Jahn-Teller distortions in $A_{1-x}B_xMnO_3$ strongly influence the transport by localizing the carriers in polaronic states [61–66]. There is now substantial evidence that transport and optical properties in manganites are dominated by the field-dependent polaronic transport and, indeed, CMR manganites are distinguished by their strong electron-lattice coupling.

Electron-phonon coupling and polarons

Thus, the double exchange is not enough to explain completely the transport properties in manganites. The electron-phonon coupling and the formation of polarons may depend on the hole doping of the manganite. A typical example is provided by $La_{1-x}Sr_xMnO_3$ (LSMO), for which the resistance is strongly dependent on the doping range. Outside the ferromagnetic concentration range (x $<$ 0.15), resistivities are high and are thermally activated, but a resistance anomaly appears around T_c for the ferromagnetic compositions (x $>$ 0.15), where there is a transition from thermally activated conduction (polaron hopping, see below) to metallic like conduction (via double exchange), see figure 2.5.

In systems where there is a sufficiently strong coupling to the local phonon modes, an

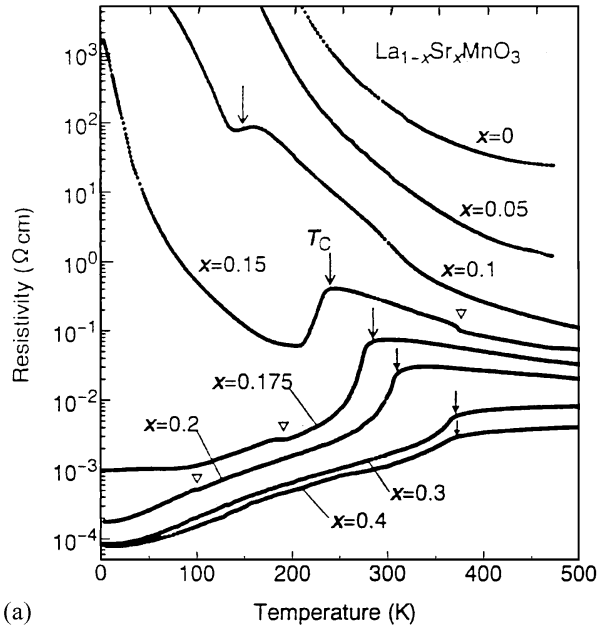

Figure 2.5: *Temperature dependence of the resistivity for single crystal $La_{1-x}Sr_xMnO_3$. Arrows indicate the Curie temperature. Open triangles indicate anomalies due to structural transitions. Taken from [67]*

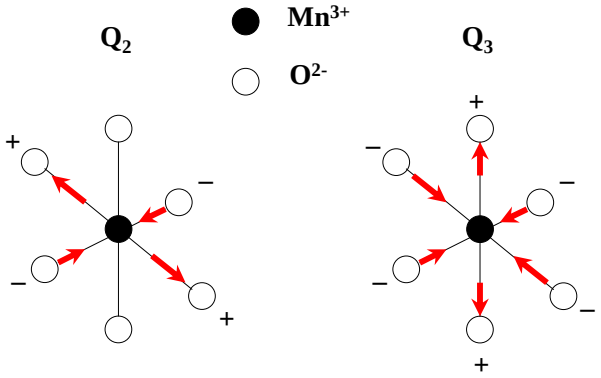

Figure 2.6: *Q_2 Jahn-Teller distortion of the basal plane and Q_3 octahedral stretching mode*

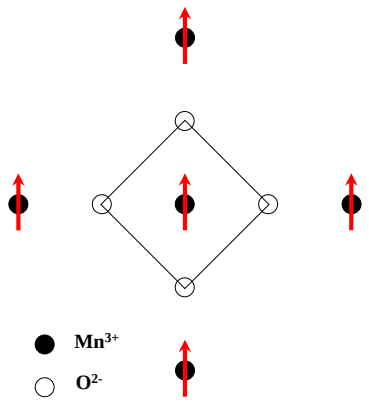

Figure 2.7: *Q_1: Magnetic or spin polaron (Breathing mode compose by $Q_2 + Q_3$)*

electron can produce a strong localized distortion of the lattice. This distortion moves with the electron, and the whole structure is called a small polaron. In general, if there is strong electron-phonon coupling, the free-carriers can become trapped and we will observe an increased resistance in the sample. Such a change in resistance is observed at the metal-insulator transition. According to Coey *et al.* [33], polarons are thought to take one of three forms. The first is a $dielectric - polaron$ where the electron bears with it a dilation of the MnO_6 octahedron associated with the breathing mode Q_3 (figure 2.6). The second is the $Jahn - Teller$ polaron Q_2 (figure 2.6) where the electron carries with it an axial distortion of the MnO_6 octahedron. The third is a magnetic $spin - polaron$ (figure 2.7) where there is a ferromagnetic polarization of the surrounding manganese core spins. The origin and formation conditions for polarons can be found in several references [68–73]. The available evidence suggests that optical conductivity in manganites is also consistent with a polaronic transport [74].

Optical properties of manganites

The dependence of the electronic structure of ($A_{1-x}B_xMnO_3$) manganites with temperature, pressure and magnetic field has been investigated intensively. Several optical features have been reported below $\approx 5eV$ (See references [73–77] and figure 2.8). As derived from a number of different reports, the optical conductivity spectrum of manganite perovskites can be understood in terms of two broad intensive bands centered around 2.0 and 4-5 eV [75–82]. Although the nature of the lower energy transitions has been somewhat controversial [79], it has been argued recently, based on cluster model calculations, that features around 2.0 eV should be attributed to intersite d-d charge transfer transitions, whereas the higher-energy transitions should be related to one-center p-d charge transfer transitions [79]. Thus, based on this model, at relatively low energies in the range of near-infrared and visible, light should induce the photoionization of Jahn-Teller polarons [as suggested by Zhao *et al.* [83], i.e., should promote the hopping of e_g electrons between neighboring sites. This feature will become relevant for the discussion of the magnetorefractive effect and its relationship with the magnetic field dependent polaron conductivity (section 4.3.1).

2.3 Magnetite

Manganite, the famous lodestone, (Fe_3O_4), is the first magnetic material known to man. It belongs to the family of the spinel ferrites, with ferrimagnetic ordering ocurring at a temperature as high as $858K$ [84]. The most notable feature of magnetite is the presence

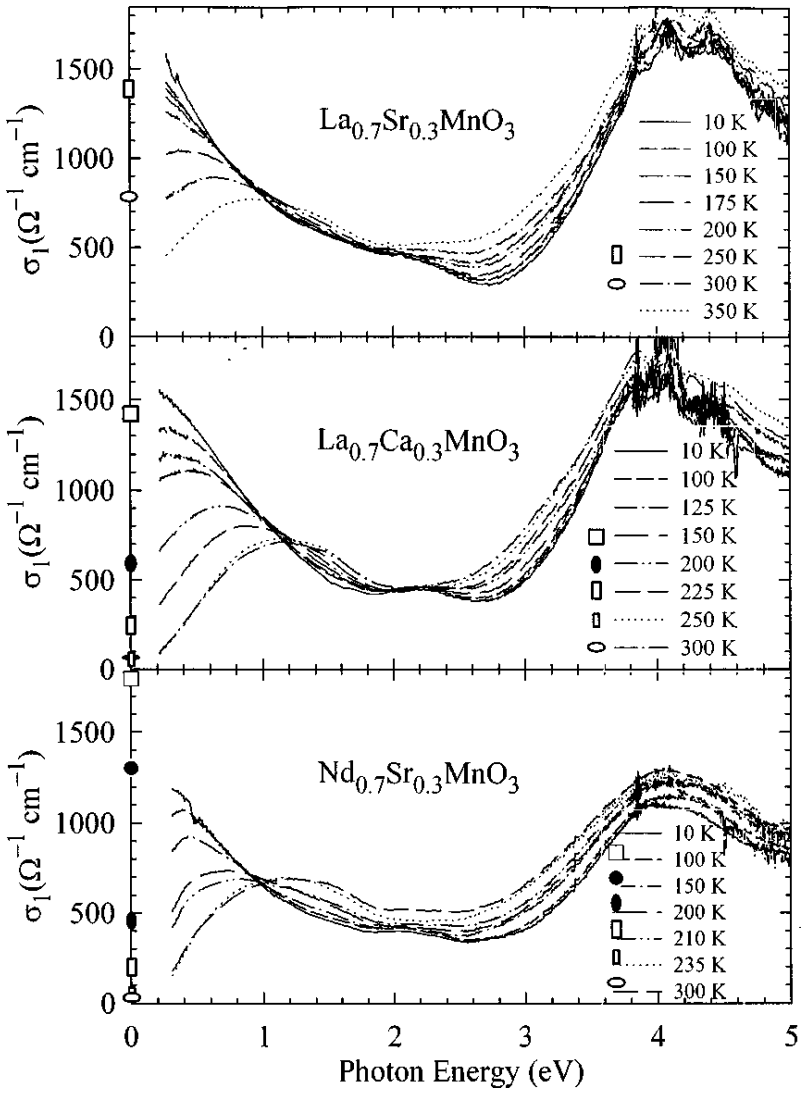

Figure 2.8: *Frequency dependence of the real part of the optical conductivity σ_1 for three samples at different temperatures. Taken from [74]*

of a metal to insulator transition (*The Verwey transition*) at a temperature of $\approx 125K$ [85–88], in which the conductivity abruptly decreases by two orders of magnitude. The nature of this transition, in spite of almost 70 years of dedicated research, is still a matter of controversy [32, 87]. The classical description of the Verwey transition in magnetite is done through purely electronic effect where charge order is argued, on the another hand, a new approach to explain this transition including electron-phonon coupling and localized states as in manganites is on debate [32].

2.3.1 Basic properties of magnetite

In the following sections, we provide details of the properties of bulk and thin flms of magnetite.

Basic Structure

Manganite (Fe_3O_4) crystallizes on the inverse spinel structure with a lattice constant of $0.8397nm$ [89]. The electronic configuration $[Fe^{3+}]_A[Fe^{2+}, Fe^{3+}]_BO_4$, where A and B mean respectively the tetrahedral and the octahedral sites in the spinel structure. The basic structure is shown in the figure 2.9. The spinel structure can be thought of as made up by alternate stacking of two different cubes as shown in the figure 2.9. The large oxygen atoms form a close-packed face-centered cubic structure with the smaller iron atoms occupying the interstitials positions. There are two types of the interstitial sites both occupied by the iron atoms:

- The tetrahedral (8) sites or $A - sites$ occupied by Fe^{3+}
- The octahedral (16) sites or $B - sites$ occupied by a mixture of Fe^{3+} and Fe^{2+}

With respect to the oxygen ions, the unit cell comprises a face centred elementary cube that contains 32 O^{2+} ions. Per unit cell this compilation contains 64 interstices of the tetrahedral type (surrounded by 4 oxygen ions) and 32 interstices of the octahedral type (surrounded by 6 oxygen ions), see figure 2.10. In Fe_3O_4 the elementary cell contains 8 Fe^{2+} and 16 Fe^{3+} ions.

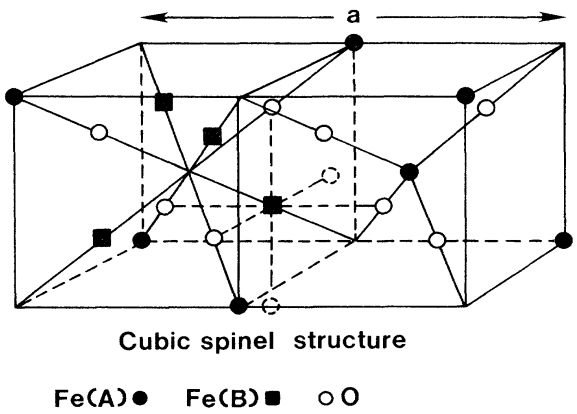

Figure 2.9: *Cubic spinel structure of Fe_3O_4 magnetite. Taken from [84]*

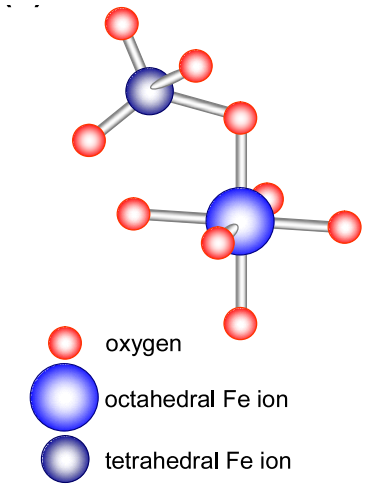

Figure 2.10: *Octahedral and tetrahedral sites in magnetite. Taken from [90]*

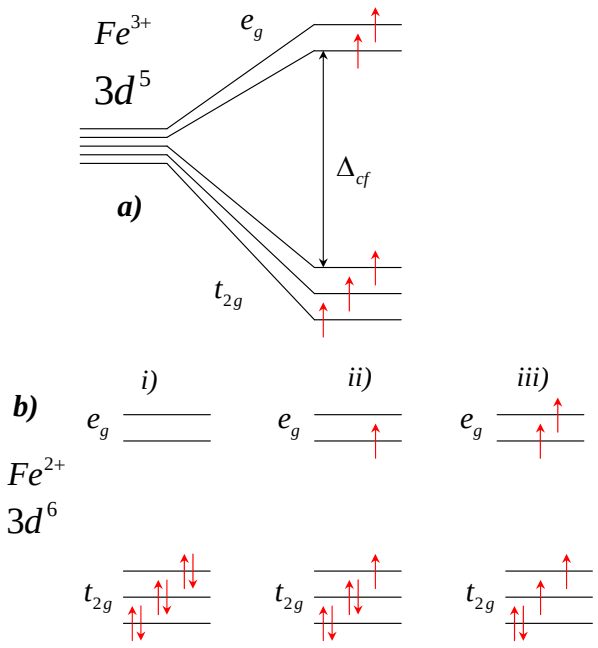

Figure 2.11: *The splitting of the* 5*d levels due to a crystal field(a),the three possible electronic configurations of* Fe^{2+} *in an octahedral site*

Conductivity and electronic structure

The high conductivity of magnetite at room temperature is claimed to be the consequence of the electron delocalization between the octahedral neighbouring Fe ions, presenting an average oxidation state of $Fe^{2.5+}$ [85, 86]. The five d orbitals split into two e_g levels and three t_{2g} levels. The two different iron ions, $Fe^{2+}(d^6)$ and $Fe^{3+}(d^5)$, are present in the octahedral sites. The Fe^{3+} ions are in a high spin state, with the 5 electrons arranged in parallel, in accordance with Hund's rule. The antiferromagnetic (AF) alignment of the two consecutive crystallographic planes causes the magnetic moment associated with these Fe^{3+} ions in the $B-site$ to be partially cancelled by the one of the Fe^{3+} ions in the $A-site$. There are three possible electronic configurations for a Fe^{2+} ion, see figure 2.11b). The high spin configuration with 4 unpaired electrons is believed to be correct because it is in agreement with the value of the magnetization measured experimentally of 1 μ_B per formula unit. The additional spin down electron of the Fe^{2+} ion in the octahedral site can hop to a neighboring Fe^{3+} site provided their spins are parallel. In the magnetically ordered state, only the $spin-down$ electron can easily move, resulting in $spin-polarised$ electron transport. The electron transport is restricted to the $B-sites$. $B-sites$ are oriented ferromagnetically because of their mutual anti-ferromagnetic coupling to the $A-site$ spins. Recent studies suggest that electrons are trapped within groups of three iron atoms, where they can no longer transport an electrical current. The localized electrons

are distributed over linear three-Fe-site units, which they call trimerons [91, 92].

Verwey transition

The most interesting characteristic of magnetite is the presence of a metal to insulator trantition, known as Verwey transition [93]. The transition temperature (T_V) is $125K$ at which the structure distorts from its cubic symmetry and it has been proposed that a charge ordering occurs at the B sites thus reducing the conductivity [85, 86]. Despite the fact that the Verwey transition has been extensively studied since the late $1940s$, its mechanism is still a matter of discussion and controversy [32, 87, 88, 94, 95]. Various theoretical models have been proposed to explain the electron transport mechanism in the $low-$ and $high-$ temperature phases, and the sudden change in conductivity at the transition point [87, 93]. However, recent studies demonstrate that the Verwey transition is a cooperative phenomenon driven by polarons, in which an interplay between lattice, charge and orbital degrees of freedom plays a decisive role. The idea that both Coulomb interactions and the $electron - phonon$ coupling are responsible for the transition was first proposed by Ihle and Lorenz [96], and their model provides a good description of the electric conductivity above T_V. Piekarz *et al.* [88, 97], have recently investigated the mechanism of the Verwey transition in terms of a group theory analysis in conjunction with electronic structure calculations and analysis of the neutron scattering data. They concluded that in the presence of electron correlations the coupling between the electrons in t_{2g} states and phonons is largely enhanced since it leads to stabilization of the orbital ordering and a lowering of the total energy. This coupling between $charge - orbital$ fluctuations and phonons can also account for the observed critical diffuse scattering observed by neutron scattering measurements, which already appears about $200K$ [98, 99].

Optical properties in magnetite

The optical properties of magnetite can be understood in terms of two main concepts: viz. inter-valence charge transfer (IVCT) and inter-sublattice charge transfer (ISCT). In IVCT transitions an electron is transferred to a neighboring cation through an optical excitation. Mixed valence compounds, i.e., compounds containing an element in two different oxidation states, such as Fe in Fe_3O_4, often shows an unusually intensive absorption in the visible range that can be attributed to IVCT transitions. In Fe_3O_4, the electron transfer between Fe^{2+} and Fe^{3+} may be mediated by O^{2-} ions, in particular when e_g orbitals are involved. Between $Fe[t_{2g}]$ orbitals direct electron transfer is possible as a result of overlap between these orbitals. On the other hand, ISCT transitions are IVCT transitions between

Fe^{3+} ions on different crystallographic sites [100, 101]. Ellipsometry and magnetooptical experiments have allowed the understanding of the electronic structure in magnetite (figure 2.12)[102]. Thus, in the optical spectra a feature at $E = 1.94eV$ is generally assigned to IVCT transitions between B (octahedral) sites $[Fe^{2+}]t_{2g} \rightarrow [Fe^{2+}]e_g$, whereas those at $E \approx 2.61eV$ and $E \approx 3.11eV$ correspond to A-B ISCT transitions ($Fe^{3+}t_2 \rightarrow [Fe^{2+}]t_{2g}$) and $[Fe^{3+}]t_2 \rightarrow (Fe^{2+})e$, respectively (See reference [102] and figure 2.12)

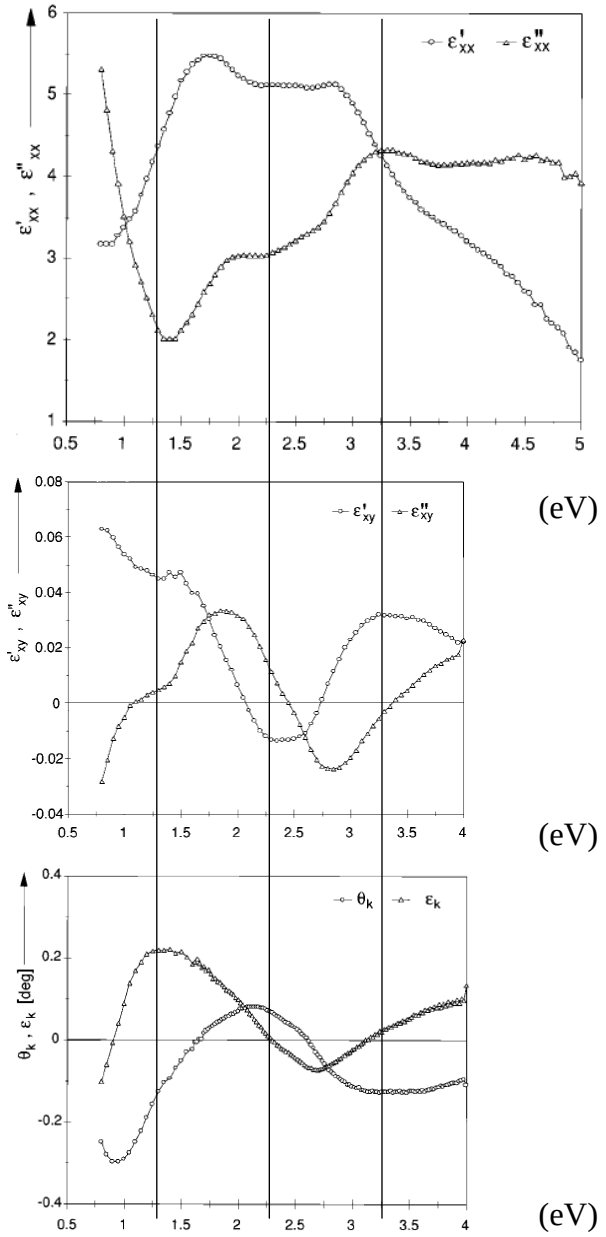

Figure 2.12: *(Top) The real and imaginary part of diagonal elements of the dielectric tensor,(Center) real and imaginary part of off-diagonal elements of the dielectric tensor,(Bottom) the rotation and ellipticity on magnetite. Taken from [102]*

CHAPTER 3

Experimental

3.1 Introduction

In this section, we give details on some of the experimental techniques that are employed for magnetooptical characterization in this Thesis. A variety of experimental ellipsometry techniques [103] have been reported in the literature to characterize the magnetooptical properties of thin films. Particularly magnetooptic vector magnetometry is widely used for monitoring the magnetization reversal and the magnetic anisotropy. As described in previous sections, three components of the magnetization vector are usually distinguished in reflection experiments: the polar component M_P (perpendicular to film interfaces), the longitudinal M_L (in-plane component parallel to the plane of light incidence), and the transverse magnetization component M_T (in-plane and perpendicular to the plane of incidence). In the following, we will give details on the methodology that we have applied to measure the magnetooptic coefficients in different configurations.

3.2 Magnetooptical transverse Kerr effect

As discussed above in chapter 1, the transverse magnetization component causes a change of the r_{pp} reflection coefficient. Thus, it will be shown that measurements of transverse Kerr are quite appropriate to disentangle in a single experiment the contributions of both magnetooptics and the magnetorefractive effect to the optical signal. In the following subsections we give a short overview of different approaches to obtain the spectral transverse signal.

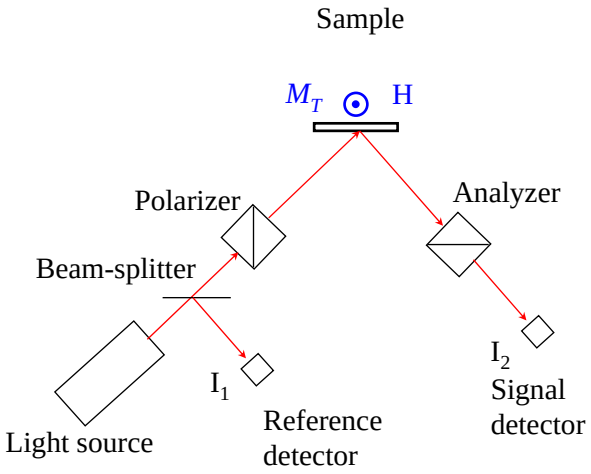

Figure 3.1: *Transverse Kerr effect differential method*

3.2.1 Overview of experimental approaches

Conventional static differential method

To measure the transverse response, static (d.c.) methods can be carried out to measure the intensity of $p-$ polarized light reflected by the magnetic surface with and without applied magnetic field (figure 3.1). The r_{pp} reflection coefficient is given by:

$$r_{pp}(M) = r_{pp}(M=0) + \Delta r_{pp}(M) \tag{3.1}$$

The first term is the reflection coefficient without magnetization and the second one is a small perturbation caused by the transverse magnetization component that includes the magnetooptical Kerr effects. The measured signal is the difference of the reflectivity:

$$|r_{pp}(M)|^2 - |r_{pp}(M=0)|^2 = 2Re[\Delta r_{pp}(M) r_{pp}(M=0)] + |\Delta r_{pp}(M)|^2 \tag{3.2}$$

The second term in Eq. 3.1 describes the transverse quadratic magnetooptical Kerr effect which is usually neglected, although, as it will be discussed in the chapters 4 and 5, a quadratic contribution can be up to two orders of magnitude larger than the linear contribution in the range of optical frequencies $(1-5eV)$ for some systems.

The static differential method has important drawbacks. On one hand, the magnetooptical coefficients are quite small, with amplitudes that are usually in the order of a few *mrad* or smaller. In addition to this, an additional serious disadvantage is the sensitivity

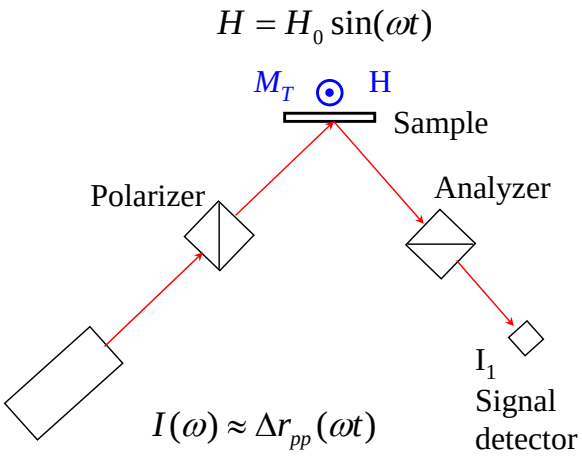

Figure 3.2: *Transverse Kerr effect using magnetic field modulation technique*

to both noise of the detectors and the vibrations of the optical elements. In order to overcome these difficulties, several modulation techniques have been developed, namely: magnetic field modulation, intensity light modulation, and phase modulation, which are described in the following.

Modulation ellipsometry techniques

Magnetic field modulation

This technique consists of applying an oscillatory magnetic field parallel to the surface of the sample (in-plane) and demodulating the signal with a lock-in amplifier as it is shown in the figure 3.2. The main disadvantage of this method is the low frequency modulation (a few kHz) limited by the huge inductance in the electromagnets, and consequently it is restricted to low magnetic fields.

Intensity light modulation

The intensity light modulation is also known as azimuth modulation. Unlike both static and magnetic field modulation methods, it exploits the modulation of the intensity of the incident light. It can be done using either an optical chopper wheel or Faraday rotators [1] placed before the polarizer as illustrated in the figure 3.3. The chopper wheel modulation is mainly limited by frequency while Faraday rotators have the same problems related to

[1] A Faraday rotator is an optical device that rotates the polarization of light due to the Faraday effect, which in turn is based on a magnetooptic effect. The plane of linearly polarized light is rotated when an oscillating magnetic field ($H_{a.c.}$) is applied parallel to the propagation direction.

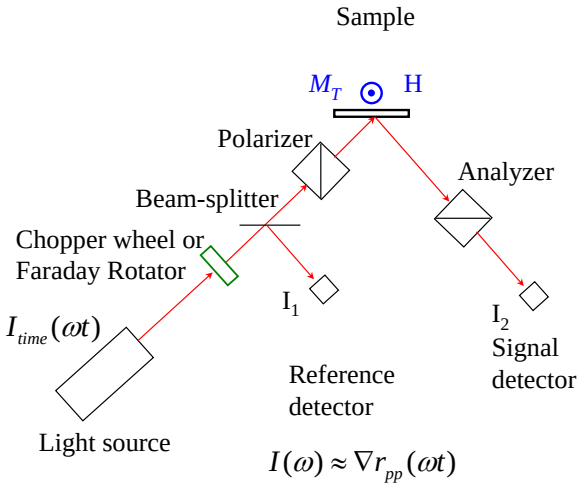

Figure 3.3: *Transverse Kerr effect using intensity light modulation technique by chopper wheel or faraday rotator*

magnetic field modulation, that is, limitations due to large inductance of the coils at high frequencies. Pioneer works using this technique were published by Florczak and Dahlberg [104, 105], and they showed a way to detect two orthogonal in-plane magnetization components using this kind of modulation. Some authors have proposed an approach based on photoelastic modulation to get high frequency modulation of the incident light intensity [106], and similar results have been obtained by using high speed chopper.

Phase modulation techniques

In this section we present the most successful method for high frequency modulation and high magnetooptical resolution. The phase modulation techniques using photo elastic modulator (PEM) have been studied for almost 30 years. This device modulates the polarization state of the light with a frequency of $\approx 50kHz$. The PEM introduces an oscillation phase between the two orthogonal polarization components of the light. This phase difference varies between the values of $+\pi/2$ and $-\pi/2$ radians. The polarization state of the light now oscillates between right circular polarization (RCP) and left circular polarization (LCP) states through right-handed and left-handed elliptical states (RCP and LCP, respectively) as is shown in the figure 3.4.

The Jones matrix representation of a PEM modulator is given by:

$$\begin{pmatrix} e^{i\varphi/2} & 0 \\ 0 & e^{-i\varphi/2} \end{pmatrix} \tag{3.3}$$

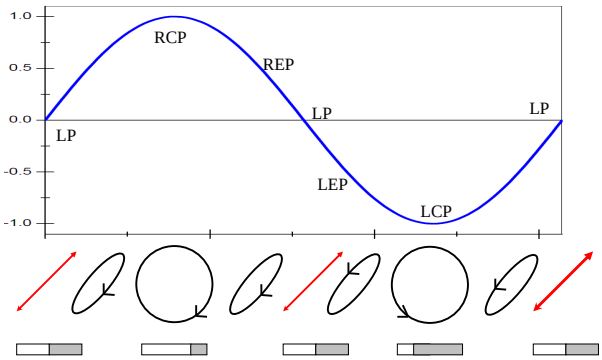

Figure 3.4: *Phase difference between the x and y components of the polarized light introduced by the PEM for a one period of the oscillation $T(1/T = 50kHz)$*

where, $\varphi = (\pi/2)\sin(\omega t)$ and $\omega = 50$ kHz.

A complete description about PEM can be found in several references [107–112]. Early reports about phase modulation and its applications in either spectroscopy and magnetooptics were published by different authors [107, 109, 113, 114]. K. Sato [110] developed an innovative method that allows a simultaneous determination of two mutual conjugate parameters, namely, Kerr rotation and reflectance magnetic circular dichroism, using a polar configuration. Furthermore they showed that in polar configuration, the reflectance magnetic circular dichroism can be related to Kerr ellipticity. Jordan and Whiting [115] modified the method with variable azimuth of the polarizer measuring a combination of longitudinal and transverse magnetooptical effect. Unfortunately, the separation of the two in-plane magnetization components remained a limitation of those techniques. The real component of transverse Kerr effect was measured using the set-up proposed by Osgood *et al.* [116, 117, 118], and P. Vavassori [119]. In those reports a Polarizer-Sample-PEM-Analyzer system was used to detect the real part of the transverse Kerr effect using the signal at the second harmonic frequency of the modulator, but the configuration does not allow the measurement of the complex transverse Kerr effect.

3.2.2 Complex transverse magnetooptical Kerr effect measured by null ellipsometry

General concepts

To measure the complex transverse magnetooptical Kerr effect, i.e., both the real and imaginary part, we built up a system based on null ellipsometry with phase modulation. The null ellipsometry is a technique based on the measurement of azimuth angles of

polarizer, compensator, and analyzer for which the detected intensity is extinguished [103]. It is highly accurate and almost free of systematic errors. Averaging the ellipsometry angles obtained for different sets of azimuth angles (null zones) gives insensitivity to azimuths misadjustments and to imperfections of the polarizing components. The main disadvantage of this method comes from both a weak signal and a parabolic intensity dependence close the null condition that can be overcome by including an azimuth modulation in the null ellipsometry system [120]. These difficulties can be still better overcome by using null ellipsometry with phase modulation as proposed by Postava *et al.* [121]. We have followed this approach to measure the transverse magnetooptical coefficient that we describe in the following. More details about null ellipsometry can be found also in the appendix C.

Ellipsometry measures the change of light polarization by measuring the complex reflectance ratio $\rho = \frac{r_{pp}}{r_{ss}} = \tan(\psi)e^{i\Delta}$, which defines the so-called ellipsometric angles Ψ and Δ. Thus, $\tan(\psi)$ is the amplitude ratio upon reflection, and Δ is the phase shift. Since ellipsometry measures the ratio (or difference) of two values (rather than the absolute value of either), it is very robust, accurate, and reproducible. For instance, it is relatively insensitive to scattering and fluctuations, and requires no standard sample or reference beam. In ellipsometry-based experiments, the complex transverse Kerr effect is defined as a small perturbation of the standard ellipsometry angles ψ and Δ. The set-up proposed by Postava *et al.* [121] is based on a Polarizer-PEM-Sample-Compensator-Analyzer configuration to measure the complex transverse signal. Indeed, the measurement of both the real and the imaginary parts of the complex transverse Kerr effect can be advantageous in many situations, e.g., to obtain the complex permittivity tensor components (1.20) or just because the two independent quantities display different depth sensitivities, which may be exploited in the determination of optical in-depth profile of samples. Also, the signal measured by the imaginary part can be stronger than real part (or viceversa), see figure 3.5.

Mathematical description

The complex transverse response is related to small perturbations of the standard ellipsometry angles ψ and Δ:

$$\psi = \psi + \delta\psi \tag{3.4}$$

$$\Delta = \Delta + \delta\Delta \tag{3.5}$$

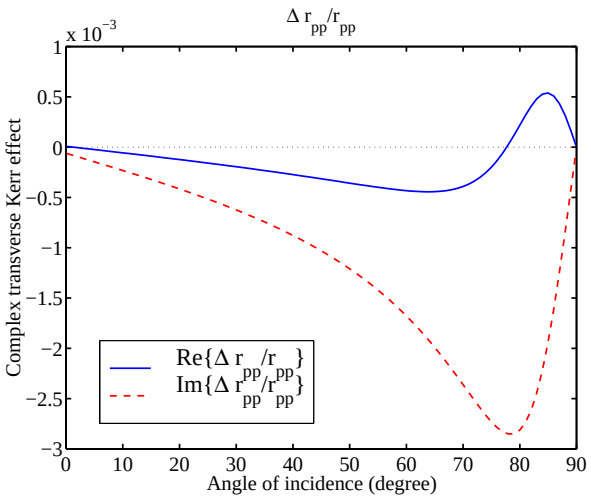

Figure 3.5: *Modeled complex transverse magnetooptical Kerr effect, with the real component (blue curve), and the imaginary (dashed red curve) components. Taken from [121]*

The complex reflectance ratio then becomes:

$$\rho = \frac{r_{pp}}{r_{ss}} = \tan(\psi + \delta\psi)e^{i(\Delta+\delta\Delta)} \tag{3.6}$$

Assuming that $\delta\Delta \ll \Delta$ and $\delta\psi \ll \psi$, i.e., $e^{i(\Delta+\delta\Delta)} \approx (1 + i\delta\Delta)\, e^{i\Delta}$ and $\tan(\psi+\delta\psi) \approx \tan(\psi) + (1 + \tan^2(\psi))\, \delta\psi$, it is possible to demonstrate that the normalized changes of the intensity of p-polarized reflected light can expressed as a function of $\delta\Delta$ and $\delta\psi$ through [121]:

$$\frac{\Delta r_{pp}}{r_{pp}} = \frac{2}{\sin(2\psi)}\delta\psi + i\delta\Delta \tag{3.7}$$

To arrive at Eq. 3.7 it is assumed that the coefficient r_{ss} is not altered by the magnetic field, as it occurs in the magnetooptic transverse signal (see chapter 1). From Eq. 3.7 we can obtain the real and imaginary part of the complex transverse magnetooptical Kerr effect:

$$\Re\tau(\delta\psi, \delta\Delta) = \Re\left(\frac{\Delta r_{pp}}{r_{pp}}\right) \tag{3.8}$$

$$\Im\tau(\delta\psi, \delta\Delta) = \Im\left(\frac{\Delta r_{pp}}{r_{pp}}\right) \tag{3.9}$$

Thus, a suitable experimental set-up has to be designed to measure $\delta\psi$ and $\delta\Delta$ and

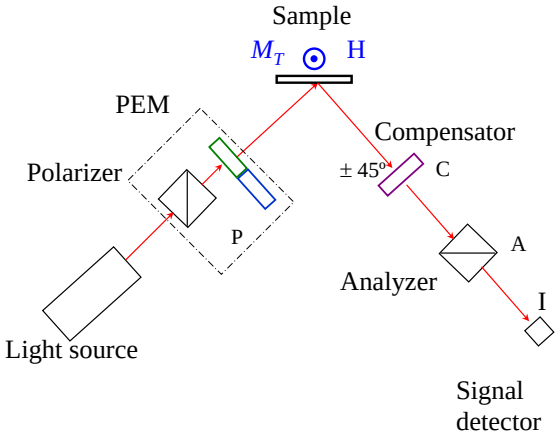

Figure 3.6: *Null ellipsometry system for the measurement of the transverse Kerr effect*

obtain the complex transverse response exploiting null ellipsometry. The schematic set-up is shown in the figure 3.6. It consists of a Polarizer-Modulator-Sample-Compensator-Analyzer geometry. The polarizer is set to 45° from ordinary (or extraordinary) PEM optical axis, being both the polarizer and PEM mechanically coupled and mounted on a rotatory stage (dashed line in the figure 3.6), with P denoting the PEM axis. A quarter wave-plate is used as compensator and is set to $C = \pm 45°$. Finally A denotes the adjustable azimuth angle of the analyzer. The Jones vector describing the polarization of light incident on the detector can be calculated as the matrix product [121]:

$$\begin{pmatrix} E_x \\ E_y \end{pmatrix} = \frac{E_0}{\sqrt{2}} \begin{pmatrix} 1 & 0 \\ 0 & 0 \end{pmatrix} \begin{pmatrix} \cos A & \sin A \\ -\sin A & \cos A \end{pmatrix} \begin{pmatrix} \cos(C) & \pm\sin(C) \\ \pm\sin(C) & \cos(C) \end{pmatrix} \begin{pmatrix} r_{ss} & 0 \\ 0 & r_{pp} \end{pmatrix} \begin{pmatrix} \cos P & -\sin P \\ \sin P & \cos P \end{pmatrix} \begin{pmatrix} e^{i\varphi/2} & 0 \\ 0 & e^{-i\varphi/2} \end{pmatrix} \begin{pmatrix} 1 \\ 1 \end{pmatrix}$$

where the signs ± correspond to the azimuth angles of the compensator $C = \pm 45°$ and E_0 denotes the amplitude of light wave coming from the polarizer. The detected intensity is obtained from:

$$I = E_x E_x^* + E_y E_y^* \tag{3.10}$$

where the asterisk $*$ denotes the complex conjugate and using the equation 3.6 it can be expressed in terms of ellipsometry angles. After matrix calculations in 3.10 one can demonstrate that the real $\Re(\Delta r_{pp}/r_{pp})$ and imaginary parts $\Im(\Delta r_{pp}/r_{pp})$ of the transverse

response are proportional to change of the second $I_{2\omega}$ and first I_{ω} harmonics of the detected signal, respectively (see Eqs. 3.11 and 3.12 below). The first (I_{ω}) and second ($I_{2\omega}$) harmonics are measured using two lock-in amplifiers that drive the PEM modulation at $50kHz$ and $100kHz$, respectively, while the I_0 signal is measured by using a d.c multimeter. Their expressions are given by:

$$\frac{I_{\omega}}{I_0} = (\pm)_C(\pm)_A \sin(2\psi)\Im\left(\frac{\Delta r_{pp}}{r_{pp}}\right) \underbrace{+\sin(2\psi)[(\theta_s - \theta_p)\sin(\Delta) - (\epsilon_s + \epsilon_p)\cos\Delta]} \quad (3.11)$$

and:

$$\frac{I_{2\omega}}{I_0} = (\pm)_C(\pm)_P(\pm)_A \sin(2\psi)\Re\left(\frac{\Delta r_{pp}}{r_{pp}}\right) \underbrace{(\mp)_P \sin(2\psi)[(\theta_s + \theta_p)\cos(\Delta) + (\epsilon_s - \epsilon_p)\sin\Delta]} \quad (3.12)$$

Where the $(\pm)_C(\pm)_P(\pm)_A$ correspond to different nulling zones [2] (see appendix C). The underbraced terms in Eqs. 3.11 and 3.12 are polar and longitudinal contributions $\theta_{s,p}, \epsilon_{s,p}$ that can be easily removed from the measured response by averaging the signal from two different nulling zones obtained for different compensator or analyzer azimuths, thus obtaining the pure transverse responses $\Re(\Delta r_{pp}/r_{pp})$ and $\Im(\Delta r_{pp}/r_{pp})$. The angle ψ in Eqs. 3.11 and 3.12 is obtained from ellipsometry experiments.

3.2.3 Measurement protocol

We have measured the complex transverse Kerr effect by recording hysteresis loops at visible wavelengths with a resolution typically in the range of $5 - 25$ nm. The complex transverse Kerr effect measurement is performed in several steps. First of all, both the temperature of the sample and the wavelength of light are chosen and adjusted. After that, we make the optical settings and start the nulling procedure, as described in the following.

Before measurement: optical settings and null procedure

After aligning the light beam through all the optical components, a nulling procedure is performed in order to obtain a zero signal in both harmonics (I_{ω} and $I_{2\omega}$). The step-by-step procedure is as follows (see also figure 3.6 for reference):

[2] The nulling zones correspond to P, A and C combinations, for which the first $I_{\omega} = 0$ and the second $I_{2\omega} = 0$ harmonics are zero.

- All the azimuth angles are measured with respect to the plane of incidence, being the reference 0° in this plane.
- The polarizer is rotated by 45° with respect to the PEM modulator axis.
- Set the azimuth of Polarizer-PEM system to $P = 0°$ (i.e., the modulator axis is set at $P = 0°$)
- Without switching on the PEM modulation and without the quarter-wave plate compensator, the analyzer is crossed so that we set the azimuth of the analyzer to $A = -45°$ until we reach a null d.c. signal.
- Without PEM modulation, we put the compensator in place and set its azimuth to obtain a maximum detected signal
- We turn on the PEM modulator and proceed with the nulling procedure.
- First harmonic (I_ω) null procedure: the azimuth of the Analyzer A is adjusted to obtain a null signal in the first harmonic.
- Second harmonic ($I_{2\omega}$) null procedure: the azimuth of the Polarizer-PEM system P is adjusted to obtain a null signal in the second harmonic.
- The last two steps must be repeated iteratively until reaching a null signal in both harmonics.

Example of a measurement

After the optical settings and null procedure, a measurement protocol (see figure 3.7) is carried out in order to remove the polar and longitudinal contributions $\theta_{s,p}, \epsilon_{s,p}$ from the as-measured $\frac{I_\omega}{I_0}$ and $\frac{I_{2\omega}}{I_0}$ signals and obtain the transverse$\Re(\Delta r_{pp}/r_{pp})$ and $\Im(\Delta r_{pp}/r_{pp})$ responses (see equations 3.11 and 3.12). We illustrate the measurement protocol for the particular case of magnetooptic hysteresis loops measured in a $La_{2/3}Ca_{1/3}MnO_3$ thin film at temperature T = 10 K and wavelength $\lambda \approx 632$ nm.

To obtain the intrinsic $\Re(\Delta r_{pp}/r_{pp})$ and $\Im(\Delta r_{pp}/r_{pp})$ signals we must measure the field dependence of the magnetooptical signals for two different null zones A_1, A_2 or $C = \pm 45°$, determined by the azimuth positions of the compensator ($C = \pm 45°$) or analyzer (A_1, A_2). In the shown example, we choose a fixed compensator position $C = +45°$, and define the two null zones by the two analyzer azimuth positions A_1, A_2. We thus have two data sets (A_1, A_2) corresponding to the magnetooptic signals (proportional to I_ω and $I_{2\omega}$) measured at each null zone. Therefore we have a set of four data:

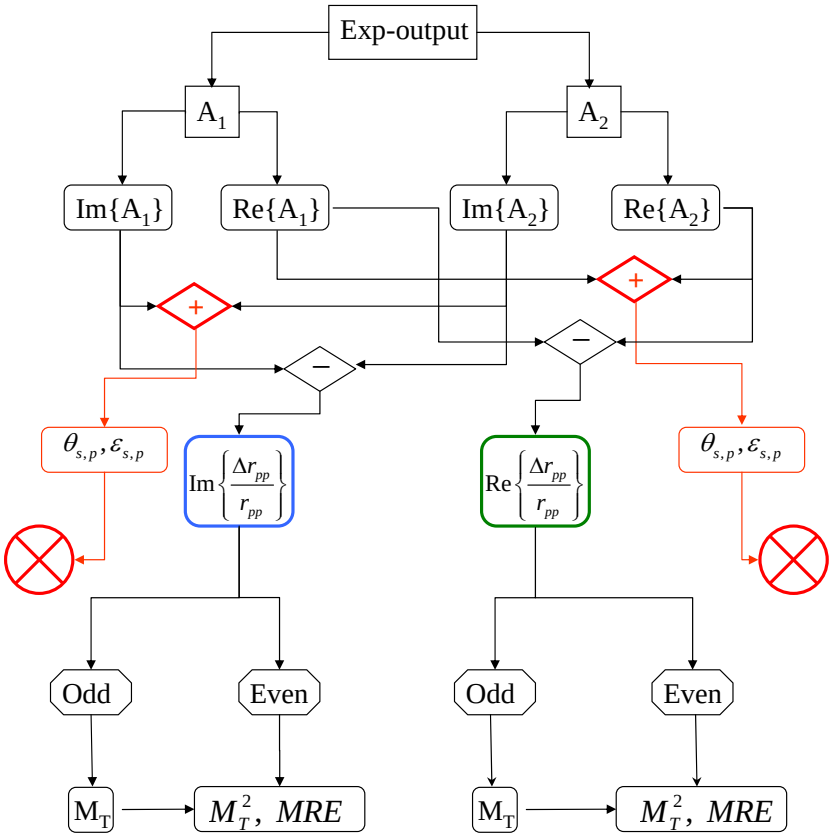

Figure 3.7: *Flux diagram of the measurement protocol*

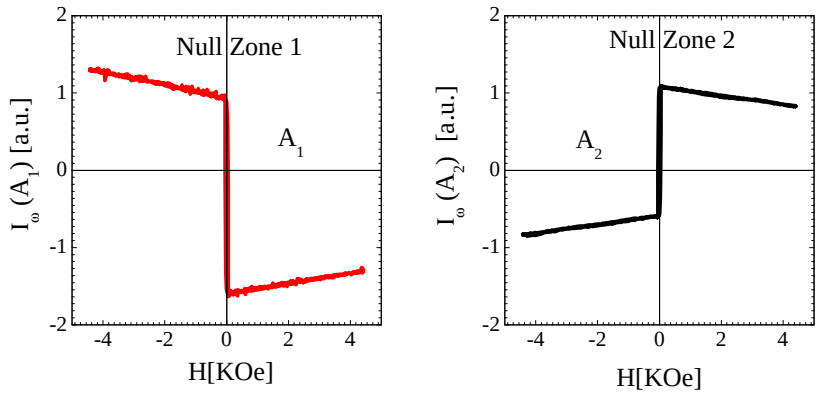

Figure 3.8: *Hysteresis loops of the light intensity detected at the first harmonic (I_ω) at the two null zone positions (A_1, A_2)*

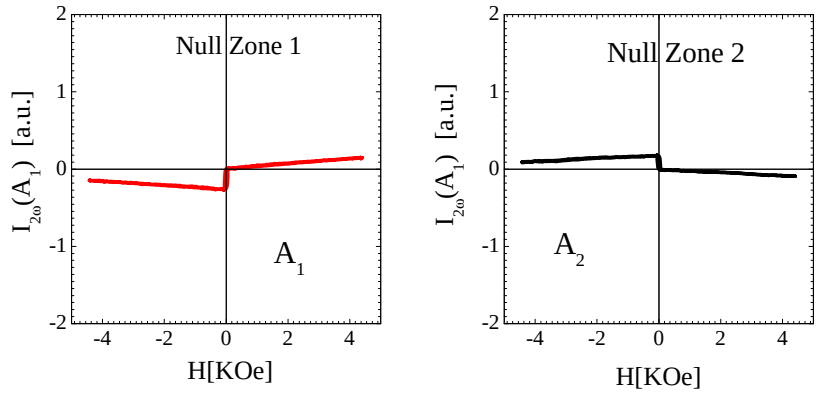

Figure 3.9: *Hysteresis loops of the light intensity detected at the second harmonic ($I_{2\omega}$) at the two null zone positions (A_1, A_2)*

- $I_\omega(A_1)$: first harmonic of the light sensed by the detector in the null zone defined by the analyzer azimuth position A_1
- $I_\omega(A_2)$: first harmonic of the light sensed by the detector in the null zone defined by the analyzer azimuth position A_2
- $I_{2\omega}(A_1)$: second harmonic of the light sensed by the detector in the null zone defined by the analyzer azimuth position A_1
- $I_{2\omega}(A_2)$: second harmonic of the light sensed by the detector in the null zone defined by the analyzer azimuth position A_2

Figures 3.8 and 3.9 show the intensity of light detected at first (I_ω) and second ($I_{2\omega}$) harmonics, respectively. According to equations 3.11 and 3.12, we can use null zone

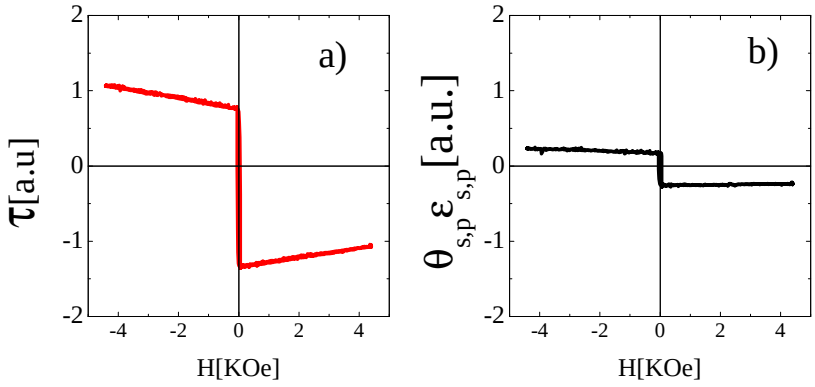

Figure 3.10: *a) Complex transverse Kerr effect* $\tau = \Im\left(\frac{\Delta r_{pp}}{r_{pp}}\right)$ *and b) longitudinal/polar contributions* $\theta_{s,p}, \epsilon_{s,p}$

averaging in order to eliminate the longitudinal and polar contributions ($\theta_{s,p}, \epsilon_{s,p}$). Once averaged we have a new set of four data:

- $\Im\left(\frac{\Delta r_{pp}}{r_{pp}}\right)$
- $\theta_{s,p}, \epsilon_{s,p}$ contributions to the $\Im\left(\frac{\Delta r_{pp}}{r_{pp}}\right)$
- $\Re\left(\frac{\Delta r_{pp}}{r_{pp}}\right)$
- $\theta_{s,p}, \epsilon_{s,p}$ contributions to the $\Re\left(\frac{\Delta r_{pp}}{r_{pp}}\right)$

The complex transverse Kerr signal $\Im\left(\frac{\Delta r_{pp}}{r_{pp}}\right)$ and longitudinal and polar contributions ($\theta_{s,p}, \epsilon_{s,p}$) are plotted in the figure 3.10. As it can be seen in the figure 3.10b $\theta_{s,p}$ and $\epsilon_{s,p}$ saturate with the magnetic field following the magnetization of the sample. However the transverse signal displayed in figure 3.10a *does not saturate* with field. As discussed in chapter 4, this non-saturating component of the transverse response of $La_{2/3}Ca_{1/3}MnO_3$ is related to the magnetorefractive effect. Because the magnetooptic and magnetorefractive components of the optical signal often exhibit distinctive symmetry with respect the magnetic field, we must extract the symmetric/antisymmetric components of $\frac{\Delta r_{pp}}{r_{pp}}$ (see chapter 4) to obtain odd-parity (linear magnetooptic coefficients) and even-parity (quadratic magnetooptic coefficients or magnetorefractive effect) contributions as follows:

$$\begin{aligned} \tau_{odd} &= \Im\left(\frac{\Delta r_{pp}}{r_{pp}}\right)_{odd} = \frac{\tau(H) - \tau(-H)}{2} \\ \tau_{even} &= \Im\left(\frac{\Delta r_{pp}}{r_{pp}}\right)_{even} = \frac{\tau(H) + \tau(-H)}{2} \end{aligned} \qquad (3.13)$$

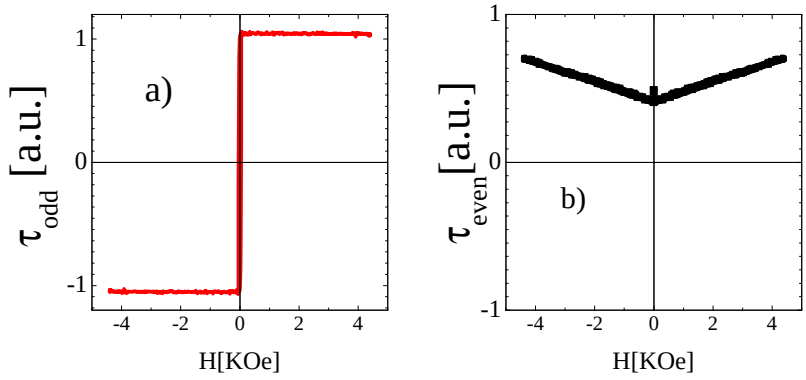

Figure 3.11: *a) Anti-Symmetric* $\tau_{odd} = \Im\left(\frac{\Delta r_{pp}}{r_{pp}}\right)_{odd}$ *and b) symmetric* $\tau_{even} = \Im\left(\frac{\Delta r_{pp}}{r_{pp}}\right)_{even}$ *contributions to to* $\Im\left(\frac{\Delta r_{pp}}{r_{pp}}\right)$ *extracted from data in figure 3.10(a)*

where we have defined $\tau = \Im\left(\frac{\Delta r_{pp}}{r_{pp}}\right)$. An analogous expression can be derived for $\Re\left(\frac{\Delta r_{pp}}{r_{pp}}\right)$. The symmetric τ_{even} and antisymmetric τ_{odd} contributions are plotted in the figure 3.11. In this Thesis we will show that the odd signals correspond to linear magnetooptical effects whereas, depending in each particular case, the even contributions can be attributed to either quadratic magnetooptical effects or to the magnetoreftactive effect (see chapters 4 and 5).

3.3 Polar and Longitudinal measurements

Polar and longitudinal Kerr effects are measured using similar optical configurations. In the polar geometry, the experiment is performed with light at normal incidence, while longitudinal Kerr is measured with light incident at 45°. A schematic sketch showing the method is given in the figure 3.12, which also exploits phase modulation of light through PEM and lock-in detection.

The Jones vector describing polarization of light incident on the detector (figure 3.12) can be calculated as the matrix product:

$$\begin{pmatrix} E_x \\ E_y \end{pmatrix} = \frac{E_0}{\sqrt{2}} \begin{pmatrix} 1 & 0 \\ 0 & 0 \end{pmatrix} \begin{pmatrix} r_{ss} & r_{ps} \\ r_{sp} & r_{pp} \end{pmatrix} \begin{pmatrix} e^{i\varphi/2} & 0 \\ 0 & e^{-i\varphi/2} \end{pmatrix} \begin{pmatrix} 1 \\ 1 \end{pmatrix}$$

Developing the product of matrices and recalling the definitions given in equations 1.27 we can derive [122]:

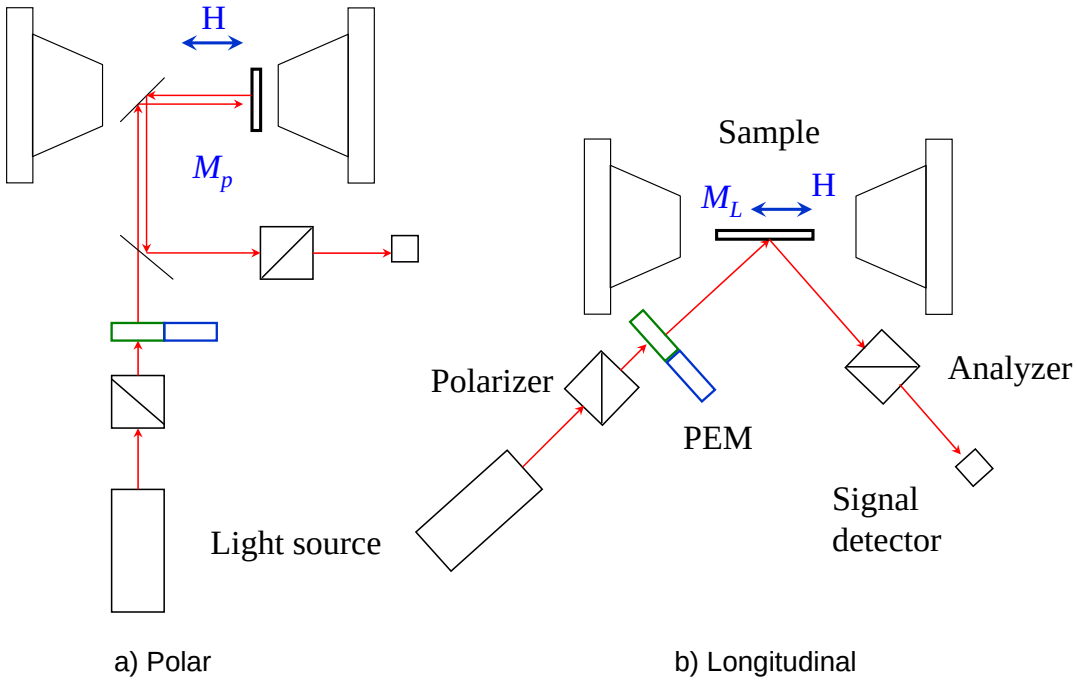

Figure 3.12: *a)Polar geometry with PEM, b)longitudinal geometric with PEM*

$$\theta_{Ks} = \frac{1}{4c}\frac{1}{J_2(\varphi_0)}\frac{I_{2\omega,s}}{I_0} \tag{3.14}$$

$$\theta_{Kp} = -\frac{1}{4c}\frac{1}{J_2(\varphi_0)}\frac{I_{2\omega,p}}{I_0} \tag{3.15}$$

$$\epsilon_{Ks} = \frac{1}{4c}\frac{1}{J_1(\varphi_0)}\frac{I_{\omega,s}}{I_0} \tag{3.16}$$

$$\epsilon_{Kp} = \frac{1}{4c}\frac{1}{J_1(\varphi_0)}\frac{I_{\omega,p}}{I_0} \tag{3.17}$$

(3.18)

Where θ_K, ϵ_K denotes the Kerr rotation and ellipticity, respectively, and the subindexes "s" and "p" indicate the state of the light polarization. The $J_i(\varphi_0)$ are the Bessel functions of the firts kind. Thus, the ellipticity ϵ and rotation θ are proportional to the first and second harmonics, respectively, and c is a calibration constant, which has to be determined experimentally.

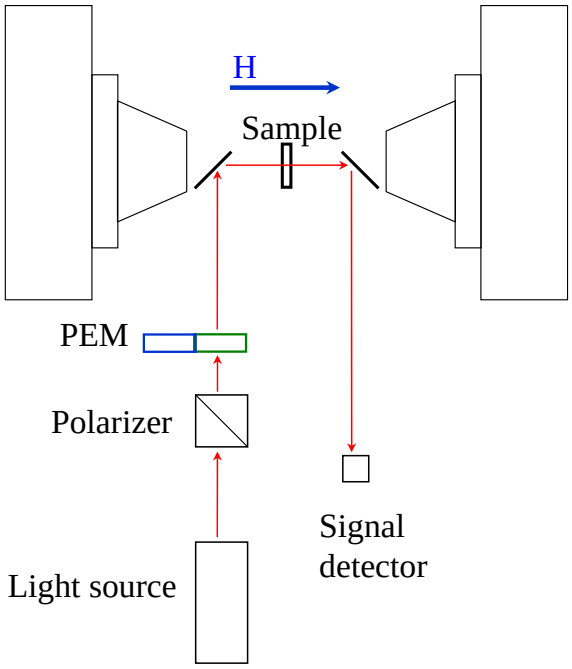

Figure 3.13: *MCD experimental set-up sketch*

3.4 Magnetic circular dichroism

The magnetic circular dichroism (MCD) was briefly described in the section 1.2, figure 1.2 b. The experiment is based on the measurement of the difference in the absorption between left- (LCP) right- (RCP) circularly polarized light, induced by a magnetic field oriented parallel to the direction of light propagation. The experimental set-up used to measure MCD, based on a Polarizer-PEM Modulator-Sample configuration, is shown in the figure 3.13. As in all the previous cases, the polarizer is set to 45° from the PEM modulation axis. The Jones vector describing the polarization state of light incident on the detector can be calculated as the matrix product:

$$\begin{pmatrix} E_x \\ E_y \end{pmatrix} = \begin{pmatrix} r_{ss} & r_{ps} \\ r_{sp} & r_{pp} \end{pmatrix} \begin{pmatrix} e^{i\varphi/2} & 0 \\ 0 & e^{-i\varphi/2} \end{pmatrix} \begin{pmatrix} \cos P \\ \sin P \end{pmatrix} = \frac{E_0}{\sqrt{2}} \begin{pmatrix} r_{ss} & r_{ps} \\ r_{sp} & r_{pp} \end{pmatrix} \begin{pmatrix} e^{i\varphi/2} & 0 \\ 0 & e^{-i\varphi/2} \end{pmatrix} \begin{pmatrix} 1 \\ 1 \end{pmatrix}$$

It can be demonstrated that[109]:

$$MCD \approx \frac{I_\omega}{I_0} \approx \Delta\kappa \tag{3.19}$$

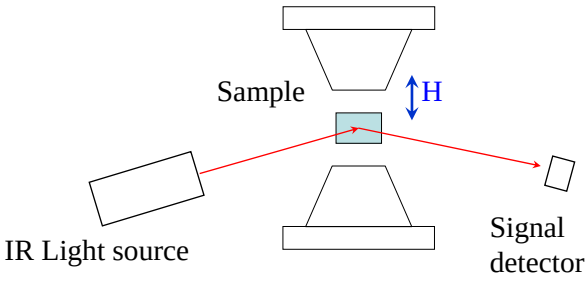

Figure 3.14: *Schematic drawing of the experimental setup including the IR spectrometer*

where $\Delta\kappa = \kappa_- - \kappa_+$ and $\kappa_\pm$ are the absorption coefficients for RCP and LCP light. We note that the MCD signal is proportional the ellipticity $MCD \approx 4\epsilon$ for the case of normal incidence. A description of MCD experimental methods can be found in the literature [109, 113, 123, 124].

3.5 Infrared spectroscopy

These experiments were carried out in the University of York in collaboration with Prof. Sarah Thompson. The infrared characterization consists on the measurement of infrared reflectivity spectra under an applied external transverse magnetic field. The instrument is shown in the figure 3.14. It consists of an optical table with a Perspex enclosure and a gas purging system, a Fourier-Transform-spectrometer with external optical components and IR detector, an electromagnet with power supply and a personal computer, which runs the software for the spectrometer.

The sample is cleaned with isopropanol and mounted on the bare sample holder with blue tack or the cooling system with thermal grease. To ensure that the sample is flat on the sample holder - tilting results in a change of the angle of incidence - the sample is pressed onto a tissue on a flat surface to level it. If the cooling system is used, it is better to check whether the vacuum pressure and the high pressure of the nitrogen gas can be reached before the fine alignment. To save gas, the gas supply is shut again after the check. In the next step the dewar of the detector is filled with liquid nitrogen. The goniometer is mounted to the frame of the magnet either together with the bare sample holder or with the cooling system containing the sample. The fine alignment is achieved by the horizontal and vertical translation of the goniometer. If the bare brass sample holder is used, the goniometer is adjusted until the highest possible signal intensity is reached, which can be monitored in the bench menu of the spectrometer software OMNIC. The goniometer is then adjusted so that the substrate peaks in the reflection spectra are optimized. After

the fine alignment the system is left to settle to reduce the amount of water vapour and CO_2. The settling time depends on the initial pollution and is between 30 and 90 minutes.

Once that the optical components are aligned with the help of the red laser and the beam is focused in the sample which is placed between the electromagnet poles, the purging system is activated, and the reflectivity spectra are recorded every 10 minutes. When the changes between consecutive spectra remain below the $\approx 0.1\%$, the system is ready for measurement.

3.5.1 Infrared reflection measurements

The actual MRE measurement consists of a reflection measurement in zero magnetic field $R(0)$,and a measurement in a magnetic field $R(H)$. The zero field spectra are averaged over two measurements (before and later the measurement in a magnetic field $R(0) = 0.5(R_{before}(0) + R_{after}(0))$ to correct for variations of the magnetic state in the sample. The MRE spectrum is calculated by using the equation:

$$MRE[\%] = \frac{R(H) - R(0)}{R(0)} \times 100\% \tag{3.20}$$

This means that an increase of the reflectivity due to the application of a magnetic field leads to positive MRE values, while a decrease of the reflectivity leads to negative MRE values. The MRE measurement is repeated three to five times depending on the noise level of the spectra and the final MRE spectrum is calculated as an average over all MRE measurements. The measured reflection spectra are normalized to a reference spectrum. This normalization corrects for the background due to the characteristics of the source, detector, optical components and the atmospheric conditions. The reference spectrum is taken after replacing the sample by a gold mirror.

Part II

Results

CHAPTER 4

Magnetorefractive effect in Manganites

The width of e_g bands in $AMnO_3$ manganite perovskites is critically dependent on the Mn-O-Mn bond angle. Experimentally it is found that it can be modulated by tuning the average ionic radius at the A-site via chemical doping. For instance, reducing the bond angle leads to a reduced Mn-Mn electronic hopping and increased electronic correlations, both of which are revealed by a reduction of the ferromagnetic Curie temperature and an enhancement of magnetoresistance [125]. Indeed, these effects are related to the progressively predominant role of Jahn-Teller electron-phonon interactions on the physics of manganites with the reduction of the e_g bandwidth. Thus, it is expected that the contribution of the magnetic field-dependent polaronic transport to the optical conductivity is regulated by these effects. With this in view, we have carried out an analysis of magnetooptical spectra of manganites of different chemical compositions in the A-site and, therefore, exhibiting different degrees of electron-phonon coupling. This has allowed us to make a link between the electron-phonon coupling strength and the magnetorefractive effect.

4.1 Magnetooptical spectroscopy of PLCMO

In $(Pr_{0.4}La_{0.6})_{0.7}Ca_{0.3}MnO_3$ (PLCMO) the average ionic radius of Pr^{3+} and La^{3+} at the A-site induces distortions of the crystal lattice so that the $Mn-O-Mn$ bond angle is strongly bent from 180°, thus decreasing the effective electron hopping and reducing the width of the e_g conduction band [125]. In other words, a substitution of La^{3+} by the smaller Pr^{3+} allows to explore bands bending effect in PLCMO while keeping the hole density (i.e., the concentration of the Mn^{4+}) constant. This, in turn, favour electronic phase segregation that turns out to be quite sensitive to structural changes and strain state [126]. These features make of PLCMO a good playground to probe the relationship

between polaron conduction and optics. Indeed, infrared optical properties of PLCMO reported by Kim *et al.* [127] described the observed spectral weight transfer using a model that includes spin double exchange and Jahn-Teller lattice coupling to holes. Due to the strongly electron-phonon coupling and colossal magnetoresistance phenomenon, PLCMO is an optimal candidate to analyze all the possible effects that can be present in the complex transverse magneto optical response, comprising both magnetooptic as well as magnetorefractive effects.

The studied PLCMO samples were prepared by the group of Dr. *Kathrin Dörr* in the Institute for Metallic Materials, (IFW) in Dresden- Germany [1]. An PLCMO film of thickness $t = 100nm$ was grown by off-axis pulsed laser deposition (PLD, KrF $248nm$ excimer laser) on monocrystalline platelets of $PMN - PT(001)$ $\left(PbMg_{1/3}Nb_{2/3}O_3)_{0.72}(PbTiO_3)_{0.28}\right)$ from stoichiometric targets of $Pr_{0.7}Ca_{0.3}MnO_3$ and $La_{0.7}Ca_{0.3}MnO_3$ [128]. The film was deposited in an oxygen pressure of $P_{O2} = 0.3mbar$ at a substrate temperature of $T = 725°C$ with a pulse frequency of $f = 2Hz$. The structural and magnetic properties of the film were fully characterized in the laboratory of Dr. *Kathrin Dörr* [128]. Of relevance for the results presented here is that the zero-field resistance shows a peak at $T_{MI} \approx 134°K$,(see figure 4.2) slightly below the Curie temperature $T_C \approx 150°K$ derived from the temperature dependence of the magnetization . The magnetic properties of PLCMO were studied by SQUID magnetometry. The magnetization dependence on temperature of PLCMO sample is shown in the figure 4.1. The d.c. magneto-transport is plotted in the figure 4.2. As expected, the application of a magnetic field leads to a large suppression of the resistance resulting in a colossal magnetoresistance, typical of such type of systems.

4.1.1 magnetooptical characterization

Temperature dependence

In this section we describe the magnetooptical properties measured in complex transverse Kerr effect taking into account the procedure detailed in the section 3.2.3. We limit ourselves to the analysis of the imaginary part $\Im\left(\frac{\Delta r_{pp}}{r_{pp}}\right)$, without losing sight that a similar treatment has been done for the real part $\Re\left(\frac{\Delta r_{pp}}{r_{pp}}\right)$. Figure 4.3 illustrates the temperature dependence of the $\Im\left(\frac{\Delta r_{pp}}{r_{pp}}\right)$ hysteresis loops recorded by shining with light of $\lambda = 475nm$.

The obvious first observation is that the recorded loops are quite distorted compared to conventional hysteresis loops, and this behaviour is dramatically dependent on temperature.

[1] Prof. K. Dörr is now installed in the Institute for Physics MLU Halle-Wittenberg, Halle, Germany

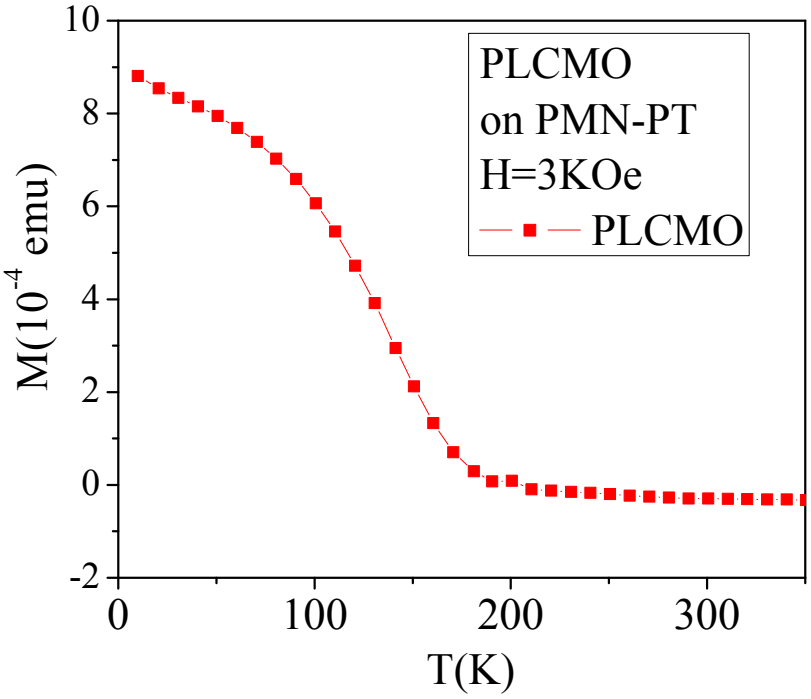

Figure 4.1: *Temperature dependence of the magnetization of a PLCMO film measured by SQUID at $H = 3kOe$.*

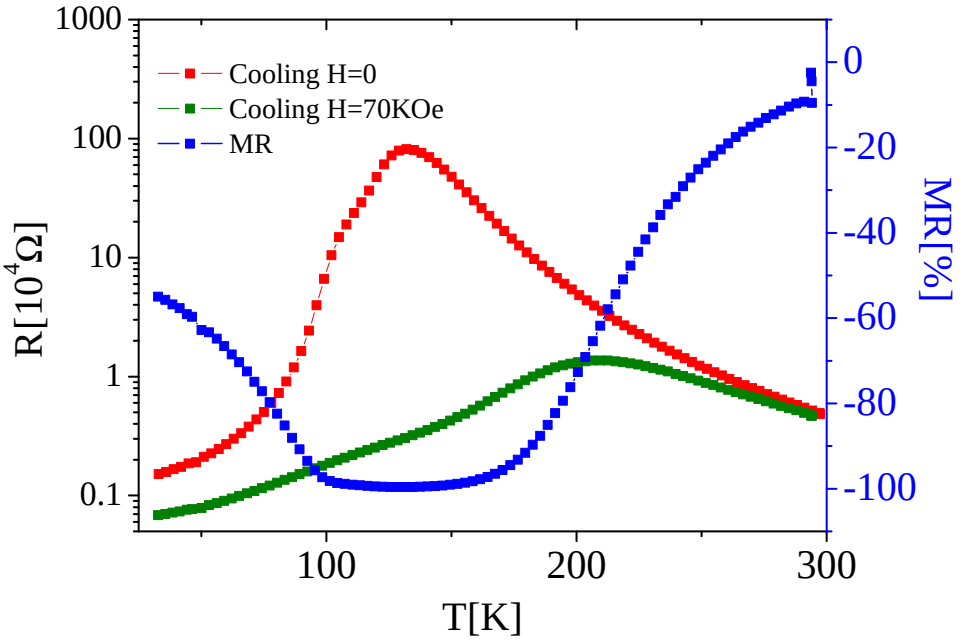

Figure 4.2: *Magneto-transport of the PLCMO film. Electrical d.c. resistance at $H = 0$ red curve, $H = 70kOe$ green curve and magnetoresistance blue curve*

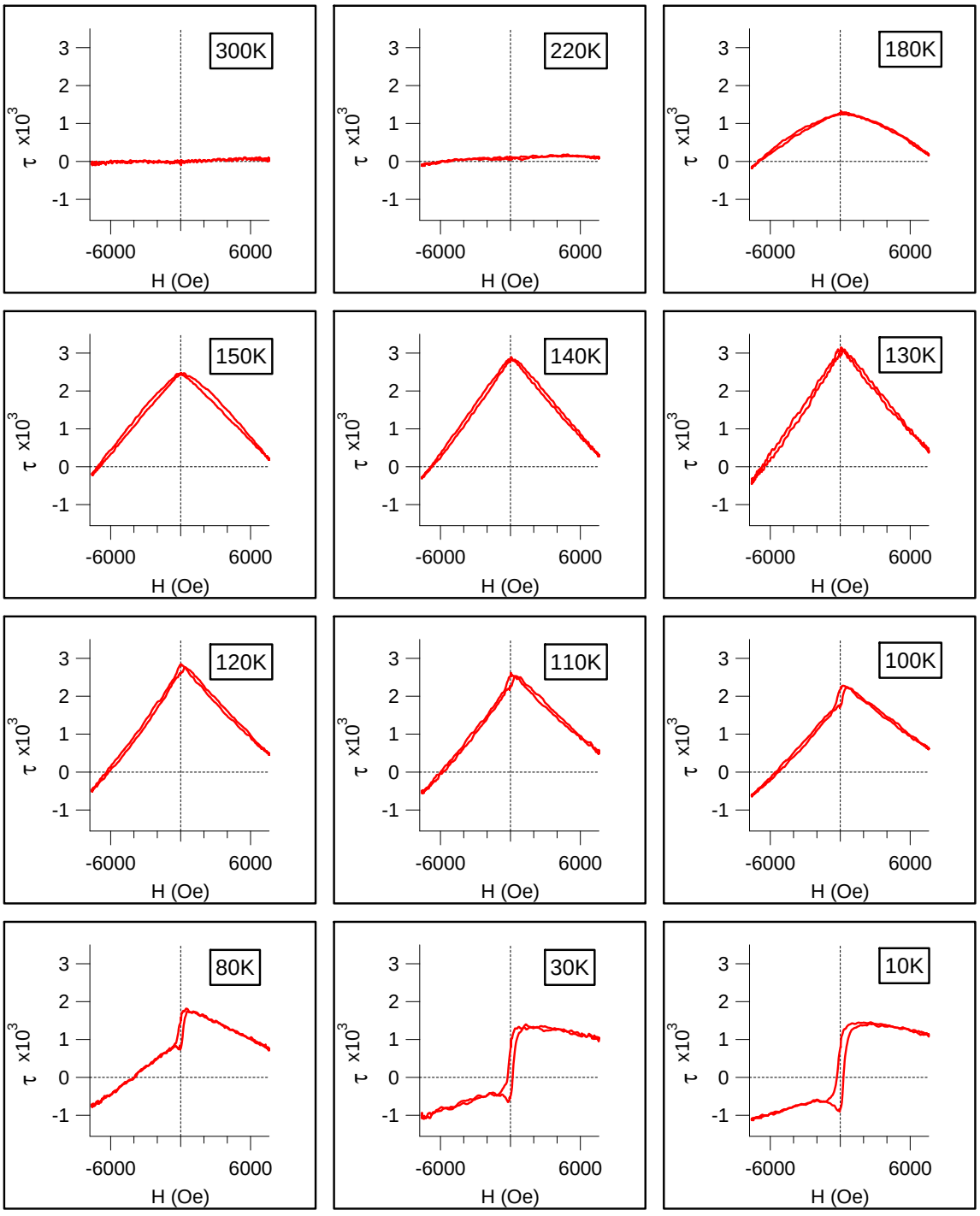

Figure 4.3: *As measured* $\tau = \Im\left(\frac{\Delta r_{pp}}{r_{pp}}\right)$ *hysteresis loops recorded at different temperatures and* $\lambda = 475nm$.

At low temperature $(10-30)$K the hysteresis loops are rather similar to those obtained by SQUID. However, as we approach the ferromagnetic transition $T_C \approx 150K$, the hysteresis loops appear progressively more distorted. The distortion consists of a contribution symmetric in magnetic field superimposed to the normal hysteresis loops, which becomes larger when $T \to T_C$. According to the magnetization curve in figure 4.1, the amplitude of the hysteresis loops should be zero from high temperature down to $T_C \approx 150K$, and conventional ferromagnetic loops with increasing amplitudes should be observed for decreasing temperatures.

In order to understand this remarkable behavior, let us split the recorded hysteresis loops into even $\Im\left(\frac{\Delta r_{pp}}{r_{pp}}\right)_{even}$ and odd $\Im\left(\frac{\Delta r_{pp}}{r_{pp}}\right)_{odd}$ contributions by using the equations 3.13. The $\Im\left(\frac{\Delta r_{pp}}{r_{pp}}\right)_{odd}$ (red curves) and even $\Im\left(\frac{\Delta r_{pp}}{r_{pp}}\right)_{even}$ (blue curves) contributions are plotted as a function of temperature in figure 4.4. We see that the odd contributions show the expected behavior for Kerr effects, which are proportional to the magnetization (see figure 4.5). However, the even contributions have a much different temperature dependence, and are observed even at $T > T_C$, suggesting a quite different origin. Indeed, the even hysteresis loops around the Curie temperature do not show any saturation up to the largest applied field (around $7kOe$, see figure 4.4) much higher than the saturation field observed in SQUID (figure 4.1), further underlying the different nature of this even contribution. Now, as we decrease the temperature and approach the Curie temperature ($T_C \approx 150K$) from above, the even contribution increases and reaches the maximum close to T_C, and then decreases for lower temperatures.

We argue that the observed even contribution to the transverse magnetooptical signal is related to the magnetorefractive effect (MRE). As it was discussed in the section 1.4, MRE results from the changes in the complex refractive index $\tilde{n}(H)$ and, thus, the optical conductivity with the magnetic field $\tilde{\sigma}(H)$, and is particularly strong in ferromagnetic manganites close to T_C [15, 129]. We can thus recognize that the changes in Δr_{pp} have two different origins as follows:

$$\Delta r_{pp} = (M.O.(M) + \tilde{n}(H)) \tag{4.1}$$

while the first term -associated to the odd-parity transverse response- is closely related to the conventional magnetooptical effects proportional to the magnetization (see figure 4.5), the second term -which does not saturate with the magnetic field- is related to the magnetorefractive effect discussed in the section 1.4. Note that the field dependence of $\Im\left(\frac{\Delta r_{pp}}{r_{pp}}\right)_{even}$ displayed in figure 4.4 indicates that the reflectance decreases with field. This

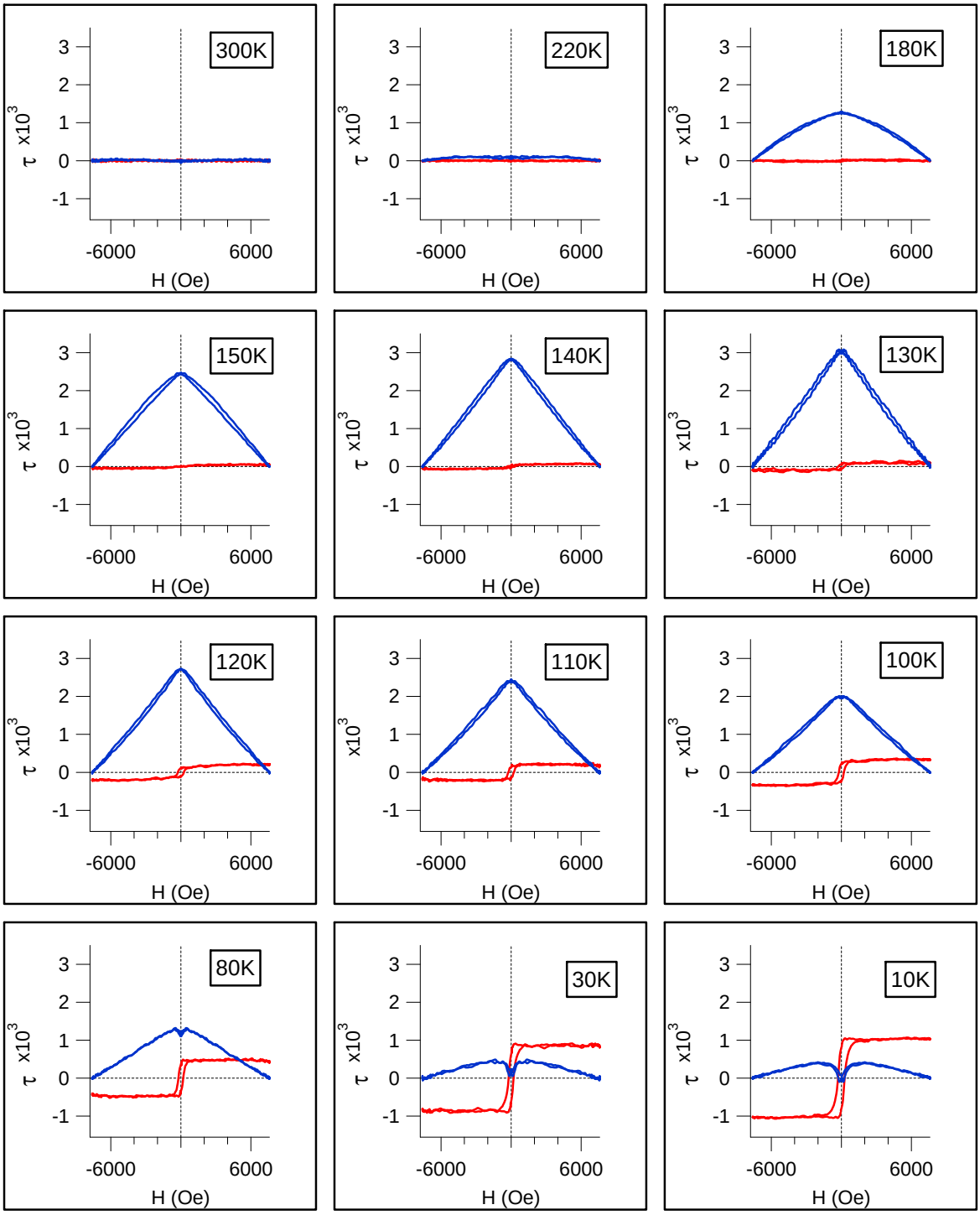

Figure 4.4: *The odd* $\tau_{odd} = \Im\left(\frac{\Delta r_{pp}}{r_{pp}}\right)_{odd}$ *(red curves) and even* $\tau_{even} = \Im\left(\frac{\Delta r_{pp}}{r_{pp}}\right)_{even}$ *(blue curves) contributions recorded at different temperatures and* $\lambda = 475nm$

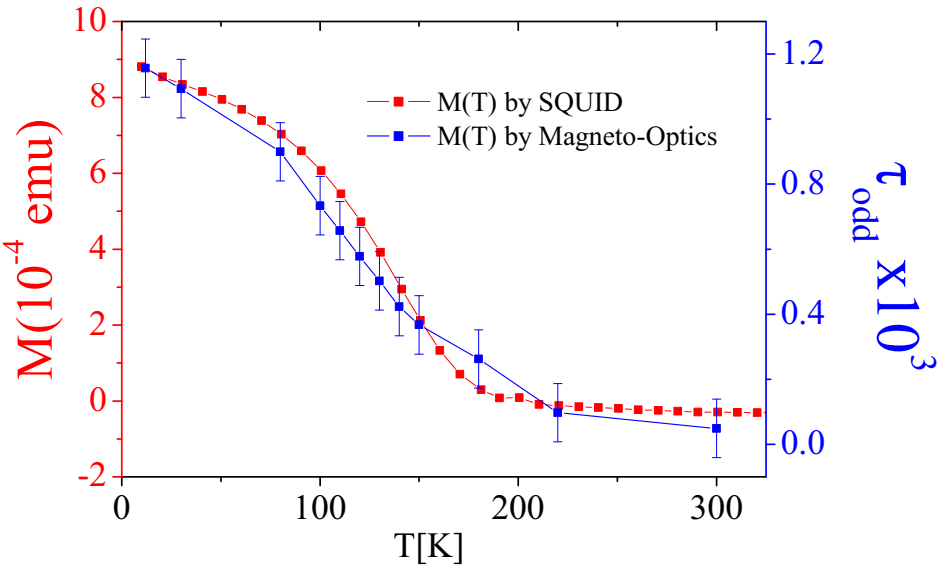

Figure 4.5: *Temperature dependence of the odd* $\tau_{odd} = \Im\left(\frac{\Delta r_{pp}}{r_{pp}}\right)_{odd}$ *contribution (blue curve) and of the magnetization measured by SQUID (red curve)*

is a clear indication that the optical conductivity indeed decreases with the field, instead of increasing, as would be expected from the negative magnetoresistance measured in dc-transport experiments. This observation is in perfect agreement with the crossover noted in the field dependence of the optical spectra of other manganites, where typically above infrared frequencies the optical conductivity is seen to decrease with field, instead of the observed increase for wavelengths longer than the near-infrared (see e. g., Fig. 6 of Ref.[130] or Fig. 2 of Ref.[131])

If now we proceed to a careful inspection of the hysteresis loops for temperatures well below the transition (e.g. for $T < 100K$), we will appreciate that there is also a small even contribution to the magnetooptical signal that, contrary to the MRE, saturates with the magnetic field. This is clearly appreciated in the blue curves of the panels 80K, 30K, and 10K of the figure 4.4. We attribute this second type of even contribution to quadratic magnetooptical (QMO) terms that develop at low temperatures and vanish with the magnetization as $T \to T_C$.

Generally, QMO coefficients are detected in the *Voigt* or *Cotton-Mouton* configuration $\kappa \perp H$(see section 1.2), and are proportional to $M_k M_l$ products (according to the equation 1.21), resulting in asymmetrical loops with contributions of even parity with respect to the applied field [116–118, 132–136]. In order to show the agreement of the even contribution observed at low temperature with these QMO effects, let us analyze the loop recorded at 10K where the magnetization is large, see figure 4.6. The even $\Im\left(\frac{\Delta r_{pp}}{r_{pp}}\right)_{even}$ and the

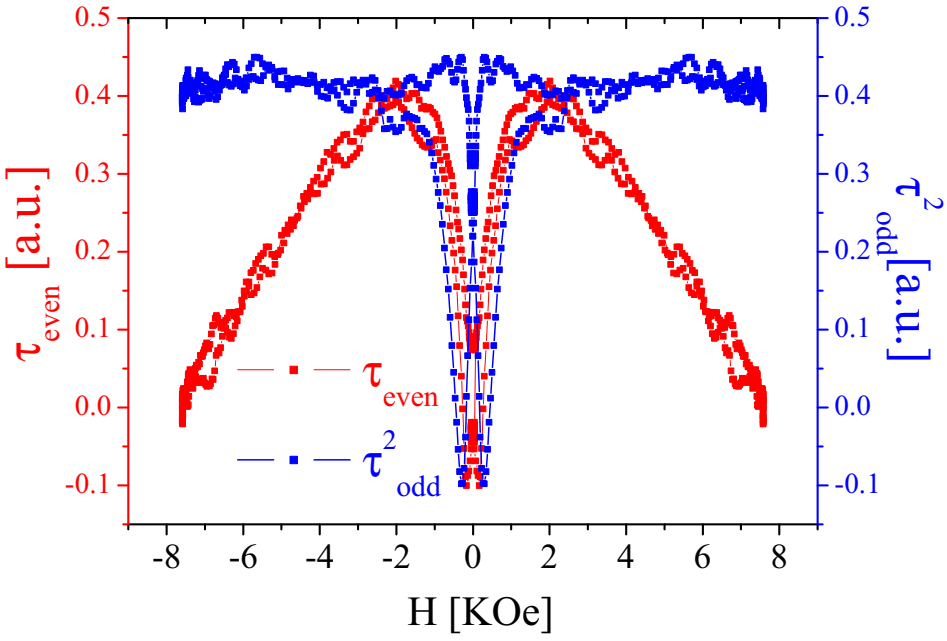

Figure 4.6: *Even contribution* $\tau_{even} = \Im\left(\frac{\Delta r_{pp}}{r_{pp}}\right)_{even}$ *(blue curve) and odd contribution* $\tau^2_{odd} = \Im\left(\frac{\Delta r_{pp}}{r_{pp}}\right)^2_{odd}$ *square (red curve) at* $T = 10K$*. The red curve was both multiplied by a arbitrary factor and shifted for an easy comparison*

squared odd $\Im\left(\frac{\Delta r_{pp}}{r_{pp}}\right)^2_{odd}$ contributions are plotted in this figure. Note that there is an agreement for low magnetic fields between the two magnitudes, confirming that the even contribution observed at the lowest temperatures is a QMO effect. The difference observed above the saturation field ($\approx 2kOe$) between $\Im\left(\frac{\Delta r_{pp}}{r_{pp}}\right)^2_{odd}$ and $\Im\left(\frac{\Delta r_{pp}}{r_{pp}}\right)_{even}$ is attributed to a small remanent magnetorefractive effect superimposed to the quadratic and linear magnetooptical coefficients. Notice that $\Im\left(\frac{\Delta r_{pp}}{r_{pp}}\right)^2_{odd}$ saturates following the magnetization, as expected.

At intermediate temperatures the QMO and MRE contributions to $\Im\left(\frac{\Delta r_{pp}}{r_{pp}}\right)_{even}$ become comparable. To illustrate how these two nonlinear terms can be unambiguously disentangled from the experiment, we display in figure 4.7 the data corresponding to $\Im\left(\frac{\Delta r_{pp}}{r_{pp}}\right)$, $\Im\left(\frac{\Delta r_{pp}}{r_{pp}}\right)_{odd}$, and $\Im\left(\frac{\Delta r_{pp}}{r_{pp}}\right)_{even}$ measured at an intermediate temperature $T = 80K$ at $\lambda = 475nm$. At this temperature, both QMO and MRE terms contribute significantly to the asymmetrical part of the loops. The low-field part of $\Im\left(\frac{\Delta r_{pp}}{r_{pp}}\right)_{even}$ corresponds to the QMO term, whereas the unsaturated high-field part corresponds to MRE and the linear magneto optical (LMO) term follows the magnetization (figure 4.7).

To conclude the discussion about the temperature dependence of the magnetooptical response, we plot the amplitudes recorded for the main three contributions -linear and

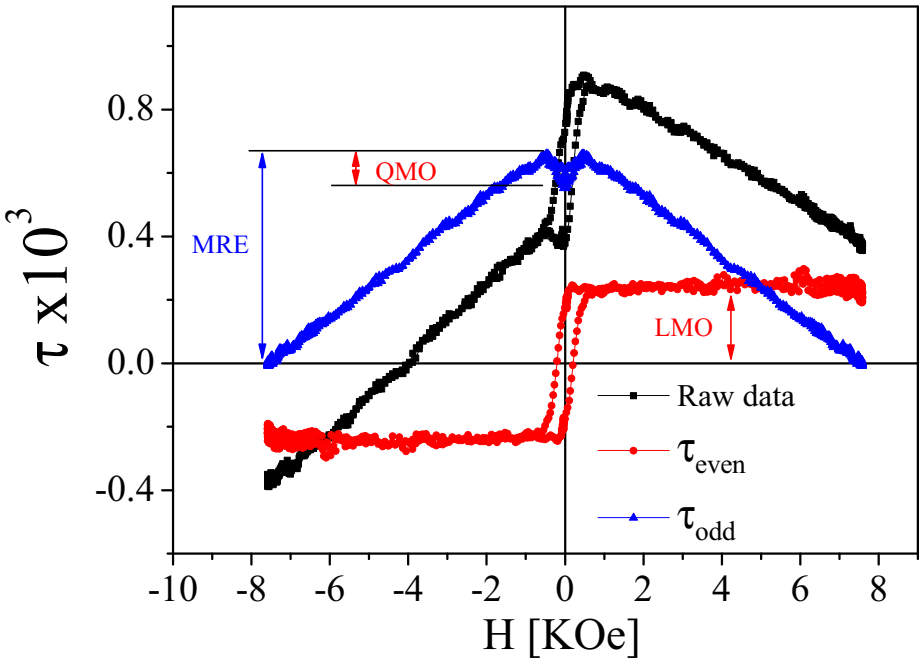

Figure 4.7: *As measured* $\tau = \Im\left(\frac{\Delta r_{pp}}{r_{pp}}\right)$ *(black curve), even contribution* $\tau_{even} = \Im\left(\frac{\Delta r_{pp}}{r_{pp}}\right)_{even}$ *(blue curve) and odd contribution* $\tau_{odd} = \Im\left(\frac{\Delta r_{pp}}{r_{pp}}\right)_{odd}$ *(red curve) measured at 80K*

quadratic magnetooptical coefficients, as well as MRE- as a function of the temperature (see figure 4.8), measured at $\lambda = 475nm$. In order to make easier the comparison between all these contributions, the data are plotted with absolute values. We see that, as expected, the QMO and LMO contributions have a similar dependence, with a transition temperature in close agreement with SQUID magnetometry measurements. On the other hand, the MRE contribution peaks around the ferromagnetic transition and is still significant at temperatures of 50 K above T_C. As we will see in next sections 4.2, and 4.3, a comparative study in other manganites indicates a correlation between the electron-phonon coupling strength and the MRE, i.e., it grows with increasing electron-phonon coupling [137], and it is strongly correlated to the Jahn-Teller distortions. The most plausible explanation of this phenomenon appears in the context of a strong suppression of polarons by magnetic field, especially around T_c. Indeed, a large magnetooptical conductivity in manganites is expected from a polaronic conduction model [68, 138–142]. Along this line, the observed MRE temperature dependence indicates that polaron conduction starts well above the Curie temperature and the effect of the magnetic field on polarons is strongest around T_C.

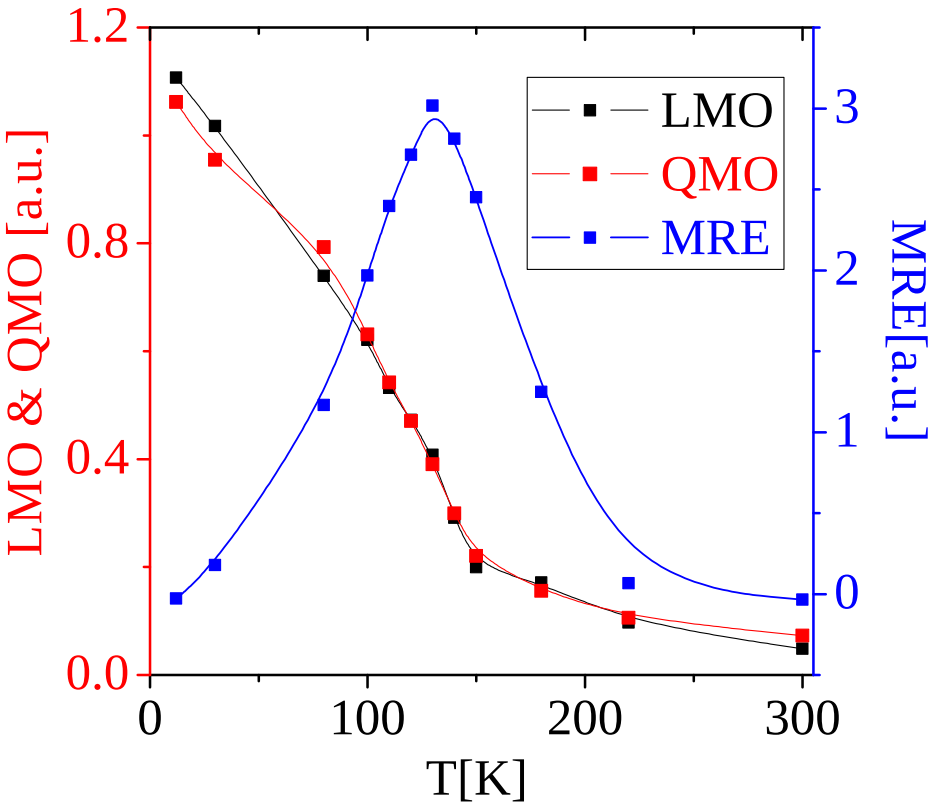

Figure 4.8: *Temperature dependence of LMO, QMO, and MRE in PLCMO*

Spectral response

We discuss now the dependence of the magnetooptical response on the photon energy. For that purpose, we select two temperatures, for which the even contribution to the magnetooptical signal is either dominated by the MRE (T= 140 K, close to T_C) or by QMO ($T = 7K$). Taking into account that QMO is related to the split orbit (SO) coupling [118], while the MRE is mainly related to the magnetic field-dependent optical conductivity, we expect a different dependence on photon energy. The as measured transverse signal $\Im\left(\frac{\Delta r_{pp}}{r_{pp}}\right)$ is plotted in figure 4.9 (7 K) and 4.11 (140 K), while the corresponding even and odd contributions $\Im\left(\frac{\Delta r_{pp}}{r_{pp}}\right)_{odd,even}$ are plotted in figure 4.10 (7 K) and 4.12 (140 K).

The spectral dependence of the Kerr transverse response was analyzed by plotting the amplitudes of the odd and even contributions obtained at the maximum applied fields H $\approx 7kOe$. The amplitude of the odd contribution -proportional to the amplitude of the transverse magnetization M_T - is shown in the figure 4.13. Because the odd spectral responses measured at 7K and 140K correspond to the intensity of magnetooptical coefficients, they are similar, as expected. Both spectral dependences exhibit a similar feature in the spectral response of the transverse Kerr effect of films of similar composition

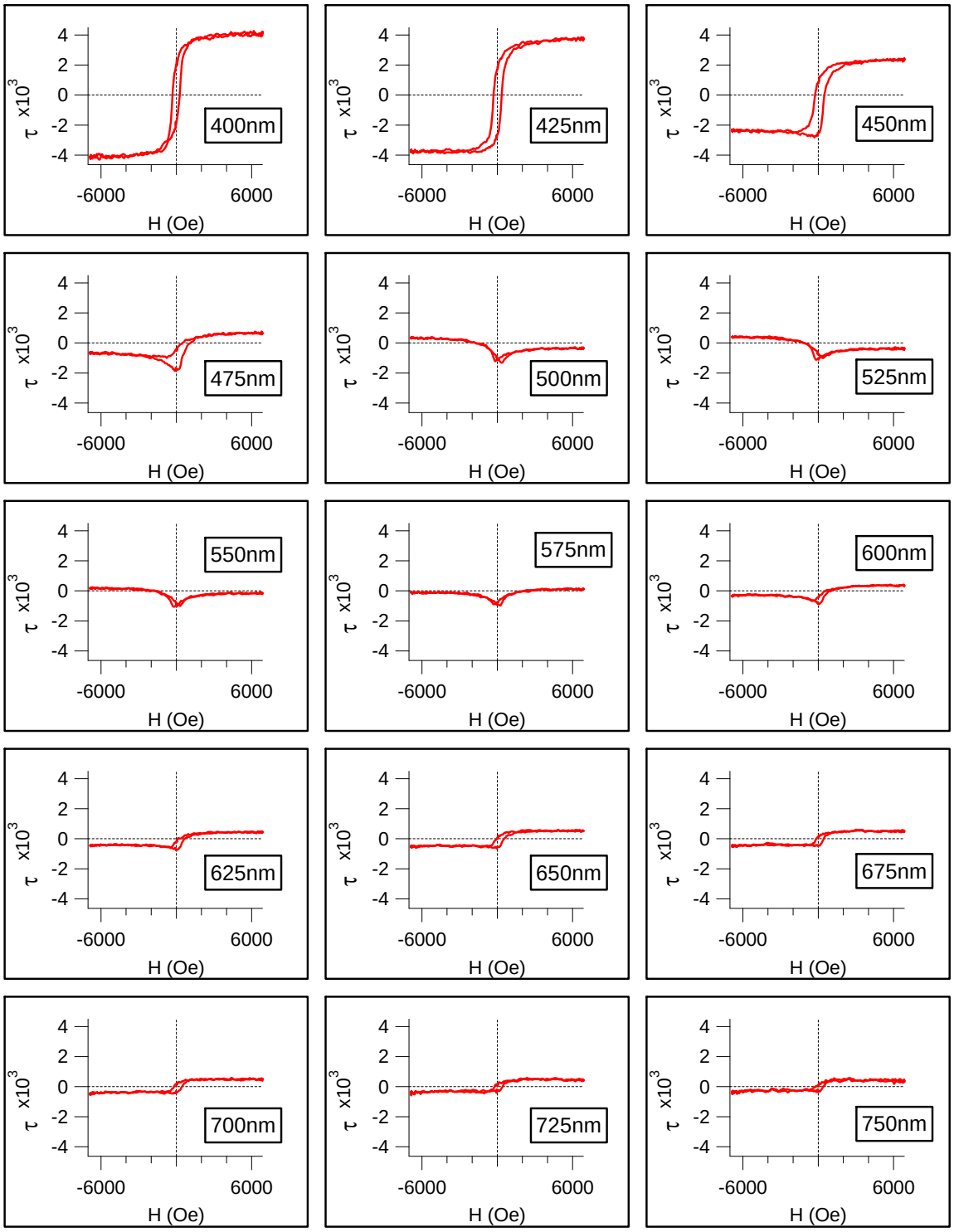

Figure 4.9: *Spectral dependence of* $\tau = \Im\left(\frac{\Delta r_{pp}}{r_{pp}}\right)$ *hysteresis loops measured at* $T = 7K$.

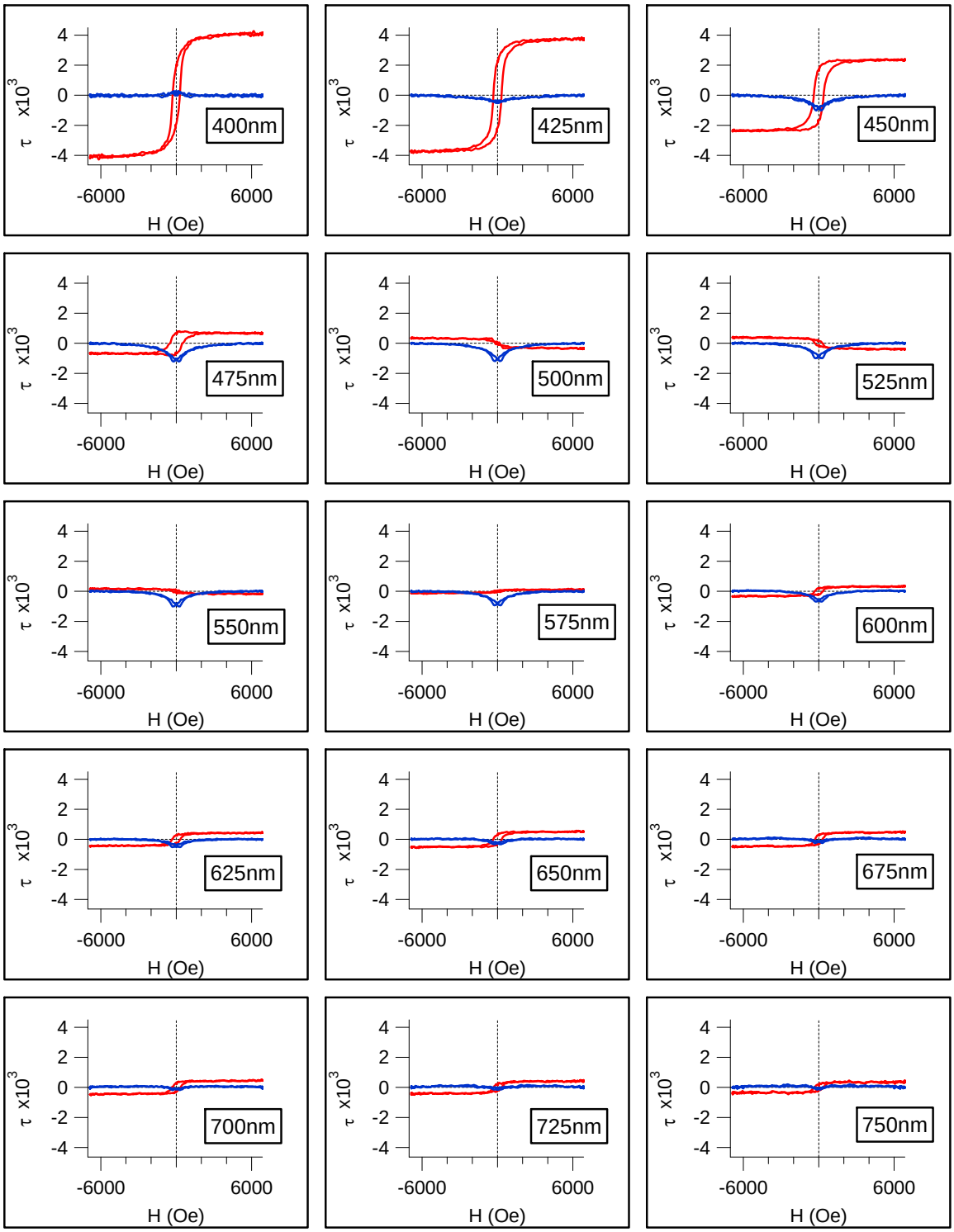

Figure 4.10: *Spectral dependence of* $\tau = \Im\left(\frac{\Delta r_{pp}}{r_{pp}}\right)_{odd,even}$ *hysteresis loops measured at* $T = 7K$*, odd contribution (red curves) and even contribution (blue curves)*

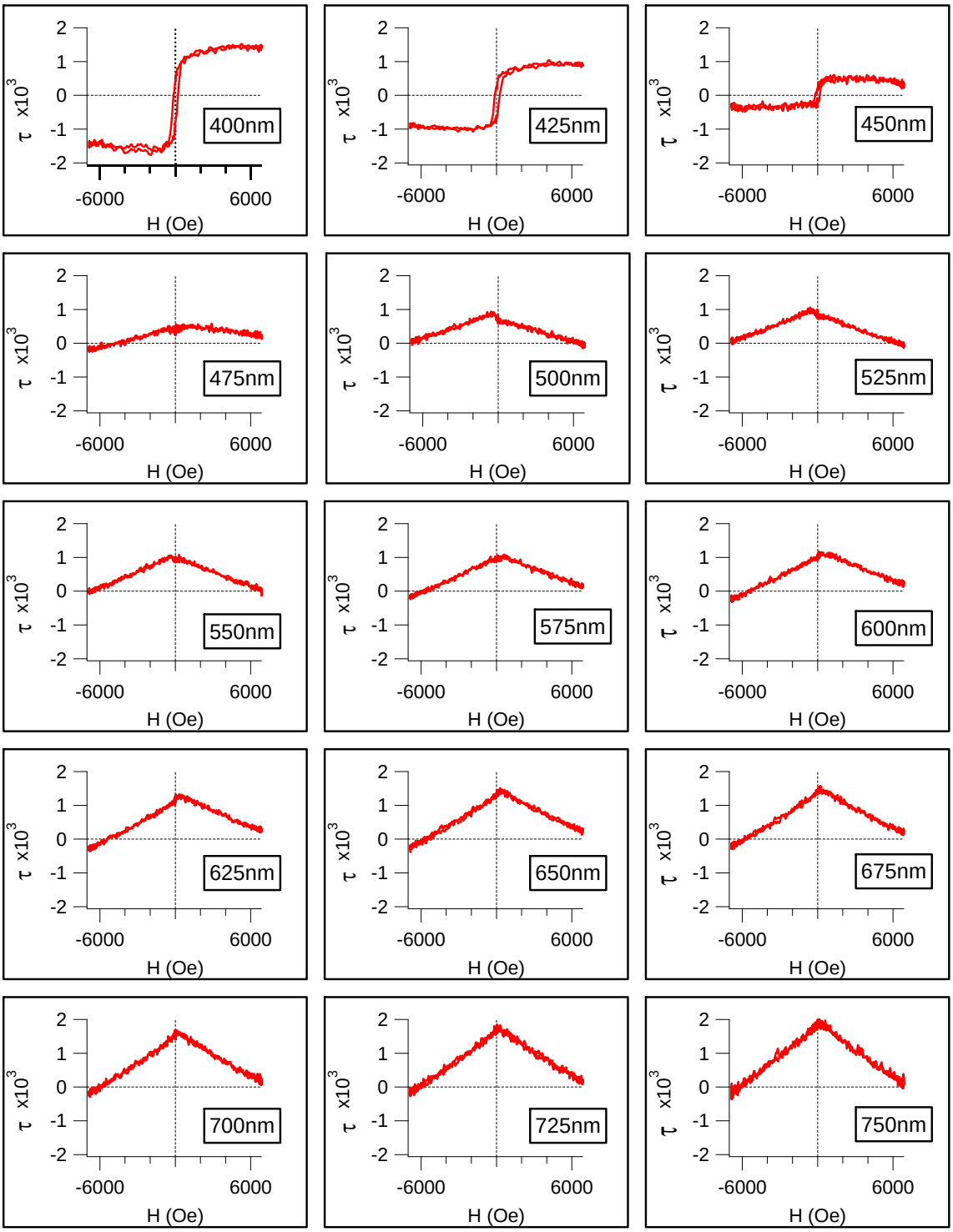

Figure 4.11: *Spectral dependence of* $\tau = \Im\left(\frac{\Delta r_{pp}}{r_{pp}}\right)$ *hysteresis loops measured at* $T = 140K$

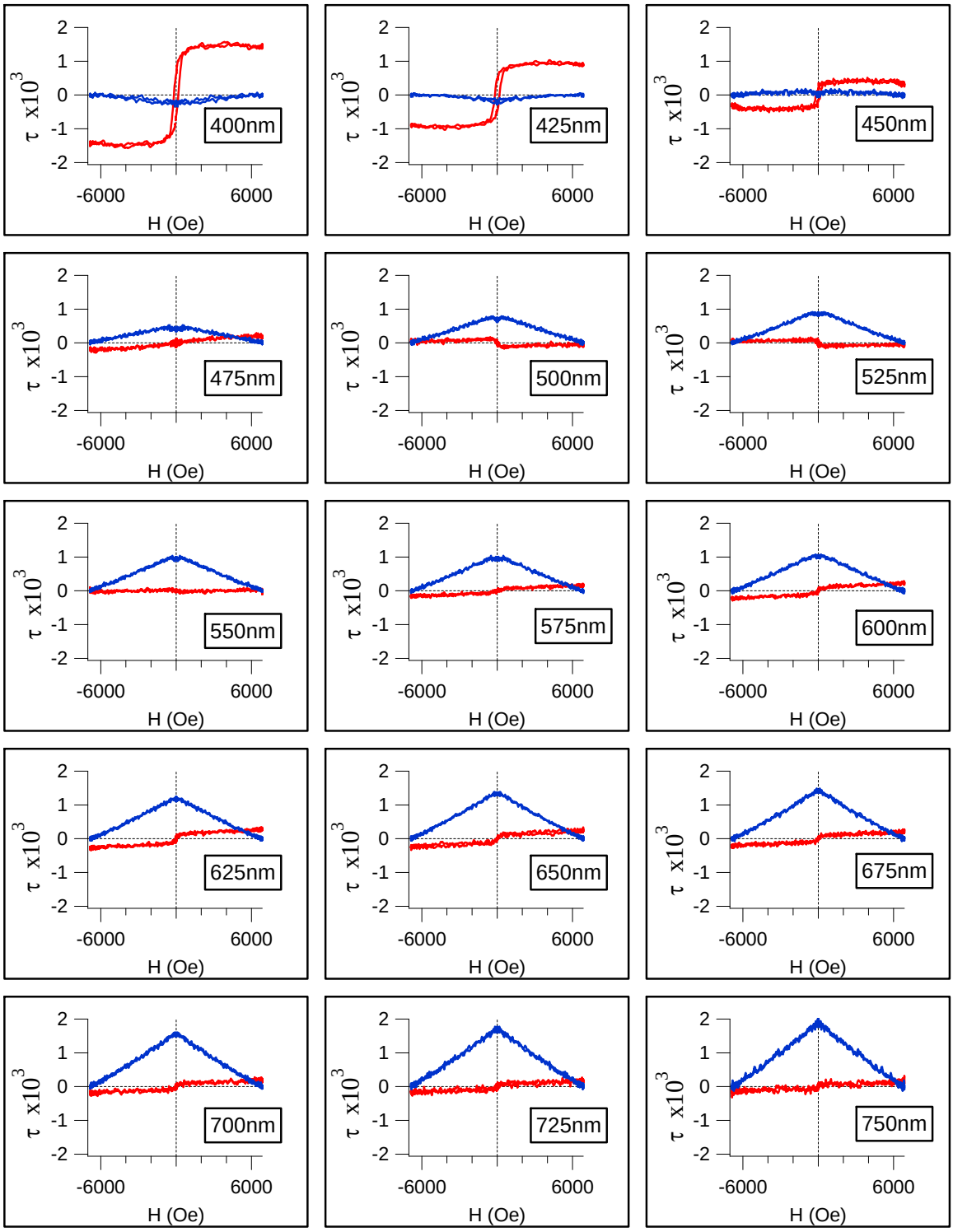

Figure 4.12: *The spectral dependence of* $\tau = \Im\left(\frac{\Delta r_{pp}}{r_{pp}}\right)_{odd,even}$ *hysteresis loops measured at* $T = 140K$*, odd contribution (red curves) and even contribution (blue curves)*

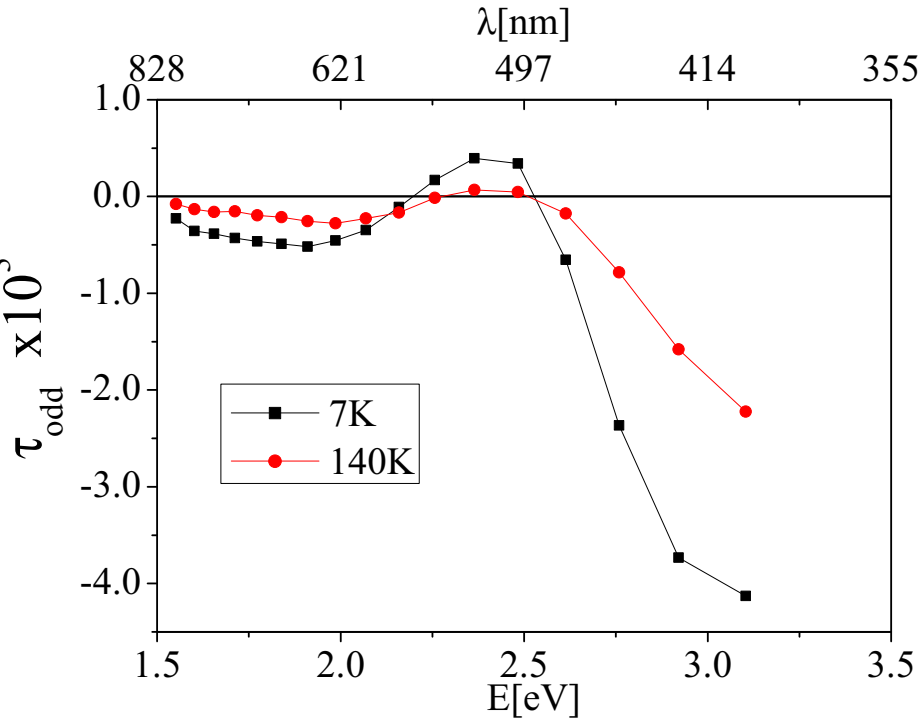

Figure 4.13: *The spectral dependence of the odd contribution measured at* $T = 7K$ *and* $T = 140K$*, respectively.* $\tau_{odd} = \Im\left(\frac{\Delta r_{pp}}{r_{pp}}\right)_{odd}$

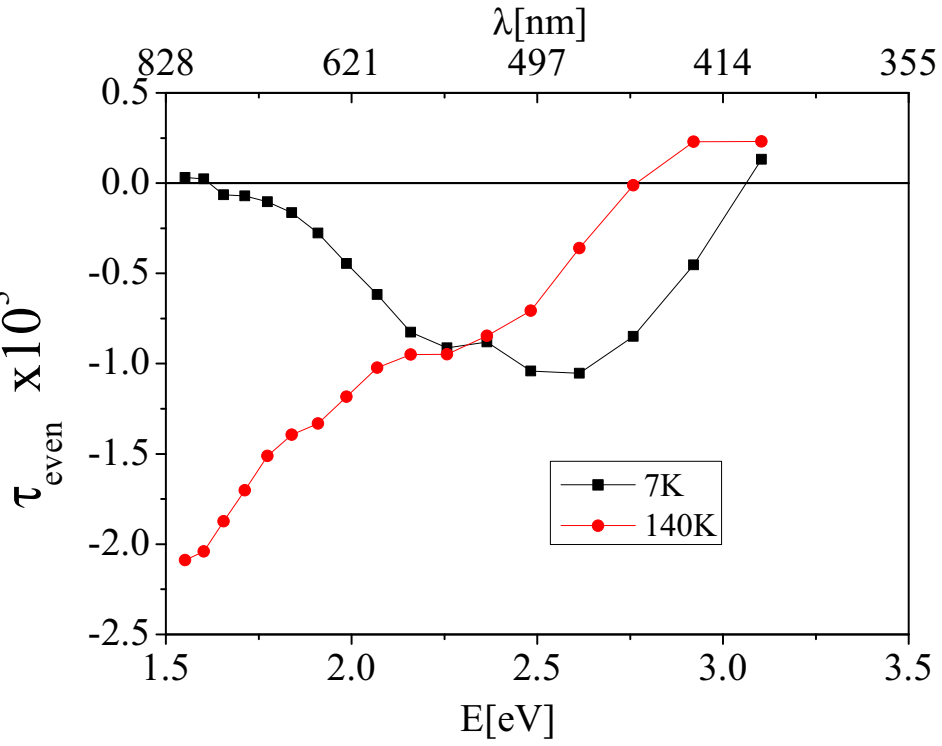

Figure 4.14: *Spectral dependence of the even contribution measured at* $T = 7K$ *and* $T = 140K$*, respectively* $\tau_{even} = \Im\left(\frac{\Delta r_{pp}}{r_{pp}}\right)_{even}$

reported on the literature [143–146]. On the other hand, figure 4.14 shows the values of the amplitudes of the even contributions that are proportional to the MRE ($T = 140K$) and to the QMO ($T = 7K$), respectively. Note that these amplitudes are defined with respect to the value at zero field and, in the case of the MRE, are negative in a wide range of wavelengths, signalling that the optical reflectance is reduced with field, as discussed above. The different origin of the two contributions results in quite dissimilar spectral responses for QMO and MRE. If we focus first on the QMO spectral response (7 K) where the QMO is larger. Quadratic effects comparable in magnitude to linear effects were reported for some ferrimagnetic and weak ferromagnetics crystals [147]. We have demonstrate that these phenomena are not restricted to such particular compounds, and indeed the quadratic effects may be dramatically enhanced at certain wavelengths[148].

A clue to understand this behavior is found in the theory of light scattering in magnetic crystals developed by Moriya [149]. The spin-dependent polarizability α tensor can be expanded in a power series up to the second order, i.e., $\alpha = \beta_{ikl}(a)\langle S_l(a)\rangle + \gamma_{iklm}(a)\langle S_l(a)S_m(a)\rangle + \delta_{iklm}(a,b)\langle S_l(a)S_m(b)\rangle + \ldots$, where i , k, l , m denote the coordinates x, y , z, and $\langle S_l(a)\rangle$, $\langle S_l(a)S_m(b)\rangle$ are averages of single ion and ionic spin pairs at sites a, b [147]. This expansion yields single-ion contributions β_{ikl},γ_{iklm} proportional to $\frac{\lambda_{SO}}{\Delta E}$ and $\frac{\lambda_{SO}}{\Delta E}$, respectively, and an inter atomic exchange δ_{ikml} term in powers of $\frac{I}{\Delta E}$, where λ_{SO}, I, and ΔE are the spin-orbit (SO) energy, the exchange integral, and the energy splitting of the relevant optical transitions [147, 149]. First-order magnetooptics is related to terms β_{ikl} linear in (SO) splitting [149, 150]. In contrast, the quadratic effects observed here cannot only depend on SO since in manganites $\frac{\lambda_{SO}}{\Delta E} \sim 10^{-2}$ [31], so that QMO effects would be orders of magnitude lower than LMO effects. However, quadratic effects also contain the interatomic exchange contribution mentioned above, which is first order in the exchange coupling I [147, 149]. Typically, in manganites, the interatomic exchange energy and the SO splitting are comparable in magnitude, i.e.,$\lambda_{SO}, I \sim 10^{-2}eV$ [31] and thus β_{ikl} and δ_{iklm} are similar in magnitude, thus, even effects (either MRE or QMO) can be as high as almost two orders of magnitude larger than the LMO. This explains the strongly asymmetric loops displayed in the figures 4.9. This may be the reason underlying the large nonconventional quadratic magnetooptical response observed in the LPCMO film. We believe that similar arguments should apply to a number of magnetic compounds.

Now, we turn to the MRE spectrum (T = 140 K). We see that whereas the QMO is peaked around 2.6 eV, the MRE shows an increasing amplitude down to the lowest photon energy, at around 1.5 eV (see figure 4.14). On the other hand, the spectral response of the MRE shows a sign reversal at an energy $\approx$ 2.75 eV and for increasing energies it shows a plateau up to the maximal explored photon energy, 3.2 eV. The discussion of

this MRE spectral response will be further detailed when comparing it with the MRE spectra of manganites with different compositions (see below) in connection with its plausible origin from the magnetic dependence of Jahn-Teller polaron conductivity and electron-phonon coupling. For that purpose, we have analyzed the complex transverse magnetooptical spectra of $LCMO$ and $LSMO$ manganites, which are known to have different electron-phonon coupling strengths, being PLCMO the compound with maximum electron-phonon interaction and $LSMO$ the weakest among these materials. From this study we will be able to conclude about the crucial role of electron-phonon coupling and polaron conductivity on the magnitude of the MRE observed around the ferromagnetic transition temperature.

4.2 Magnetooptical spectroscopy of LCMO

$La_{0.7}Ca_{0.3}MnO_3$ (LCMO) thin films were grown by our group at the ICMAB by radio-frequency sputtering on (110)-oriented $SrTiO_3$ (STO) substrates. These films, extensively characterized by x-ray diffraction, were found to be epitaxial with high crystalline quality [53, 151], for growth conditions and reports on the structural characterization). The figure 4.15 shows the main magneto-transport features of a LCMO thin film with thickness $t = 70nm$. This figure was already shown in the section 2.2.1 in order to introduce the basic properties of manganites, but we reproduce it here for convenience. The temperature dependence of the magnetization is shown in the panel 4.15a),indicating a clear paramagnetic to ferromagnetic transition at the Curie temperature around $T_C \approx 260K$. The inset shows the ferromagnetic hysteresis loop measured at $T = 10K$. In the panel 4.15b) we have plotted both resistivity with and without external magnetic field. The magnetoresistance is shown in the panel 4.15c). As expected, the application of a magnetic field leads to a large suppression of the resistance resulting in a negative colossal magnetoresistance, typical for LCMO.

Temperature dependence

As carried out previously in the section 4.1, the as measured complex transverse data were split into even $\Im\left(\frac{\Delta r_{pp}}{r_{pp}}\right)_{even}$ and odd $\Im\left(\frac{\Delta r_{pp}}{r_{pp}}\right)_{odd}$ contributions by using the equation 3.13. Figure 4.16 shows the amplitude of both contributions measured at a wavelength $\lambda = 632.8nm$ as a function of the temperature. As seen in this figure, whereas the temperature dependence of $\Im\left(\frac{\Delta r_{pp}}{r_{pp}}\right)_{odd}$ follows that of the magnetization, the $\Im\left(\frac{\Delta r_{pp}}{r_{pp}}\right)_{even}$ has a temperature dependence strikingly similar to that of colossal magnetoresistance

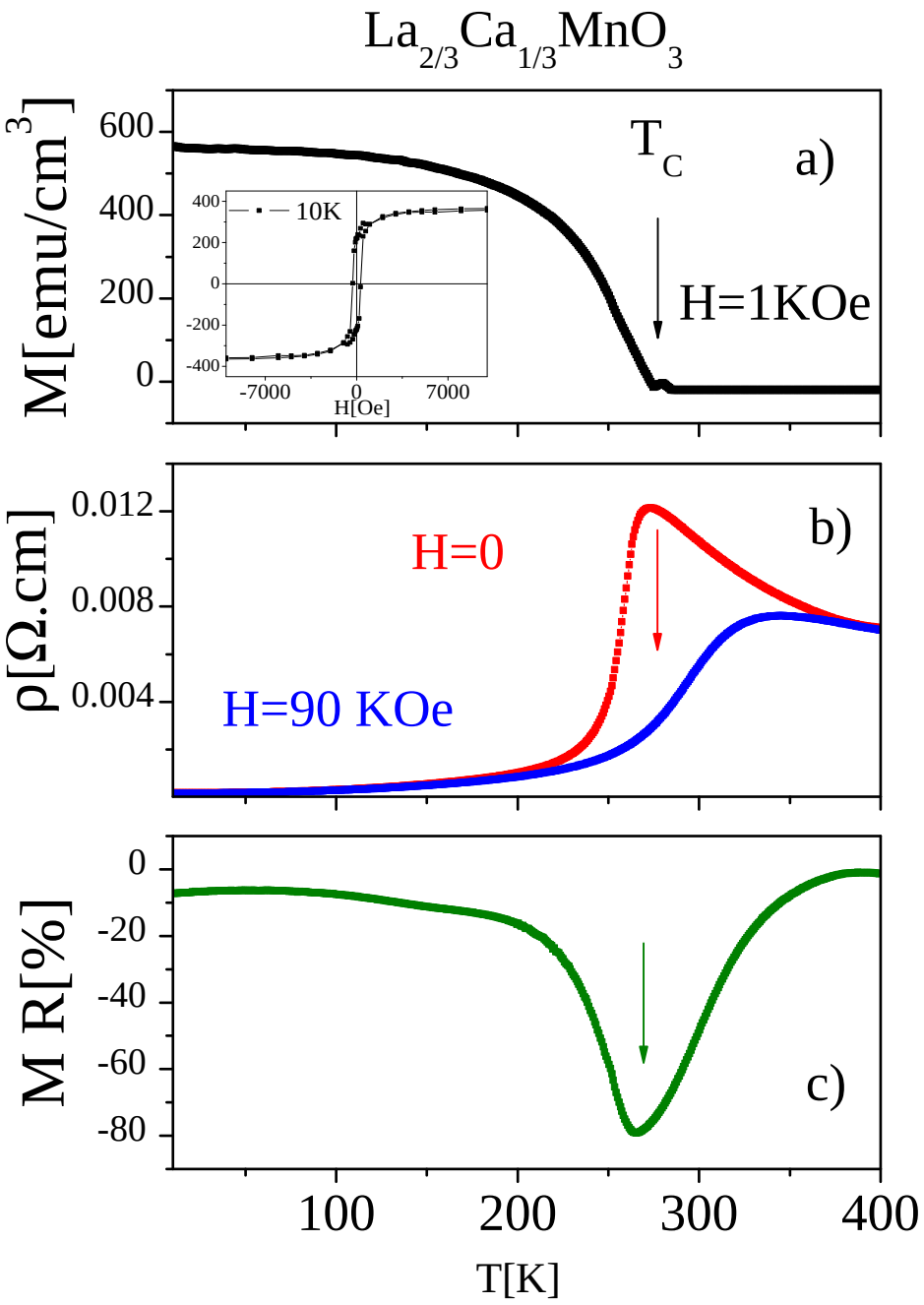

Figure 4.15: *Magnetization and magnetotransport of the LCMO thin film. a) Temperature dependence of the magnetization measured by SQUID at a field $H = 1kOe$. The inset shows a ferromagnetic loop measured at 10 K. b) Resistivity versus temperature measured under $H = 0$ T and $H = 9$ T. c) Magnetoresistance versus temperature.*

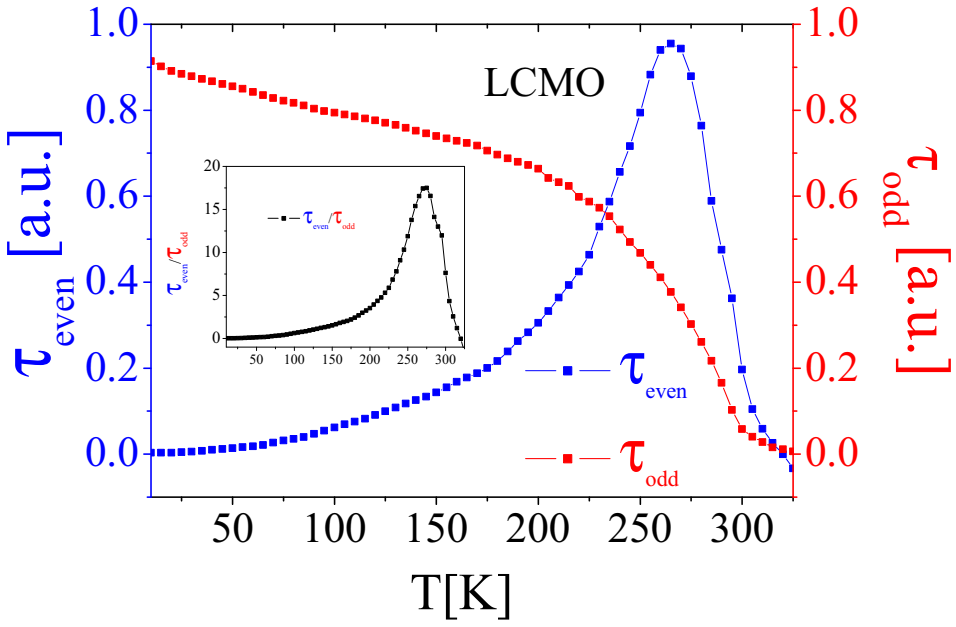

Figure 4.16: *Temperature dependence of the* $\tau_{odd} = \Im\left(\frac{\Delta r_{pp}}{r_{pp}}\right)_{odd}$ *and* $\tau_{even} = \Im\left(\frac{\Delta r_{pp}}{r_{pp}}\right)_{even}$ *contributions measured at wavelength* $\lambda = 632.8nm$. *The ratio* $\frac{\Im\left(\frac{\Delta r_{pp}}{r_{pp}}\right)_{even}}{\Im\left(\frac{\Delta r_{pp}}{r_{pp}}\right)_{odd}}$ *is plotted in the inset*

(CMR) (see figure 4.15c)), being close to T_C much larger than the odd counterpart. Indeed, as illustrated by data in figure 4.16, the MRE response $\Im\left(\frac{\Delta r_{pp}}{r_{pp}}\right)_{even}$ of LCMO films is about a factor ≈ 20 larger than the corresponding Kerr signal $\Im\left(\frac{\Delta r_{pp}}{r_{pp}}\right)_{odd}$ at temperatures close to the ferromagnetic transition [2]. That the strong $\Im\left(\frac{\Delta r_{pp}}{r_{pp}}\right)_{even}$ peak around T_C is uncorrelated with Kerr effects is further confirmed by measurements in the transverse geometry with p-polarized light at normal incidence. For symmetry reasons, the magnetooptical transverse Kerr response is forbidden in this configuration (Freiser [152]). However, we have confirmed that still an enhancement of $\Im\left(\frac{\Delta r_{pp}}{r_{pp}}\right)_{even}$ at $\alpha = 0°$, albeit lower than that measured at $\alpha = 45°$, is clearly visible close to T_C (See figure 4.17), thus confirming MRE as the origin of the observed effect. The reduction of reflectance from $\alpha = 45°$ to $\alpha = 0°$ may be related to the change in reflectance with α [137].

[2]Notice that the units of the vertical axes in figure 4.16 have been normalized to make easier the comparison between the odd and even contributions to the transverse signal

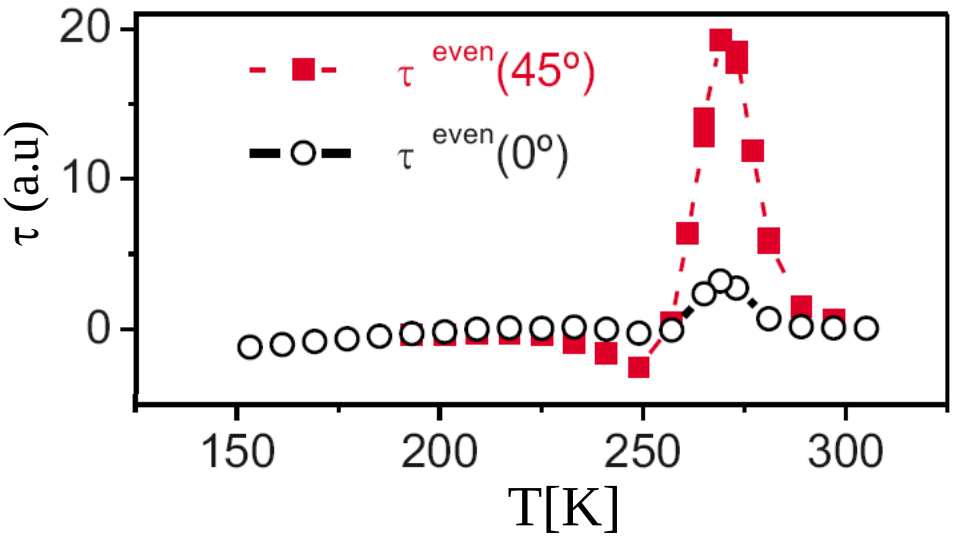

Figure 4.17: *Temperature dependence of the even contribution* $\Im\left(\frac{\Delta r_{pp}}{r_{pp}}\right)_{even}$ *of the LCMO thin film measured at normal incidence* $\alpha = 0°$ *(black curve) and oblique incidence* $\alpha = 45°$ *(red curve)*

Spectral response

We analyzed the dependence of the odd $\Im\left(\frac{\Delta r_{pp}}{r_{pp}}\right)_{odd}$ and even $\Im\left(\frac{\Delta r_{pp}}{r_{pp}}\right)_{even}$ contributions as a function of the incident photon energy in the range $\approx$ 1.5 eV - 3.5 eV. We focused our analysis to temperatures close to the ferromagnetic transition, where we know that the MRE is the largest. In particular, figure 4.18 shows the spectra of the magnetooptical odd contribution $\Im\left(\frac{\Delta r_{pp}}{r_{pp}}\right)_{odd}$ for three temperatures slightly below the Curie temperature T_C. As expected from its proportionality to the magnetization, the $\Im\left(\frac{\Delta r_{pp}}{r_{pp}}\right)_{odd}$ signal increases for decreasing temperature, although the rate depends on the photon energy, being the largest around the spectral region centered at 2.75 eV. We note that the spectral response shown in figure 4.18 is in excellent agreement with previous transverse Kerr spectra measured in doped manganites with similar doping [146], exhibiting a large negative peak around $E = 2.5eV$ together with an additional feature near $E = 1.6$ eV. On the other hand we have plotted in figure 4.19 the spectra of the even magnetooptical contribution, $\Im\left(\frac{\Delta r_{pp}}{r_{pp}}\right)_{even}$ for the same set of temperatures around the Curie temperature T_C. The spectra display a prominent peak at around 2.2 - 2.4 eV indicating that the strongest MRE is occurring at those photon energies. As discussed above, the MRE increases as the temperature approaches the transition temperature from below. The spectra of figure 4.19 will be discussed later on in conjunction with those of other manganites in relationship with the physics of MRE.

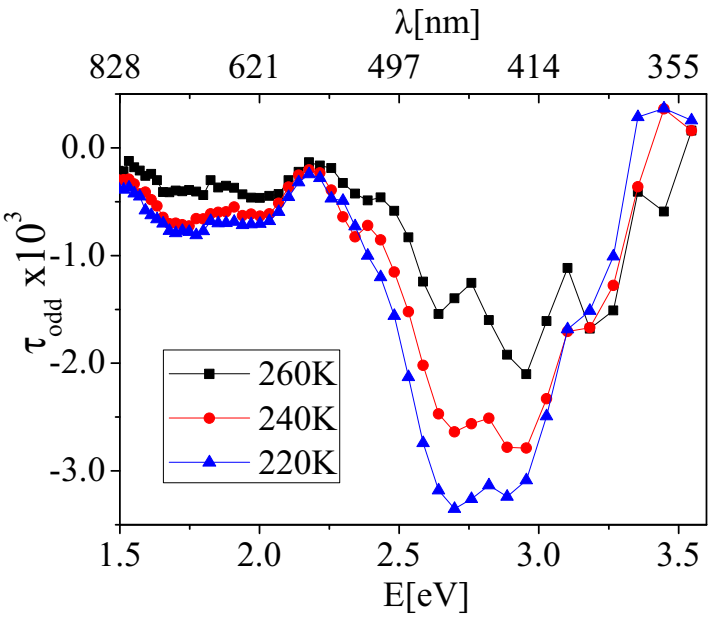

Figure 4.18: *Temperature dependence of spectra of the odd contribution* $\tau_{odd} = \Im\left(\frac{\Delta r_{pp}}{r_{pp}}\right)_{odd}$ *of LCMO*

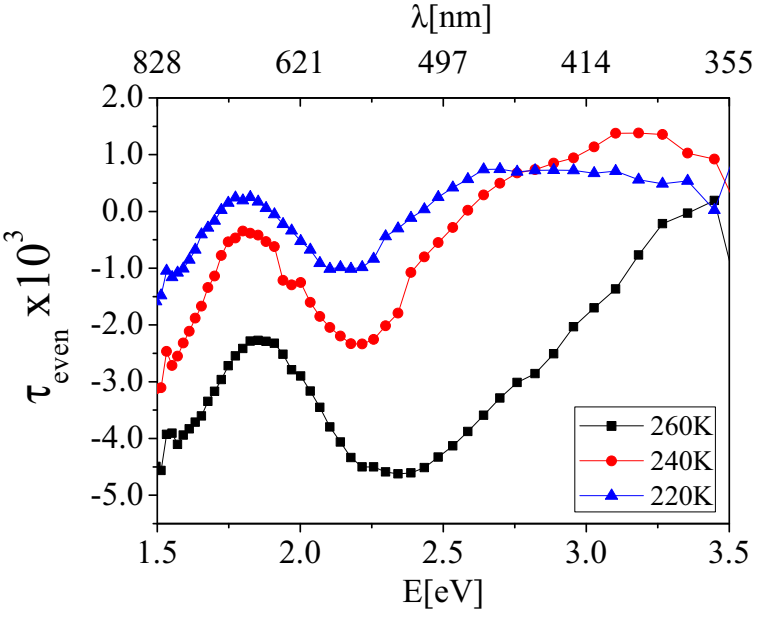

Figure 4.19: *Temperature dependence of spectra of the even contribution* $\tau_{even} = \Im\left(\frac{\Delta r_{pp}}{r_{pp}}\right)_{even}$ *of LCMO*

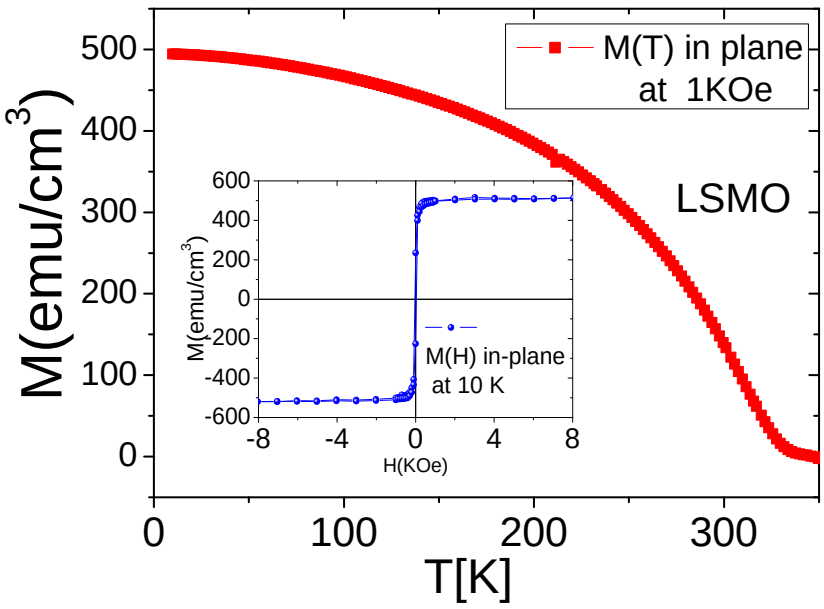

Figure 4.20: *Magnetization temperature dependence on LSMO. Magnetization field dependence (In-set)*

4.3 Magnetooptical spectroscopy of LSMO

$La_{0.7}Sr_{0.3}MnO_3$ (LCMO) thin films were grown by our group at the ICMAB by Pulsed Laser Deposition (PLD) technique on (110)-oriented $SrTiO_3$ (STO) substrates. The deposition was made at an oxygen pressure of 0.2 mbar and keeping the substrate at a temperature of $725°C$. After growth, the films were allowed to cool down to room temperature. The thickness of the sample, calculated by means of X-ray reflectometry (XRR) measurements was $20nm$.

These films, extensively characterized by x-ray diffraction, were found to be epitaxial with high crystalline quality [153]. The figure 4.20 shows the main magnetic features of a LSMO thin film with thickness $t = 20nm$. The Curie temperature is around to $T_C = 325K$

Temperature dependence

Following the same protocols as for the previously analyzed manganites, we have studied the temperature dependence of the odd and even contributions of the Kerr transverse response. Figure 4.21 shows the temperature dependence of $\Im\left(\frac{\Delta r_{pp}}{r_{pp}}\right)_{odd}$ and $\Im\left(\frac{\Delta r_{pp}}{r_{pp}}\right)_{even}$ measured by using light of wavelength $\lambda \approx 632$ nm at the highest applied magnetic field H $\approx 7kOe$, where both reach maximum values. The odd contribution $\Im\left(\frac{\Delta r_{pp}}{r_{pp}}\right)_{odd}$ is seen

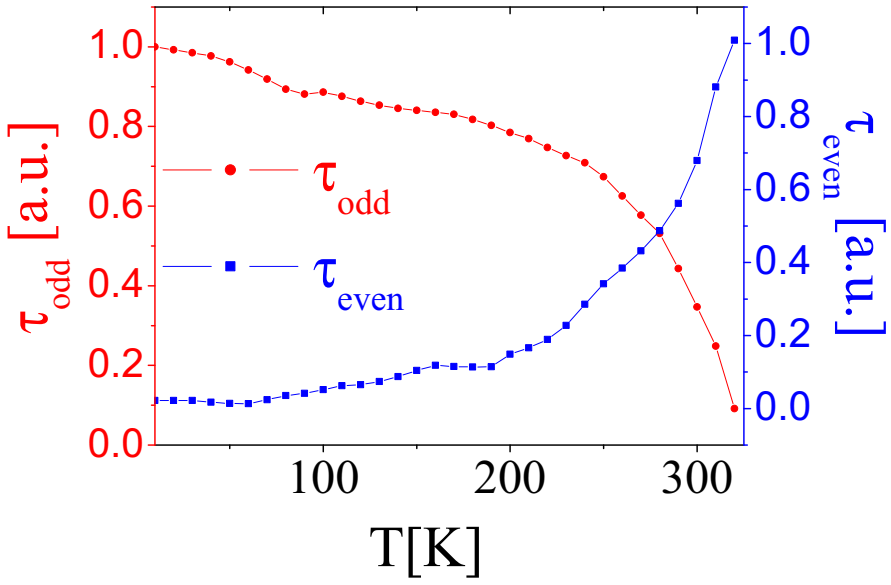

Figure 4.21: *Temperature dependence of the odd* $\Im\left(\frac{\Delta r_{pp}}{r_{pp}}\right)_{odd}$ *and even* $\Im\left(\frac{\Delta r_{pp}}{r_{pp}}\right)_{even}$ *contributions of* $La_{0.7}Sr_{0.3}MnO_3$ *thin film, measured at* $\lambda = 632.8nm$

to follow the temperature dependence of the magnetization measured by SQUID (see also figure 4.22), whereas the even contribution $\Im\left(\frac{\Delta r_{pp}}{r_{pp}}\right)_{even}$ is steadily increasing up to highest measured temperature T $\approx$ 320 K, in agreement with the expected MRE peak around the $T_C \approx 340K$. Thus, the temperature dependence of the Kerr transverse signal reproduce the same trends observed for the other manganites.

Spectral response

The spectra of $\Im\left(\frac{\Delta r_{pp}}{r_{pp}}\right)_{odd}$ are plotted in the figure 4.23 for two temperatures close to T_C, where we observe two main features at $E = 2.5$eV and $E = 3.0$eV in close similarity of the spectra of LCMO. The spectra of $\Im\left(\frac{\Delta r_{pp}}{r_{pp}}\right)_{even}$ are shown in the figure 4.24 for the same temperatures that again resemble the spectra of LCMO, with a peak located at energy around 2.2 eV.

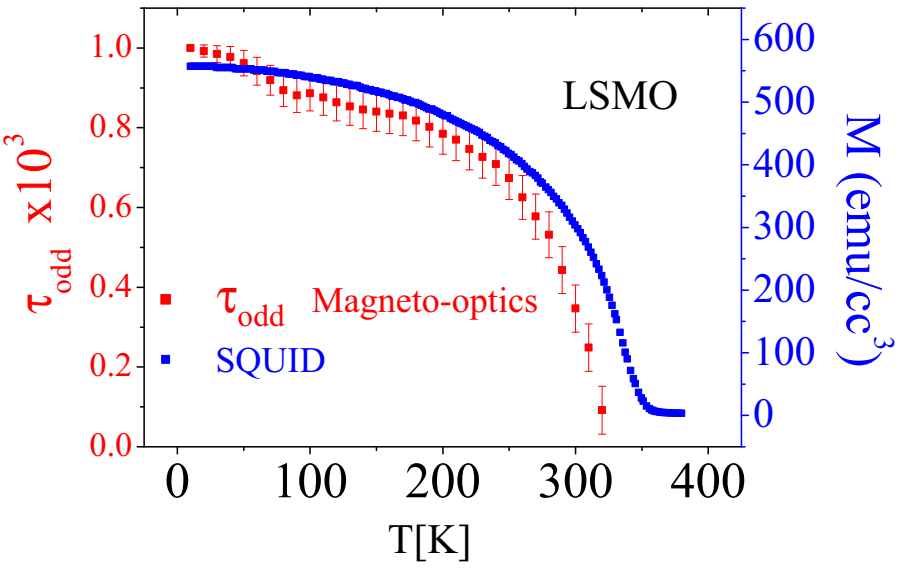

Figure 4.22: *Temperature dependence of the magnetization $M(T)$ measured by SQUID (blue curve) and odd contribution $\tau_{odd} = \Im\left(\frac{\Delta r_{pp}}{r_{pp}}\right)_{odd}$ measured at $\lambda = 632.8$nm (black curve) of the LSMO thin film.*

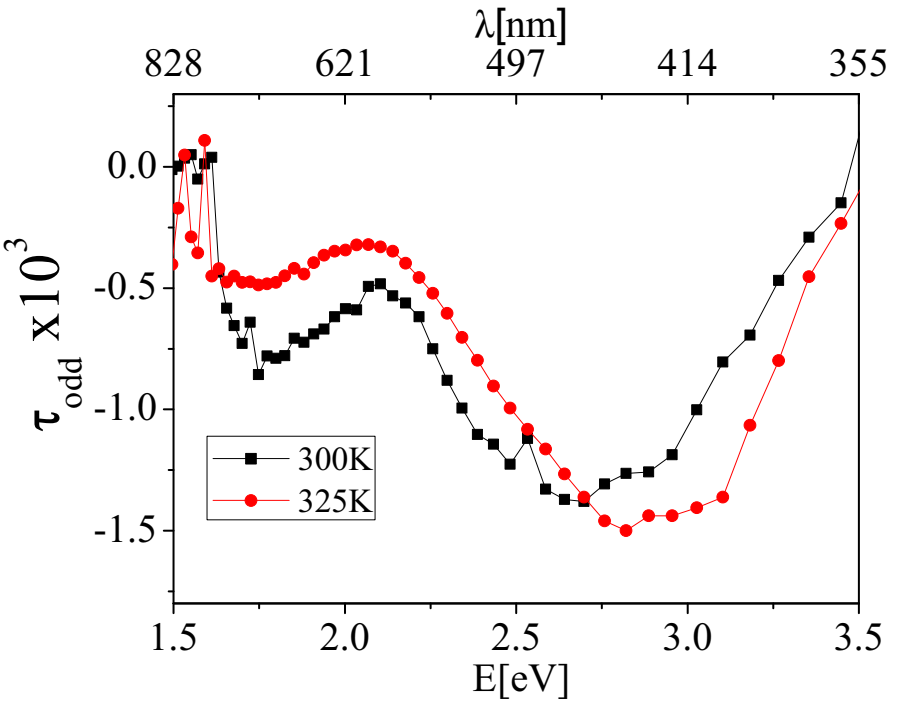

Figure 4.23: *Temperature dependence of the odd contribution spectra $\tau_{odd} = \Im\left(\frac{\Delta r_{pp}}{r_{pp}}\right)_{odd}$ of LSMO*

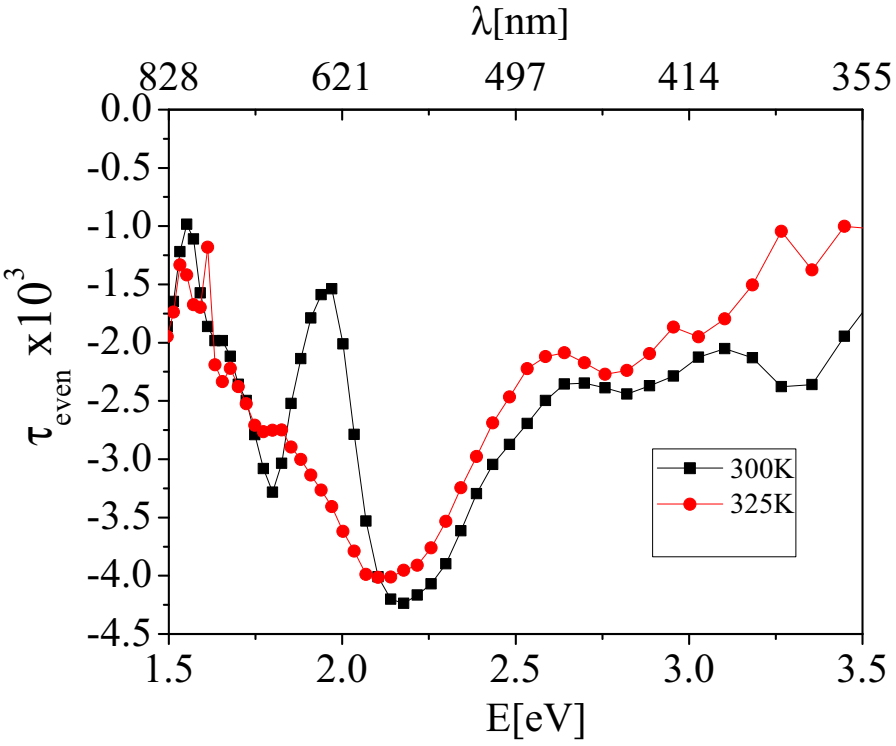

Figure 4.24: *Temperature dependence of the even contribution spectra* $\tau_{even} = \Im\left(\frac{\Delta r_{pp}}{r_{pp}}\right)_{even}$ *of LSMO*

4.3.1 Magnetorefractive effect and electron-phonon coupling

To investigate the link between the MRE and the CMR physics we replot for convenience in figure 4.25 the spectral responses of the amplitudes of the even contributions $\Im\left(\frac{\Delta r_{pp}}{r_{pp}}\right)_{even}$ to the transverse signal measured in PLCMO, LCMO and LSMO films. Note that in all cases these spectral responses, which are proportional to the MRE, are negative, indicating that for most wavelengths the reflectance is decreasing with field. This behavior is radically different to what happens at lower frequencies from dc to infrared, where the reflectance is increased with field, in agreement with the negative colossal magnetoresistance measured in dc transport. The sign reversal of the field dependence with field is related to a spectral weight transfer in the optical conductivity. As discussed in previous works [130, 131, 154], the Drude free electron-like contribution to the optical conductivity is overruled at optical frequencies by bound-electron resonances, such as polarons. Accordingly, at photon energies in the order of $\sim$ 1 eV and above, the spectral response is dominated by optical transitions among energetic levels split by Jahn-Teller distortions, which appear only in a narrow range of temperatures around the ferromagnetic transition. As soon as a magnetic field is applied, the Jahn-Teller distortions are thwarted and a spectral weight

transfer occurs towards lower frequencies. As a consequence, according to this model, the optical conductivity at visible frequencies must decrease with magnetic field, as observed experimentally. Thus, one would expect that by tuning the electron-phonon coupling in manganites, one should modulate the intensity of the MRE observed close to the ferromagnetic transition. We have achieved this by analyzing the optical properties of manganites of different chemical compositions at the A-site, namely PLCMO, LCMO and LSMO. In particular, among these compounds, LSMO has the largest e_g electron kinetic energy and the weakest effective electron-phonon interaction while in LCMO and especially PLCMO the kinetic energy is smaller and then the electron-phonon interaction is stronger [74].

The spectral response of the amplitudes of $\Im\left(\frac{\Delta r_{pp}}{r_{pp}}\right)_{even}$ is plotted for PLCMO (figure 4.25a), LCMO (figure 4.25b) and LSMO (figure 4.25c) at temperatures nearby the ferromagnetic transition. As discussed in section 2.2.1, the relevant optical transitions occurring in the analyzed range of energies are probably related to inter-site hopping of e_g electrons between neighboring sites, for which transitions around $2.0eV$ are predicted [75–82]. Within this picture, the MRE should be the strongest for photons with energies resonant with inter-site $d-d$ hopping. Our results show that in all cases the maximum amplitude in the measured range of photon energies is located in the interval $\approx$ 1.5 - 2.3 eV (figure 4.25), which is consistent with the suppression of polaron conductivity at energies close to the inter-site hopping. We are thus in position to assess the impact of electron-phonon coupling on the MRE and magneto-polaron conductivity.

To address this issue, we have quantified the MRE intensity by defining a figure of merit as:

$$\rho = \frac{\Im\left(\frac{\Delta r_{pp}}{r_{pp}}\right)_{even}}{\Im\left(\frac{\Delta r_{pp}}{r_{pp}}\right)_{odd}} \tag{4.2}$$

for which the value has been calculated at the temperature and photon energy at which the MRE amplitude is maximum. This figure of merit is displayed in the figure 4.26. In this figure, in addition to PLCMO, LCMO and LSMO, other two oxides, magnetite (Fe_3O_4, which will be discussed in the next chapter) and $SrRuO_3$ (SRO, for which is known that Ru^{4+} is not a Jahn-Teller ion and the electron-phonon coupling is much weaker than in manganites). The figure 4.26, shows the ratio $\rho = \frac{\Im\left(\frac{\Delta r_{pp}}{r_{pp}}\right)_{even}}{\Im\left(\frac{\Delta r_{pp}}{r_{pp}}\right)_{odd}}$ in a narrow window around transition temperature for all compounds. The amplitude of the ratio varies largely: it is the highest for the PLCMO film, whereas for SRO the signal is almost 4 orders of magnitude lower than that of PLCMO, as it might be expected from the

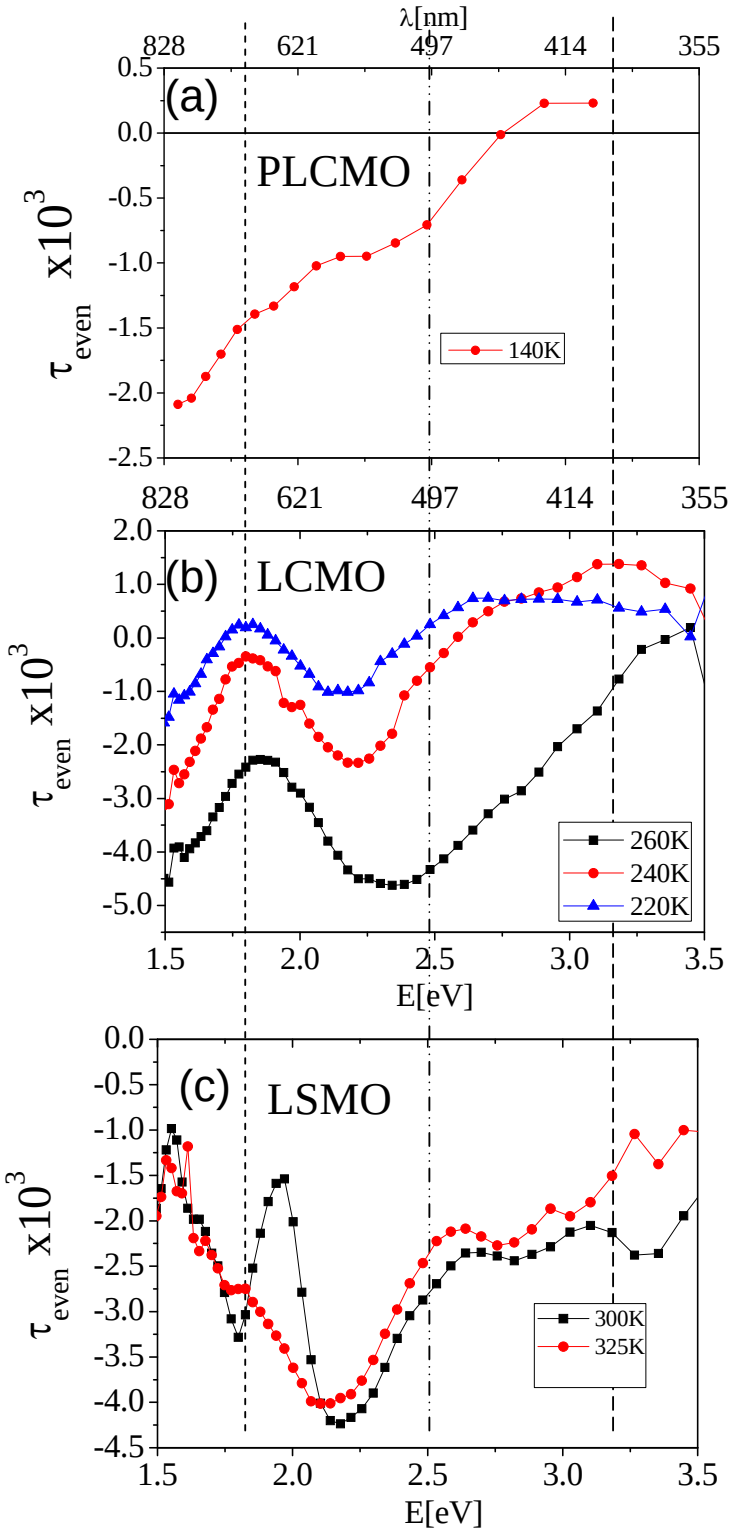

Figure 4.25: *Spectra of the even contribution* $\tau_{even} = \Im\left(\frac{\Delta r_{pp}}{r_{pp}}\right)_{even}$ *close to* T_c*, (a)PLCMO, (b)LCMO, and (c)LSMO thin films*

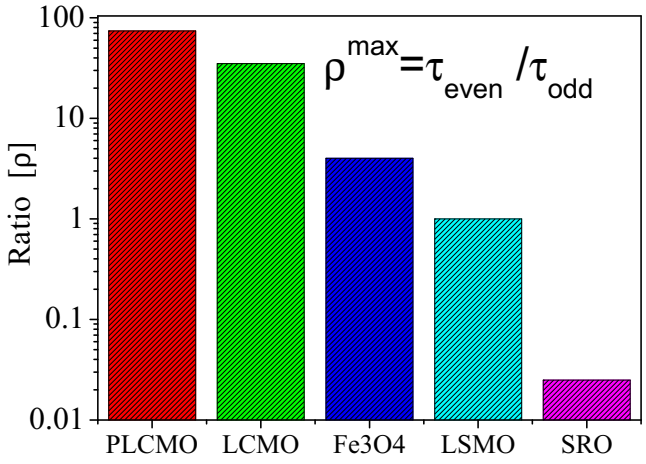

Figure 4.26: *The figure of merit* $\rho = \frac{\Im\left(\frac{\Delta r_{pp}}{r_{pp}}\right)_{even}}{\Im\left(\frac{\Delta r_{pp}}{r_{pp}}\right)_{odd}}$ *is evaluated at temperatures close to* T_C *for different magnetic oxides. Maximum value over all the energies is reported*

significantly smaller magnetoresistance of SRO with respect to manganites [155]. Finally, the LSMO film shows a significantly smaller MRE intensity than that observed in LPCMO and LCMO, as expected from its relatively wide e_g band and less relevant electron-phonon coupling.

We have confirmed the relationship between the MRE intensity and electron-phonon coupling by defining an alternative figure of merit, in which for all the materials the ratio 4.2 is calculated close to the respective T_C, but now at the same wavelength ($\lambda = 632nm$). The corresponding plot is shown in figure 4.27. In spite of the slightly different criterion, the general trends are conserved, i.e., PLCMO and LCMO show the strongest MRE intensification, whereas magnetite and LSMO are intermediate and SRO has a negligible MRE. Overall, our results indicate conclusively that the CMR physics and the Jahn-Teller coupling are basic ingredients for the MRE enhancement observed around the ferromagnetic transition.

Finally we close the discussion showing a normalized temperature dependence of even contribution for all the studied materials. The figure 4.28 shows the $\Im\left(\frac{\Delta r_{pp}}{r_{pp}}\right)_{even}$ as function of the T/T_C.

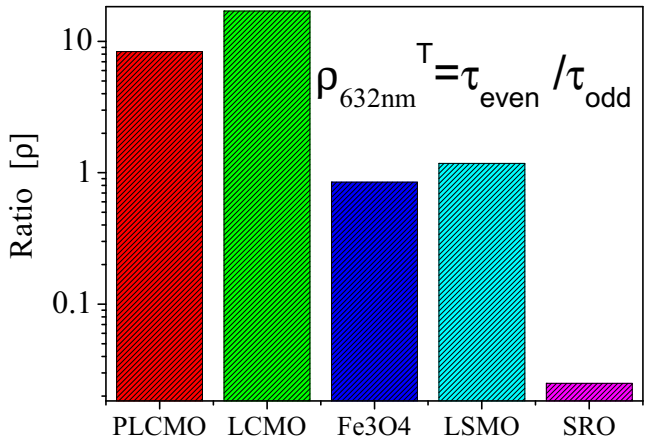

Figure 4.27: *The figure of merit* $\rho = \frac{\Im\left(\frac{\Delta r_{pp}}{r_{pp}}\right)_{even}}{\Im\left(\frac{\Delta r_{pp}}{r_{pp}}\right)_{odd}}$ *is evaluated for different magnetic oxides at the same wavelength* $\lambda = 632.8$*nm. Maximum value over temperatures is reported*

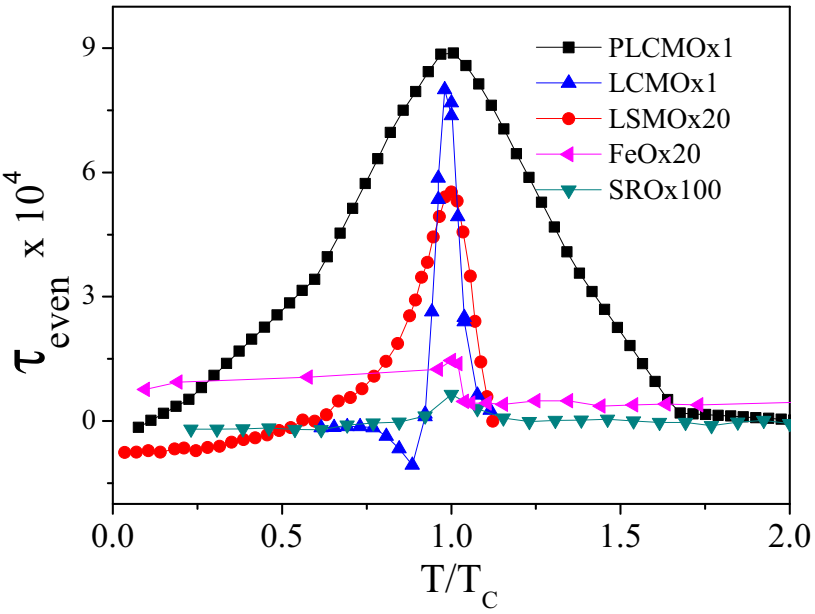

Figure 4.28: *The* $\Im\left(\frac{\Delta r_{pp}}{r_{pp}}\right)_{even}$ *as function of the* T/T_C *is evaluated for different magnetic oxides at the same wavelength* $\lambda = 632.8$*nm*

4.4 Magnetorefractive effect detected by magnetoreflectance in the visible range

So far the magnetorefractive effect has been detected in complex transverse Kerr configuration with $p-$ polarized incident light. We have thus demonstrated that in these experiments it is possible to separate the magnetooptical contributions from the MRE. Although measuring the MRE by exploiting the transverse response has the advantage of giving simultaneous information of magnetism and transport, the MRE is usually measured in magnetoreflectance (MR) by applying a magnetic field (H) and measuring the reflectance (R) of unpolarized light, having direct access to MRE, however the MRE obtained by MR is a convoluted information including magnetooptical contributions (linear and quadratic) at magnetic fields lowers than saturation field. Facing those arguments the straightforward data obtained by MR must to treated with special attention.

Taking account that MRE reported on the literature by MR (usually IR at high magnetic fields) is rather different of MRE obtained by complex transverse Kerr effect let' to compare both approaches. To check the consistency of our measurements obtained in a magnetooptical configuration, we have carried out magnetoreflectance experiments at ICMAB in collaboration with Dr. A. V. Telegin (Institute of Metal Physics, Ural Branch of the Russian Academy of Sciences, Yekaterinburg) and Prof. A.B. Granovsky (Moscow State University), on $La_{0.7}Ca_{0.3}MnO_3$ thin films grown by metalorganic vapor phase epitaxy (MOVPE) on $LaAlO_3$ (001) single crystal substrates [156]. In these experiments, we determined the magnetoreflectance $\Delta R/R$ of unpolarized light as:

$$\Delta R/R = \frac{R(H) - R(0)}{R(0)} \tag{4.3}$$

thus respecting the same sign convention as used in MRE extracted from the complex transverse response (see also equation 3.20 and section 3.5.1). In equation 4.3 $R(H)$ and $R(0)$ are the reflectance values measured with and without magnetic field, respectively.

Figure 4.29 shows the MR spectra measured in a field $H = 11kOe$ by shining with unpolarized light two LCMO thin films grown by MOVPE with thicknesses $t = 50nm$ and $t = 320nm$, respectively. In the same Figure, we replot the MRE data extracted from the transverse response for the LCMO thin film grown by pulsed laser deposition, with thickness $t = 50nm$. In this way, we can compare the MRE spectra obtained in the same material by two different approaches. According with the physical origins discussed above, the observed differences in the MRE spectra for each particular case are clear, thus the

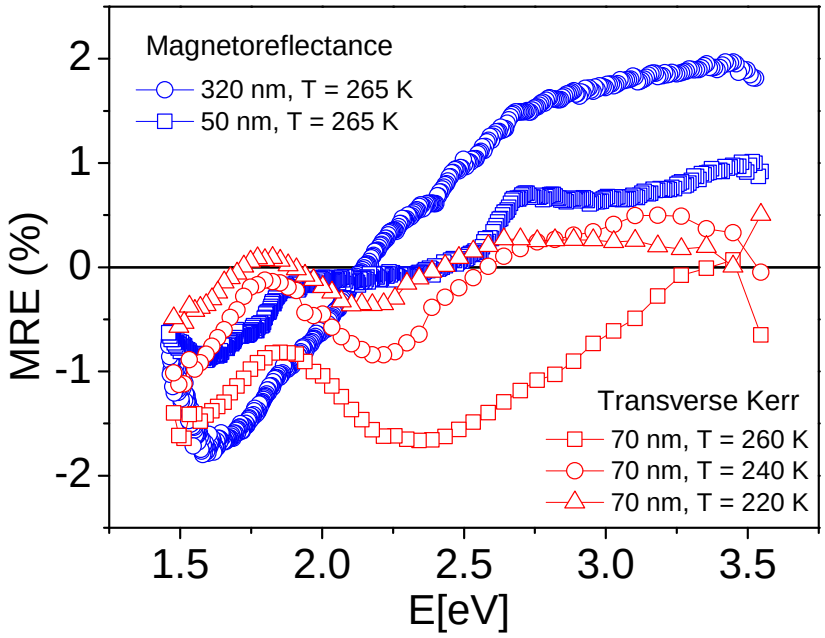

Figure 4.29: *Magnetorefractive effect measured by magnetoreflectance (LCMO thin films grown by MOVPE) and by magnetooptical transverse effect (LCMO thin film grown by pulsed laser deposition).*

data in Figure 4.29 indicates that the microscopic structural properties may be strongly influential. This is illustrated by the fact that films grown by the same method (MOVPE) exhibit some dissimilarities in the spectra measured at the same temperature $T = 265K$. In this case, the slightly different MRE response may be due to changes in the structural condition of the films when varying their thickness. On the other hand, temperature is also an important factor that shapes the MRE spectral response. This is indicated by the strong dependence on temperature of the MRE spectra measured in the LCMO thin film grown by pulsed laser deposition. However, in spite of these variations in the MRE spectra, we observe common trends in Figure 4.29. First, the maximum MRE values in the visible are about 2% whatever the methodology used to determine it. Secondly, the maximum values are attained in the lower range of photon energies within the interval E = 1.5 - 2.3 eV, whereas for increasing photon energy the MRE reverses sign from negative to positive within the interval E = 2.5 - 3.4 eV. Therefore, these results show that both magnetoreflectance and transverse magnetooptical spectroscopy are appropriate to analyze the spectral response of the MRE.

4.5 Magnetorefractive effect in the infrared

So far we have studied the magnetooptical properties of manganites in the visible range, which involves bound states and Jahn-Teller polarons in the optical response. In order to complete the analysis in the low energy regime, we have studied the effect of selected samples using infrared radiation, for which a strong contribution to the optical properties should come from free electrons. For that purpose, in collaboration with Prof. Sarah Thompson at the University of York, we have carried out magnetoreflectance experiments in the infrared. The set up at York allowed us to obtain the MR in a range of wavelengths $\lambda \approx 5\mu m - 22\mu m$, covering photon energies $E \approx 0.055 - 0.25$ eV.

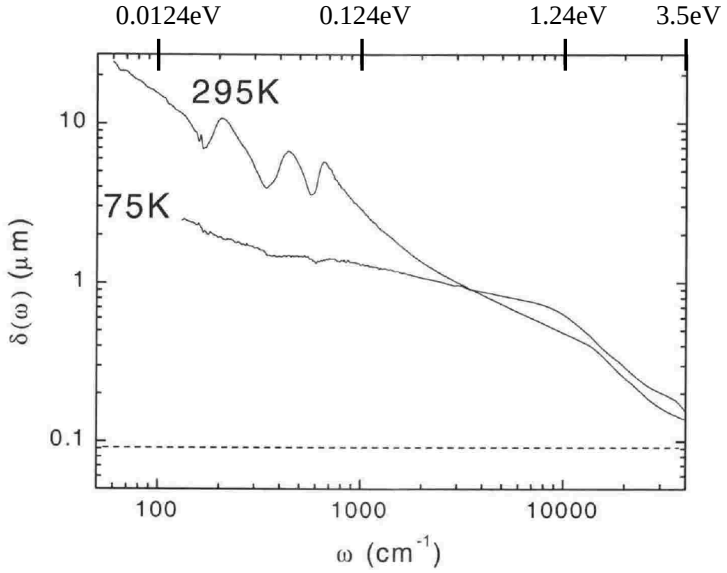

Figure 4.30: *Skin depth $\delta(\omega)$ of $La_{0.735}Ca_{0.265}MnO_3$ measured at 295K and 75K. Taken from [157]*

Because of the large penetration (skin depth) of infrared radiation in solids and the low thickness of films (typically below 100 nm), the optical properties of the substrates may contribute substantially to the as-measured spectral response. As an illustration, the skin depth for LCMO in the low energy regime is shown in the figure 4.30 [157]. The figure shows that the skin depth ranges from tens of microns in the far-infrared to a few hundreds of nanometers towards the visible. Thus, for far- and mid-infrared, the optical properties of the substrates on top of which the manganite films are grown have a large contribution to the global optical response. Taking into account these effects, we start the discussion on the optical properties of the substrates, which in our case where $SrTiO_3$ (STO) single crystals.

Reflectivity spectra were recorded at normal incidence $\theta = 0°$ on a bare STO substrate (Figure 4.31). To analyze the optical properties we considered a four-parameter model to describe the form of the dielectric function in the substrate. This model uses a factorized form of the dielectric function and takes the form:

$$\epsilon_{sub}(\kappa) = \epsilon_{sub\infty} * \prod_{j=1}^{n} \frac{\kappa_{L_j} - \kappa^2 - i\gamma_{L_j}\kappa}{\kappa_{T_j} - \kappa^2 - i\gamma_{T_j}\kappa} \tag{4.4}$$

This model assumes that the transverse optical (TO) phonon modes are the poles of the dielectric response, while the longitudinal optical (LO) phonon modes are the zeroes [158]. The reflectivity spectrum of Figure 4.31 was simulated by using the equation 4.4, and the phonon parameters to fit the data are shown in the table 4.1 -the parameters were taken from Boris *et al.* [158]-.

ω_{jT}	γ_{jT}	ω_{jL}	γ_{jL}
92	16	171	3.8
175	6.2	476	5.3
443.5	18.6	443.8	18.6
544	17	793	24
635.1	43	635.2	40
710.1	41	710.8	41

Table 4.1: *Best fit phonon parameters by the equation 4.4 for STO at 300 K*

The sharp spike seen in figure 4.31 at approximately $15\mu m$ is caused by CO_2 absorption of the IR light and is a contaminant that should be ignored. Figure 4.31 testify the quality of these fittings, which reproduce the features of the experimental spectra. In particular, it reproduces the minima observed at approximately $11\mu m$ and $21\mu m$, which correspond to the first and the second phonon bands in STO, respectively [158].

Now we proceed to the analysis of the reflectance spectra of the manganite films deposited on (001)-oriented STO substrates. For that purpose we studied a series of manganite films, including one LCMO film (thickness t = 70nm) and two LSMO films -with thicknesses t=17nm and t=41nm, respectively-. Figure 4.32 shows the reflectance spectra of the bare substrate as well as manganite films on STO measured at zero magnetic field ($H = 0T$). From this figure it is shown that although the spectral response is modified by the manganite film, a large contribution from the substrate is evident, as expected from the large penetration of infrared radiation into the samples.

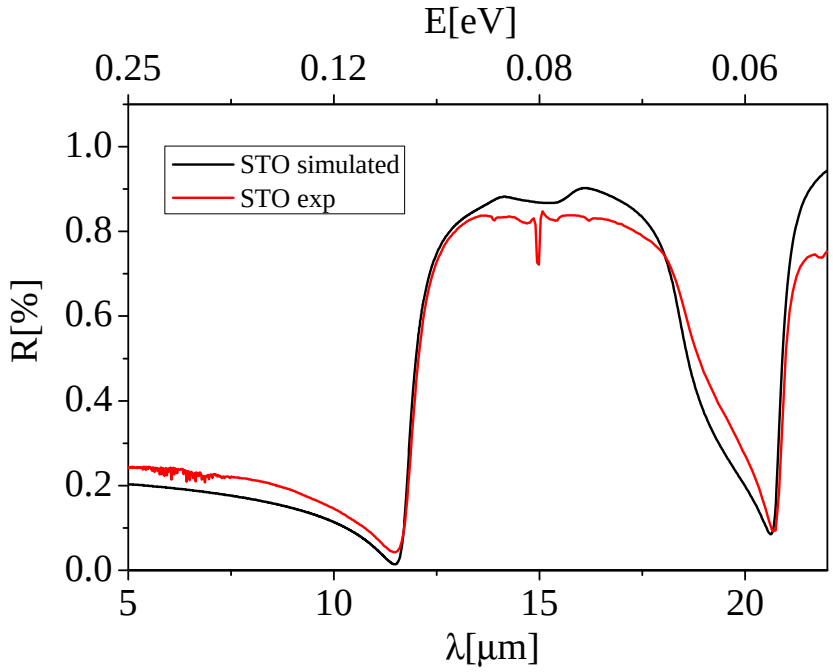

Figure 4.31: *Experimental (red line) and simulated (equation 4.4, black line) reflectivity of the STO substrate.*

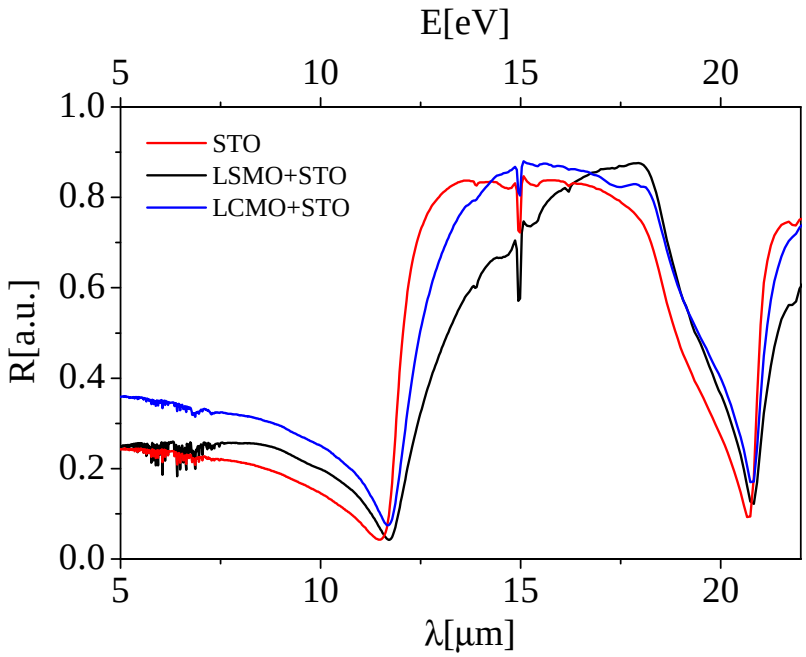

Figure 4.32: *Reflectance spectra of the bare substrate (STO) and LCMO and LSMO thin films on the STO substrate.*

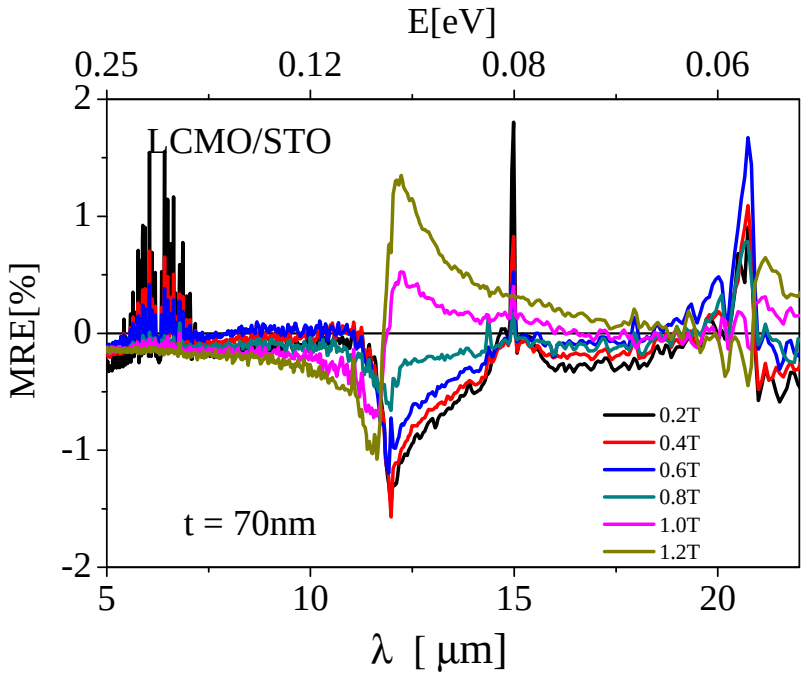

Figure 4.33: *MRE spectra in the far- and mid-infrared of a LCMO thin film with thickness t = 70nm for different applied magnetic fields.*

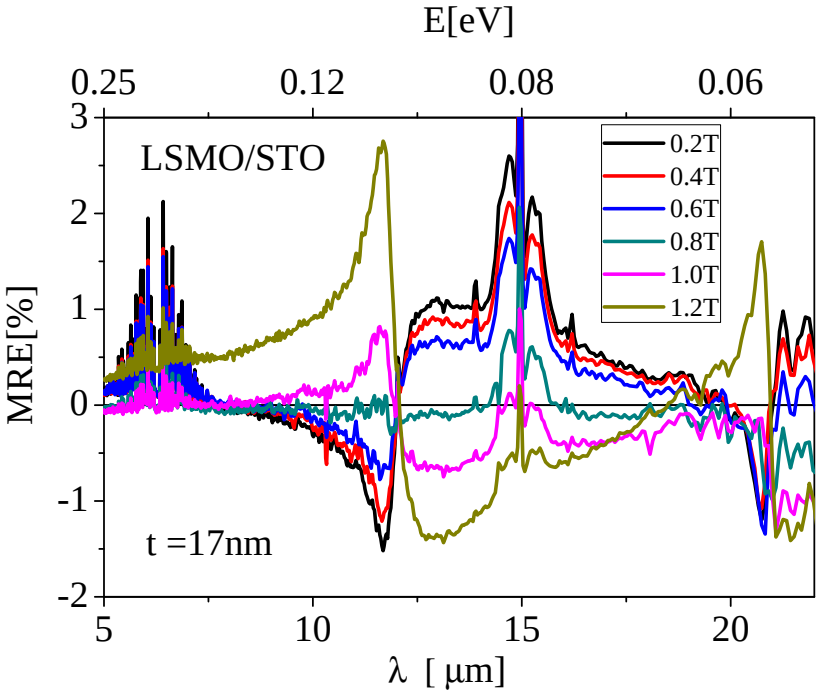

Figure 4.34: *MRE spectra in the far- and mid-infrared of a LSMO thin film with thickness t = 17nm for different applied magnetic fields.*

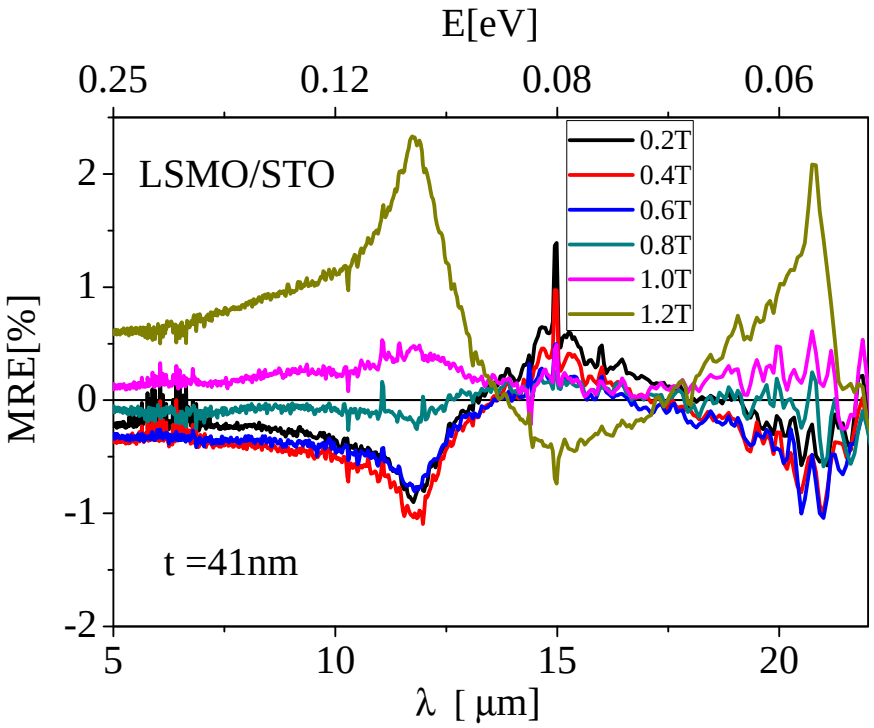

Figure 4.35: *MRE spectra in the far- and mid-infrared of a LSMO thin film with thickness $t = 41nm$ for different applied magnetic fields.*

To obtain the MRE response, reflectance spectra were recorded at different applied fields up to $H = 12kOe$, and the MRE values were obtained by applying the equation 4.3. Note that by subtracting the zero field data from the spectra measured under field we suppress the contribution from the substrate, provided that the latter has no magnetic dependence, as it should be for STO. The resulting MRE spectra are displayed in figures 4.33, 4.34 and 4.35. From these figures, we observe the following common trends for both materials:

(i) The maximum MRE in the analyzed range of wavelengths ($\lambda \approx 5\mu m - 22\mu m$) is about 2 - 3% and, thus, comparable to maximum values of MRE in the visible (figure 4.29).

(ii) The most relevant MRE is developed within a spectral region around $\lambda \approx 10\mu m - 20\mu m$, becoming progressively smaller towards the visible.

Note that a positive MRE (higher reflectivity under applied fields) should be expected for CMR manganites with strong negative magnetoresistance -i.e., exhibiting an increase of conductivity with fields-, provided that the optical response to magnetic fields is fundamentally associated to delocalized carriers (Drude model). Nevertheless, the experimental MRE spectra in the range of far- and mid-infrared wavelengths are well far away from

this simple picture: the MRE shows both positive and negative values, with an intricate structure that depends on the magnitude of the applied fields. Therefore, the optical response giving way to MRE can not be described only in terms of free electron-like Drude contribution and other contributions of different nature have to be taken into account.

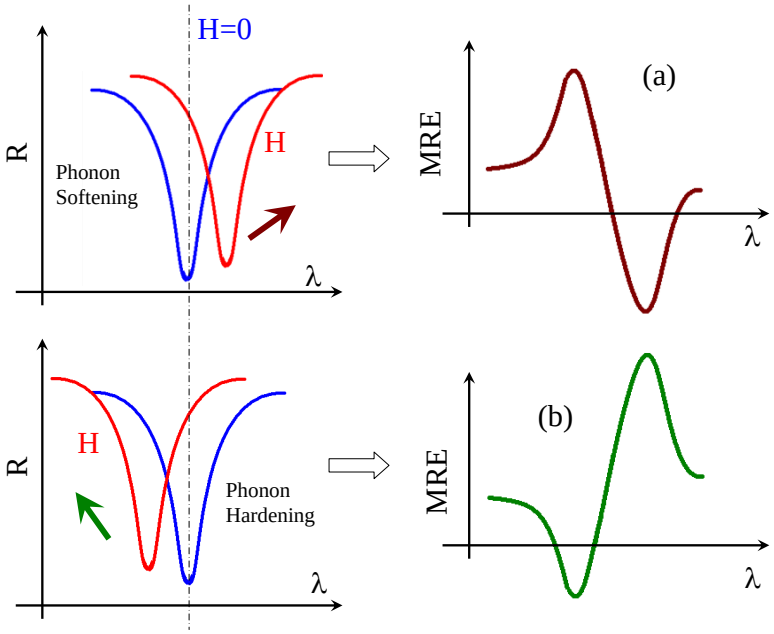

Figure 4.36: *Schematic of phonon softening induced by magnetic field (a) and a field-induced phonon hardening(b)*

Interestingly, a different mechanism, based on spin-phonon coupling in manganites may be responsible for the observed complex MRE spectral response in the infrared. In fact, reports exist on the dependence of phonon vibration modes in magnetic field, so that the resonance frequencies at which the lattices are excited can be shifted by the applied fields [30, 130, 159, 160]. A schematic representation of the field dependence of reflectance spectra is given in figure 4.36. This figure represents in a schematized way the effect of the Drude response and phonon resonance shift on the reflectance spectra under magnetic fields: figure 4.36(a) depicts the effect of phonon softening with field, whereas figure 4.36(b) illustrates a field-induced phonon hardening. When added to the effect of the Drude response -which is always assumed to be a positive contribution to MRE- the global effect is to induce a complex spectral response exhibiting both negative and positive values depending on the wavelength range. Note that in the literature, phonon modes with energies below $0.1eV$ correspond to optical phonon modes[160]. These values are in a reasonable agreement with the described model and experimental data (figures 4.33, 4.34 and 4.35), which seem to indicate that a first phonon band should be present at around $\lambda \approx 12\mu$ m. According to this simplistic model, the MRE response

at high fields seems to be affected by phonon softening in LCMO (figure 4.33), whereas in LSMO phonon hardening may be predominant (figures 4.34 and 4.35). Whatever the particular mechanism for field-induced modulation of phonon spectra, it is clear from the experimental data that the MRE spectral response in the far- and mid-infrared is affected fundamentally by the evolution of phonon modes with magnetic fields.

4.6 Conclusions

Our exhaustive analysis of the MRE phenomenon in a broad spectral range covering from the near ultraviolet up to the far-infrared ($\lambda \approx 0.39\mu m - 22\mu m$) allows to understand the physical mechanisms lying behind the MRE complex spectral response of manganites: (i) At visible wavelengths, the MRE is associated to the field-dependent polaron conductivity, being the suppression of Jahn-Teller polarons with magnetic fields the ultimate mechanism for this behavior. This conclusion is reinforced by the experimental observation of the correlation between the MRE response and the electron-phonon coupling strength. (ii) At far- and mid-infrared wavelengths, the MRE can not described solely in terms of a Drude free electron-like optical response to fields: field-induced softening/hardening of lattice vibrational modes have to be invoked to understand the MRE response at these wavelengths.

CHAPTER 5

Magnetorefractive effect in Magnetite

The samples of magnetite studied here were prepared by the group led by Prof. Igor Shvets at the Centre for Research on Adaptive Nanostructures and Nanodevices (CRANN), School of Physics, Trinity College Dublin, Ireland.

5.1 Magnetite thin films

A magnetite thin film with thickness $t = 120$ nm was grown on a Magnesium Oxide MgO (001) single crystal substrate using oxygen-plasma-assisted molecular-beam epitaxy (DCA MBE M600). The growth of the Fe_3O_4 film was carried out by means of electron-beam evaporation of metallic Fe in the presence of free oxygen radicals ($1.1 \times 10^{-5}\, Torr$) (more preparation details can be found elsewhere [161–163]).

The magnetization was measured by SQUID magnetometry. The temperature dependence of the in-plane magnetization M(T) is shown in figure 5.1 measured under different applied magnetic fields. We observe that at ≈ 102 K these curves exhibit a kink signalling the Verwey transition in this film. This reduce Verwey temperature compared to the high reported temperature ≈ 125 K reported in bulk magnetite [85–88] can be related to the formation of anti-phase boundaries (APB). These are defects appearing during the thin film growth due to the difference in symmetry between Fe_3O_4 and MgO [164]. The kink in the M(T) curves of figure 5.1 is originated by a change of the magnetic anisotropy across the Verwey transition, which is smoothed upon the application of fields $> 7kOe$. In order to complete the study, a synthetic crystal of Fe_3O_4 was also fully characterized. It was grown employing the skull melting technique and showed a Verwey transition temperature $T_V = 119K$ [89].

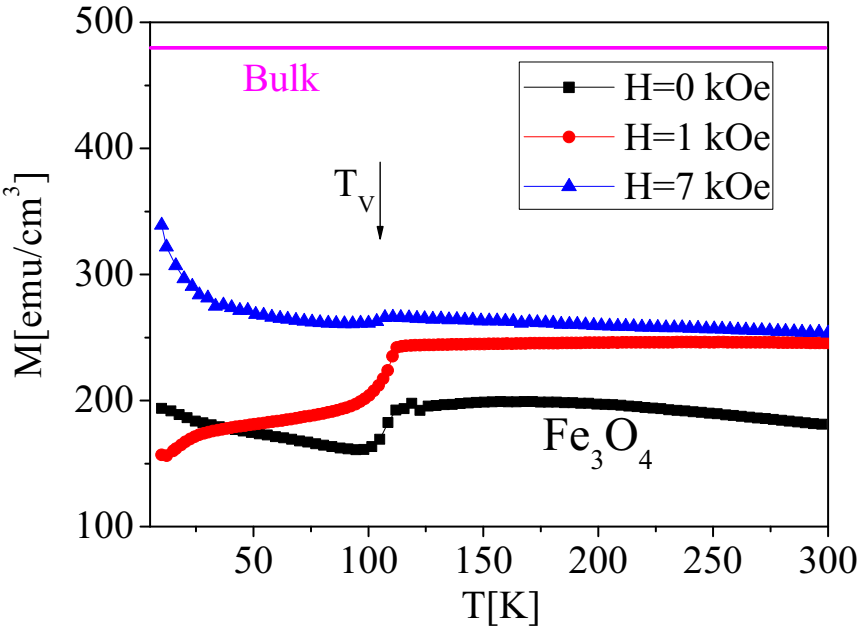

Figure 5.1: *In plane magnetization temperature dependence of Fe_3O_4 thin film*

5.1.1 Magnetooptical characterization

Figure 5.2 shows the hysteretic loops of the imaginary part of the complex transverse Kerr effect $\Im\left(\frac{\Delta r_{pp}}{r_{pp}}\right)$ measured at a wavelength $\lambda = 632nm$ for different temperatures around the Verwey transition. As done in chapter 4, we have split mathematically the spectra between even $\Im\left(\frac{\Delta r_{pp}}{r_{pp}}\right)_{even}$ and odd $\Im\left(\frac{\Delta r_{pp}}{r_{pp}}\right)_{odd}$ contributions by using the equation 3.13. In the figure 5.3 we have plotted the amplitudes of the odd and even hysteresis loops, as well as the coercive field as a function of the temperature. A first inspection of figure 5.3 immediately reveals that the Verwey transition can be observed for all these parameters which undergo abrupt changes in their values across the transition, at $T_V \approx 102K$.

The spectral dependence of the odd and even contributions $\Im\left(\frac{\Delta r_{pp}}{r_{pp}}\right)_{odd,even}$ measured at $T = 110K$ is displayed in figure 5.4. This temperature is chosen because of its proximity to the Verwey temperature, where the even contribution is the largest (see figure 5.3). We see that the shape of both the odd and even contributions is strongly dependent on light frequency. Concerning the spectra of the odd signal, we observe that the hysteresis loops reverse the sign between $\lambda = 500$nm and $\lambda = 475$nm, in agreement with the observed sign reversal of the magnetooptical constants of magnetite in the visible region [100, 165–168]. This still more visible when we plot the amplitudes of the spectra in figure 5.5, where the even contribution is also plotted.

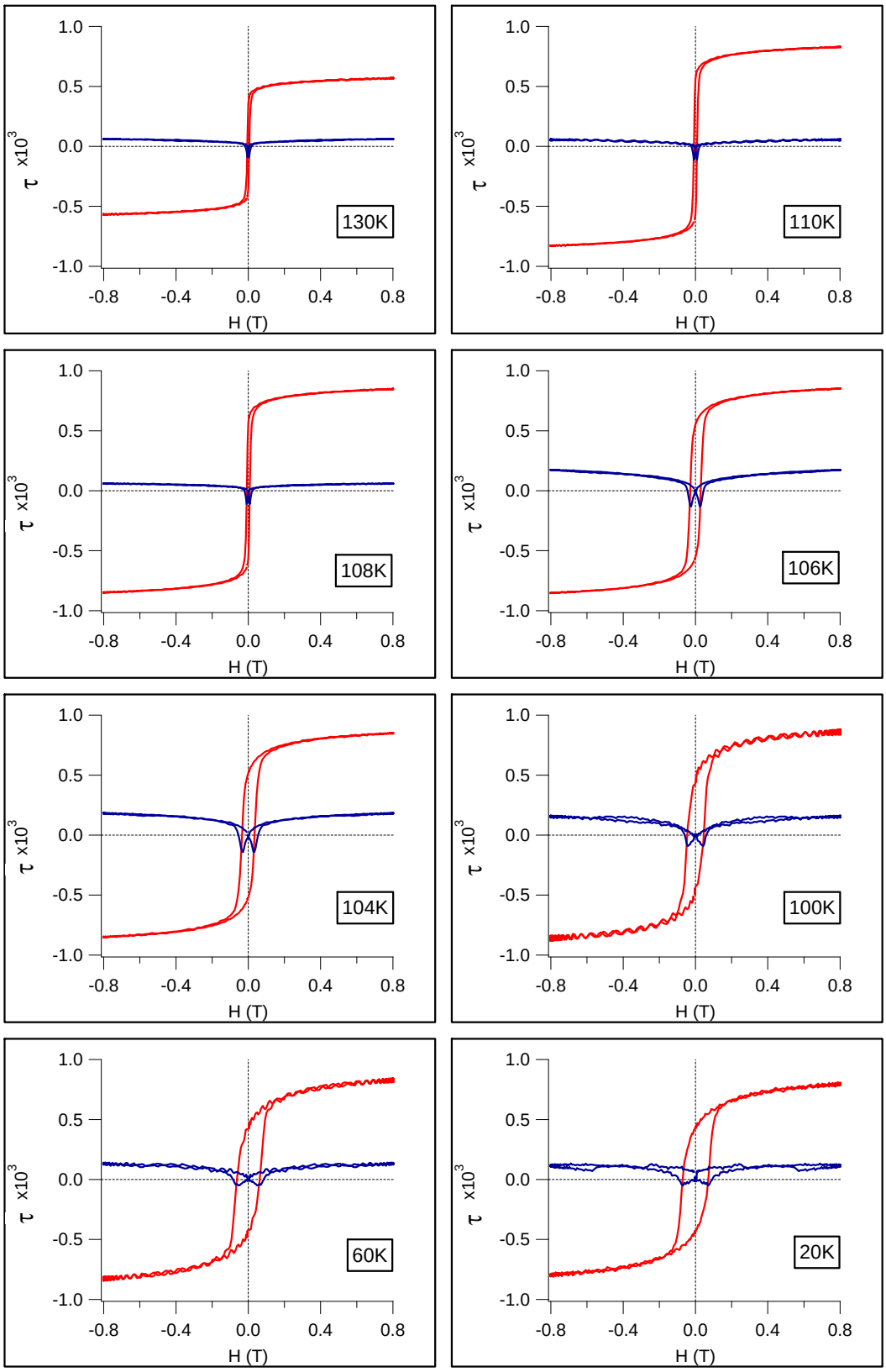

Figure 5.2: *Temperature dependence of the odd contribution* $\tau_{odd} = \Im\left(\frac{\Delta r_{pp}}{r_{pp}}\right)_{odd}$ *(red curves) and even contribution* $\tau_{even} = \Im\left(\frac{\Delta r_{pp}}{r_{pp}}\right)_{even}$ *(blue curves) hysteresis loops of* Fe_3O_4 *thin film at* $\lambda = 632.8nm$

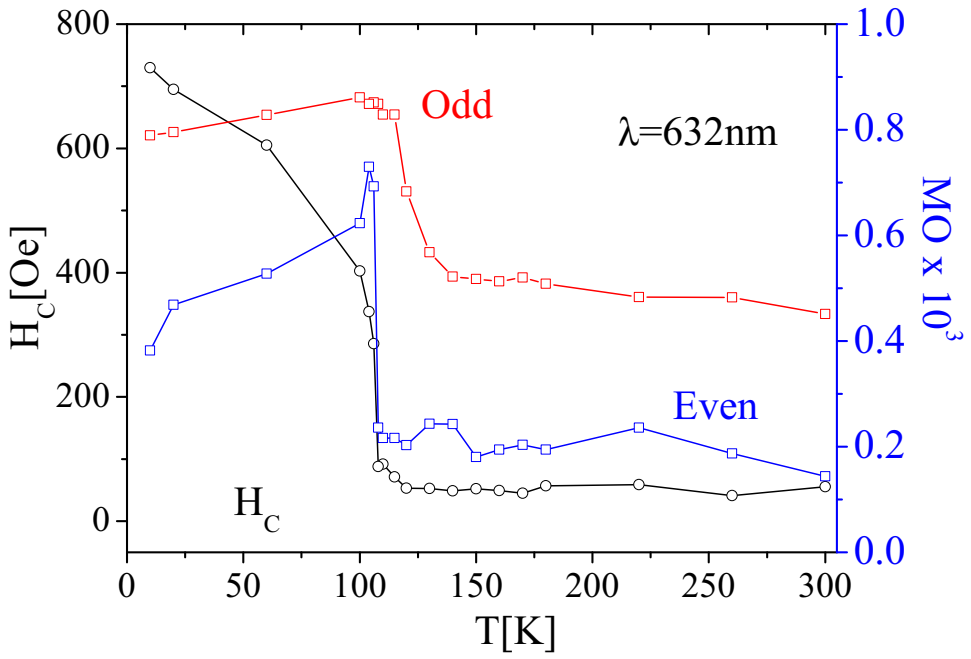

Figure 5.3: *The coercive field H_c (black curve), odd $\tau_{odd} = \Im\left(\frac{\Delta r_{pp}}{r_{pp}}\right)_{odd}$ (red curve), and even $\tau_{even} = \Im\left(\frac{\Delta r_{pp}}{r_{pp}}\right)_{even}$ (blue curve) contributions.*

Now we address the origin of the even contribution $\Im\left(\frac{\Delta r_{pp}}{r_{pp}}\right)_{even}$ and identify whether QMO or MRE are responsible for such phenomena. For that purpose, we analyze the loops measured at $\lambda = 450$nm and $T = 100$K, i.e., close to T_V and for a wavelength for which the even contribution is rather large. First, we note that both odd and even signals saturate at roughly the same field, thus suggesting that both contributions are correlated. To better illustrate this correlation, we have plotted the even $\Im\left(\frac{\Delta r_{pp}}{r_{pp}}\right)_{even}$ and the squared odd $\Im\left(\frac{\Delta r_{pp}}{r_{pp}}\right)^2_{odd}$ contributions in the same figure 5.6. The resulting curves are those expected for a even contribution proportional to magnetization square (M^2) relationship, i.e. the even-parity contributions to the magnetooptical signal are quadratic in the magnetization, as expected for QMO effects, and thus at first sight it would indicate that this is their origin. However, as the magnetoresistance (MR) in several systems is found to be proportional M^2 and it is known that MRE is proportional to MR, this still leaves the MRE as a possible source of even contribution.

To check this possibility, we plotted in the figure 5.7 the even contribution $\Im\left(\frac{\Delta r_{pp}}{r_{pp}}\right)_{even}$ together with the normalized d.c. magnetoresistance measured at $T = 80$K. Figure 5.7 clearly indicates that the observed even-parity loops measured at optical frequencies are proportional to the hysteretic resistance loops measured in d.c. transport. This striking coincidence shows that the dc-magnetoresistive response is effectively quadratic in the

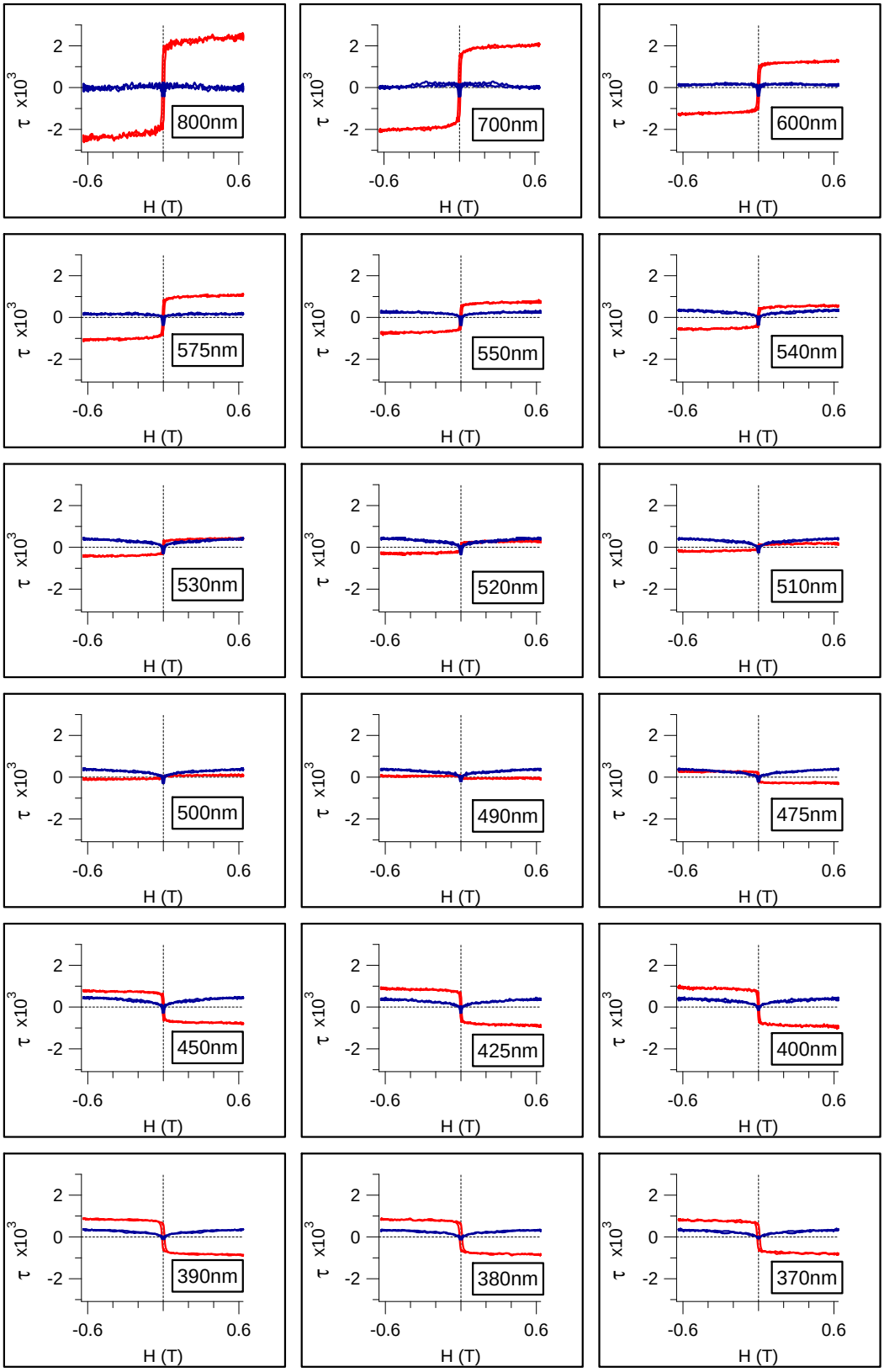

Figure 5.4: *The odd contribution* $\tau_{odd} = \Im\left(\frac{\Delta r_{pp}}{r_{pp}}\right)_{odd}$ *(red curves) and even contribution* $\tau_{even} = \Im\left(\frac{\Delta r_{pp}}{r_{pp}}\right)_{even}$ *(blue curves) spectral dependence of* Fe_3O_4 *thin film at* $T = 110K$.

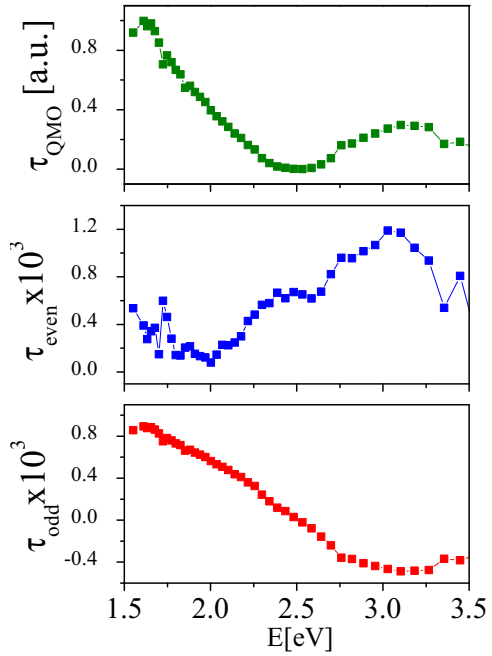

Figure 5.5: *The odd* $\tau_{odd} = \Im\left(\frac{\Delta r_{pp}}{r_{pp}}\right)_{odd}$ *(red curve), and even* $\tau_{even} = \Im\left(\frac{\Delta r_{pp}}{r_{pp}}\right)_{even}$ *(blue curve) magnetooptical amplitudes and quadratic magnetooptical effect* $\tau^2_{odd} = \Im\left(\frac{\Delta r_{pp}}{r_{pp}}\right)^2_{odd}$ *(QMO-green curve) calculated from odd contribution at* $T = 110K$.

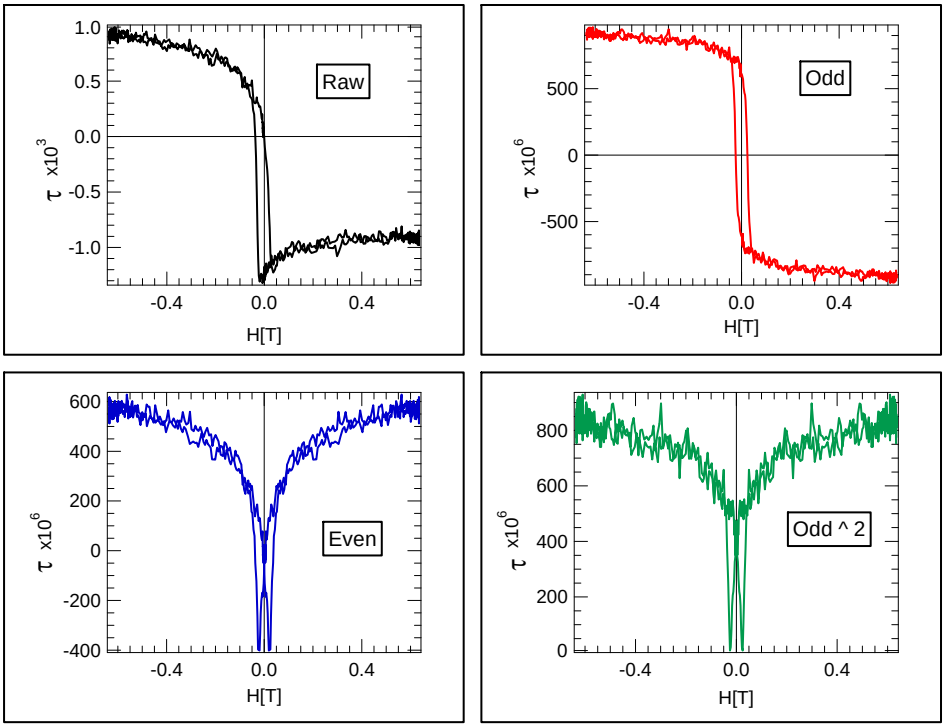

Figure 5.6: *Measurement at* $\lambda = 450nm$ *and* $T = 100K$*, raw data (black curve), odd (red curve), even (blue curve), and QMO (green curve)-calculed from the odd contribution.*

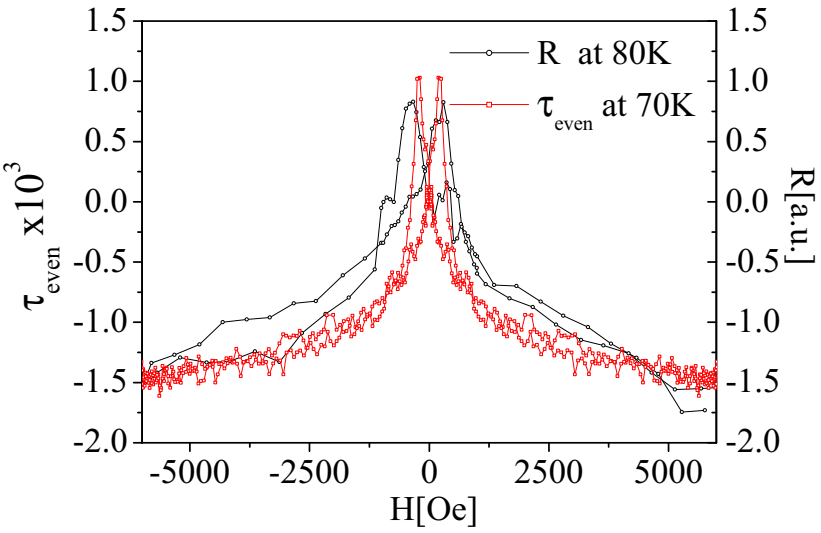

Figure 5.7: *The field dependent* $\tau_{even} = \Im\left(\frac{\Delta r_{pp}}{r_{pp}}\right)_{even}$ *measured at* $T = 70K$ *is normalized and plotted together with the normalized values of the magnetic field dependence of the resistance* $R(H)$ *of the thin film measured at* $T = 80K$

.

magnetization, and the even-parity magnetooptical response mimics the field dependence of d.c. electrical resistivity.

To clarify further the origin of the even $\Im\left(\frac{\Delta r_{pp}}{r_{pp}}\right)_{even}$ loops, we analyzed their temperature dependence at some suitable frequency. The evolution of the even contribution with temperature is illustrated in figure 5.8, where we plot the even contribution loops of the thin film (measured at $\lambda = 500$nm) at several different temperatures. It is clear from this figure that close to the Verwey transition $T_V \approx 102K$ the amplitude of the even-parity contribution is large, i.e. it reaches a value of $\approx 10^{-3}$ at $T = 100K$, whereas for temperatures away from the transition temperature the values of $\Im\left(\frac{\Delta r_{pp}}{r_{pp}}\right)_{even}$, although still clearly visible, are significantly reduced. To illustrate the temperature dependence of $\Im\left(\frac{\Delta r_{pp}}{r_{pp}}\right)_{even}$ we plotted its amplitude by taking its maximum values at each temperature. Thus, in figure 5.9a) we show the even amplitude for thin film and single crystal measured at different temperatures in the range of $10K << T << 300K$. This figure clearly shows that the even-parity contribution is strongly peaked at the Verwey temperature. Note also the relatively slow decay with temperature away from the transition, making the effect observable even at room temperature, i.e. about $T = 200K$ above the transition. The close agreement of the temperature evolution of the even contribution and the Verwey transition suggests that the anomalous magnetooptical response is correlated to the electrical transport properties of magnetite.

To check this correlation, we plotted in figure 5.9b) the temperature dependence of the

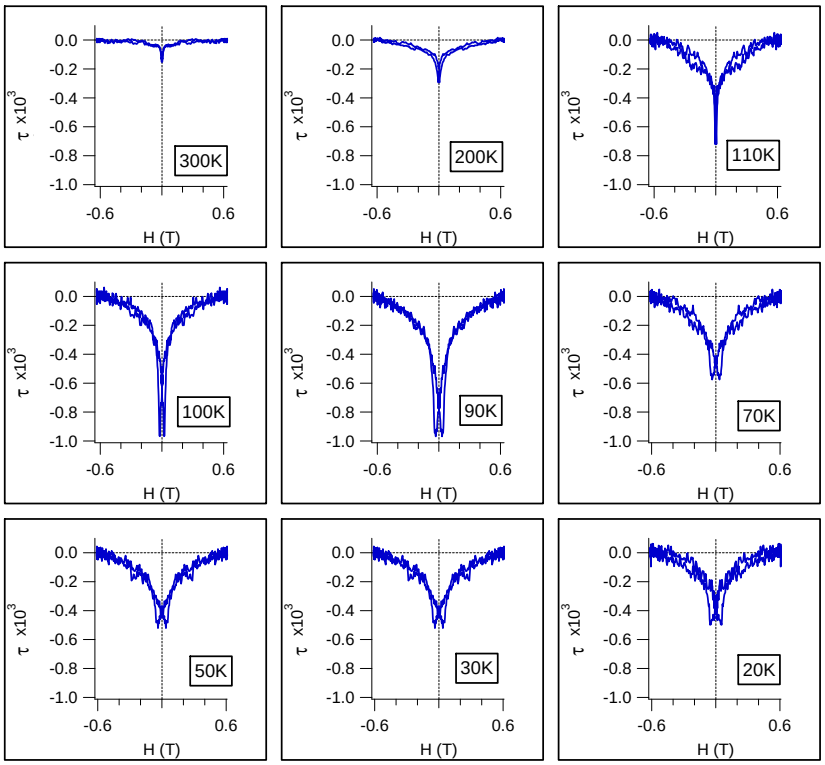

Figure 5.8: *Temperature dependence of* $\tau_{even} = \Im\left(\frac{\Delta r_{pp}}{r_{pp}}\right)_{even}$ *measured at* $\lambda = 450nm$.

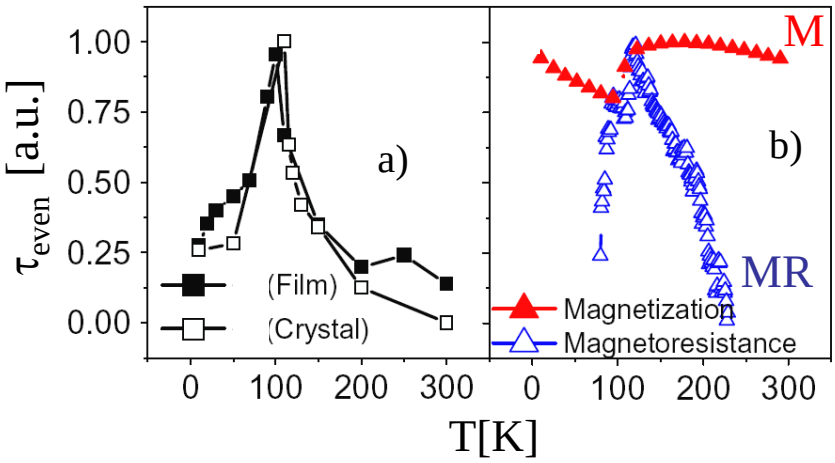

Figure 5.9: *a) Temperature dependences of the even contribution* $\tau_{even} = \Im\left(\frac{\Delta r_{pp}}{r_{pp}}\right)_{even}$ *measured in both the magnetite single crystal* ($\lambda = 600nm$) *and thin film* ($\lambda = 500nm$). *b)The normalized values of the temperature dependence of the magnetoresistance (blued open triangles) and the magnetization (red solid triangles) are also plotted. The field was applied in the plane for both cases, and the magnetization was measured at zero field after field cooling at* $H = 7kOe$.

normalized magnetoresistance measured in the thin film. The magnetoresistance is defined as $MR(H) = (R(H = 0) - R(H = 70kOe))/R(H = 0)$. We observe that, similarly to the amplitude of the even parity magnetooptical response, the $MR(H)$ curve is also peaked at the Verwey temperature (figure 5.9b)), in agreement with a strongest MR close to the transition reported previously by other authors Arora *et al.* [161], Ziese [169]). In contrast, the temperature dependence of the magnetization (figure 5.9b)) differs strongly from that of both $\Im\left(\frac{\Delta r_{pp}}{r_{pp}}\right)_{even}$ and MR. Both the magnetoresistance and the magnetization displayed in figure 5.9b) were measured in the thin film by applying the field along a [001]-direction in the film plane, and the magnetization was measured in zero field after cooling the sample under a field $H = 7kOe$.

The data shown in figure 5.9 further support the correlation between $\Im\left(\frac{\Delta r_{pp}}{r_{pp}}\right)_{even}$ and MRE. One notices that the temperature dependence of the even magnetooptical τ_{even} response, having a maximum at T_V as shown in figure 5.9a), mimics the temperature dependence of the diffuse neutron scattering intensity observed in magnetite crystals (Shapiro *et al.* [98]), which has been taken as a signature of the presence of uncorrelated polarons that survive well above the Verwey transition ([88, 170]). Our observation suggests that the MRE response observed in these magnetooptical experiments arises from magnetic-field dependent polaronic transport. Interestingly enough, the magneto-polaronic effects extend well above T_V, up to room temperature, similarly to the physics of the manganites discussed in the previous chapters.

Figure 5.10 shows the temperature dependence of the even $\Im\left(\frac{\Delta r_{pp}}{r_{pp}}\right)_{even}$ contribution measured at $\lambda = 500$nm. We observe that indeed, its largest value occurs at the Verwey temperature $T_V = 102$K (identified by the abrupt jump of the coercive field plotted in figure 5.10a). We also note that the amplitude of the even contribution is slowly decaying away from the transition temperature but strikingly its signature is still visible at temperatures as high as $T \approx 300K$, indicating that this unusual magnetooptic response survives even 200K above the Verwey transition. On the other hand, polarons in magnetite arise from a gradual enhancement of electron-phonon coupling when lowering temperature and approaching T_V [99]. Shapiro *et al.* [98] determined the temperature dependence of the diffuse neutron scattering intensity ξ in magnetite, from which it was inferred that polarons survive well above the Verwey transition (see references [98, 99]). In figure 5.10b we have plotted the $\xi(T)$ data reported in Fig. 4 by Shapiro *et al.* [98] together with the temperature dependence of the even contribution $\Im\left(\frac{\Delta r_{pp}}{r_{pp}}\right)_{even}$. It is clear from this figure that the even contribution follows the temperature dependence of $\xi(T)$, thus signaling that the former must reflect the field effect on polarons, i. e., it reveals the magnetic character of polarons in magnetite.

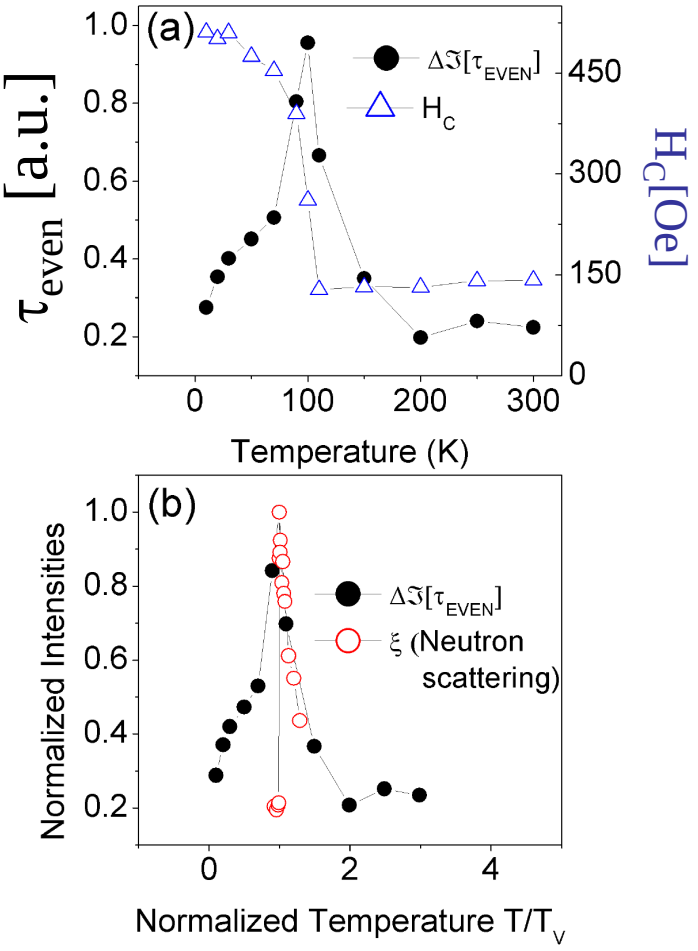

Figure 5.10: *(a) Temperature dependence of even contribution and coercive field. (b) Normalized intensities of diffuse neutron scattering and even contribution as a function of the temperature normalized to T_V. Taken from reference Shapiro* et al. *[98]*

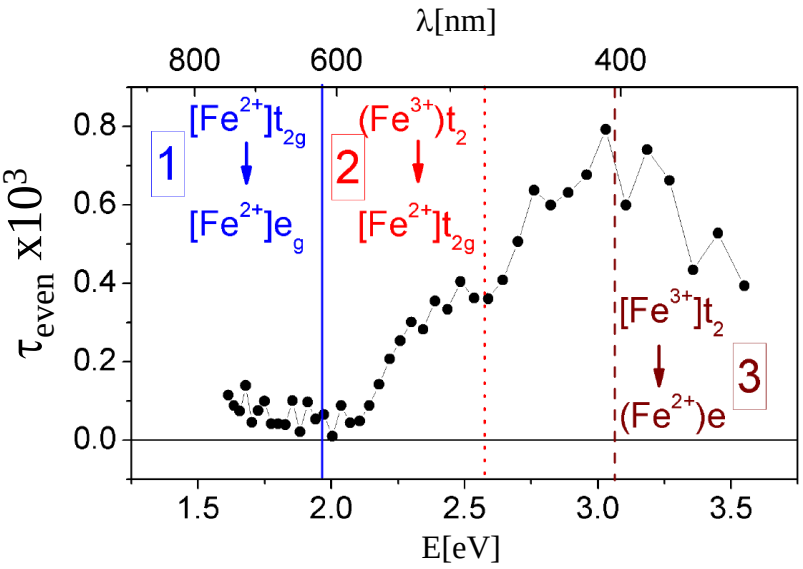

Figure 5.11: *Dependence of* $\tau_{even} = \Im\left(\frac{\Delta r_{pp}}{r_{pp}}\right)_{even}$ *on the photon energy. Intra-lattice* $B \rightarrow B$ *and inter-sublattice* $B \rightarrow A$ *optical transitions discussed by Fontijn* et al. *[102] are indicated with numbers*

5.1.2 Spectral response

In figure 5.11 we have plotted $\Im\left(\frac{\Delta r_{pp}}{r_{pp}}\right)_{even}(\lambda)$ as a function of the photon energy E of the incident light. Vertical lines in this Figure -labeled with numbers- indicate the photon energies corresponding to different optical transitions reported in magnetite. According to the spectral assignment discussed in the section 2.3.1 figure 2.12, the spectral feature centered at $E = 1.94eV$ is generally assigned to transitions between B (octahedral) sites $[Fe^{2+}]t_{2g} \rightarrow [Fe^{2+}]e_g$, while those centered at $E \approx 2.61eV$ and $E \approx 3.11eV$, correspond to the A (tetrahedral sites)-B intersublattice transitions $(Fe^{3+}t_2 \rightarrow [Fe^{2}+]t_{2g})$ and $[Fe^{3+}]t_2 \rightarrow (Fe^{2}+)e$, respectively [102]. The positions of these transitions are marked in the spectral magnetooptical data of the figure 5.11. Our data in figure 5.11 indicate that $B \rightarrow B$ transitions are not sensitive to the applied magnetic fields, whereas $A \rightarrow B$ transitions are strongly affected by fields. Thus, our experiments can discriminate the frequency selectivity of the effect of magnetic field on the optical transitions of magnetite.

We discuss now the frequency selectivity of these magnetopolarons shown in figure 5.11. We recall for convenience our key observations related to the energy dependence of $\Im\left(\frac{\Delta r_{pp}}{r_{pp}}\right)_{even}(M)$: (i) $A \rightarrow B$ optical transitions are affected by magnetic fields, whereas $B \rightarrow B$ transitions remain unaffected; and the maximal sensitivity to the magnetic field occurs at (ii) the coercive field and (iii) at the Verwey temperature. The different sensitivity to the magnetic fields of inter- $(A \rightarrow B)$ and intra- $(B \rightarrow B)$ sublattice optical transitions

can be understood in terms of local polaron-induced distortions. It is well accepted that polaron conductivity of magnetite is associated to carrier hoping in the B-sublattice [32, 97]. Thus, local lattice distortions, expected essentially only in B-sites, may be accompanied by a local modification of the magnetic anisotropy with respect to the host lattice. The latter should change the optical transition rates due to the modified spin configuration of the distorted site. In this picture, the observed frequency selectivity of the optical response should arise as a field-induced suppression of the polaron-induced cooperative B-site distortions. This accounts for the field insensitivity of $B \rightarrow B$ transitions and naturally provides a direct explanation of the field sensitivity of $A \rightarrow B$ transitions and of the observed temperature dependence of the even-component of magnetooptical response.

To conclude, our work has demonstrated that the magnetooptical response of magnetite is dominated by the magnetic character of polarons which is manifested in a strikingly broad range of temperatures, at least up to room temperature. Beyond this result, we have evidence that the optical response of polarons to magnetic fields is strongly enhanced for particular optical transitions, i. e., those which involve inter-sublattice electron transfers. This frequency-selective phenomenon provides important clues to understand the physics of the metal-insulator transition in magnetite.

CHAPTER 6

Magnetooptical spectroscopy of colloidal dispersions

6.1 Introduction

To analyze properly the photonic effects on the magnetooptical response, we need a reference material in which the magnetic material (nanoparticles in our case) is randomly distributed in space, in contrast to their periodically ordered arrangement when embedded in photonic crystals. One convenient approach to achieve random distributions of the magnetic material is to disperse the magnetic nanoparticles in solvents forming colloidal dispersions. At the same time, as described in chapter 7, magnetic liquid dispersions are used to infiltrate the photonic crystals with the magnetic nanoparticles. For these reasons, we have investigated the magnetooptical properties of these magnetic liquids and have developed a fast magnetooptical characterization method for colloidal liquid dispersions of magnetic nanoparticles [171]. Because the size of the particles is in the colloidal range -in our case typically in the order of 10 nm- these systems are often referred to as magnetic colloids or magnetic colloidal dispersions [172]. Although magnetic colloids are ferromagnetic on the molecular scale, they resemble a paramagnet on the colloidal scale, with the major difference that the magnetic moments of magnetic colloids are much larger than the moments in a paramagnet (typical values are $10^{-19} Am^2$ for magnetic colloids and $10^{-23} Am^2$ for paramagnets)[172]. We present here a flexible and versatile methodology to characterize the magnetic properties of magnetic liquid dispersions that, eventually, should be also suitable to study fundamental problems related to properties of nanosized particles -i.e., surface effects-.

6.2 Applications of magnetic fluids

An important property of concentrated ferrofluids is that they are strongly attracted by permanent magnets, while their liquid character is preserved. The attraction can be strong enough to overcome the force of gravity. Many applications of ferrofluids are based on this property. Other applications are being developed also in information technology, biotechnology and energy/environmental related technologies[171, 173, 174]. For the specific case of magnetic colloids two different applications are highlighted here, the biomedical applications (contrast agents MRI, magnetic hyperthermia therapies, and guided drug delivery [174] and the fabrication of novel magnetophotonic colloidal crystals [175–177].

For both applications, high quality materials are needed either to have a better understanding of the size-dependent properties of the magnetic nanoparticles or to allow the control of the collective behavior of the nanoparticle assembly. Consequently, synthetic methods producing nanoparticles uniform in composition, size, shape, internal structure, and surface chemistry are needed to reduce the complexity of the system. Over the last 10 years, enormous advances have been made toward improving nanoparticle fabrication. High quality nanoparticles, in terms of the requirements mentioned above, can be synthesized by high temperature thermal decomposition of organometallic compounds resulting in colloidal dispersions of the nanoparticles in organic media [171, 173, 174]. A drawback of this method is the low amount of material produced in each batch, typically on the order of $100mg$. On the other hand, nanoparticles are commonly dispersed in liquids in a wide range of applications, and appropriate tools to characterize them in such environments are rather scarce. Moreover, because of the growing interest of magnetic colloids for biomedical applications, there is a need of techniques to measure diluted concentrations of magnetic nanoparticles and to correlate the magnetic response of these liquids with particle aggregation or surface particle functionalization. The work presented here is a contribution toward these purposes. Thus, the possibility of using a fast magnetic characterization technique able to probe small quantities of material dispersed in liquid carriers is of enormous interest. Beyond these applications, surface modifications have found widespread applications in medicine. Therefore the development of a suitable technique to sensitively monitor changes in the electronic configuration and eventually the magnetic response of nanomaterials is crucial [171]. Facing these challenges, we report here on a convenient methodology based on a magnetooptical set-up that allows a quick characterization of magnetic particles stabilized in liquid media. Nickel colloidal dispersions were prepared at ICMAB, in collaboration with Dr. Anna Roig [171]. For that purpose,

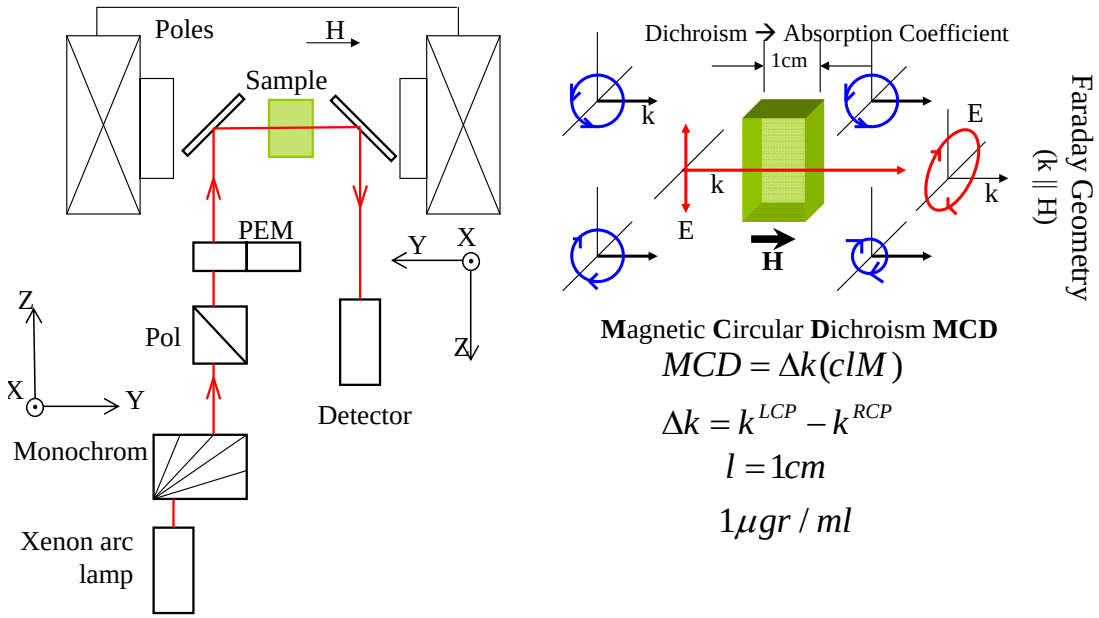

Figure 6.1: *Set up to measure the MCD in magnetic colloidal dispersions.*

nickel nanoparticles were synthesized by high-temperature solution-phase method adapting the procedures reported by Chen *et al.* [178] and Murray *et al.* [179]. The details on the preparation of these nanoparticles are out of the scope of this Thesis, and they can be found in Ph-D Oana Pascu [180] and reference [171].

6.3 Magnetooptical characterization of colloidal dispersions of nickel nanoparticles

We have characterized the magnetooptical properties of the magnetic colloidal dispersions by carrying out magnetic circular dichroism (MCD) spectroscopy, which measures the relative difference of optical absorption between right- and left-circularly polarized light (see section 1.2, figure 1.2 b). The experiment is based on the measurement of the difference in the absorption between left circularly polarized (LCP) light and right circularly polarized light, induced in the sample by a magnetic field oriented parallel to the direction of light propagation. The experimental set-up used for magnetic MCD is sketched in the figure 3.13.

The samples consisted of colloidal dispersions of volume $1.5mL$ with different concentrations of Ni nanoparticles in hexane. The nanoparticles were previously coated with an appropriate surfactant to avoid clustering [171]. The magnetooptical measurements were performed by placing the samples into a glass square cuvette for which the optical path

of the light was $l = 1cm$ and the thickness of the cuvette walls was $1mm$ (see figure 6.1). These experiments were carried out for the concentrations listed in the table 6.1:

NP's size	M	mg/mL Ni
$8nm$	1.7^{-4}	0.0083
$8nm$	1.7^{-3}	0.083
$8nm$	2.6^{-3}	0.1264
$8nm$	4.0^{-3}	0.1938
$8nm$	5.1^{-3}	0.25
$15nm$	1.7^{-4}	0.0092
$15nm$	1.7^{-3}	0.092
$15nm$	2.6^{-3}	0.1404
$15nm$	4.0^{-3}	0.2149
$15nm$	5.1^{-3}	0.28

Table 6.1: *Concentrations of the nickel colloidal dispersions. Column labeled 'M' give the molar concentrations.*

Notice that all of the molar concentrations are reported in the basis of moles of Ni atoms and that for concentrations given in $mg/mLNi$ the amount of surfactant has been corrected [171]. These concentrations represent volume fractions of nanoparticles in the range of $0.9 - 30ppm$. The amount of magnetic material used for the analysis was of $0.012mg$ for the most diluted sample and of $0.12mg$ for the most concentrated one. The background magnetooptical spectroscopic signal was subtracted from the raw experimental data by recording the spectra of glass cuvette filled with bare hexane solvent. The subtraction was made assuming that the background and the nanoparticle magnetooptical signals are additive [1].

In a first set of experiments, we established that the range of concentrations for which our magnetooptical set-up was able to probe the properties of the Ni nanoparticle dispersions was within a $10^{-5} - 10^{-2}M$ concentration range [2]. We verified that the concentrations below $10^{-5}M$ were too diluted and the magnetooptical signal too weak to be properly analyzed, even though still sufficient to be measured, whereas for concentrations above $10^{-2}M$ the magnetic field ($|H| \leq 6kOe$) promoted the aggregation of nanoparticles in

[1] We are currently exploring experimentally and theoretically the effects of the optical interactions of magnetic nanoparticles and the solvent on the magnetooptical response, O. Vlasin et al., in preparation

[2] The sensitivity to the concentration is determined by the optical path l. We give the sensitivity for $l \approx 1$ mm.

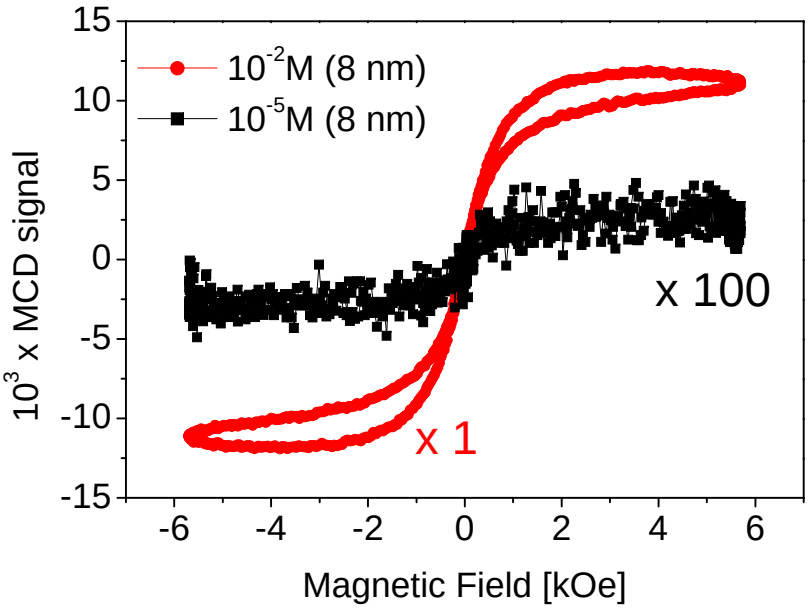

Figure 6.2: *MCD loops of colloidal dispersions of Ni nanoparticles of diameter 8nm for the two extreme concentrations,* $10^{-5}M$ *and* $10^{-2}M$*. The data corresponding to* $10^{-5}M$ *are magnified by a factor 100.*

clusters thereby distorting the magnetic hysteresis loops and precluding the analysis of the intrinsic nanoparticle properties. The figure 6.2 shows the recorded magnetooptical loops for the two extreme concentrations, $10^{-5}M$ and $10^{-2}M$. In particular we appreciate in this figure that the loop measured at a concentration $10^{-2}M$ shows an anomalous shape (the upper and lower branches of the loops do not coincide) that departs significantly from the super-paramagnetic behavior observed for more diluted dispersions; these effects are due to field-dependence nanoparticle aggregation and precipitation for those higher concentrations.

Once determined the concentration window within which we can detect the intrinsic magnetooptical properties of colloidal suspensions, we have carried out measurements for five different concentrations as listed in the table 6.1. We have measured the spectral dependence of the magnetooptical hysteresis loops (figure 6.3). As discussed above, the linear contribution coming from the glass cuvette filled with bare hexane solvent was removed to estimate the amplitude of the hysteresis loops. As expected, the magnitude of the loops is a strong function of the probe light wavelength, and this spectral dependence is discussed below. It is immediately evident from these measurements that the data can provide information on some magnetic characteristics of the system, such as the remnant magnetization and coercive and anisotropy fields. In particular, we observe that for the

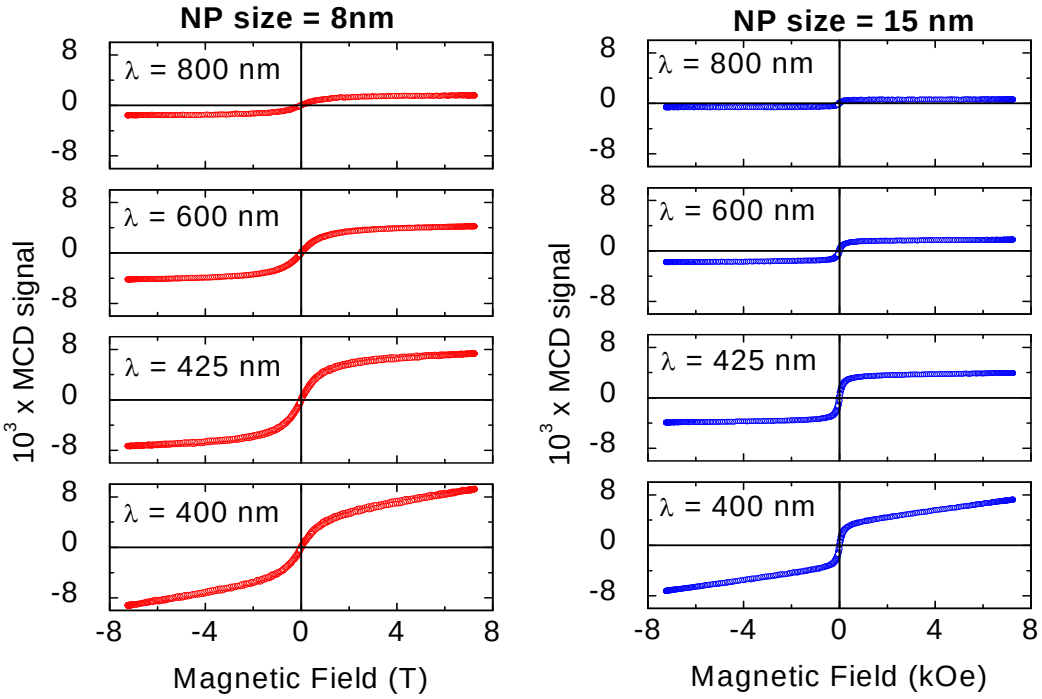

Figure 6.3: *MCD hysteresis loops recorded at selected wavelengths and at the same concentration* $(1.7x10^{-3}M)$ *for* $8nm$ *and* $15nm$ *Ni nanoparticles colloidal dispersions.*

investigated nanoparticle sizes the remnant magnetization is less than about 1% of the saturated value and that the coercive field is virtually null, indicating that the colloidal dispersions exhibit a super-paramagnetic behavior even with the short time scale of the measurement.

We carried out magnetic characterization of the dispersed nickel nanoparticles by quantum interference device (SQUID) magnetometry. The sample was prepared using a plastic capsule filled with compacted cotton which was impregnated with $500\mu L - Ni$ solution of $10mg/mL - 8nm - Ni$ nanoparticles giving $4.1mg$ of Ni (30 times more solid material than the amount used for the characterization in the most concentrated sample). The Magnetization data is presented in units of emu/gNi (after subtraction of the mass of surfactant around the nanoparticles). Figure 6.4 shows magnetooptical and SQUID measurements, demonstrating the consistency of both techniques. The size effects can be evidenced by the different anisotropy fields observed for the two systems. We observe that the field necessary to saturate the magnetization of the set with nanoparticles with size $15nm$ is around $1.5kOe$, whereas the anisotropy field of the set of nanoparticles ($8nm$) is much higher, of the order of $5kOe$. We see, as expected, that both the magnetooptical and the SQUID hysteresis loops confirm that the set of smaller nanoparticles dispersions

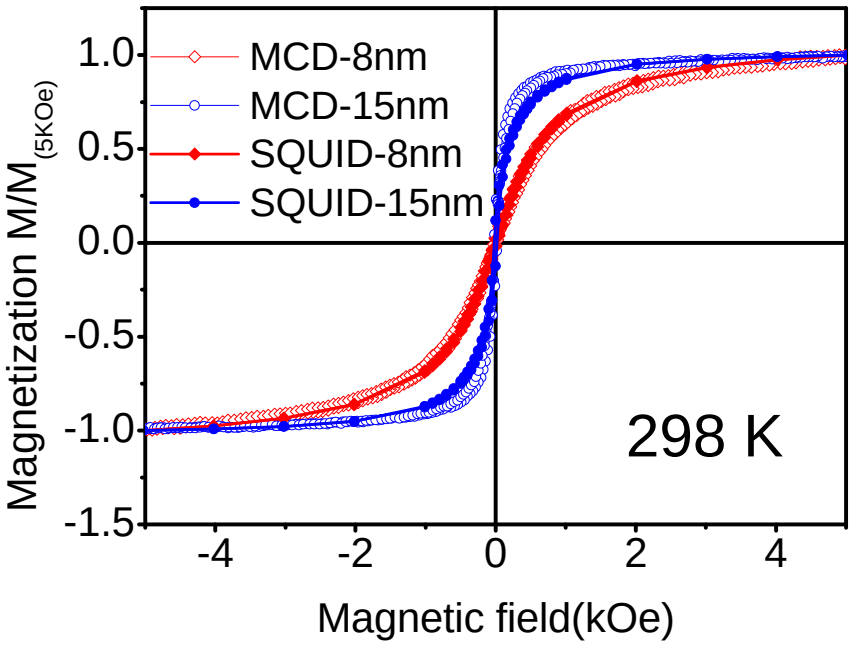

Figure 6.4: *Comparison of the normalized loops obtained by the two techniques, SQUID and MCD. Hysteresis loops were taken at* $298K$ *for* $8nm$ *and* $15nm$ *Ni nanoparticles, respectively*

are magnetically much harder than the bigger nanoparticles.

Additionally, from SQUID measurements (See figure 6.5), we observe that the magnetization value is strongly dependent on the size of the nanoparticles, being $18emu/g$Ni for the nanoparticles with diameter $8nm$ and $42emu/g$ for the $15nm$ nanoparticles (closer to the Ni bulk value $M_s = 56.7emu/g$).

We discuss now the wavelength dependence of the saturated magnetooptical signal measured for different light wavelengths within the range $400nm \leq \lambda \leq 800nm$. In figure 6.6 we have plotted these spectra for the concentrations listed in the table 6.1. As described above, we have subtracted from the raw measured signal the background magnetooptical signal, arising from the contributions of the glass container and hexane solvent. The spectral dependence of the MCD signal is displayed in figure 6.6. We observe in this figure that for all concentrations and nanoparticle sizes the spectral shape is very similar and exhibits a maximum at wavelengths $\lambda \approx 450nm$ and photon energies $E \approx 2.75eV$. From the experimental spectral response displayed in figure 6.6 we can select an optimal spectral region for which we observe the highest sensitivity to MCD. This is relevant if we want to use the recorded MCD signal as a means to determine the concentration of a given colloidal dispersion of Ni nanoparticles. Note that the MCD is proportional to the net magnetization and, therefore, any eventual non-magnetic or anti-ferromagnetic shell

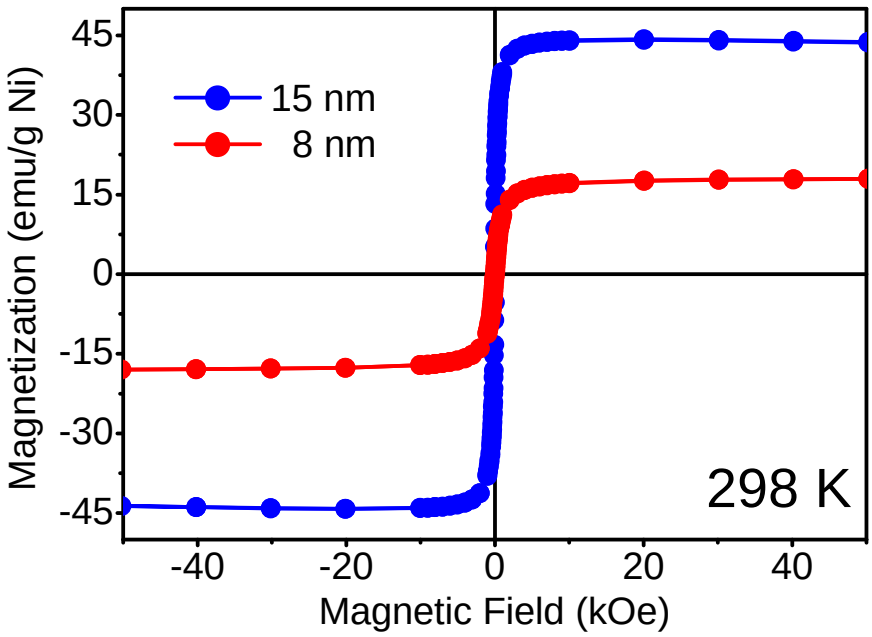

Figure 6.5: *Magnetic hysteresis loops measured by SQUID for the two sets of Ni nanoparticles.*

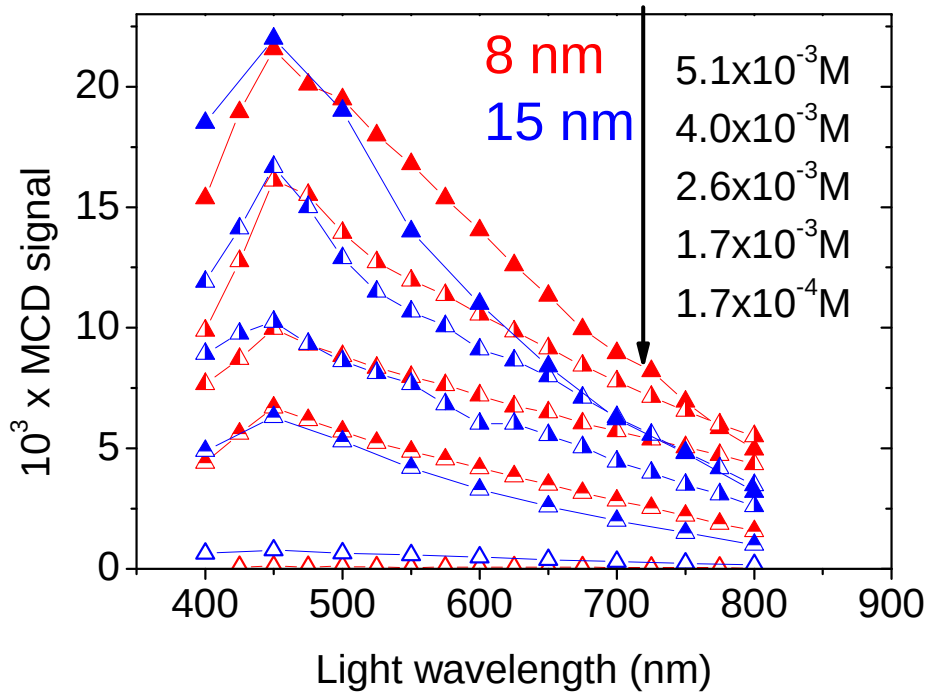

Figure 6.6: *MCD spectral response for different concentrations of Ni magnetic nanoparticles with diameters 8nm and 15 nm.*

forming on the nanoparticle signal does not contribute to the magnetooptical signal.

To illustrate the potentiality of this methodology, we have plotted in figure 6.7 for each set of colloidal dispersions (nanoparticles with sizes 8 and 15 nm) the values of the MCD signal measured at $\lambda \approx 450nm$ at the five different concentrations shown in figure 6.6. Figure 6.7 shows that a linear relationship can be established between the recorded MCD and the concentration of Ni nanoparticles. The same linear relationship is observed for any other wavelength, the only effect being a change of the slope (see figure 6.7b). The error bar in figure 6.7a is around 5% of the average MCD value for the more diluted concentrations while it goes to around 1% for the more concentrated dispersions. These experiments confirm that the methodology presented here is a powerful and straightforward means to determine with large accuracy the concentration of Ni nanoparticles dispersed in liquid media. We emphasize that for our specific experimental conditions, given the sensitivity of the MCD set-up to detect signals $a.c./d.c$ below 10^{-3} (see figure 6.2), our method can detect concentrations as small as $1\mu g/mL$. Finally, we note that the MCD signals depend slightly on the nanoparticles size. Indeed, from the figure 6.6 we observe that the MCD at wavelengths $\lambda \geq 450nm$ is somewhat higher for the $8nm$ nanoparticles than for the $15nm$ set. This trend is just the opposite of the measured magnetization by SQUID (see figure 6.5), thus reflecting that MCD contains richer information than the magnetization, since the optical characterization is intimately coupled to the electronic structure of the systems that could depend on the nanoparticle size. This observation is also at the root of the distinct slope of the sensitivity curves shown in figure 6.6. The detailed understanding of these effects is beyond of the scope of this Thesis but it clearly shows that the magnetooptical technique here described is extremely sensitive to size effects and thus it may be well suited to explore the effect of a specific surface functionalization on the properties of magnetic nanoparticles or to in-situ monitor chemical reactions.

6.4 Conclusions

In summary, we have presented a fast and versatile methodology to characterize the magnetic properties of magnetic nanoparticles in colloidal dispersions exploiting magnetooptical spectroscopy. Using this method, intrinsic properties such as the magnetic anisotropy as well as coercive fields can be obtained straightforwardly. In addition, we show that proper calibration of the magnetooptical signal and careful selection of the wavelength of the probe light can yield a high sensitivity to highly diluted concentrations of magnetic nanoparticles colloidal dispersions allowing the accurate determination of the nanoparticle concentration. The flexibility of the method presented here makes it suitable for the in-situ

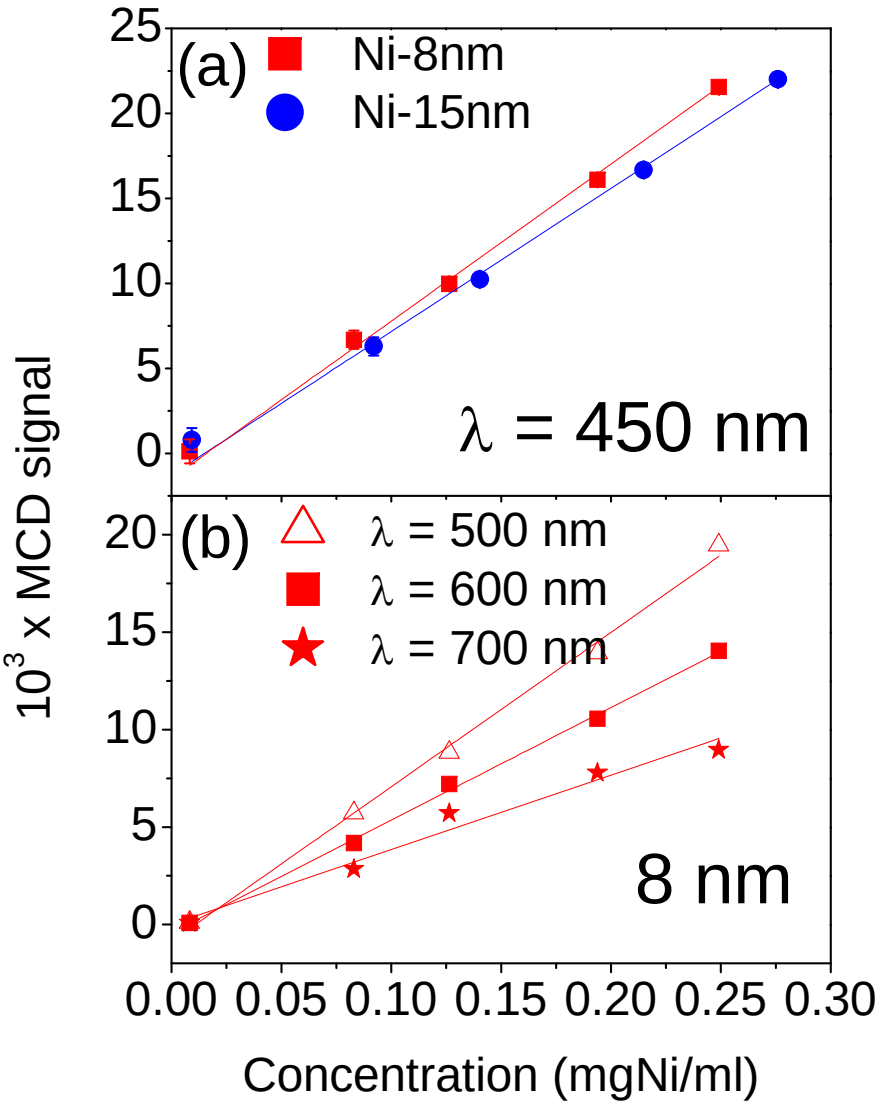

Figure 6.7: *(a) Linear dependence of the magnetooptical response as a function of the Ni concentration measured at $\lambda = 450nm$ for both the $8nm$ and $15nm$ subsets. (b) Linear dependence of the magnetooptical response as a function of the Ni concentration measured at different wavelengths for the $8nm$ subset*

test of colloidal dispersions that are used in such state in specific applications and also its integration in mass-scale analysis in production lines. The capabilities of the experimental approach presented here can be largely expanded if the strong sensitivity of magnetooptical signals to the surface magnetic properties is properly exploited. For instance, real-time MCD monitoring could be used to track in-situ chemical reactions that modify the surface state of the nanoparticles and the physical properties of the nanoparticles, as is the case of thiol-functionalized Au nanoparticles [181].

CHAPTER 7

Magneto-photonic crystals

7.1 Motivation

The large enhancement of the intrinsic magnetooptical properties is crucial to integrate magnetooptic thin film materials into optical device applications. A way towards such objectives is nanostructuring the matter, in such a way as to exploit geometrical resonances rather than electronic ones to increase significantly the intensity of the magnetooptical effects [182–185]. An illustrative example are the photonic crystals, which are a special kind of nanostructured materials in which the permittivity is periodically modulated on the scale of the optical wavelength, giving rise to a deep modification of the spectral optical response [186–195].

The addition of a magnetic component into these structures, the so-called magnetophotonic crystals (MPCs), has two further interesting effects. On one hand, it breaks time inversion symmetry, allowing nonreciprocal effects in light propagation [194, 196]. On the other hand, light is slowed at frequencies of the photonic band edges, strongly increasing the light-matter interaction and enhancing the magnetooptical response [9, 82, 197]. Several approaches have been carred out in one- (1D) and two-dimensional (2D) MPCs, where it has been demonstrated that the magnetooptical response is enhanced. Nevertheless, the achievement of high-quality 3D-MPCs is much more complex due to the difficulty of maintaining high quality long-range structural order and, therefore, the attainment of an optimal (magneto-) optical response, comparable at least to that of 1D-MPCs, remains a challenging issue. Thus, 3D magnetophotonic crystals (3D-MPCs) are being postulated as appropriate platforms to tailor the magnetooptical spectral response of magnetic materials and to incorporate this functionality in a new generation of optical devices. Our approach to 3D-MPCs has been based on the use of direct and inverse

dielectric opals infiltrated with magnetic nanoparticles. For that purpose, especial mention is made to the collaboration with Dr. Anna Roig from the ICMAB and her PhD student Oana Pascu who were responsible of optimizing and preparing the 3D-MPCs samples which are analyzed here. A deep description of the materials preparation is given in the Thesis of Oana Pascu, and in the references included below in this Thesis.

7.2 Magnetophotonic crystals: state-of-the-art

Early reports about magnetophotonic crystals appeared around 1998, concerning the study of 1D-MPCs carried out by Inoue *et al.* [182]. They found that the magnetooptical properties of 1D-MPC structures are almost governed by the degree of localization of light, which can be controlled by varying the number of reflection layers in the films. A year later, Inoue *et al.* [183] showed the first experimental evidence of magnetooptical enhancement in 1D-MPCs, who also found that it is always accompanied by a large reduction of the reflectivity. Levy *et al.* [184] and Kato *et al.* [198] predicted huge Faraday rotations $\approx 45^\circ$ and transmittance $\approx 95\%$ in 1D-MPCs, suitable for applications in optical insulators. In 2003 a comprehensive review of magnetic photonic crystals was presented by Lyubchanskii *et al.* [199], where they predicted the MPC materials as a new class of devices for photonics applications, and a new direction in photonics called magnetophotonics. In 2004 Lyubchanskii *et al.* [200] calculated the transverse magneto optical response of 1D magnetic photonic crystals and compared it with polar and longitudinal signals, and Fedyanin *et al.* [197] reported experimentally enhancements by factors up to $\approx 10^2$ in both Faraday rotation angle and intensity of second harmonic generation signals. Recent reports in 2008 by Takahashi *et al.* [201] have shown huge Kerr rotation ($\approx -2.2^\circ$) in 1D-MPCs. Crystals of higher dimensionality have also been investigated. For instance, Zvezdin and Belotelov [185] reported the first calculation dealing with magnetooptical properties of two dimensional photonic crystals. Similar theoretical works and calculations in 2D MPCs were presented by Merzlikin *et al.* [202]. The general magnetooptical properties of 1D-, 2D- and 3D-MPCs were studied by Belotelov and Zvezdin [203] and Belotelov *et al.* [204] and Inoue *et al.* [205] discussed the new functionalities associated to these MPCs, such as band Faraday effect, magnetic super-prism effect and non-reciprocal or magnetically controllable photonic band structure. Interestingly, recent works have also pointed to the possibility of coupling photonic effects to other optical phenomena. In this line, Granovsky *et al.* [7] analyzed the integration of magnetooptical effects, magnetophotonic crystal and the magnetorefractive effect, and Boriskina *et al.* [9] explored theoretically the possibility of exploiting magnetophotonic crystals to enhance the magnetorefractive effect.

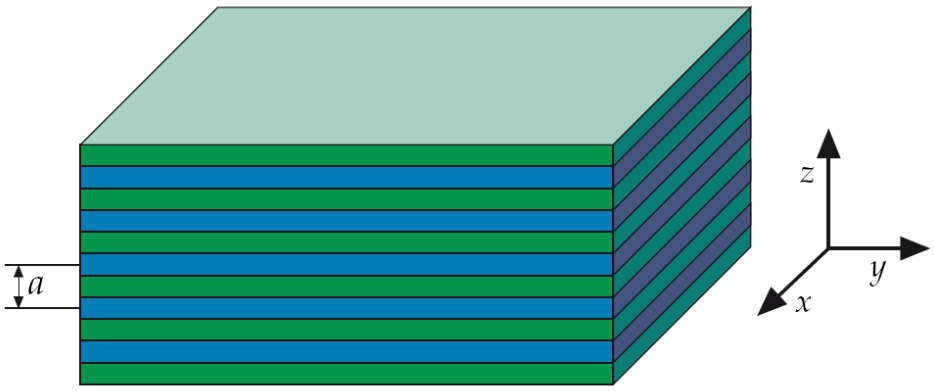

Figure 7.1: *One-dimensional photonic crystal. Taken from [192]*

The promising results reported for 1D- and 2D-MPCs [185, 205] have spurred the research on 3D photonic crystals, in which the periodicity in the three dimensions should allow a better integration in devices with an enhanced functionality [188, 205–207]. Nevertheless, efforts aimed at the achievement of 3D-MPCs are challenged by the difficulty of having the required high-quality long-range structure along the three directions in space and high magnetic content [208–213]. The major challenge in 3D-MPCs is the achievement of high magnetic content in crystals with large structural order in the three dimensions.

7.3 Basic properties of photonic crystals

Let us consider a multilayer film, with spatial period a (see figure 7.1). The system is periodic in z and homogeneous in the xy plane. The modes in this structure are given by [192]:

$$H_{n,k_z,k_\parallel}(r) = e^{ik_\parallel \cdot \rho} e^{ik_z z} u_{n,k_z,k_\parallel}(z) \tag{7.1}$$

where, $k_\parallel$, k_z, and n are the wave vector in the plane, the wave vector in the z direction, and the band number respectively. The function $u(z) = u(z + R)$ is periodic and R is an integer multiple of the spacial period a. The modes can propagate in the plane xy because $k_\parallel$ can assume any value, but k_z is restricted within a finite interval, the one dimensional Brillouin zone. Let us consider a primitive lattice vector in real space $a\hat{z}$, then the primitive reciprocal lattice vector is $(2\pi/a)\hat{z}$ and the Brillouin zone is $-\pi/a < k_z < \pi/a$.

Now, let us consider waves that propagate entirely in the z direction, i.e. $k_\parallel = 0$. In the figure 7.2, we plot $\omega_n(k)$ for different permittivity contrast between layers [192]. Figure 7.2a shows a system in which all of the layers have the same dielectric constant, whereas

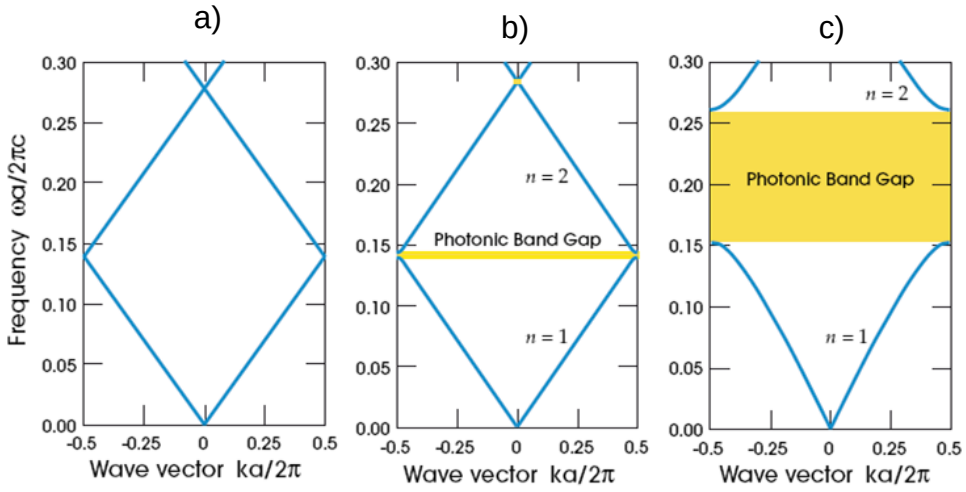

Figure 7.2: *The photonic band structure for different contrast between layers. Taken from [192]*

the figure 7.2b is a structure with alternative dielectric constant of 12 and 13, and finally in the figure 7.2c is plotted a structure with much higher dielectric contrast of 13 to 1.

In the homogeneous case *a*) the speed of the light is reduced by the refractive index, and the modes are given by:

$$\omega(k) = \frac{ck}{\sqrt{\epsilon}} \tag{7.2}$$

Because k repeats itself outside the Brillouin zone, the light line folds back into the zone when it reaches an edge. It can be understood relabeling in the solutions $k + 2\pi/a$ by k. There is a gap in frequency between the upper and lower branches of the lines and, thus, there is no allowed mode inside the crystal that has a frequency within this gap, regardless the value of k. Figure 7.2c shows that the gap width is strongly dependent on the permittivity contrast between the layers of the photonic crystal. This gap is known as **Photonic Band Gap (PBG)**. The PBG usually is characterized by the quality factor or **gap-midgap ratio**, defined by:

$$gap - midgap\, ratio = \frac{\Delta\omega}{\omega_m} \tag{7.3}$$

where, $\Delta\omega$ is the width of the PBG, and ω_m is the frequency at the middle of the gap and it is usually expressed in percentage.

The main mechanism underlying the optical and magnetooptical properties of magnetophotonic crystals is the strong photon confinement with wavelengths in the vicinity of the PBG that leads to an enhancement of the effective optical path, which results in a large enhancement of the linear and nonlinear magnetooptical responses of the media[9, 197, 201].

7.4 Materials preparation

The samples studied in this section were provided by the Photonic Crystal Group under advise of Prof. Ceferino Lopez at the Instituto de Ciencia de Materiales de Madrid (ICMM). This collaboration was done under the context of Proyecto Intramural de Fronteras (PIF-CSIC)-"Hacia una nueva generación de de cristales fotónicos sintonizables".

The approach to prepare 3D-MPCs is based on the fabrication of artificial direct and inverse opals. Direct opals are built up by dielectric (SiO_2) spheres that self-assemble in an ordered fcc crystalline arrangement (see figure 7.3), leaving holes between the spheres which may be filled with magnetic material to form the magnetophotonic crystals. The inverse opals were synthesized by first building up direct opals of polystyrene (PS) spheres; subsequently the host material (Al_2O_3, SiO_2) was infiltrated between the PS spheres by chemical vapor deposition (CVD) or atomic layer deposition (ALD) and finally the original PS spheres were removed by dissolution with toluene leaving behind spherical voids in the structure [195]. At the end of the process, both direct and inverse opals were infiltrated with the magnetic nanoparticles by immersion in an aqueous dispersion to form the magneto-photonic crystals. After the immersion, the opals were pulled out of the solution using a vertical stepping motor to precisely control the speed. This step can be repeated several times to increase the magnetic loading. For details and parameters preparation see Oana Pascu Ph-D thesis [180],[214]

7.5 Optical and magnetooptical characterization

7.5.1 Optical characterization

A realistic representation of an opal structure on a glass substrate is depicted in figure 7.4. During the synthesis of a magnetophotonic crystals many defects may be created, such as vacancies, dislocations, cracks as well as thickness fluctuations due to presence of terraces. All these features can have a critical influence in both optical and magnetooptical crystal properties.

For the optical/magnetooptical characterization, one of the most relevant aspects is related to the dimensions of the system. As depicted in figure 7.4, the beam light propagates along the normal to the structure and the magnetic field -for magnetooptical characterization- was generally applied also along the normal. A typical opal structure has a thickness around $\approx 1 - 10\mu m$, while the thickness of the glass substrate is usually

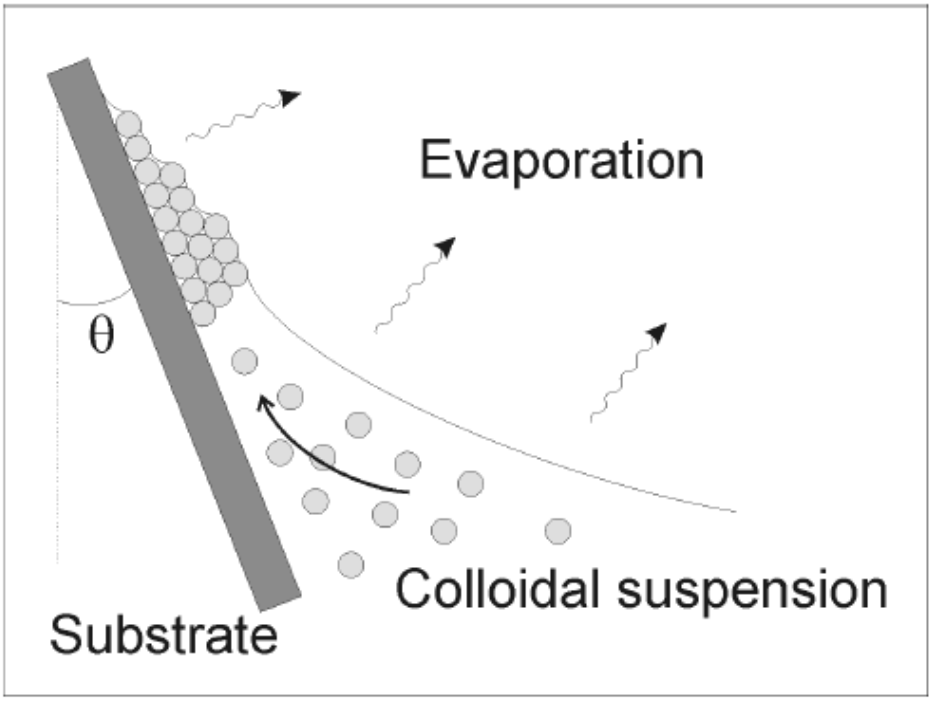

Figure 7.3: *Schematic of the vertical deposition method. A substrate (dark grey) is placed in a colloidal suspension which wets it. The substrate is inclined at an angle θ. Ordering of the spheres takes place at the meniscus. Taken from [215]*

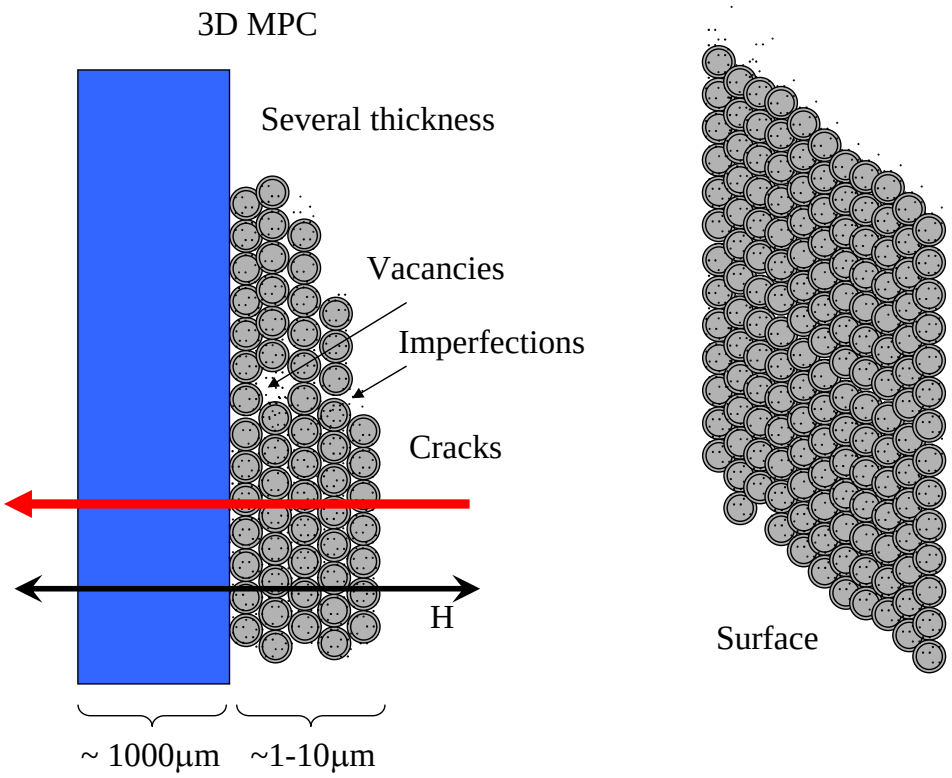

Figure 7.4: *Sketch of a magnetophotonic crystal*

2 orders magnitude larger. Because of the surface roughness, reflection experiments are often difficult due to largely scattered light and, therefore, transmission experiments were also carried out for the magnetooptical characterization. This implied that the optical response from the glass substrate may have a very large influence on the as-measured optical spectra. Another aspect to mention is the spot size of the light beam. Large spot sizes are prone to probe more defects on the opal surface, whereas smaller spot sizes have larger possibilities to probe zones of the opal with less defects. For that purpose we made a special effort to reduce as much as possible the spot size in our set-up, achieving sizes around $400\mu m$.

Finally, the defects are basically any interruption of an otherwise perfectly periodic structure. The effect of disorder in a photonic crystal is to introduce localized states and generate incoherent scattering. Since the optical properties of a photonic crystal rely on the existence of energy bands, which arises as a consequence of coherent scattering of light, the presence of disorder will certainly affect its optical performance. If disorder takes place in a random manner (unwanted defects) the optical properties of a photonic crystal may be completely spoiled. Forbidden intervals are filled with localized states which, for a given amount of disorder may even close an existing PBG turning the density of electromagnetic modes inside to a non-zero value [215].

The relevance of defects on the optical properties is discussed in what follows from our experiments. The identification of the photonic band gap was carried out by both reflectance and transmittance measurements. In the presence of disorder light propagating through the crystal is scattered by the different imperfections of the lattice and the incident beam is attenuated, originating a diffuse cone around it. This affects reflectance and transmittance spectra in different manners. Reflectivity peaks become less intense, rounded in shape and asymmetric [216–218]. On the other hand, the transmission increases for those wavelengths contained in the photonic band gap, while decreasing for those wavelengths outside of the PBG [219–221].

Figure 7.5 shows both reflectance and transmittance spectra performed on a photonic crystal consisting of a direct polystyrene opal with $320nm$ diameter spheres. These spectra present high (low) reflectance (transmittance) for frequencies contained within the photonic band gap. Although the photonic band gap around to $\approx 740nm$ is observed in both measurements, there are differences between the two spectra. The reflectance measurement shown in figure 7.5 was performed using a micro-spot ($\approx 50\mu m$) based system in the laboratory of Dr. A. Blanco (ICMM-CSIC), so that the optical properties were probed at a very local level and the influence of defects and imperfections of the opal was reduced. Note that the oscillations observed in the reflection spectrum in figure 7.5

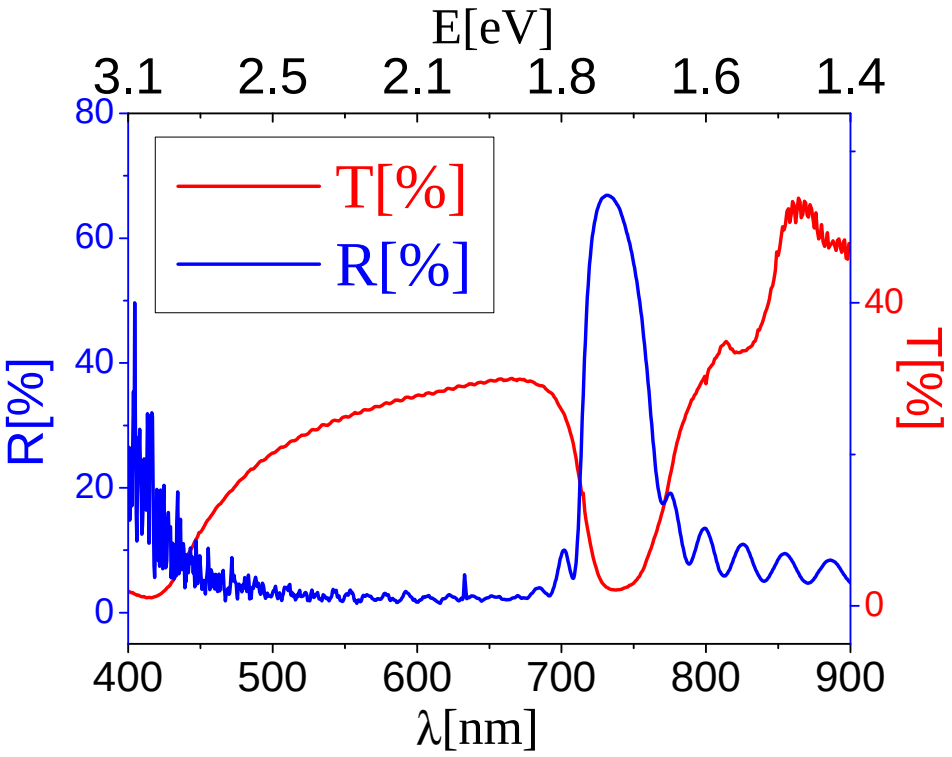

Figure 7.5: *Reflectance (red line) and transmittance (black line) spectra of a direct opal (polystyrene spheres) with diameter* $320nm$.

Label	Type	Material	d
$PS-D-260nm$	Direct	Polystilene	260nm
$Al_2O_3-I-260nm$	Inverse	Alumina	260nm
$SiO_2-D-325nm$	Direct	Silica	325nm

Table 7.1: *List of opals analyzed in figures 7.7, 7.8, and 7.9*

are due to Fabry-Perot resonances originated by interference of light reflected at both interfaces of the sample [222]. On the other hand, the transmittance spectra in figure 7.5 was measured in our laboratory at ICMAB using a home-made spectrometer with larger spot size ($\approx 400\mu m$). A larger influence of defects and imperfections due to the increased spot size is visible mainly as a slight reduction of the transmission dip as well as a broadening of the photonic bandgap.

Since the distribution of defects and thickness fluctuations in the opal is inhomogeneous, the optical properties may strongly dependent on the location of the beam spot on the surface. As an illustration, reflectance measurements in different zones of the sample are shown in figure 7.6. Also in transmission experiments, which were used in the

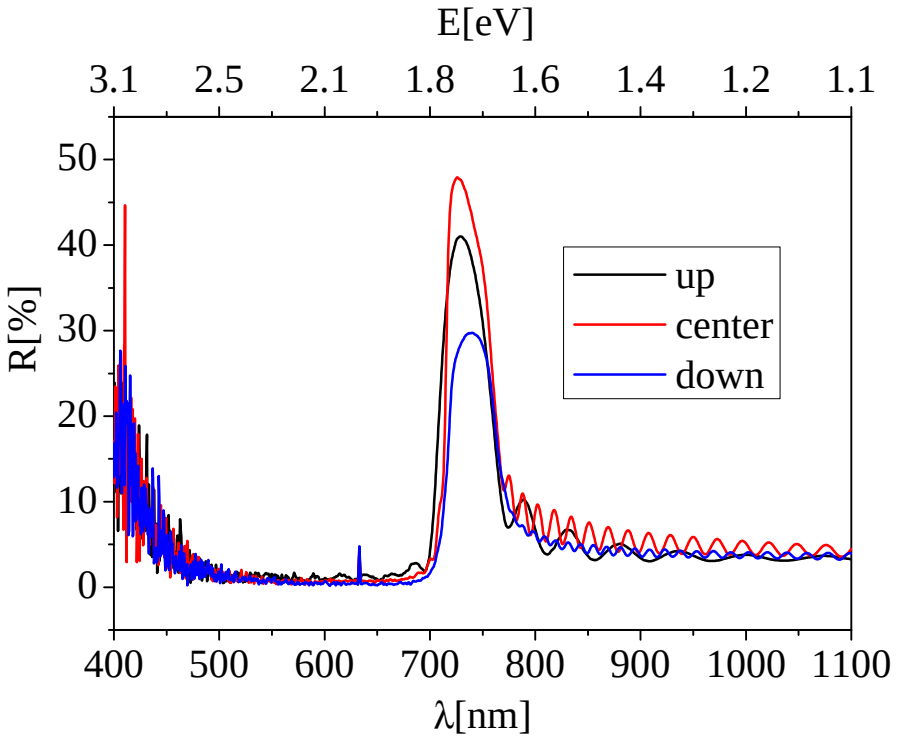

Figure 7.6: *Reflectance spectra recorded at different zones of a direct opal (polystyrene spheres) with diameter 320nm.*

magnetooptical characterization, exhibit this kind of effects. To discuss this issue, we have collected transmittance spectra on different zones for three different samples listed in table 7.1.

The transmittance spectra for the samples listed in the table 7.1 are shown in figures 7.7, 7.8, and 7.9, respectively. From these figures it is clear that the optical and magnetooptical properties are strongly dependent on the beam position (zones labelled as Z_i). We can conclude, then, that if we want to correlate the optical properties of opals (photonic band gap) with the magnetooptical properties (magnetooptical enhancement) both kind of measurements (optical and magnetooptical) must be performed at the very same location, to avoid the effects associated with any eventual spatial inhomogeneities in the photonic crystals.

7.5.2 Magnetooptical characterization

The measurement of Kerr rotation and ellipticity is hampered seriously due to the low reflectance of the samples. This is why most of the magnetooptical spectroscopy experiments were performed in transmission. As an example, figure 7.11 displays the wavelength

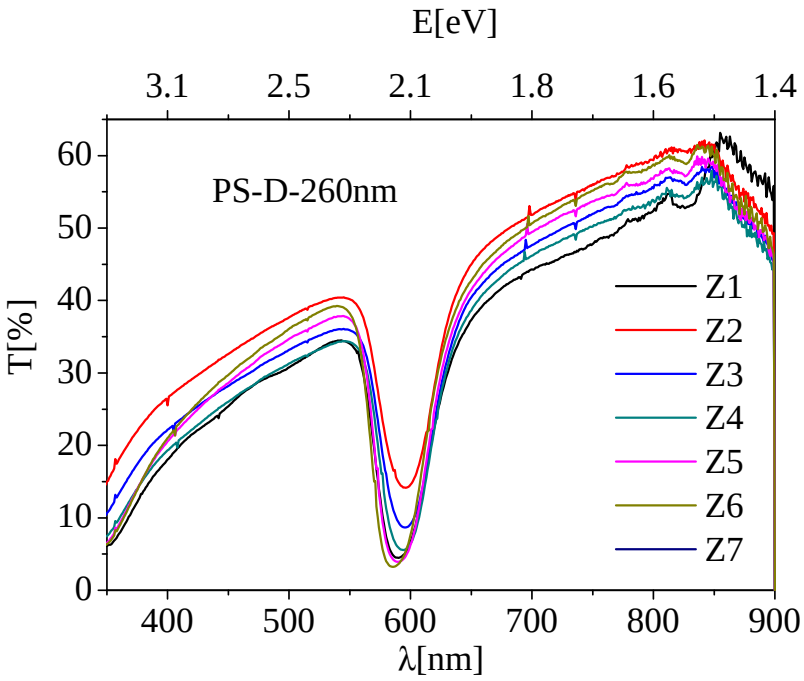

Figure 7.7: *The transmittance at different zones Z_i of sample $PS - D - 260nm$*

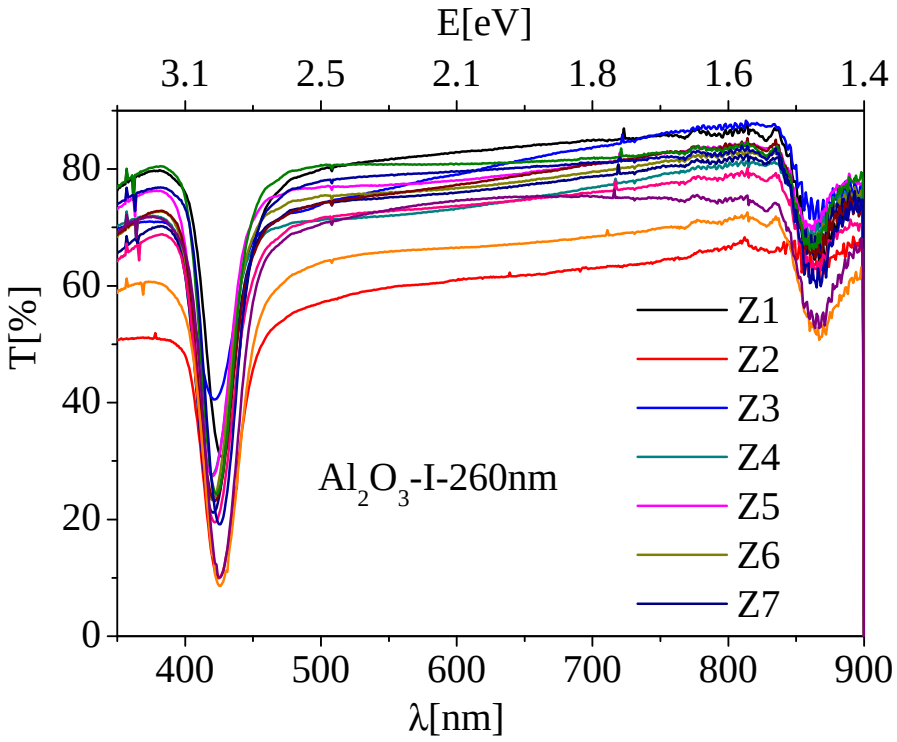

Figure 7.8: *The transmittance at different zones Z_i of sample $Al_2O_3 - I - 260nm$*

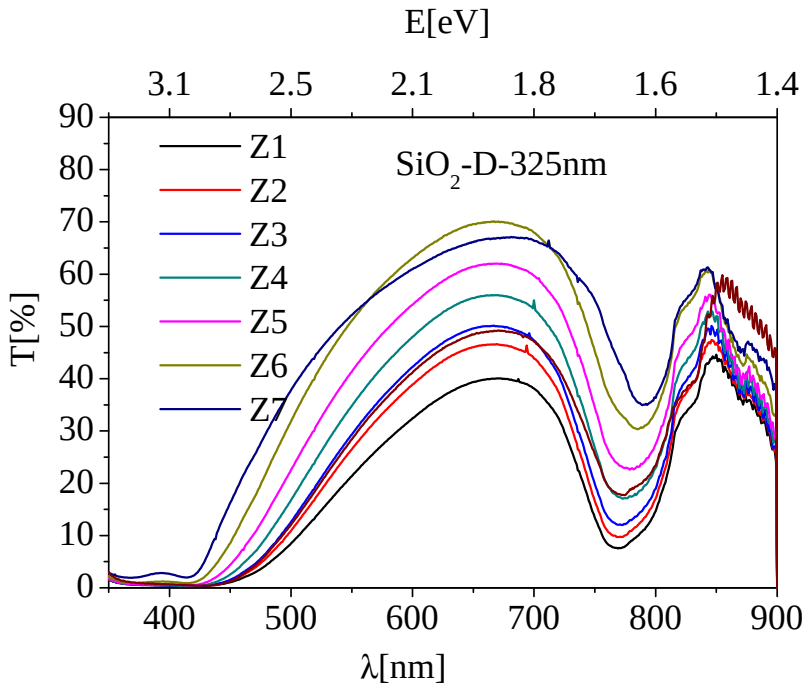

Figure 7.9: *The transmittance at different zones Z_i of sample $SiO_2 - D - 325nm$*

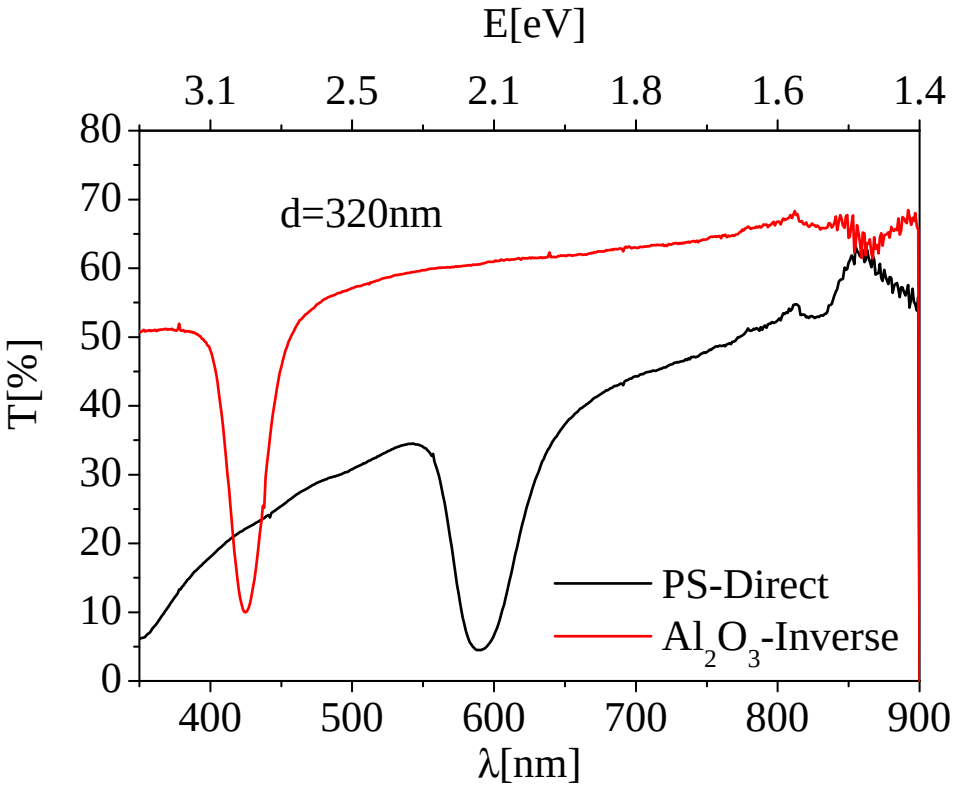

Figure 7.10: *The transmittance for $PS - D - 260nm$ and $Al_2O_3 - I - 260nm$ samples, with $d = 260nm$ periodicity*

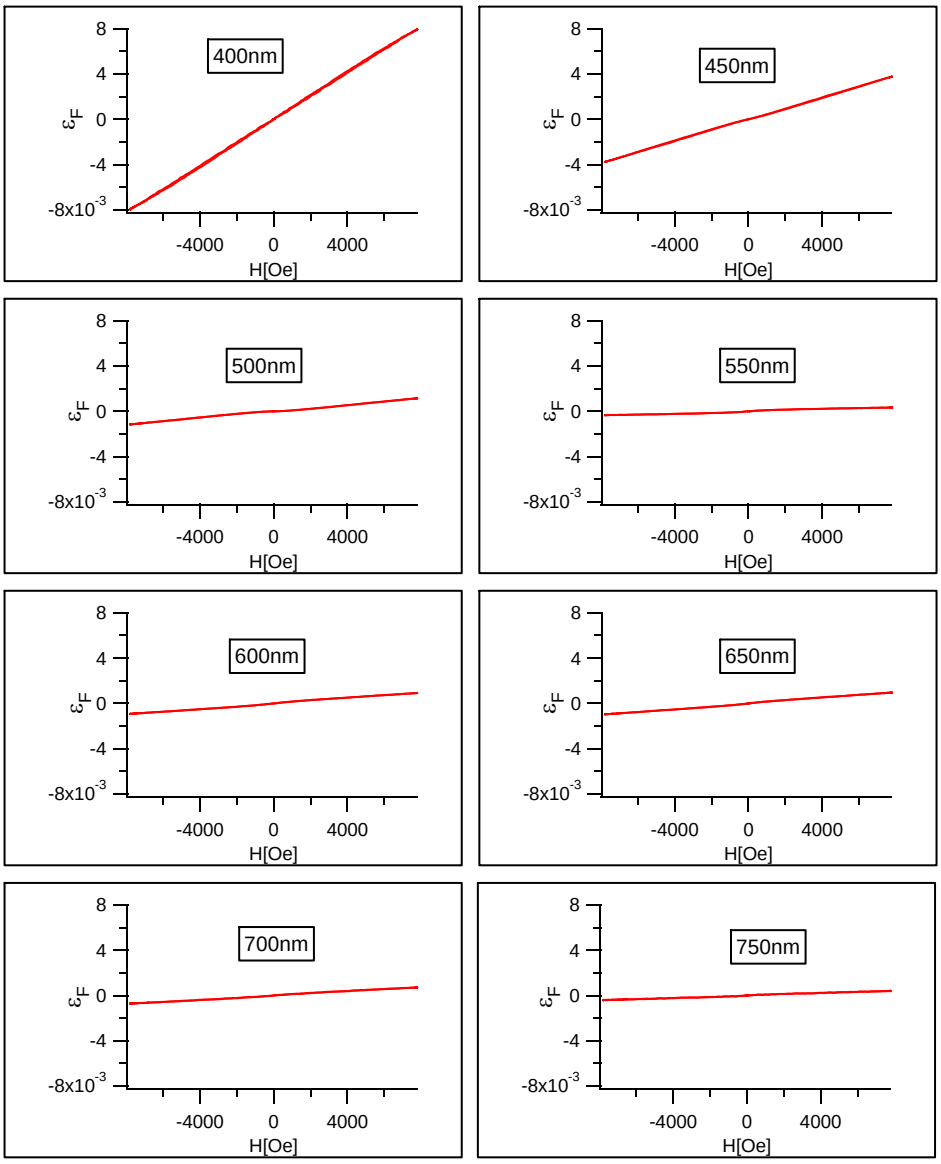

Figure 7.11: *The Faraday ellipticity ϵ_F spectral dependence for $PS - D - 260nm$ sample.*

dependence of the Faraday ellipticity of a representative opal. Instead of a magnetic loop, this figure shows an almost linear dependence with the magnetic field. This linear dependence comes from the Faraday ellipticity of the glass substrate. Due to much larger thickness of the glass substrate with respect to the opal, the optical properties of the samples were overwhelmingly dominated by the substrate. Thus, the magnetooptical signal coming from the magnetic nanoparticles distributed within the opals remained largely masked by the large linear magnetooptical contribution from the glass substrates, which made the analysis of the spectra quite difficult. Similar results were found in Faraday rotation not shown-. In spite of this, still a small feature close to $H = 0$ -small deviation of the linear behaviour- could be observed in measurements of the Faraday ellipticity (see figure 7.11). As was discussed before in the section 1.2 and taking into account that rotation is closely related to real part of the refractive index while ellipticity is connected to light absorption, this suggests that the magnetooptical signal of the magnetic material becomes more relevant in absorption experiments.

It will be proved to be advantageous to characterize the magnetooptical properties by measuring the magnetic circular dichroism (MCD), see section 1.2. The MCD experiments are based on the measurement of the difference in the absorption between left circularly polarized (LCP) light and right circularly polarized light, induced in the sample by a magnetic field oriented parallel to the direction of light propagation. The experimental set-up used for magnetic MCD is sketched in the figure 3.13. MCD spectra are proportional to the ellipticity ϵ, but the magnetooptical signal is significantly larger. It can be shown that the equation 3.19[167]:

$$MCD \approx \frac{I_\omega}{I_0} \approx \Delta\kappa \approx 4 \times \epsilon \tag{7.4}$$

where $\Delta\kappa = \kappa_+ - \kappa_-$ and κ_+ and κ_- are the extinction absorption coefficients of right- and left-circularly polarized light, respectively [223]. Thus, the MCD should be four times the value of the ellipticity. This is why in the following we measured preferentially MCD to probe the effect of the photonic band gap of the opal crystals on the magnetooptical response.

MCD spectra measured for different wavelengths within the range $\lambda = 400 - 800nm$ are shown in figure 7.12. The experiments were carried-out following the procedure described in the section 3.4. A quick inspection of the figure reveals that the contribution from the magnetic opal is much more emphasized than in the measurements of Faraday ellipticity performed in the same sample displayed in the figure 7.11. Still, however, a linear contribution to the MCD from the glass substrate remained (figure 7.12). After

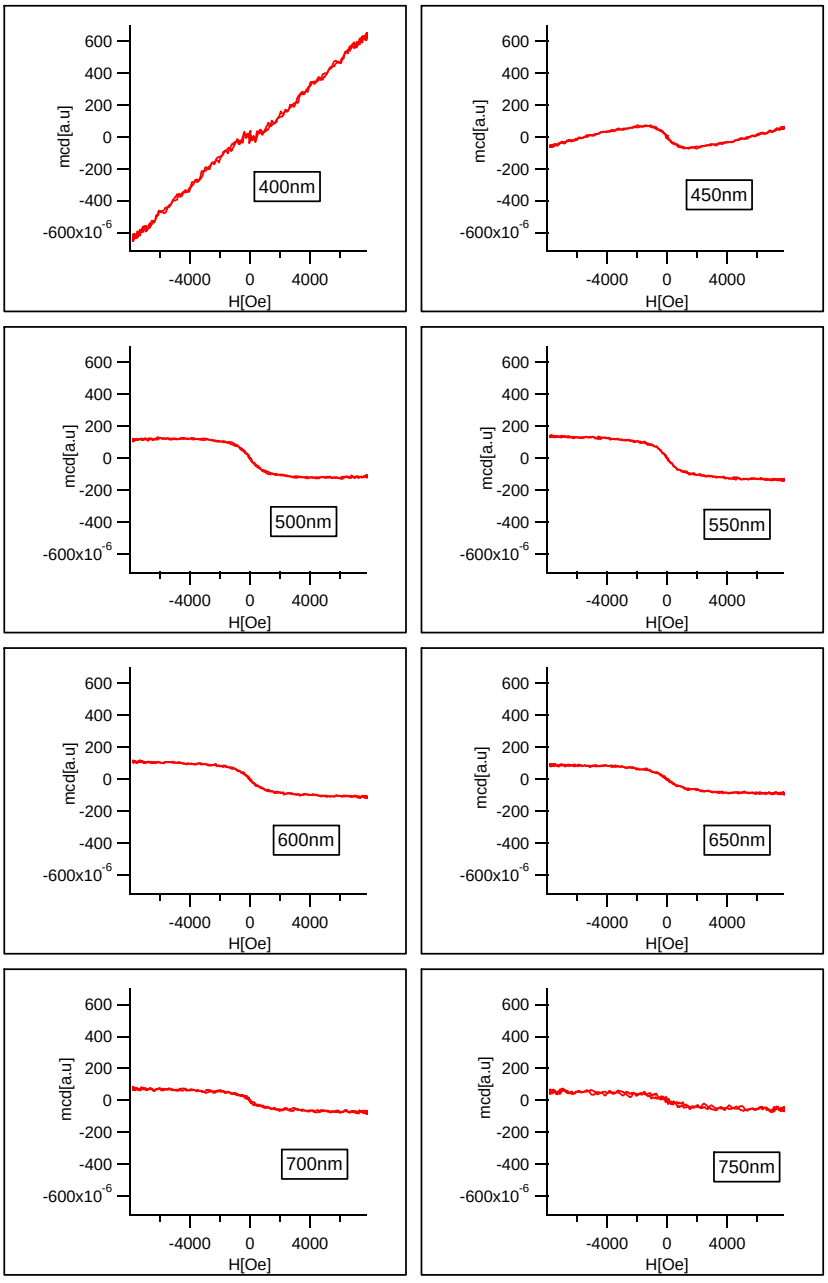

Figure 7.12: *Magnetic circular dichroism at several wavelengths for sample* $PS - D - 260nm$.

Label	Type	Material	d
$MPC1$	Inverse	Silica	467nm
$MPC2$	Inverse	Silica	380nm

Table 7.2: *List of maghemite infiltrated opals analyzed in figures 7.15 and 7.15.*

subtraction of this linear contribution, the MCD signal is plotted in the figure 7.13.

7.5.3 Magnetophotonic response of three-dimensional opals

The main purpose of our study of magneto-photonic crystals is to explore the effect of the photonic bandgap on the enhancement of the magnetooptical response. To progress in this issue, we discuss first silica-based inverse opals infiltrated with maghemite magnetic nanoparticles as shown in the images 7.14. They are $10nm$ in diameter, with narrow particle size distribution ($\sigma < 10\%$) and superparamagnetic at room temperature, with a saturation magnetization at $300K$ of $30emu/g$ and a blocking temperature lower than $60K$ [171]. The samples description is shown in table 7.2.

Due to the different periodicity of the photonic crystals, the corresponding photonic band gaps occurred at different wavelengths. This is seen in the reflectance spectra of figure 7.15, which were recorded using micro-spot with size $\approx 50\mu m$, at the laboratory of Prof. Cefe López, and Dr. Álvaro Blanco (Instituto de Ciencia de Materiales de Madrid (ICMM-CSIC). We see in this figure that the photonic band gap for $MPC1$ is centered at $\lambda = 830nm$, whereas for $MPC2$ it is centered at $\lambda = 572nm$.

The samples were infiltrated with different amounts of nanoparticles by either using two infiltration cycles (sample $MPC1$) or just one ($MPC2$). Thus, we expect that the loading of magnetic material of $MPC1$ will be higher than that of $MPC2$. Room temperature measurements by SQUID magnetometry of $MPC1$ and $MPC2$ revealed superparamagnetic behaviour of the material with saturation fields about $M_s = 3kOe$ (see figure 7.16), thus confirming that the magnetic nanoparticles do not magnetically interact with each other once being infiltrated in the opal.

Saturation magnetization values were $M_s = 3.05emu/cm^3$ for $MPC1$ and $M_s = 1.07emu/cm^3$ for $MPC2$ (referred to the opal volume). These values correspond to a magnetic loading of 1.9% and 0.7%, respectively (volume percentages). The higher magnetization of sample $MPC1$ is in agreement with its higher magnetic filling.

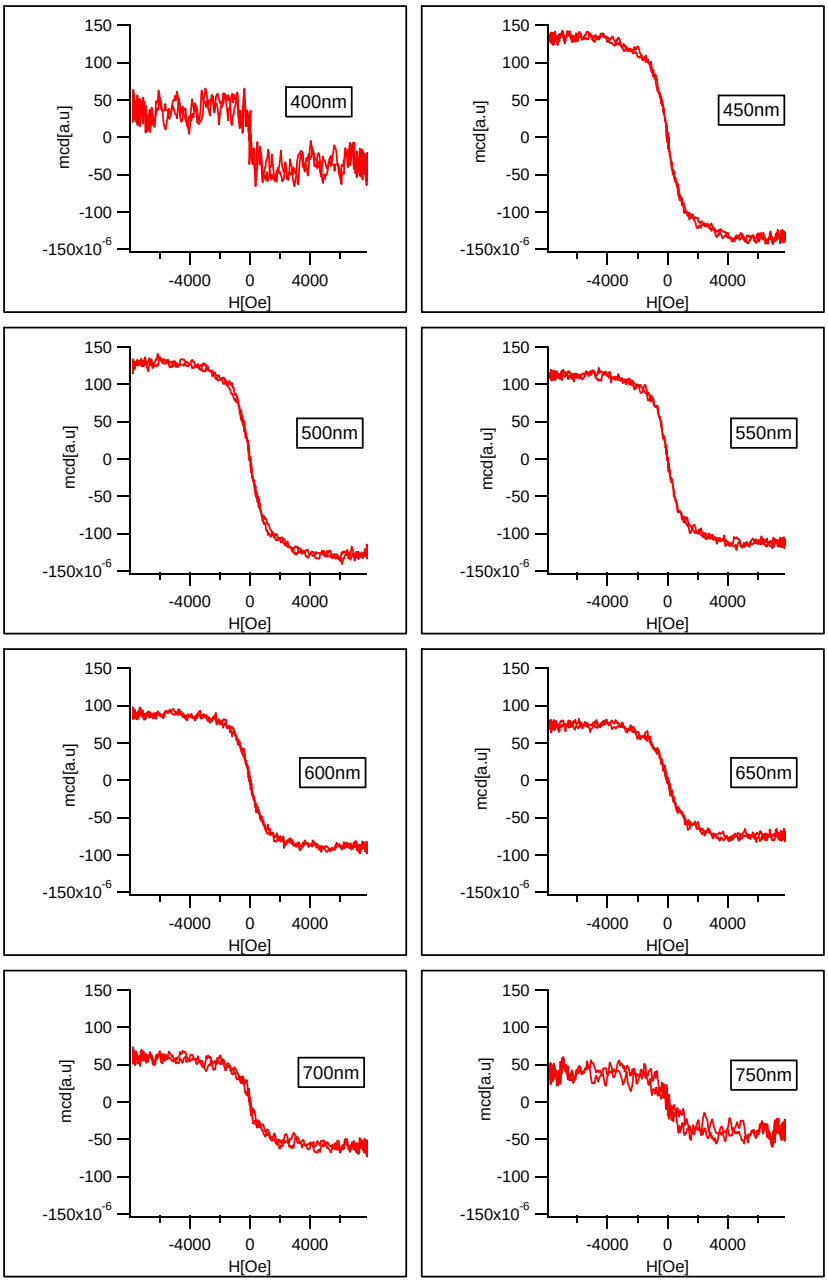

Figure 7.13: *Magnetic circular dichroism (linear contribution removed) at several wavelengths for sample* $PS - D - 260nm$.

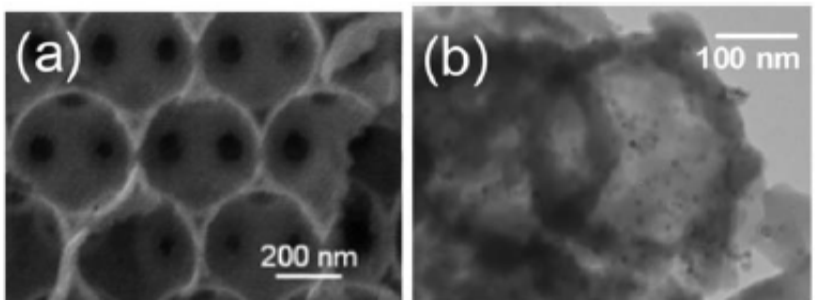

Figure 7.14: *(a)SEM image of a silica inverse opal infiltrated with maghemite nanoparticles; (b) TEM image of the same sample showing the regular distribution of magnetic nanoparticle*

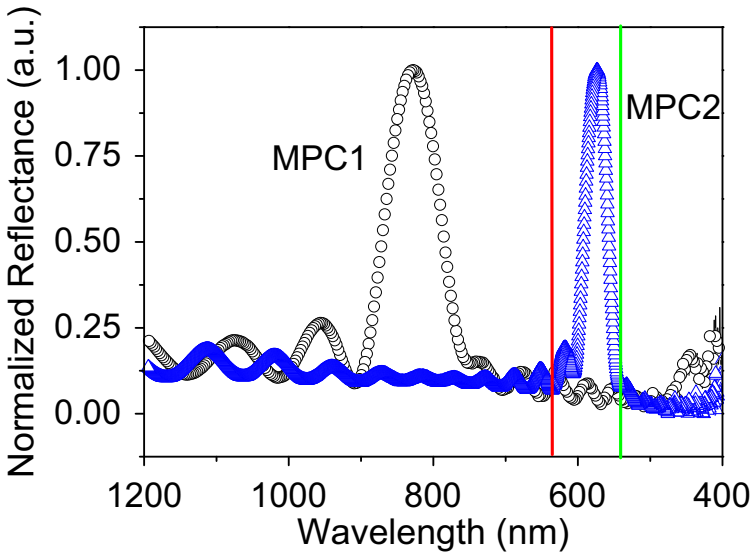

Figure 7.15: *Reflectivity spectrum as a function of the wavelength of the samples MPC1 and MPC2. Red curve ($\lambda = 542nm$) and green ($\lambda = 632.8nm$) wavelength are indicated by the vertical lines*

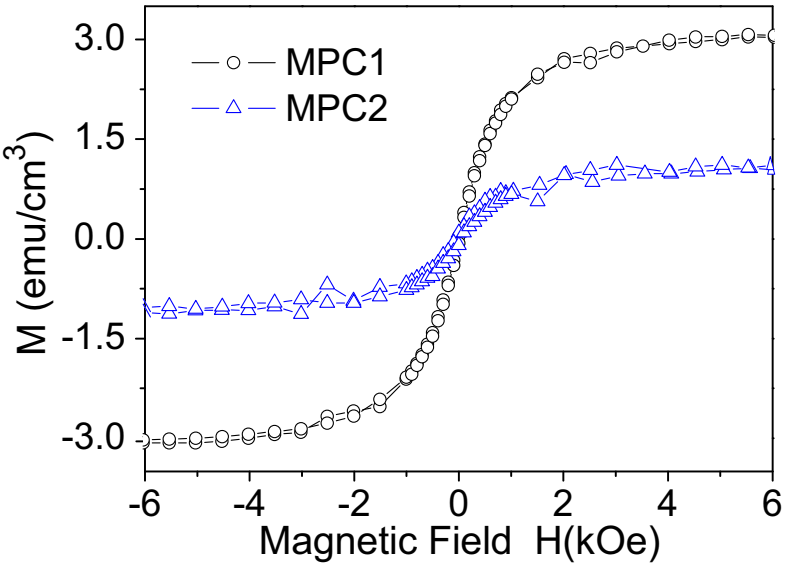

Figure 7.16: *Magnetic hysteresis loops of samples MPC1 and MPC2 measured by SQUID. The magnetization is referred to the opal volume*

Figure 7.17 shows Kerr rotation hysteresis loops measured at a wavelength $\lambda = 632.8nm$. An inspection of results in figure 7.17 shows that the hysteresis loops by magnetooptical Kerr effect are in a good agreement with those obtained by SQUID magnetometry (see figure 7.16). This fact indicates that the infiltration of inverse opals with magnetic nanoparticles is a convenient way to fabricate magneto-photonic crystals and also that the magnetization and Kerr rotation can be controlled by the filling factor. Indeed, the Kerr rotation of sample $MPC1$ is significantly higher than that of $MPC2$, which, as noted above, is consistent with a higher degree of magnetic nanoparticles filling of $MPC1$ with respect to $MPC2$. Moreover, we note that the ratio of the Kerr rotations measured for $MPC1$ and $MPC2$ ($0.2/0.05mrad$, see figure 7.17), is larger than that of the magnetization ratio ($3.05/1.07emu/cm^3$, see figure 7.16). This indicates that the Kerr rotation is not simply proportional to the overall magnetization of the $MPCs$. This behavior, which contrasts with results in bulk materials, indicates the existence of an enhancement in the magnetooptical response of the $MPCs$ [213].

In order to further explore these promising results, we carried out the magnetooptical characterization of Al_2O_3 inverse opals infiltrated with Nickel (Ni) nanoparticles. In this case, we studied the optical and magnetooptical properties of these $3D$ magneto-photonic crystals by performing optical transmittance (OT), circular dichroism (CD), and magnetic circular dichroism (MCD) spectroscopy in the range of wavelengths $\lambda = 400 - 800nm$. As discussed above, the MCD signal is proportional and much stronger than the Faraday ellipticity [3, 150, 167, 223], and it was used to track the photonic effects

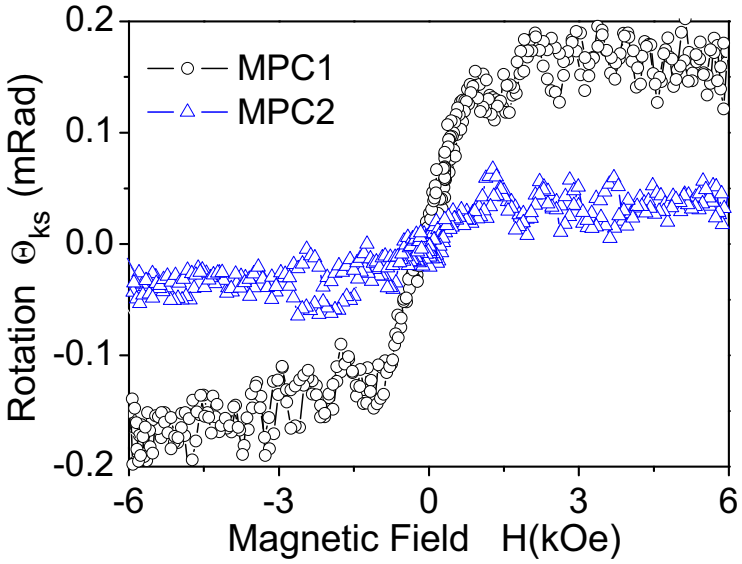

Figure 7.17: *Kerr rotation of samples MPC1 and MPC2 obtained with red laser* $\lambda = 632.8nm$

on the magnetooptical spectra. The optical transmittance spectra were taken at normal incidence and allowed us to measure the stop-band frequencies of the magneto-photonic crystals.

The figure 7.18 (left axis) shows the OT for the blank non-infiltrated opal (solid squares) as well as the opals infiltrated with $15nm$ and $8nm$ nano-particle (solid triangles). We note that in figure 7.18 the optical transmittance and magnetic circular dochroism spectra are given in arbitrary units and have been shifted in order to facilitate their visual inspection. We observe in figure 7.18 that the blank opal exhibits a photonic band centered at $\lambda \approx 537nm$, whereas after the infiltration with the Ni nanoparticles the photonic band gap experiences a red-shift. This effect is very weak for the opal infiltrated with $15nm$ nanoparticles, whereas it is substantial ($\approx 18nm$) shift for the opals infiltrated with $8nm$ nanoparticles. The magnitude of the photonic band band red-shift is directly related to the degree of the opal infiltration [214].

We performed CD experiments by recording the intensity of the light transmitted through the opals (see inset of figure 7.19) while sweeping the wavelengths in the absence of any magnetic field ($H = 0$). For nonoptically active systems a null CD signal should be expected, but due to their particular compact fcc periodic structure, photonic crystals can indeed exhibit a significant CD near the stop-band frequencies, especially at off-normal incidence [224, 225]. Here we show that this effect can be quite large even near to normal incidence. Indeed, we see in 7.19 that the CD spectrum of the opal infiltrated with $8nm$ Ni nanoparticles is significantly large around the stop band ($\approx 550nm$ see figure 7.18). The

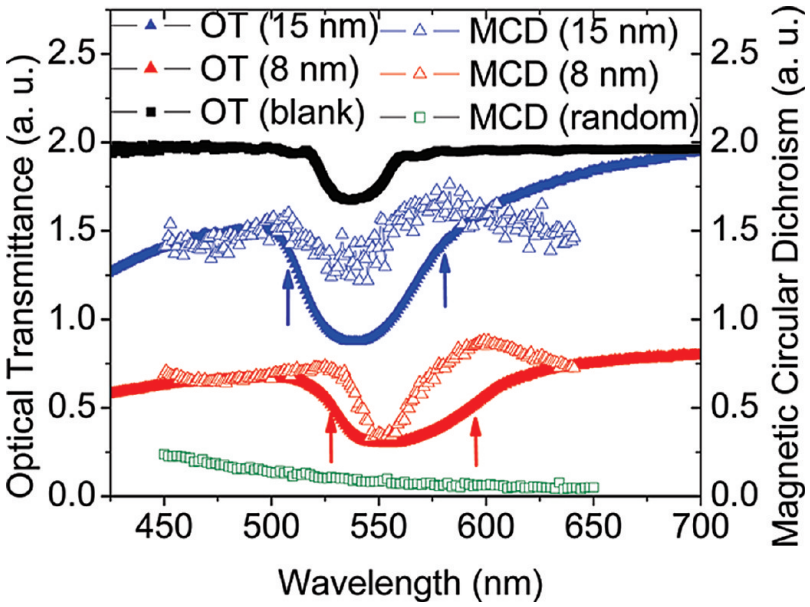

Figure 7.18: *Optical transmittance of a non-infiltrated opal (blank) and opals infiltrated with* $15nm$ *and* $8nm$ *Ni nanoparticles. The figure also shows the magnetic circular dichroism spectra of opals infiltrated with nanoparticles as well as the MCD spectra of Ni nanoparticles distributed randomly on a glass substrate*

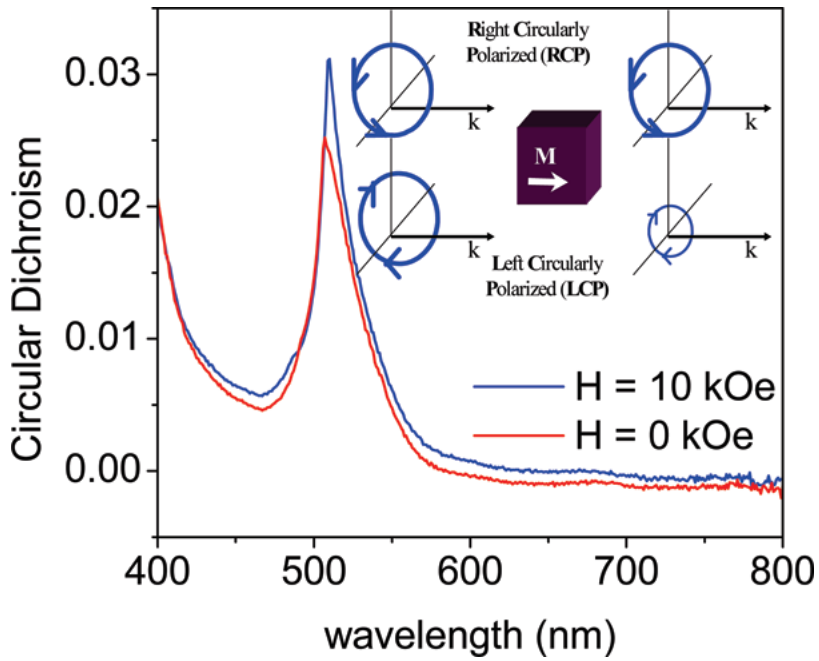

Figure 7.19: *Circular dichroism (CD) spectra at zero field and at field* $H = 10kOe$ *of an inverse opal infiltrated with* $8nm$ *Ni nanoparticles. The sketch in the inset shows the principle of the CD experiment.*

application of a field of $H = 10kOe$ (well above the saturation field on the Ni nanoparticles) induces only an additional moderate increase of around 30% of the CD response. Thus, much of the optical activity of these $3D$ magneto-photonic crystals has a nonmagnetic origin; it results from the geometry of the opal structure, and thus this technique does not allow disentangling the distinct contributions to the optical activity. We used then a distinct strategy to determine the intrinsic magnetooptical response of the crystals. For that purpose, we recorded the whole series of full hysteresis MCD loops of the $3D$ magneto-photonic crystals with $1nm$ step resolution, from $\lambda = 400nm$ to $\lambda = 800nm$. The maximum amplitude of each hysteresis loop was then used to compute the MCD spectral response. As an illustration, we show in figure 7.20d the MCD spectrum measured using this procedure, while figure 7.20a-c displays the full hysteresis loops at selected wavelengths.

Once the protocol to measure the intrinsic MCD is established, we discuss now the magnetooptical spectral responses of the photonic crystals and their relation to their optical properties. The figure 7.18 depicts the OT (left axis) and MCD (right axis) spectra obtained at the same spot (diameter $\approx 2mm$) in opals infiltrated with $8nm$ and $15nm$ nickel nanoparticles. Additionally, the figure 7.18 shows the MCD spectrum of a sample consisting of $8nm$ nanoparticles distributed randomly on a glass substrate (empty squares). This spectrum is the reference of the MCD response of the Ni nanoparticles free of any crystal-induced photonic effect. Figure 7.18 immediately reveals a deep modification of the MCD spectra of the two $3D$ magneto-photonic crystals with respect to that of the randomly distributed Ni nanoparticles. More specifically, a clear signature is observed of a magnetooptic enhancement in the form of two prominent shoulders in the MCD spectra around the two stop-band edge frequencies (which are indicated by arrows). Note that the frequency shift of the optical stop-band positions of the $3D$ magneto-photonic crystals infiltrated with $8nm$ and $15nm$ nanoparticles is perfectly reproduced by the shift of the features of the MCD spectra induced by the photonic band effects. Therefore, the intensive modification of the magnetooptical response in close proximity of the band edge frequencies is in agreement with the theoretical predictions [185] and is a direct consequence of the strong increase of light-matter interaction due to photonic band flattening and the resulting reduction of the light group velocity at band edge wavelengths [226]. We finally point out that the photonic effect on magnetooptics in the $3D$ magneto-photonic crystals infiltrated with $8nm$ is slightly larger than that of the one infiltrated with $15nm$ nanoparticles (see figure 7.18), in agreement with the larger impregnation of Ni nanoparticles inside the crystal in that case compared to the former.

We have thus demonstrated that an optimal infiltration of inverse opals with magnetic

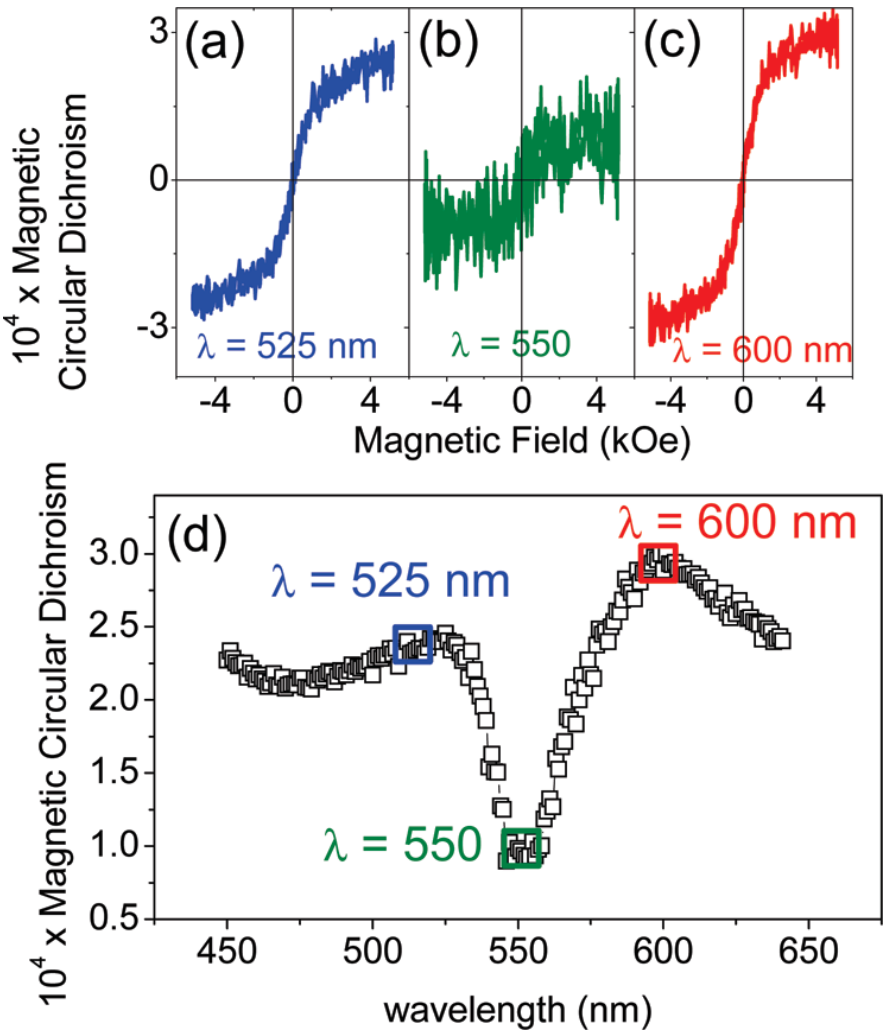

Figure 7.20: *Magnetic circular dichroism spectrum of an inverse opal infiltrated with 8nm Ni nanoparticles is shown in (d). The data are obtained from the maximum amplitude of the full MCD hysteresis loops (see panels (a)-(c) for these loops at three selected wavelengths)*

nanoparticles is a powerful strategy to customize the magnetooptical spectral response of magnetic materials and that is operative at least on the order of the millimeter (roughly the probe light spot size in our experiments). This shows that the structural order required to observe the photonic band induced effects is preserved in the same length scale, which makes still more appealing the approach here described for applications using lasers as light sources. Now that we have demonstrated the occurrence of a magnetophotonic response in magnetic opals, we proceed in the following to analyze the effects of the optical contrast and the magnetic load on the intensity of these effects.

Effect of the optical contrast in the magnetophotonic response

We present here the evidence of the close correlation between the photonic-induced magnetooptical enhancement and the permittivity contrast of the constituent materials of the magnetic opals. For that purpose, we have compared the magnetooptical spectra of two different crystals, namely, a direct opal of SiO_2 spheres and an inverse Al_2O_3 opal. Because the refractive index of SiO_2 ($n = 1.4562$ at $\lambda = 505nm$)[227] is significantly higher than that of air ($n = 1$), the permittivity contrast in the inverse opal is significantly larger than in the direct opal (see the sketches of direct 7.21 and inverse 7.22 opals presenting different permittivity contrast with respect to the air). Therefore, one should expect a larger magnetophotonic effect in inverse opals compared to direct opals. To address this issue, we have carried the magnetooptical spectroscopy of direct and inverse opals both infiltrated with Ni nanoparticles, as shown in figures 7.21 and 7.22, respectively. These figures show the magnetooptical response as well the transmission spectra (left axis) of each of these crystals as well as the magnetooptical spectrum of Ni nanoparticles distributed randomly on a glass substrate. The spectrum of the Ni nanoparticles is included to compare ordered and disordered systems, that is, to discriminate the intrinsic response from the magnetophotonic properties. Comparing figures 7.21 and 7.22 it becomes clear that the optical contrast is directly connected on the magnetophotonic properties, being the magnetophotonic response larger for the inverse opals compared to that of direct opals.

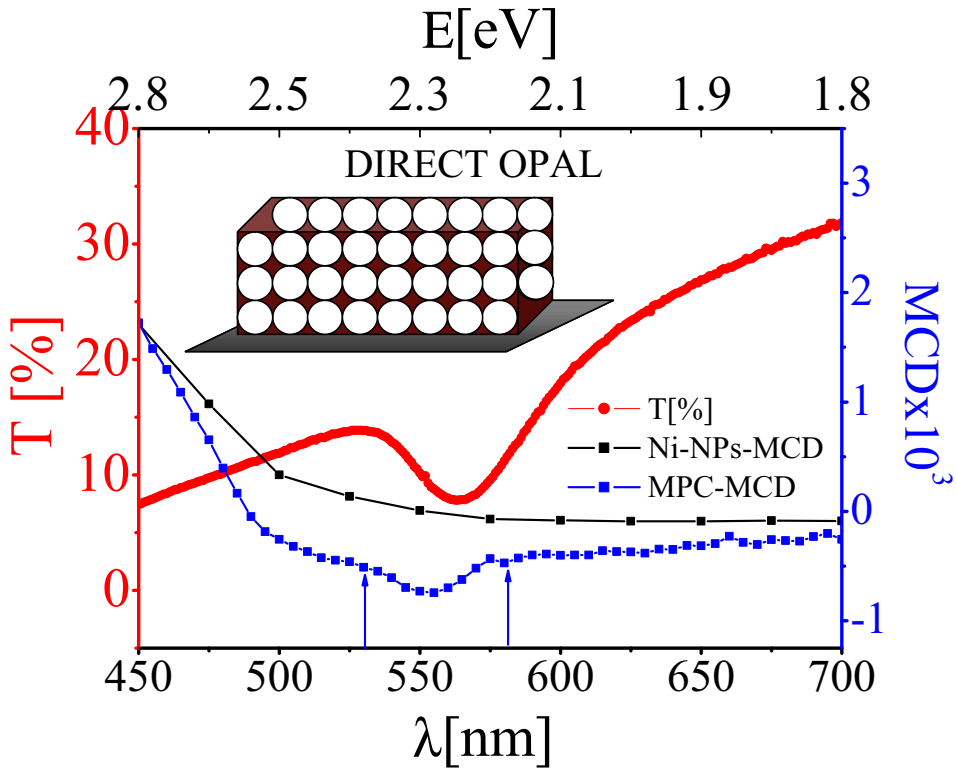

Figure 7.21: *Transmittance and MCD on direct opal infiltrated with Ni nanoparticles*

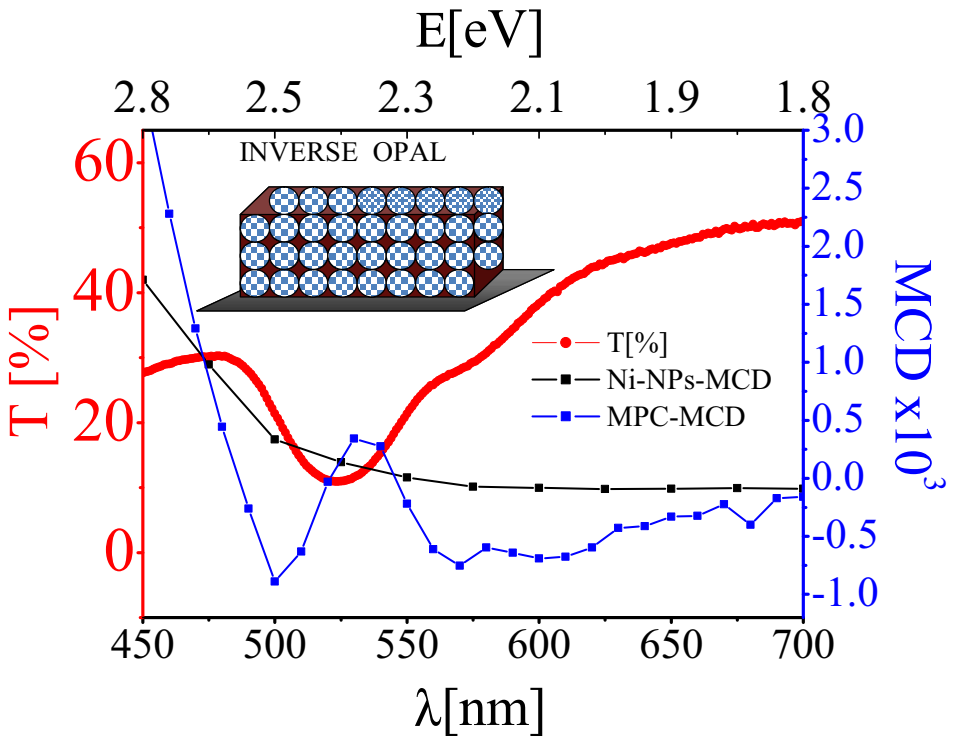

Figure 7.22: *Transmittance and MCD on inverse opal infiltrated with Ni nanoparticles*

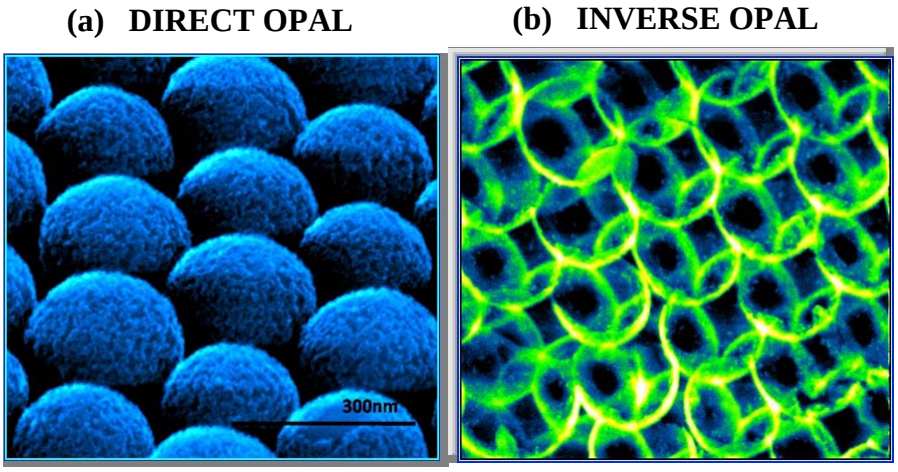

Figure 7.23: *SEM images of direct and inverse opal coated by conformal coating of $MnFe_2O_3$ nanoparticles [228]*

Effect of the magnetic material content in the magnetophotonic response

We have explored the effect of the magnetic material content on the magnetophotonic response. As described above, the infiltration of opals in nanoparticle colloidal dispersions gives rise to magnetic filling factors of about 10%. Since the magnetophotonic response should scale with the amount of magnetic material, we have explored alternative strategies to increase further the content of magnetic material. Oana Pascu and Anna Roig have faced successfully this important challenge by developing an extremely fast and versatile synthetic approach, based on microwave assisted sol-gel chemistry, that allows a conformal nanometric coating of intricate three-dimensional structures [180, 228]. Using this technique, magnetic load filling factor between $\approx 10\% \rightarrow 50\%$ were obtained [228] thus enhancing the magnetophotonic response. Direct and inverse opals where impregnated with magnetic material -the spinel $MnFe_2O_4$ in this case- that formed a conformal nanometric coating on the cavity walls of the opal structures [228]. Figure 7.23 shows two scanning electronic microscopy (SEM) pictures of direct (a) and inverse (b) opals that confirm the homogeneous and uniform $MnFe_2O_4$ coverage of the opal structures. The details of the structural characterization of this nanometric coating are given in elsewhere [180, 228].

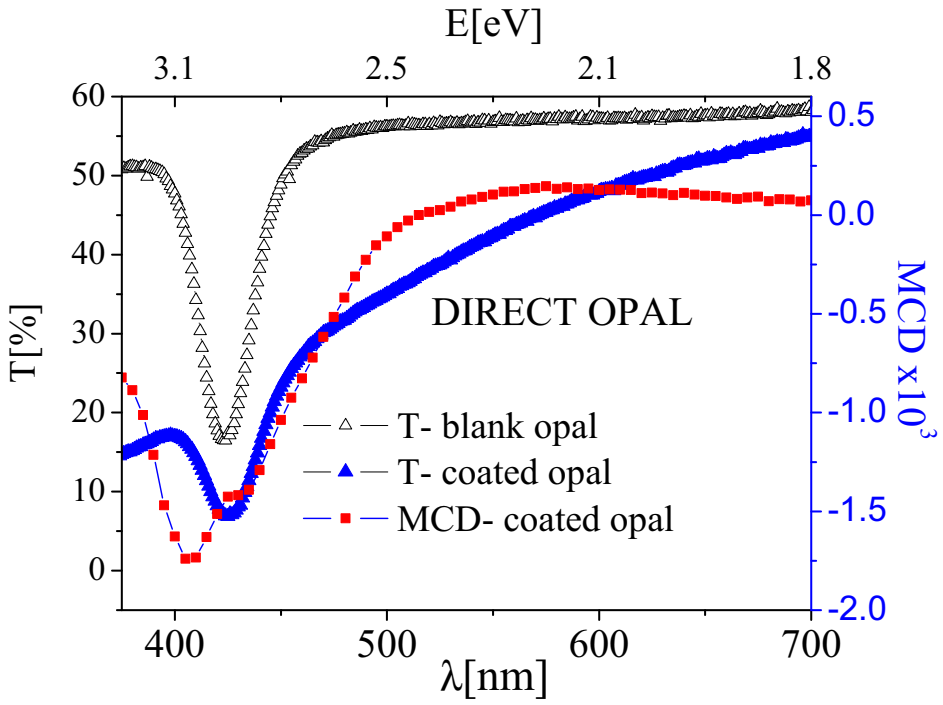

Figure 7.24: *Transmittance and MCD on direct opal coated by conformal coating of $MnFe_2O_3$ nanoparticles [228]*

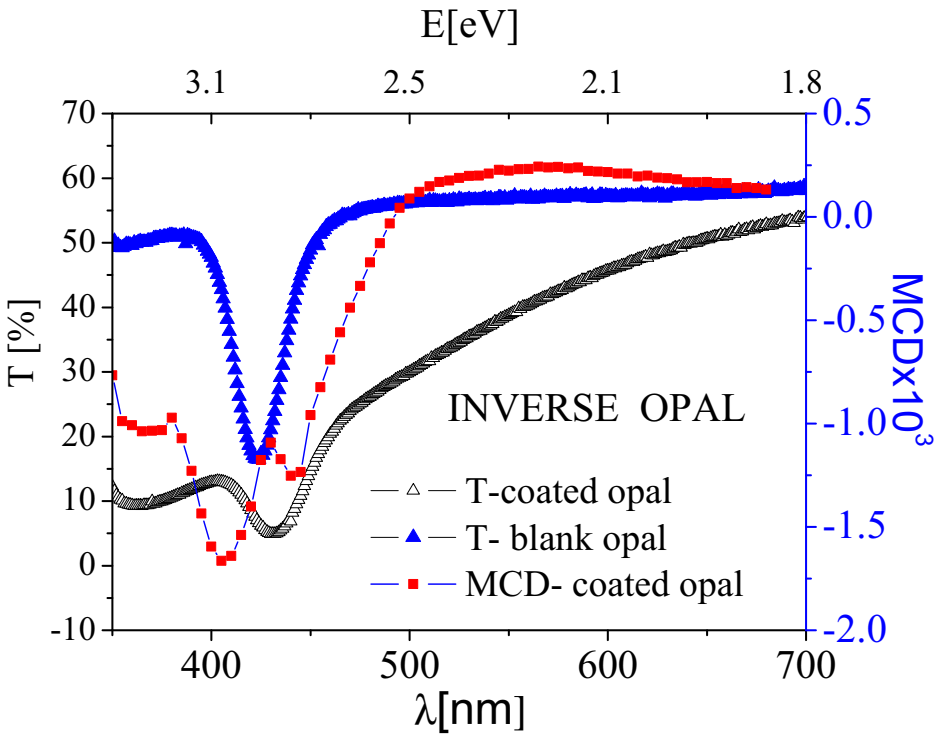

Figure 7.25: *Transmittance and MCD on inverse opal coated by conformal coating of $MnFe_2O_3$ nanoparticles [228]*

Figures 7.24 and 7.25 show the MCD spectra (right axis) of the direct and inverse opals, respectively. These figures also includes the transmittance spectra (left axis) of each of these crystals as well as the MCD spectrum of $MnFe_2O_4$ nanoparticles distributed randomly on a glass substrate. As the results presented in the chapter 6, the disordered system gives the reference magnetooptical response of randomly distributed $MnFe_2O_4$ nanoparticles and, thus, in the absence of any photonic effect. A common feature observed for all the optical spectra of the magnetic opals (figures 7.24 and 7.25) is that the MCD response is deeply modified with respect to that of the randomly distributed nanoparticles, indicating that the photonic band structure of the crystals radically influences the magnetooptical properties of the manganese ferrite nanoparticles. Interestingly, we observe that the magnetooptical enhancement in opal coated by conformal coating, is optimized with respect to that observed in opals infiltrated by immersion in colloidal dispersions that had, generally, lower magnetic content. The large signal enhancement is readily appreciated by the appearance of two prominent shoulders that indicate strong photonic effects in the vicinity of the band-edge frequencies (see figure 7.25). In conclusion, using this methodology, we have achieved a conformal coverage of large areas of three-dimensional opals with a super-paramagnetic manganese ferrite layer, yielding magnetophotonic crystals with excellent quality [228]. The use of a ternary oxide for the ultra-thin coating demonstrates the potential of this methodology to realize three-dimensional structures with complex materials that may find applications beyond photonics, such as energy, sensing or catalysis, provided that a conformal coverage of other materials is achieved. Therefore, this new approach will contribute to the rapidly expanding field of advanced techniques for the fabrication of three-dimensional complex systems.

Part III

Appendix

APPENDIX A

Magnetic vectometry exploiting null ellipsometry magneto-optics

In section 3.2.2 of chapter 3 we demonstrated that null ellipsometry can be adapted to obtain a complex magneto-optical response that is a combination of transverse and longitudinal/polar components (see Eqs. 3.11, 3.12). Thus, in a single experiment, we can obtain simultaneous information of the magneto-optical coefficients that are proportional to the magnetization components that are out of the plane of incidence (transverse) and contained in that plane (longitudinal/polar). We apply these characteristics to obtain information of the magnetic components in a Fe_3O_4 single crystal.

The imaginary transverse Kerr responses obtained from two different nulling zones at analyzer azimuths $(A_1, A_2 = \pm A)$ are given by:

$$I_{A1} = +\sin(2\psi)\Im\left(\frac{\Delta r_{pp}}{r_{pp}}\right) \underbrace{+\sin(2\psi)[(\theta_s - \theta_p)\sin(\Delta) - (\epsilon_s + \epsilon_p)\cos\Delta]} \tag{A.1}$$

$$I_{A2} = -\sin(2\psi)\Im\left(\frac{\Delta r_{pp}}{r_{pp}}\right) \underbrace{+\sin(2\psi)[(\theta_s - \theta_p)\sin(\Delta) - (\epsilon_s + \epsilon_p)\cos\Delta]} \tag{A.2}$$

Note that the underbraced terms consist of polar and longitudinal contributions $\theta_{s,p}, \epsilon_{s,p}$, whereas the first term contains the transverse response. Considering that θ_s is not much different from θ_p, and that ϵ_s is not much different from ϵ_p, i.e. $\epsilon_p, \epsilon_s = \epsilon$, the first term in the underbraced expression vanishes, and we obtain:

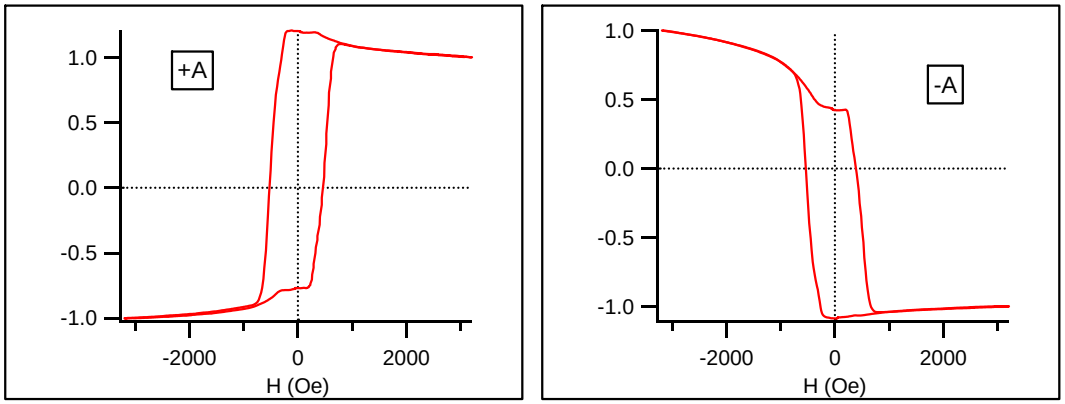

Figure A.1: *Measurement of the complex transverse Kerr effect using the proposed method at two analyzer positions* $\pm A$

$$\xi = \frac{I_{A1} + I_{A2}}{2} = -\sin(2\psi)[(\epsilon)\cos\Delta] \tag{A.3}$$

$$\tau = \frac{I_{A1} - I_{A2}}{2} = \sin(2\psi)\Im\left(\frac{\Delta r_{pp}}{r_{pp}}\right) \tag{A.4}$$

where ξ is a magnetooptical quantity proportional to the magnetization parallel to the plane of incidence ($\xi \propto M_{L,P}$), which depends on polar and longitudinal ellipticity, and τ is a transverse magneto-optical quantity proportional to M_T, perpendicular to the plane of incidence ($\tau \propto M_T$).

Figure A.1 shows the hysteresis loops obtained by null ellipsometry in different nulling zones for $A = \pm A$ to obtain the complex transverse Kerr signal. We note that these experiments are carried out by applying the magnetic field perpendicular to the plane of incidence and along an arbitrary direction in the crystal. By averaging in these two nulling zones (A.4), we obtain the magneto-optical quantities ξ and τ that are shown in figure A.2.

After removal of the quadratic effects proportional to M_T^2 and M_L^2, we obtain the components of both the longitudinal/polar (parallel to plane of incidence $M\ \|$) and transverse (perpendicular to plane of incidence $M\ \perp$). The transverse and in-plane magnetization are shown in figure A.3. The transverse magnetization $M_T \approx M_\perp$ shows a conventional hysteresis loop, where the magnetization vector saturates for high magnetic fields, indicating that the direction of the applied field is close to an easy magnetic axis. On the other hand, the in-plane longitudinal/polar $M_L, M_P \approx M_\parallel$ magneto-optical loop -which is proportional to the magnetization perpendicular to the application of the magnetic field-

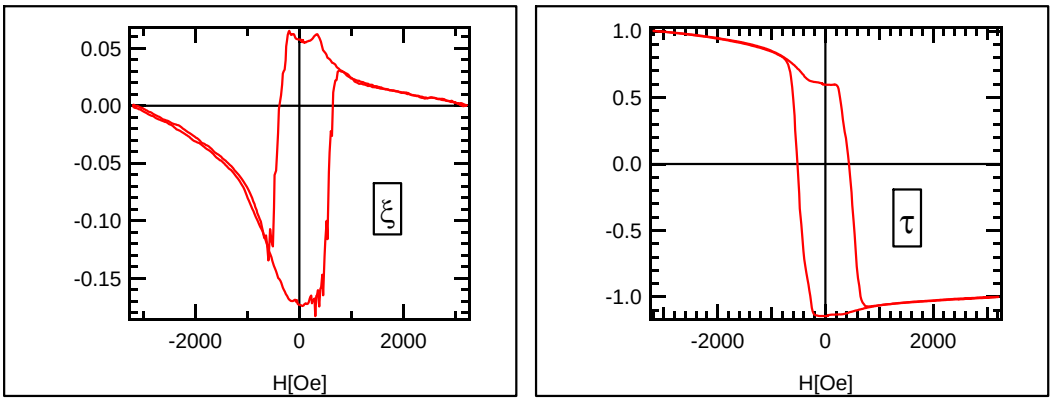

Figure A.2: *The magneto-optical quantities ξ and τ obtained by averaging over different nulling zones*

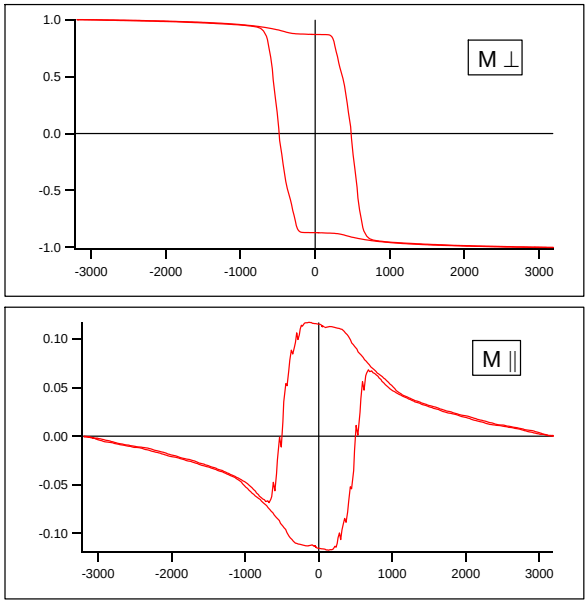

Figure A.3: *Transverse M_T and longitudinal/polar M_L, M_s magnetization, perpendicular and parallel to the plane of incidence, respectively*

is compatible with a coherent rotation of the magnetization during its reversal. Thus, for high fields, the magnetization vector is forced to be aligned along the direction of the field direction and, in consequence, the $M_{\parallel}$ component vanishes. However, in zero field, when the magnetization is aligned along the easy axis, gives a small in-plane component, resulting from a slight misalignment of the easy axis with respect to the field direction. Note that this is coherent with the slight reduction of the transverse loop is slightly reduced (figure A.3).

The procedure here described can be carried out for many field orientations and be exploited to achieve a full study of the magneto-optical anisotropy, as shown in figure A.4.

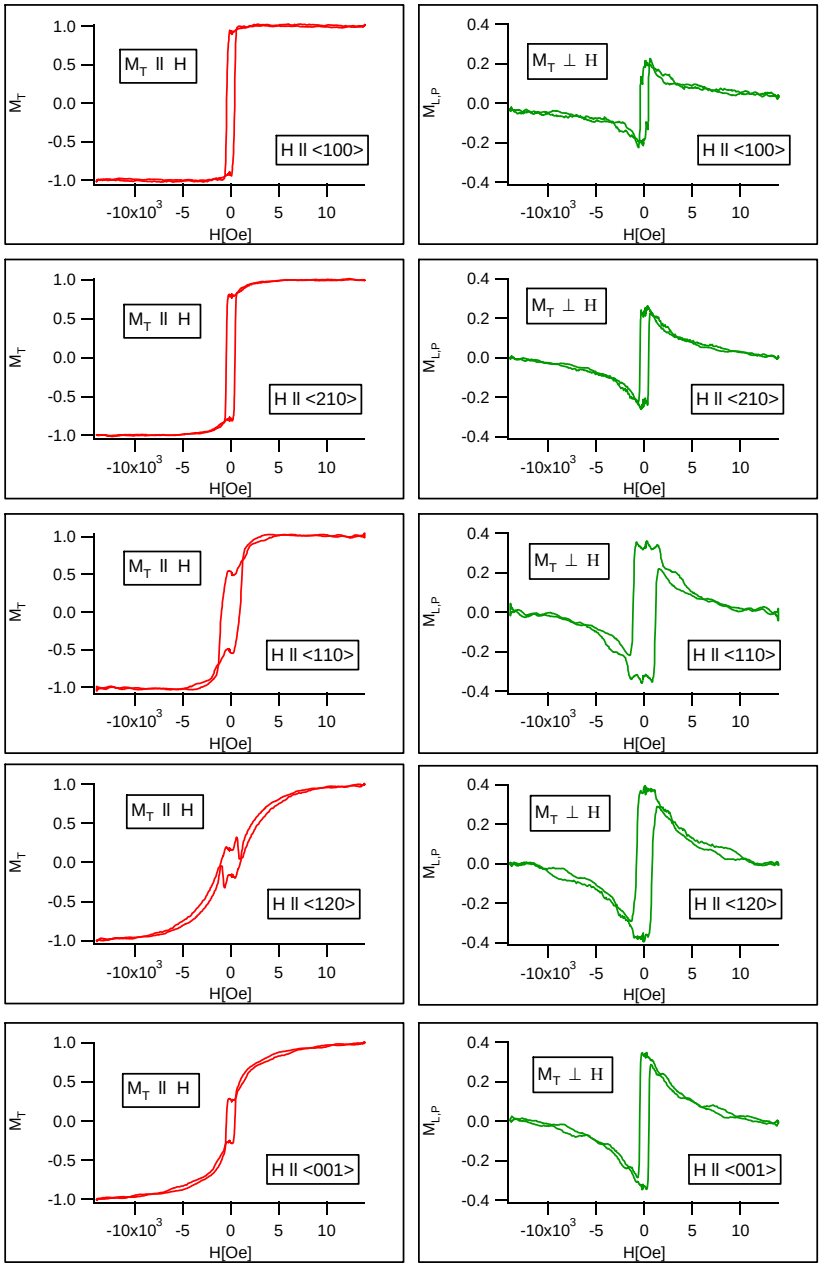

Figure A.4: *Transverse M_T and longitudinal/polar M_L, M_P magnetization, perpendicular and parallel to the plane of incidence respectively at several crystal orientations*

APPENDIX B

Experimental set-up at ICMAB

The experimental set-up designed and constructed at ICMAB to make both room temperature and low temperature complex transverse Kerr magneto-optical Kerr spectroscopy measurements is relatively complex. This section describes the elements and operation mode of the experimental set-up used for most of measurements. Technical information and specifications will be included.

Complex transverse Kerr effect spectroscopy based on Null ellipsometric: The apparatus

The components of the apparatus are listed below:

1. Anti-vibratory table
2. Glan-Thompson Polarizer ($\epsilon \approx 5X10^{-}5$)
3. Photo Elastic Modulator
4. Rotation stage (Azimuth $\pm P$)
5. Compensator (Achromatic / monochromatic Quarter wave-plate)
6. Rotation stage (Azimuth $\pm C$)
7. Glan-Thompson Analizer ($\epsilon \approx 5X10^{-}5$)
8. Rotation stage (Azimuth $\pm A$)
9. Photo-detector (Si-Diode) or Photo multiplier.

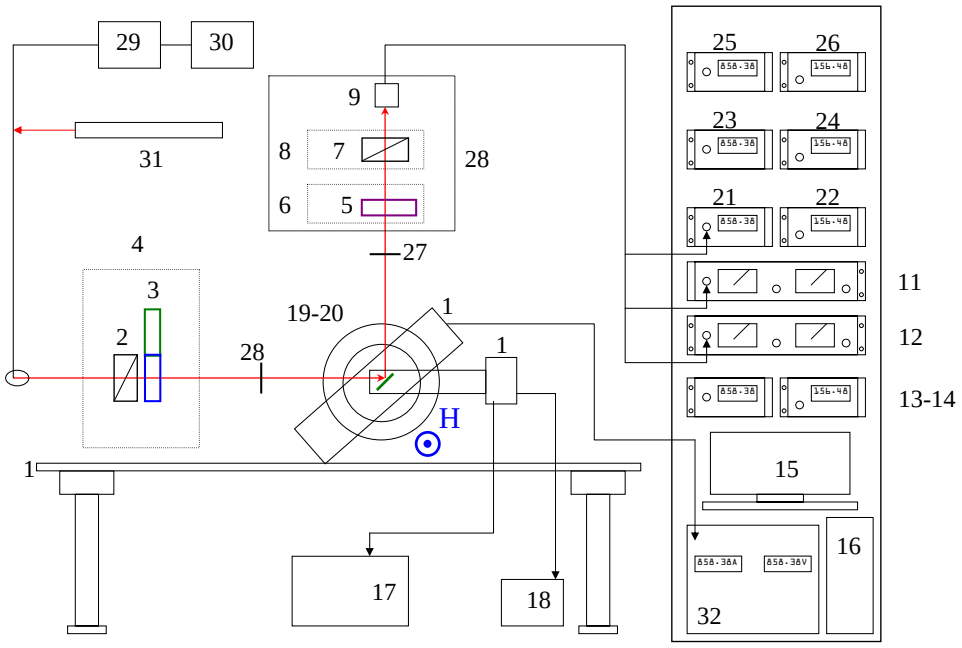

Figure B.1: *Complex transverse Kerr effect spectroscopy based on null ellipsometric: experimental set-up.*

10. Electromagnet (3 Tesla)
11. Lock-in amplifier I (I_ω :First harmonic $50KHz$)
12. Lock-in amplifier II ($I_{2\omega}$:Second harmonic $100KHz$)
13. Gaussmeter controller
14. Temperature controller
15. PC interface
16. GPIB/USB/RS232 interfaces
17. Helium compressor
18. Rotatory Pump
19. Sample
20. Transverse Hall probe
21. Photo multiplier driver
22. HeNe laser Driver

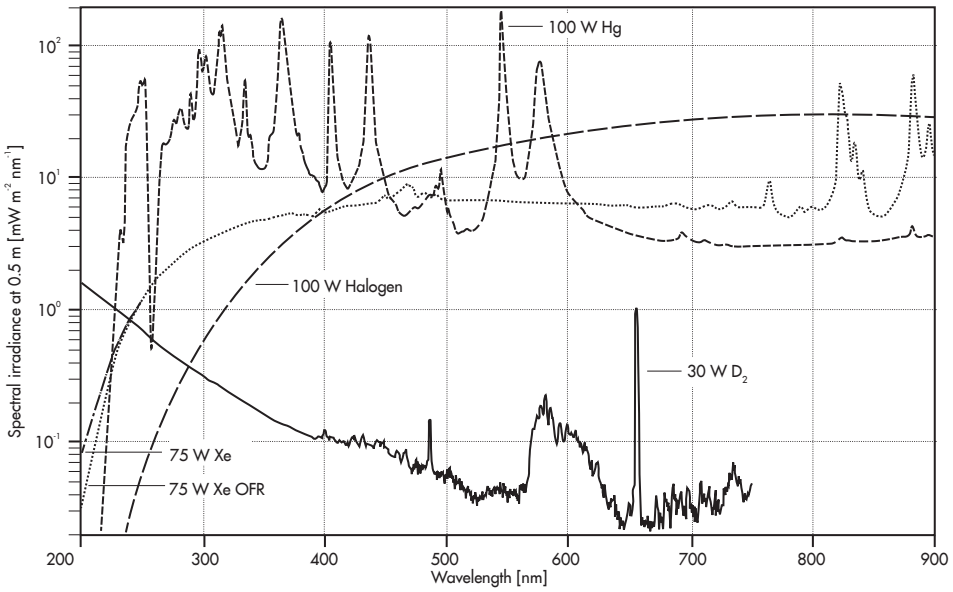

Figure B.2: *Lamp spectra and irradiance of 75W Xenon arc lamp. Taken from LOT-ORIEL web-page*

23. Diode laser driver
24. Rotatory stage driver
25. IR diode driver
26. Vacuum meter
27. Lenses
28. Lenses
29. Monochromator
30. Xenon lamp
31. HeNe laser
32. Electromagnet power supply
33. Cryostat

The mechanical, optical, and electronic part of the apparatus is drawn schematically in the figure B.1. The light source for the visible and ultraviolet part of the spectrum is a $75W$ ultra high stability Xenon arc lamp. The lamp spectra and its irradiance are shown in the figure B.2.

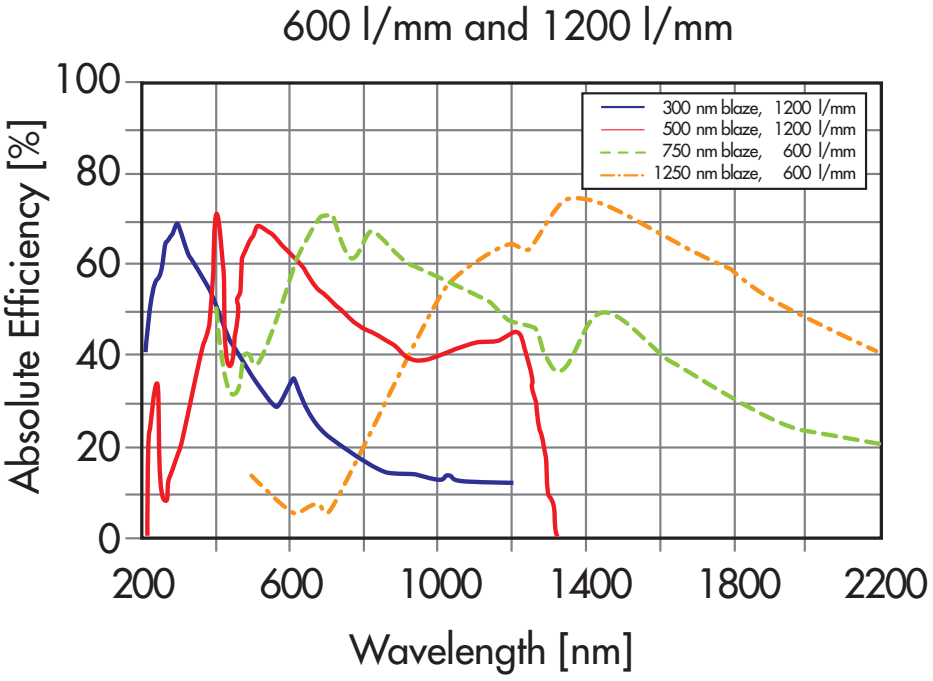

Figure B.3: *Typical efficient curves for 600 and 1200 line gratings, different blaze.Taken from LOT-ORIEL web-page*

The emitted light is reflected into a Zolix $Omni-\lambda 150$ monochromator by a concave mirror. The energy region of monochromator is from $0.6-6.8eV(180-2200nm)$. Differents gratings (blaze,pitch) have been used for the ultraviolet, visible, and near infrared part of the spectrum. The absolute efficiency for different gratings is shown in the figure B.3.

In some experiments, after to monochromator the light is interrupted by a chopper wheel to allow phase sensitive detection of d.c. contribution. Via multimode optical fiber $500\mu M$, mirror, and lenses the beam passes band filters which block the high orders of monochromator. The next lens focusses the beam on the sample in the cryostat. Between the lens and cryostat two important optical components are placed.

The Glan-Thompson polarizer which can be used in the energy range $0.5-5.5eV(225-2480nm)$(See transmission spectra figure B.4). The photo elastic modulator (Model Hinds Instruments $P100$) modulates the polarization state with a frequency of $50kHz$ as described in the section 3.2.1. The sample is placed in Janis Research closed cycle refrigerator (CCR) system(Model $CCS-3505$), which reach temperatures between $10-325K$. The head of cryostat is placed between electromagnet(Lakeshore $HV-04$) poles, which providing magnetic fields up $3.0T$. Magnet is driven by a bipolar power supply which can be modulated up to $0.2Hz$ with $70A$.

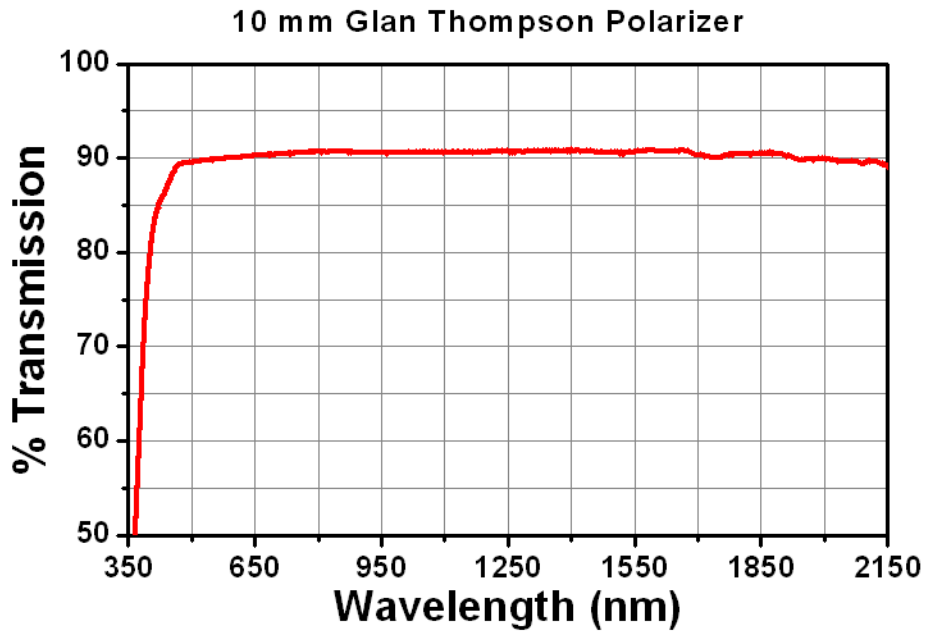

Figure B.4: *Typical transmission of the calcite Glan-Thompson polarizer . Taken from Thorlabs web-page*

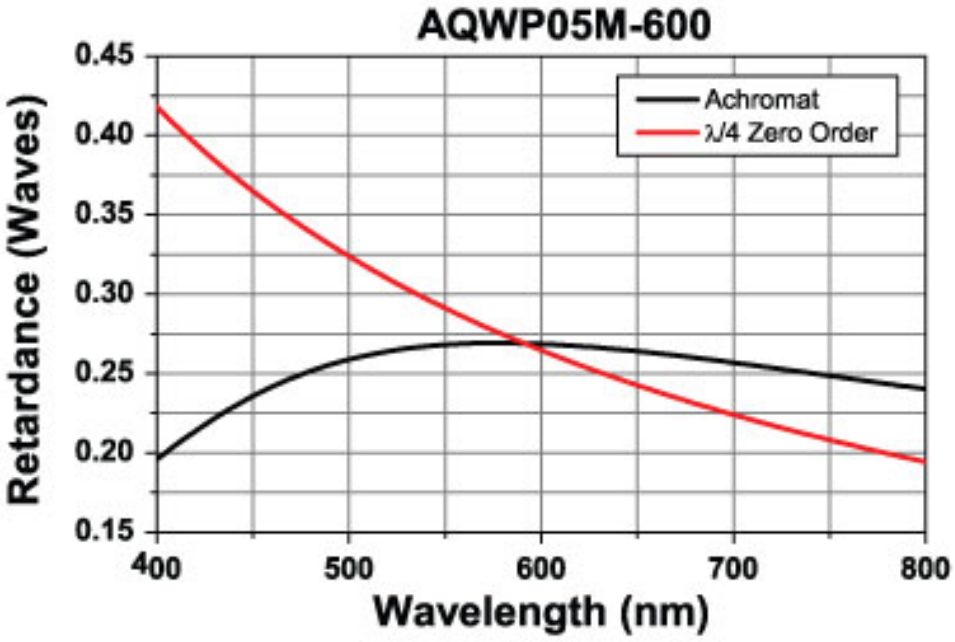

Figure B.5: *Comparation of the retardance of an achromatic quarter wave plate vs zero-order achromatic wave plates* $600nm$ *. Taken from Thorlabs web-page*

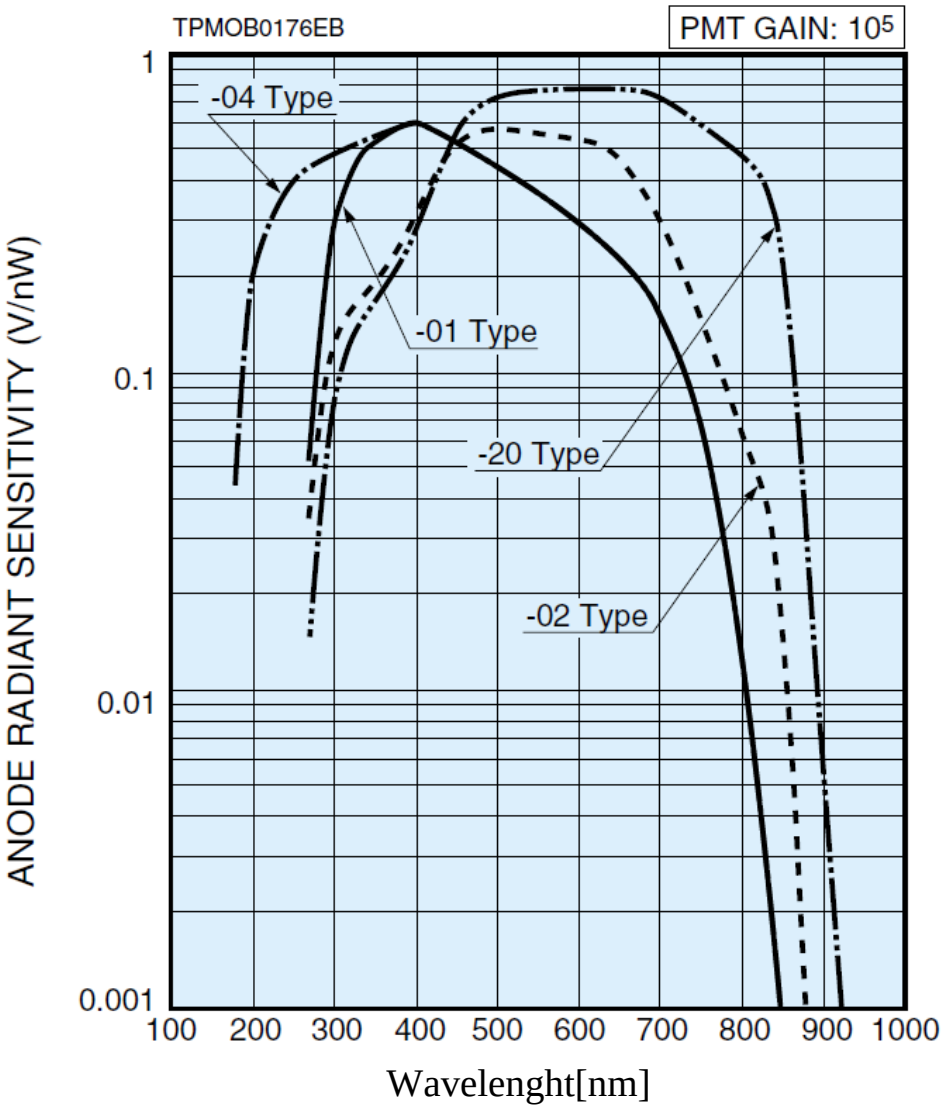

Figure B.6: *Spectral response of photomultiplier. Taken from Hamamatsu web-page*

For spectral measurement the compensator used is a achromatic wave plate,the energy region of the compensator is from $1.55 - 3.1eV(400 - 800nm)$. The figure B.5 shows the retardance of the achromatic quarter wave plate vs zero-order achromatic wave plates $600nm$. The analyzer is a Glan-Thompson prism of the same type as the polarizer.

The reflected light is detected by an Hamamatsu extremely high sensitivity and fast response photomultiplier tube (PMT-H9656-04). The sensitivity of the photomultiplier is shown in the figure B.6. The signal from the detector is split into three components: I_0, I_ω, and $I_2\omega$. A multimeter ($DMM191$ Keithley) is used to measure I_0, and two lock-in amplifiers dual phase lock-in are used to measure I_ω, and $I_2\omega$. Furthermore, a Lakeshore 325 is used as temperature controller and a Lakeshore $455 - DSP$ gaussmeter

drive a transverse Hall probe to measure real time magnetic field. All the control and meters devices are interfaced to the computer via either GPIB, USB, or RS232. Complete automatic control is performed using a home made CVI Labwindows program.

APPENDIX C

Null ellipsometry

The null ellipsometry was the basis of the first ellipsometry instrument, developed originally by Drude. Usually the system consist on Polarizer - Compensator - Sample - Analyzer (PCSA). In this method, the polarizer and the analyzer are rotated so that the detected light intensity becomes zero, and (ψ, Δ) values are estimated from the rotation angles of the polarizer and analyzer. Thus, if we judge light intensity by human eye, measurement can be performed without using electrical equipment. This is the reason why Drude was able to construct the ellipsometer more than 100 years ago.

Recently, a new method for null ellipsometer with phase modulation was developed by Postava *et al.* [120]. The phase modulation adds a good signal-to-noise ratio, high sensitivity, and linearity near null positions to the traditional high-precision nulling system. The ellipsometric angles ψ and Δ are obtained by azimuth measurement of the analyzer and the polarizer-PEM system, for which the first and second harmonics of modulator frequency cross the zeros.

Postava *et al.* [120] showed the the ellipsometric angles ψ, and Δ are directly related to the azimuth angles of polarizer and analyzer, which can be obtained by nulling of signals at second- and first-harmonic frequency of the modulator, respectively.

The null ellipsometric system (PMSCA) is shown in the figure C.1. The system consists of the polarizer, which is mechanically connected to the modulator (PEM) and rotated by 45° from the modulator axis. Both components can slowly rotate and their azimuth angle P can be precisely monitored during the rotation. Note that P denotes the azimuth of the modulator optical axis.

As describe in the section 3.2.2, the intensities are given by:

$$I_0 = \left[1 + \cos 2A \cos\phi + (1 - \cos 2A \cos\phi) \tan^2\psi\right] /2 \qquad \text{C.1}$$

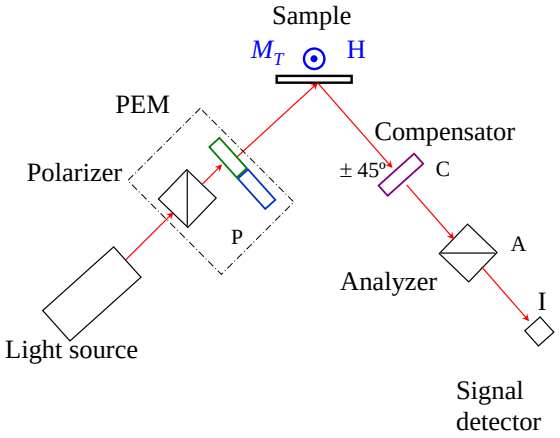

Figure C.1: *Null ellipsometry system for transverse Kerr effect measurement*

$$I_s = \tan\psi\,(\sin 2A \sin\Delta \pm \sin\phi \cos 2A \cos\Delta) \tag{C.2}$$

$$I_c = -\sin 2P\left[1 + \cos 2A\cos\phi - (1 - \cos 2A\cos\phi)\tan^2\psi\right]/2+ \tag{C.3}$$
$$+\cos 2P \tan\psi(\sin 2A\cos\Delta \pm \sin\phi\cos 2A\cos\Delta)$$

The main idea of the proposed ellipsometric method is to search for nulls of the first I_ω and the second harmonic $I_{2\omega}$ signal. the first and second harmonic frequency of the modulator are proportional to:

$$I_\omega \propto (I_S\cos\varphi_0 - I_C\sin\varphi_0) \tag{C.4}$$
$$I_2\omega \propto (I_S\sin\varphi_0 - I_C\cos\varphi_0) \tag{C.5}$$

Consequently, the signals I_ω and $I_{2\omega}$ cross simultaneously the zeros for $I_S = 0$ and $I_C = 0$. In the case of ideal modulators ($\varphi_0 = 0$) $I_\omega \propto I_S$ and $I_2\omega \propto I_C$, whereas for real modulator ($\varphi_0 \neq 0$) a coupling between I_S and I_C arises.

The condition $I_S = 0$, which relates mainly to null of I_ω signal, can be adjusted by rotation of the analyzer (see C.3). The analyzer azimuth angle A directly relates to Δ by:

$$\tan\Delta = \pm\frac{\sin\phi}{\tan 2A} = \sin\phi\tan\left(\pm\left(2A \pm \pi/2\right)\right) \tag{C.6}$$

where the first sign is related to the azimuth of compensator $C = \pm 45°$ and the

second sign in the term $(2A \pm \pi/2)$ corresponds to the periodicity of the function tangents. Similarly, the condition $I_C = 0$, which relates mainly to the null of $I_2\omega$ signal, can be adjusted by rotation of the polarizer-PEM system (see C.3). The azimuth angle P directly relates to ψ by equations:

$$\tan\psi = \pm\alpha_- \mp \tan P, \tan\psi = \pm\alpha_- \mp \tan(P - \pi/2), for C = +45^\circ \quad \text{C.7}$$

$$\tan\psi = \pm\alpha_- \pm \tan P, \tan\psi = \pm\alpha_- \pm \tan(P - \pi/2), for C = -45^\circ \quad \text{C.8}$$

C.9

and α is given by:

$$\alpha_\pm = \frac{\sqrt{1 - \cos^2\phi\cos^2\Delta} \pm \cos\phi\sin\Delta}{\sin\phi} \quad \text{C.10}$$

where $\alpha_+\alpha_- = 1$, and $\alpha_p m(90^\circ) = 1$, and the formula $\tan 2P = 2\tan P/(1 - \tan^2 P)$ and equation C.6 were used. Two solutions and the signs in equation C.9 correspond to the periodicity of the functions $\tan 2A$ and $\tan 2P$. Different signs in equation C.6 and C.9 correspond to different zones,i.e.,different azimuth angles P,A, for which the null intensity is obtained. The table C.1 summarizes the different zones obtained by the null ellipsometer with phase modulation in the case of ideal compensator ($\psi = 90^\circ$).

Zone	C	$A(I_\omega = 0)$	$P(I_{2\omega} = 0)$	Δ	ψ
1	$+45^\circ$	$\Delta/2 + \pi/4$	ψ	$2A - \pi/2$	P
2	$+45^\circ$	$\Delta/2 + \pi/4$	$\psi + \pi/2$	$2A - \pi/2$	$P - \pi/2$
3	$+45^\circ$	$\Delta/2 - \pi/4$	$-\psi$	$2A + \pi/2$	$-P$
4	$+45^\circ$	$\Delta/2 - \pi/4$	$-\psi + \pi/2$	$2A + \pi/2$	$-P + \pi/2$
5	-45°	$-\Delta/2 + \pi/4$	ψ	$-2A - \pi/2$	P
6	-45°	$-\Delta/2 + \pi/4$	$\psi + \pi/2$	$-2A - \pi/2$	$P - \pi/2$
7	-45°	$-\Delta/2 - \pi/4$	$-\psi$	$-2A + \pi/2$	$-P$
8	-45°	$-\Delta/2 - \pi/4$	$-\psi + \pi/2$	$-2A + \pi/2$	$-P + \pi/2$

Table C.1: *Null zones*

APPENDIX D

Optical Response

Optical response can be expressed using several physical magnitudes. viz. Optical conductivity, reflectivity, dielectric constant-known as relative permittivity (real and imaginary part), imaginary part of the inverse dielectric constant, complex refractive index, (real index, extinction coefficient),and absorption coefficient. Lets consider each one of them separately starting with the basic concepts:

DC Electrical Conductivity

According with Drude model the Ohm law is:

$$E = \rho j \tag{D.1}$$

where E is the Electric field, ρ is the resistivity and j is the current density. Hence the current density can be write in terms of DC electrical conductivity σ as follow:

$$j = \sigma E \tag{D.2}$$

The electrical conductivity σ is obtained by:

$$\sigma = \frac{ne^2\tau}{m} \tag{D.3}$$

where n is the electron densities, e, m are the electron charge and mass, respectively, and τ is the relaxation time. Some times it is write as the damping constant: $\gamma_0 = \frac{1}{\tau_0}$.

AC Electrical Conductivity

In order to describes the AC conductivity, the Drude model include a frictional damping term in the equation of motion. Then the equation of motion for the momentum $P(t)$ per electron becomes:

$$\frac{dp(t)}{dt}\frac{-p(t)}{\tau} - eE(t) \tag{D.4}$$

where lets consider time-dependent electric field $E(t)$ in the form:

$$E(t) = Re\left(E\left(\omega\right)e^{-i\omega t}\right) \tag{D.5}$$

The momentum:

$$p(t) = Re\left(p\left(\omega\right)e^{-i\omega t}\right) \tag{D.6}$$

the current density is:

$$j(t) = Re\left(j\left(\omega\right)e^{-i\omega t}\right) \tag{D.7}$$

using:

$$j\left(t\right) = -\frac{ne}{m}p\left(t\right) \tag{D.8}$$

and substituting the complex $p(t)$ and $E(t)$ into the equation of motion is obtained:

$$j(\omega) = \frac{ne^2}{m(\frac{1}{\tau} - i\omega)}E(\omega) \tag{D.9}$$

it can be write this results as:

$$j(\omega) = \sigma(\omega)E(\omega) \tag{D.10}$$

where $\sigma(\omega)$ the frequency-dependent or AC conductivity is given by:

$$\sigma(\omega) = \frac{\sigma_0}{1 - i\omega\tau}, \sigma_0 = \frac{ne^2\tau}{m} \tag{D.11}$$

Dielectric Constant

In the present of a the specific current density j the Maxwell equations are:

$$\nabla \cdot E = 0; \nabla \cdot H = 0; \nabla \times E = -\frac{1}{c}\frac{\partial H}{\partial t}\nabla \times H = -\frac{4\pi}{c}j + \frac{1}{c}\frac{\partial E}{\partial t} \tag{D.12}$$

writing j in terms of E, we then find:

$$-\nabla^2 E = \frac{\omega^2}{c^2}\left(1 + \frac{4\pi i\sigma(\omega)}{\omega}\right)E \tag{D.13}$$

This has the form of the usual wave equation;

$$-\nabla^2 E = \frac{\omega^2}{c^2}\epsilon(\omega)E \tag{D.14}$$

with a complex dielectric constant given by:

$$\epsilon(\omega) = 1 + \frac{4\pi i\sigma(\omega)}{\omega} \tag{D.15}$$

Substituting the conductivity term we found:

$$\epsilon(\omega) = 1 - \frac{\omega_p^2}{\omega(\omega - i\gamma_0)} \tag{D.16}$$

The first approximation at high frequencies $\omega\tau \gg 1$ give

$$\epsilon(\omega) = 1 + \frac{\omega_p^2}{\omega^2} \tag{D.17}$$

where ω_p is known as the plasma frequency, is given by:

$$\omega_p^2 = \frac{4\pi ne^2}{m} \tag{D.18}$$

Convention

The dielectric constant $\epsilon(\omega)$ and optical conductivity $\sigma(\omega)$ enter into a determination of the optical properties of a solid only in the combination:

$$\tilde{\epsilon}(\omega) = \epsilon_1(\omega) + i\frac{4\pi\sigma'(\omega)}{\omega} \tag{D.19}$$

Where $\epsilon_1(\omega)$ is the real part of the dielectric constant and $\sigma'(\omega)$ is the real part of the optical conductivity. This convention enables the optical theories of the metals to use the same notation as is used for insulators.

Refractive index

It's defined as complex refractive index $\tilde{n}(\omega) = n + ik$, where n is known as the refractive index and k the extinction coefficient. Using

$$\tilde{\epsilon}(\omega) = \tilde{n}^2(\omega) \tag{D.20}$$

we found:

$$\tilde{\epsilon}(\omega) = \epsilon_1 + i\epsilon_2 = \tilde{n}^2(\omega) \tag{D.21}$$

then the real part $\epsilon_1(\omega)$ of dielectric function is given by:

$$\epsilon_1(\omega) = n^2 - k^2 \tag{D.22}$$

and the imaginary part $\epsilon_2(\omega)$ is given by:

$$\epsilon_2(\omega) = \frac{4\pi\sigma'(\omega)}{\omega} = 2nk \tag{D.23}$$

Conversion between refractive index and dielectric constant is done by:

$$n = \sqrt{\frac{\sqrt{\epsilon_1^2 + \epsilon_2^2 2} + \epsilon_1}{2}}; k = \sqrt{\frac{\sqrt{\epsilon_1^2 + \epsilon_2^2 2} - \epsilon_1}{2}} \tag{D.24}$$

Optical conductivity

It can be straightforwardly derived from the general relationship:

$$\sigma(\omega) = \frac{\sigma_0}{1 - i\omega\tau} \tag{D.25}$$

and connects with plasma frequency as follow:

$$\sigma(\omega) = -i\frac{\omega_p^2}{4\pi(\omega - i\gamma_0)} \tag{D.26}$$

it can be write as:

$$\sigma(\omega) = \sigma'(\omega) + i\sigma''(\omega) \tag{D.27}$$

where the real part $\sigma'(\omega)$ is given by:

$$\sigma'(\omega) = \frac{\omega_p^2\gamma_0}{4\pi(\omega^2 + \gamma_0^2)} \tag{D.28}$$

and the imaginary part $\sigma''(\omega)$ is given by:

$$\sigma''(\omega) = -i\frac{\omega_p^2\omega}{4\pi(\omega^2 + \gamma_0^2)} \tag{D.29}$$

Absorption coefficient

The absorption coefficient $\alpha(\omega)$ is related to the extinction coefficient via:

$$\alpha(\omega) = \frac{2\omega k(\omega)}{c} \tag{D.30}$$

The skin depth $\delta(\omega)$ is calculated by taking the inverse of the absorption coefficient:

$$\delta(\omega) = \frac{1}{\alpha(\omega)} \tag{D.31}$$

Reflectivity

In ideal conditions a plane wave is normally incident from vacuum on a medium with dielectric constant $\tilde{\epsilon}(\omega)$ the fraction r of the power reflected (reflectivity) is given by:

$$r(\omega) = \frac{|E^r|^2}{|Ei|^2} = \left|\frac{1-\tilde{n}(\omega)}{1+\tilde{n}(\omega)}\right|^2 = \frac{(1-n)^2+k^2}{(1+n)^2+k^2} \tag{D.32}$$

Polarization and ellipsometry constants

Lets consider a polarized beam parallel $E \parallel$ named "p" and perpendicular $E \perp$ named "s" to the plane of incident, with a incidence angle θ, the Fresnel equations give us:

$$\tilde{r}_p = \frac{E_p^r}{E_p^i} = \frac{\tilde{n}^2 cos\theta - \sqrt{\tilde{n}^2 - sin^2\theta}}{\tilde{n}^2 cos\theta + \sqrt{\tilde{n}^2 - sin^2\theta}}; \tilde{r}_s = \frac{E_s^r}{E_s^i} = \frac{cos\theta - \sqrt{\tilde{n}^2 - sin^2\theta}}{cos\theta + \sqrt{\tilde{n}^2 - sin^2\theta}}; \tag{D.33}$$

The ratio of the Fresnel coefficients, ρ, is then defined as:

$$\rho = \frac{\tilde{r}_p}{\tilde{r}_s} = tan\psi e^{i\Delta} \tag{D.34}$$

where Δ appears as part of a complex phase shift in relation to ψ, which defines the magnitude of the reflectivity.

Bibliography

[1] P. Weinberger, *John kerr and his effects found in 1877 and 1878*, Philosophical Magazine Letters **88**, 897 (2008).

[2] J. Kerr, *On reflection of polarized light from the equatorial surface of a magnet*, Philosophical Magazine Series 5 **5**, 161 (1978).

[3] A. K. Zvezdin and V. A. Kotov, *Modern Magnetooptics and Magnetooptical Materials*, edited by J. M. D. C. T. College, Dublin, D. R. Tilley, and U. S. Malaysia, Studies in Condensed Matter Physics (Taylor & Francis, Institute of Physics Publishing. Bristol and Philadelphia., 1997) pp. 1–381, general Physics Institute (IOF RAN), Moscow.

[4] B. H. A. Y. Antonov, Victor., *Electronic structure and magneto-optical properties of solids* (Springer New York, 2004).

[5] A. Granovsky, Y. Sukhorukov, A. Telegin, V. Bessonov, E. Ganshina, A. Kaul, I. Korsakov, O. Gorbenko, and J. Gonzalez, *Giant magnetorefractive effect in manganite films*, Journal of Experimental and Theoretical Physics **112**, 77 (2011), 10.1134/S106377611005105X.

[6] Y. P. Sukhorukov, A. V. Telegin, A. B. Granovskii, E. A. Ganshina, S. V. Naumov, N. V. Kostromitina, L. V. Elokhina, and J. Gonzalez, *Magnetorefractive effect in lcmo in the infrared spectral range*, Journal of Experimental and Theoretical Physics **111**, 355 (2010), atoms, Molecules, Optics Physics and Astronomy.

[7] A. Granovsky, E. Ganshina, A. Yurasov, Y. Boriskina, S. Yerokhin, A. Khanikaev, M. Inoue, A. Vinogradov, and Y. Sukhorukov, *Magnetorefractive effect in nanostructures, manganites, and magnetophotonic crystals based on these materials*, Journal of Communications Technology and Electronics **52**, 1065 (2007), 10.1134/S1064226907090185.

[8] A. Yurasov, Y. Boriskina, E. Ganshina, A. Granovsky, and Y. Sukhorukov, *Magnetorefractive effect in manganites*, Physics of the Solid State **49**, 1121 (2007), 10.1134/S1063783407060170.

[9] J. Boriskina, S. Erokhin, A. Granovsky, A. Vinogradov, and M. Inoue, *Enhancement of the magnetorefractive effect in magnetophotonic crystals*, Physics of the Solid State **48**, 717 (2006), 10.1134/S1063783406040160.

[10] I. Bykov, E. Ganshina, A. Granovsky, V. Gushchin, A. Kozlov, T. Masumoto, and S. Ohnuma, *Magnetorefractive effect in granular alloys with tunneling magnetoresistance*, Physics of the Solid State **47**, 281 (2005), 10.1134/1.1866407.

[11] A. Granovsky, M. Inoue, J. Clerc, and A. Yurasov, *Magnetorefractive effect in nanocomposites: Dependence on the angle of incidence and on light polarization*, Physics of the Solid State **46**, 498 (2004), 10.1134/1.1687868.

[12] A. Granovsky, I. Bykov, E. Ganshina, V. Gushchin, M. Inoue, Y. Kalinin, A. Kozlov, and A. Yurasov, *Magnetorefractive effect in magnetic nanocomposites*, Journal of Experimental

and Theoretical Physics **96**, 1104 (2003), 10.1134/1.1591221.

[13] A. Granovsky, V. Gushchin, I. Bykov, A. Kozlov, N. Kobayashi, S. Ohnuma, T. Masumoto, and M. Inoue, *Giant magnetorefractive effect in magnetic granular cofe-mgf alloys*, Physics of the Solid State **45**, 911 (2003), 10.1134/1.1575334.

[14] I. Bykov, E. Ganshina, A. Granovsky, and V. Gushchin, *Magnetorefractive effect in granular films with tunneling magnetoresistance*, Physics of the Solid State **42**, 498 (2000), 10.1134/1.1131238.

[15] J. C. Jacquet and T. Valet, *A new magnetooptical effect discovered on magnetic multilayers: The magnetorefractive effect*, Magnetic Ultrathin Films, Multilayers and Surfaces, **1**, 447 (1995), edited by A. Fert et al . MRS Symposia Proceedings No. 348 (Materials Research Society, Pittsburgh).

[16] A. B. Granovsky and M. Inoue, *Spin-dependent tunnelling at infrared frequencies: magnetorefractive effect in magnetic nanocomposites*, Journal of Magnetism and Magnetic Materials **272-276**, E1601 (2004), proceedings of the International Conference on Magnetism (ICM 2003).

[17] S. Uran, M. Grimsditch, E. E. Fullerton, and S. D. Bader, *Infrared spectra of giant magnetoresistance fecrfe trilayers*, Phys. Rev. B **57**, 2705 (1998).

[18] J. van Driel, F. R. de Boer, R. Coehoorn, G. H. Rietjens, and E. S. J. Heuvelmans-Wijdenes, *Magnetorefractive and magnetic-linear-dichroism effect in exchange-biased spin valves*, Phys. Rev. B **61**, 15321 (2000).

[19] R. Mennicke, D. Bozec, V. Kravets, M. Vopsaroiu, J. Matthew, and S. Thompson, *Modelling the magnetorefractive effect in giant magnetoresistive granular and layered materials*, Journal of Magnetism and Magnetic Materials **303**, 92 (2006).

[20] J. T. S. Mennicke, R.T.; Matthew, *Correlation of giant magnetoresistance with infrared magnetorefractive spectra*, IEEE Transactions on Magnetics **42**, 2627 (2006).

[21] A. Yurasov, A. Granovsky, S. Tarapov, and J.-P. Clerc, *High-frequency magnetoimpedance in nanocomposites*, Journal of Magnetism and Magnetic Materials **300**, e52 (2006), the third Moscow International Symposium on Magnetism 2005.

[22] D. Bozec, V. G. Kravets, J. A. D. Matthew, S. M. Thompson, and A. F. Kravets, *Infrared reflectance and magnetorefractive effects in metal–insulator cofe-al[sub 2]o[sub 3] granular films*, Journal of Applied Physics **91**, 8795 (2002).

[23] V. G. Kravets, D. Bozec, J. A. D. Matthew, and S. M. Thompson, *Calculation of the magnetorefractive effect in giant magnetoresistive granular films*, Journal of Applied Physics **91**, 8587 (2002).

[24] V. G. Kravets, D. Bozec, J. A. D. Matthew, S. M. Thompson, H. Menard, A. B. Horn, and A. F. Kravets, *Correlation between the magnetorefractive effect, giant magnetoresistance, and optical properties of co-ag granular magnetic films*, Phys. Rev. B **65**, 054415 (2002).

[25] V. G. Kravets, L. V. Poperenko, I. V. Yurgelevych, A. M. Pogorily, and A. F. Kravets, *Optical and magneto-optical properties and magnetorefractive effect in metal-insulator granular films*, Journal of Applied Physics **98**, 043705 (2005).

[26] V. Kravets, *Effect of magnetic field on the ir optical properties of dielectrics*, Optics and Spectroscopy **100**, 869 (2006), 10.1134/S0030400X06060105.

[27] V. Kravets, *Comparison of magnetoreflection from cofe; multilayer and granular films in the infrared spectral region*, Optics and Spectroscopy **102**, 717 (2007), 10.1134/S0030400X07050116.

[28] V. Kravets and L. Poperenko, *Specific features of the magnetoreflection of co-based amorphous ribbons in the ir region*, Optics and Spectroscopy **104**, 890 (2008), 10.1134/S0030400X08060155.

[29] M. Imada, A. Fujimori, and Y. Tokura, *Metal-insulator transitions*, Rev. Mod. Phys. **70**, 1039 (1998).

[30] Y. Okimoto and Y. Tokura, *Optical spectroscopy of perovskite-type manganites*, Journal of Superconductivity **13**, 271 (2000), 10.1023/A:1007708218202.

[31] E. Dagotto, *Nanoscale Phase Separation and Colossal Magnetoresistance*, edited by E. Dagotto (Springer Series in Solid-State Sciences, Berlin, 2002).

[32] J. Garcia and G. Subías, *The verwey transitiona new perspective*, Journal of Physics: Condensed Matter **16**, R145 (2004).

[33] J. M. D. Coey, M. Viret, and S. von Molnar, *Mixed-valence manganites*, Advances in Physics **48**, 167 (1999).

[34] E. Dagotto, T. Hotta, and A. Moreo, *Colossal magnetoresistant materials: the key role of phase separation*, Physics Reports **344**, 1 (2001).

[35] M. B. Salamon and M. Jaime, *The physics of manganites: Structure and transport*, Rev. Mod. Phys. **73**, 583 (2001).

[36] D. M. Edwards, *Ferromagnetism and electron-phonon coupling in the manganites*, Advances in Physics **51**, 1259 (2002).

[37] B. Martinez, J. Fontcuberta, A. Seffar, J. L. Garca-Munoz, S. Pinol, and X. Obradors, *Spin-disorder scattering and localization in magnetoresistive perovskites*, Phys. Rev. B **54**, 10001 (1996).

[38] J. Fontcuberta, B. Martinez, A. Seffar, S. Pinol, J. L. Garcia-Munoz, and X. Obradors, *Colossal magnetoresistance of ferromagnetic manganites: Structural tuning and mechanisms*, Phys. Rev. Lett. **76**, 1122 (1996).

[39] V. Laukhin, J. Fontcuberta, J. L. Garcia-Munoz, and X. Obradors, *Pressure effects on the metal-insulator transition in magnetoresistive manganese perovskites*, Phys. Rev. B **56**, R10009 (1997).

[40] J. L. Garcia-Munoz, J. Fontcuberta, B. Martinez, A. Seffar, S. Pinol, and X. Obradors, *Magnetic frustration in mixed valence manganites*, Phys. Rev. B **55**, R668 (1997).

[41] J. L. Garcia-Munoz, M. Suaaidi, J. Fontcuberta, and J. Rodrguez-Carvajal, *Reduction of the jahn-teller distortion at the insulator-to-metal transitionin mixed valence manganites*, Phys. Rev. B **55**, 34 (1997).

[42] L. Balcells, J. Fontcuberta, B. Martinez, and X. Obradors, *High-field magnetoresistance at interfaces in manganese perovskites*, Phys. Rev. B **58**, R14697 (1998).

[43] R. Senis, V. Laukhin, B. Martinez, J. Fontcuberta, X. Obradors, A. A. Arsenov, and Y. M. Mukovskii, *Pressure and magnetic-field effects on charge ordering in lcmo*, Phys. Rev. B **57**, 14680 (1998).

[44] J. Fontcuberta, V. Laukhin, and X. Obradors, *Bandwidth dependence of the charge-order and curie temperatures in manganese perovskites*, Phys. Rev. B **60**, 6266 (1999).

[45] V. Skumryev, J. Nogues, J. S. Munoz, B. Martinez, R. Senis, J. Fontcuberta, L. Pinsard, A. Revcolevschi, and Y. M. Mukovskii, *Anomalous anisotropic ac susceptibility response of: Relevance to phase separation*, Phys. Rev. B **62**, 3879 (2000).

[46] B. Martinez, R. Senis, L. Balcells, V. Laukhin, J. Fontcuberta, L. Pinsard, and A. Revcolevschi, *Stability under pressure and magnetic field of the ferromagnetic-insulating*

phase in lightly doped crystals, Phys. Rev. B **61**, 8643 (2000).

[47] M. Bibes, L. Balcells, S. Valencia, S. Sena, B. Martinez, J. Fontcuberta, S. Nadolski, M. Wojcik, and E. Jedryka, *Thickness dependence of surface roughness and transport properties of lcmo epitaxial thin films*, Journal of Applied Physics **89**, 6686 (2001).

[48] M. Bibes, L. Balcells, S. Valencia, J. Fontcuberta, M. Wojcik, E. Jedryka, and S. Nadolski, *Nanoscale multiphase separation at lcmo interfaces*, Phys. Rev. Lett. **87**, 067210 (2001).

[49] J. Nogues, V. Skumryev, J. S. Munoz, B. Martinez, J. Fontcuberta, L. Pinsard, and A. Revcolevschi, *Paramagnetic behavior and correlation between high- and low-temperature structural and magnetic transitions in single-crystal perovskites*, Phys. Rev. B **64**, 024434 (2001).

[50] V. Laukhin, B. Martinez, J. Fontcuberta, and Y. M. Mukovskii, *Pressure effects on the structural phase transition in single crystals*, Phys. Rev. B **63**, 214417 (2001).

[51] M. Bibes, S. Valencia, L. Balcells, B. Martinez, J. Fontcuberta, M. Wojcik, S. Nadolski, and E. Jedryka, *Charge trapping in optimally doped epitaxial manganite thin films*, Phys. Rev. B **66**, 134416 (2002).

[52] M. Bibes, V. Laukhin, S. Valencia, B. Martínez, J. Fontcuberta, O. Y. Gorbenko, A. R. Kaul, and J. L. Martínez, *Anisotropic magnetoresistance and anomalous hall effect in manganite thin films*, Journal of Physics: Condensed Matter **17**, 2733 (2005).

[53] I. C. Infante, F. Sanchez, J. Fontcuberta, M. Wojcik, E. Jedryka, S. Estrade, F. Peiro, J. Arbiol, V. Laukhin, and J. P. Espinos, *Elastic and orbital effects on thickness-dependent properties of manganite thin films*, Phys. Rev. B **76**, 224415 (2007).

[54] M. Gajek, M. Bibes, F. Wyczisk, M. Varela, J. Fontcuberta, and A. Barthelemy, *Growth and magnetic properties of multiferroic lcbmo thin films*, Phys. Rev. B **75**, 174417 (2007).

[55] M. Bibes, *Creixement i estudi de capes primes de manganites de valencia mixta*, Ph.D. thesis, Instituto de Ciencia de Materiales de Barcelona - Concejo Superior de Investigaciones Cientificas (ICMAB-CSIC) Universidad Automoma de Barcelona Institut National des Sciences Appliquees de Toulouse (2001).

[56] G. C. Herranz, *Growth mechanisms and functionalities of epitaxial metalic ferromagnetic oxide thin films*, Ph.D. thesis, Universitat de Barcelona (2004).

[57] I. C. Infante, *(001) and (110) LCMO epitaxial ferromagnetic electrodes: a comparative study*, Ph.D. thesis, Instituto de Ciencia de Materiales de Barcelona - Concejo Superior de Investigaciones Cientificas (ICMAB-CSIC) Universidad Automoma de Barcelona (2008).

[58] R. X. Marti, *Growth and characterization of magnetoelectric YMnO3 epitaxial thin films*, Ph.D. thesis, Instituto de Ciencia de Materiales de Barcelona - Concejo Superior de Investigaciones Cientificas (ICMAB-CSIC) Universidad Automoma de Barcelona (2009).

[59] C. Zener, *Interaction between the d shells in the transition metals*, Phys. Rev. **81**, 440 (1951).

[60] C. Zener, *Interaction between the d-shells in the transition metals. ii. ferromagnetic compounds of manganese with perovskite structure*, Phys. Rev. **82**, 403 (1951).

[61] A. J. Millis, P. B. Littlewood, and B. I. Shraiman, *Double exchange alone does not explain the resistivity of*, Phys. Rev. Lett. **74**, 5144 (1995).

[62] A. J. Millis, R. Mueller, and B. I. Shraiman, *Fermi-liquid-to-polaron crossover. i. general results*, Phys. Rev. B **54**, 5389 (1996).

[63] A. J. Millis, R. Mueller, and B. I. Shraiman, *Fermi-liquid-to-polaron crossover. ii. double exchange and the physics of colossal magnetoresistance*, Phys. Rev. B **54**, 5405 (1996).

[64] A. J. Millis, B. I. Shraiman, and R. Mueller, *Dynamic jahn-teller effect and colossal magnetoresistance in*, Phys. Rev. Lett. **77**, 175 (1996).

[65] A. J. Millis, *Lattice effects in magnetoresistive manganese perovskites*, Nature **392**, 147 (1998).

[66] A. J. Millis, T. Darling, and A. Migliori, *Quantifying strain dependence in colossal magnetoresistance manganites*, Journal of Applied Physics **83**, 1588 (1998).

[67] A. Urushibara, Y. Moritomo, T. Arima, A. Asamitsu, G. Kido, and Y. Tokura, *Insulator-metal transition and giant magnetoresistance in lsmo*, Phys. Rev. B **51**, 14103 (1995).

[68] Y. Sun, X. Xu, and Y. Zhang, *Variable-range hopping of small polarons in mixed-valence manganites*, Journal of Physics: Condensed Matter **12**, 10475 (2000).

[69] J. M. D. Coey, M. Viret, L. Ranno, and K. Ounadjela, *Electron localization in mixed-valence manganites*, Phys. Rev. Lett. **75**, 3910 (1995).

[70] D. Louca, T. Egami, E. L. Brosha, H. Roder, and A. R. Bishop, *Local jahn-teller distortion in observed by pulsed neutron diffraction*, Phys. Rev. B **56**, R8475 (1997).

[71] S. J. L. Billinge, R. G. DiFrancesco, G. H. Kwei, J. J. Neumeier, and J. D. Thompson, *Direct observation of lattice polaron formation in the local structure of*, Phys. Rev. Lett. **77**, 715 (1996).

[72] T. A. Tyson, J. M. de Leon, S. D. Conradson, A. R. Bishop, J. J. Neumeier, H. Roder, and J. Zang, *Evidence for a local lattice distortion in ca-doped lmo*, Phys. Rev. B **53**, 13985 (1996).

[73] S. G. Kaplan, M. Quijada, H. D. Drew, D. B. Tanner, G. C. Xiong, R. Ramesh, C. Kwon, and T. Venkatesan, *Optical evidence for the dynamic jahn-teller effect in ndsrmno*, Phys. Rev. Lett. **77**, 2081 (1996).

[74] M. Quijada, J. Cerne, J. R. Simpson, H. D. Drew, K. H. Ahn, A. J. Millis, R. Shreekala, R. Ramesh, M. Rajeswari, and T. Venkatesan, *Optical conductivity of manganites: Crossover from jahn-teller small polaron to coherent transport in the ferromagnetic state*, Phys. Rev. B **58**, 16093 (1998).

[75] J. H. Jung, K. H. Kim, D. J. Eom, T. W. Noh, E. J. Choi, J. Yu, Y. S. Kwon, and Y. Chung, *Determination of electronic band structures of using optical-conductivity analyses*, Phys. Rev. B **55**, 15489 (1997).

[76] J. H. Jung, K. H. Kim, T. W. Noh, E. J. Choi, and J. Yu, *Midgap states of doping-dependent optical-conductivity studies*, Phys. Rev. B **57**, R11043 (1998).

[77] Y. Okimoto, T. Katsufuji, T. Ishikawa, A. Urushibara, T. Arima, and Y. Tokura, *Anomalous variation of optical spectra with spin polarization in double-exchange ferromagnet: Lsmo*, Phys. Rev. Lett. **75**, 109 (1995).

[78] S. Cooper, *Optical spectroscopic studies of metal-insulator transitions in perovskite-related oxides*, in *Localized to Itinerant Electronic Transition in Perovskite Oxides*, Structure lamp, Bonding, Vol. 98, edited by J. Goodenough (Springer Berlin Heidelberg, 2001) pp. 161–219.

[79] A. S. Moskvin, A. A. Makhnev, L. V. Nomerovannaya, N. N. Loshkareva, and A. M. Balbashov, *Interplay of $p-d$ and $d-d$ charge transfer transitions in rare-earth perovskite manganites*, Phys. Rev. B **82**, 035106 (2010).

[80] T. Arima and Y.Tokura, *Optical study of electronic structure in perovskite-type rmo3 (r=la, y; sc, ti, v, cr, mn, fe, co, ni, cu)*, Journal of the Physical Society of Japan **64**, 2488 (1995).

[81] Y. Okimoto, T. Katsufuji, T. Ishikawa, T. Arima, and Y. Tokura, *Variation of electronic structure in as investigated by optical conductivity spectra*, Phys. Rev. B **55**, 4206 (1997).

[82] K. Takenaka, K. Iida, Y. Sawaki, S. Sugai, Y. Moritomo, and A. Nakamura, *Optical reflectivity spectra measured on cleaved surfaces of lsmo evidence against extremely small drude weight*, Journal of the Physical Society of Japan **68**, 1828 (1999).

[83] Y. G. Zhao, J. J. Li, R. Shreekala, H. D. Drew, C. L. Chen, W. L. Cao, C. H. Lee, M. Rajeswari, S. B. Ogale, R. Ramesh, G. Baskaran, and T. Venkatesan, *Ultrafast laser induced conductive and resistive transients in lcmo charge transfer and relaxation dynamics*, Phys. Rev. Lett. **81**, 1310 (1998).

[84] Z. Zhang and S. Satpathy, *Electron states, magnetism, and the verwey transition in magnetite*, Phys. Rev. B **44**, 13319 (1991).

[85] E. Verwey and P. Haayman, *Electronic conductivity and transition point of magnetite*, Physica **8**, 979 (1941).

[86] E. J. W. Verwey and E. L. Heilmann, *Physical properties and cation arrangement of oxides with spinel structures i. cation arrangement in spinels*, The Journal of Chemical Physics **15**, 174 (1947).

[87] F. Walz, *The verwey transition - a topical review*, Journal of Physics: Condensed Matter **14**, R285 (2002).

[88] P. Piekarz, K. Parlinski, and O. acute, *Origin of the verwey transition in magnetite: Group theory, electronic structure, and lattice dynamics study*, Phys. Rev. B **76**, 165124 (2007).

[89] R. Ramos, *Anisotropic magnetotransport properties of epitaxial magnetite thin films*, Ph.D. thesis, Trinity College Dublin (2009).

[90] V. V. Shchennikov and S. V. Ovsyannikov, *Is the verwey transition in magnetite driven by a peierls distortion?*, Journal of Physics: Condensed Matter **21**, 271001 (2009).

[91] M. S. Senn, J. P. Wright, and J. P. Attfield, *Charge order and three-site distortions in the verwey structure of magnetite*, Nature **481**, 173 (2012).

[92] J. P. Attfield, *Condensed-matter physics: A fresh twist on shrinking materials*, Nature **480**, 465 (2011).

[93] E. J. W. Verwey, *Electronic conduction in magnetite and its transition point at low temperatures*, Nature **144**, 327 (1939).

[94] G. K. Rozenberg, M. P. Pasternak, W. M. Xu, Y. Amiel, M. Hanfland, M. Amboage, R. D. Taylor, and R. Jeanloz, *Origin of the verwey transition in magnetite*, Phys. Rev. Lett. **96**, 045705 (2006).

[95] W. Eerenstein, T. T. M. Palstra, T. Hibma, and S. Celotto, *Origin of the increased resistivity in epitaxial films*, Phys. Rev. B **66**, 201101 (2002).

[96] D. Ihle and B. Lorenz, *Small-polaron conduction and short-range order in magnetite*, Journal of Physics C: Solid State Physics **19**, 5239 (1986).

[97] P. Piekarz, K. Parlinski, and A. M. Oleifmmode, *Mechanism of the verwey transition in magnetite*, Phys. Rev. Lett. **97**, 156402 (2006).

[98] S. M. Shapiro, M. Iizumi, and G. Shirane, *Neutron scattering study of the diffuse critical scattering associated with the verwey transition in magnetite*, Phys. Rev. B **14**, 200 (1976).

[99] Y. Yamada, N. Wakabayashi, and R. M. Nicklow, *Neutron diffuse scattering in magnetite due to molecular polarons*, Phys. Rev. B **21**, 4642 (1980).

[100] W. F. J. Fontijn, *Magneto-optical spectroscopy of spinel type ferrites in bulk materials and layered structures*, Ph.D. thesis, Technische Universiteit Eindhoven (1998).

[101] S. Wittekoek, T. J. A. Popma, J. M. Robertson, and P. F. Bongers, *Magneto-optic spectra and the dielectric tensor elements of bismuth-substituted iron garnets at photon energies*

between 2.2-5.2 ev, Phys. Rev. B **12**, 2777 (1975).

[102] W. F. J. Fontijn, P. J. van der Zaag, M. A. C. Devillers, V. A. M. Brabers, and R. Metselaar, *Optical and magneto-optical polar kerr spectra of magnetite*, Phys. Rev. B **56**, 5432 (1997).

[103] R. Azzam and N. M. Bashara, *Ellipsometry and polarized light* (Notrh-Holland publishing Company Amsterdam, 1977).

[104] J. M. Florczak and E. D. Dahlberg, *Detecting two magnetization components by the magneto-optical kerr effect*, Journal of Applied Physics **67**, 7520 (1990).

[105] J. M. Florczak and E. D. Dahlberg, *Magnetization reversal in (100) fe thin films*, Phys. Rev. B **44**, 9338 (1991).

[106] T. C. Oakberg, *Magneto-optic kerr effect*, HINDS Instruments **1**, 1 (2005).

[107] S. N. Jasperson and S. E. Schnatterly, *An improved method for high reflectivity ellipsometry based on a new polarization modulation technique*, Review of Scientific Instruments **40**, 761 (1969).

[108] J. C. Kemp, *Piezo-optical birefringence modulators: New use for a long-known effect*, J. Opt. Soc. Am. **59**, 950 (1969).

[109] K. W. Hipps and G. A. Crosby, *Applications of the photoelastic modulator to polarization spectroscopy*, The Journal of Physical Chemistry **83**, 555 (1979), http://pubs.acs.org/doi/pdf/10.1021/j100468a001 .

[110] K. Sato, *Measurement of magneto-optical kerr effect using piezo-birefringent modulator*, Japanese Journal of Applied Physics **20**, 2403 (1981).

[111] J. C. Kemp, *Polarized light and its interaction with modulating devices: a methodology review*, Hinds Instruments **1**, 1 (1987).

[112] D. Yang, J. C. Canit, and E. Gaignebet, *Photoelastic modulator: polarization modulation and phase modulation*, Journal of Optics **26**, 151 (1995).

[113] G. A. Osborne, J. C. Cheng, and P. J. Stephens, *A near-infrared circular dichroism and magnetic circular dichroism instrument*, Review of Scientific Instruments **44**, 10 (1973).

[114] K. Sato, *Reflectance magneto-circular dichroism of cdcr2se*, Journal of the Physical Society of Japan **43**, 719 (1977).

[115] S. M. Jordan and J. S. S. Whiting, *Detecting two components of magnetization in magnetic layer structures by use of a photoelastic modulator*, Review of Scientific Instruments **67**, 4286 (1996).

[116] R. Osgood, R. White, and B. Clemens, *Asymmetric magneto-optic response in epitaxial fe(110)mo(110) thin films*, IEEE Transactions on Magnetics **31**, 3331 (1995).

[117] R. M. Osgood, B. M. Clemens, and R. L. White, *Asymmetric magneto-optic response in anisotropic thin films*, Phys. Rev. B **55**, 8990 (1997).

[118] R. M. I. Osgood, B. M. Clemens, and R. L. White, *Second-order magneto-optic effects in anisotropic thin films (abstract)*, Journal of Applied Physics **79**, 6189 (1998).

[119] P. Vavassori, *Polarization modulation technique for magneto-optical quantitative vector magnetometry*, Applied Physics Letters **77**, 1605 (2000).

[120] K. Postava, A. Maziewski, T. Yamaguchi, R. Ossikovski, S. Visvovsky, and J. Pivstora, *Null ellipsometer with phase modulation*, Opt. Express **12**, 6040 (2004).

[121] A. Postava, K.; Maziewski, A. Stupakiewicz, A. Wawro, L. T. Baczewski, S. Visnovsky, and T. Yamaguchi, *Transverse magneto-optical kerr effect measured using phase modulation*, Journal of the European Optical Society **1**, 06017 (2006), rapid publications, vol. 1 06017.

[122] K. Postava, *Calibration magneto-optical system*, Report **1**, 1 (2003).

[123] P. Stephens, *Magnetic circular dichroism*, Annual Review of Physical Chemistry **25**, 201 (1974).

[124] W. R. Mason, *A practical guide for magnetic circular dichroism spectroscopy*, edited by Wiley (john Wiley and Sons-Intercience, 2007).

[125] H. Y. Hwang, S.-W. Cheong, P. G. Radaelli, M. Marezio, and B. Batlogg, *Lattice effects on the magnetoresistance in doped lmo*, Phys. Rev. Lett. **75**, 914 (1995).

[126] M. C. Dekker, *Phase-separated manganites: The effect of reversible elastic lattice strain on the electronic properties*, Ph.D. thesis, Fakultaat Mathematik und Naturwissenschaften der Technischen Universitat Dresden (2010).

[127] K. H. Kim, J. H. Jung, D. J. Eom, T. W. Noh, J. Yu, and E. J. Choi, *Scaling behavior of spectral weight changes in perovskite manganites plcmo*, Phys. Rev. Lett. **81**, 4983 (1998).

[128] M. C. Dekker, A. D. Rata, K. Boldyreva, S. Oswald, L. Schultz, and K. Dorr, *Colossal elastoresistance and strain-dependent magnetization of phase-separated plcmo thin films*, Phys. Rev. B **80**, 144402 (2009).

[129] S. M. Stirk, S. M. Thompson, and J. A. D. Matthew, *Emissivity - a remote sensor of giant magnetoresistance*, Applied Physics Letters **86**, 102505 (2005).

[130] Y. Okimoto, Y. Tomioka, Y. Onose, Y. Otsuka, and Y. Tokura, *Optical study of in a magnetic field: Variation of electronic structure with charge ordering and disordering phase transitions*, Phys. Rev. B **59**, 7401 (1999).

[131] J. H. Jung, H. J. Lee, T. W. Noh, Y. Moritomo, Y. J. Wang, and X. Wei, *Magnetic-field-dependent optical studies of a layered antiferromagnet psmo*, Phys. Rev. B **62**, 8634 (2000).

[132] J. Hamrle, S. Blomeier, O. Gaier, B. Hillebrands, H. Schneider, G. Jakob, K. Postava, and C. Felser, *Huge quadratic magneto-optical kerr effect and magnetization reversal in the heusler compound*, Journal of Physics D: Applied Physics **40**, 1563 (2007).

[133] J. Hamrle, S. Blomeier, O. Gaier, B. Hillebrands, H. Schneider, G. Jakob, B. Reuscher, A. Brodyanski, M. Kopnarski, K. Postava, and C. Felser, *Ion beam induced modification of exchange interaction and spin-orbit coupling in the heusler compound*, Journal of Physics D: Applied Physics **40**, 1558 (2007).

[134] J. Hamrle, S. Blomeier, O. Gaier, B. Hillebrands, H. Schneider, G. Jakob, and a. C. F. K. Postava, *Huge quadratic magneto-optical kerr effect and magnetization reversal in the heusler compound*, arXiv **1**, 1 (2007).

[135] K. Postava, D. Hrabovsky, J. Pivstora, A. R. Fert, S. Vivsnovsky, and T. Yamaguchi, *Anisotropy of quadratic magneto-optic effects in reflection*, Journal of Applied Physics **91**, 7293 (2002).

[136] K. Postava, H. Jaffres, A. Schuhl, F. N. V. Dau, M. Goiran, and A. R. Fert, *Linear and quadratic magneto-optical measurements of the spin reorientation in epitaxial fe films on mgo*, Journal of Magnetism and Magnetic Materials **172**, 199 (1997).

[137] D. Hrabovsky, J. M. Caicedo, G. Herranz, I. C. Infante, F. Sanchez, and J. Fontcuberta, *Jahn-teller contribution to the magneto-optical effect in thin-film ferromagnetic manganites*, Phys. Rev. B **79**, 052401 (2009).

[138] A. S. Alexandrov and A. M. Bratkovsky, *Colossal magneto-optical conductivity in doped manganites*, Phys. Rev. B **60**, 6215 (1999).

[139] A. S. Alexandrov and A. M. Bratkovsky, *Theory of colossal magnetoresistance in doped*

manganites, Journal of Physics: Condensed Matter **11**, 1989 (1999).

[140] G.-m. Zhao, *Polarons in colossal magnetoresistive and high-temperature superconducting materials*, in *Polarons in Advanced Materials*, Springer Series in Materials Science, Vol. 103, edited by A. S. Alexandrov (Springer Netherlands, 2007) Chap. IV, pp. 569–597.

[141] A. Machida, Y. Moritomo, and A. Nakamura, *Spectroscopic evidence for formation of small polarons in doped manganites*, Phys. Rev. B **58**, R4281 (1998).

[142] A. S. Alexandrov and A. M. Bratkovsky, *Massive spectral weight transfer and colossal magneto-optical effect in doped manganites*, Journal of Applied Physics **87**, 5016 (2000).

[143] E. A. Ganshina, O. Y. Gorbenko, A. G. Smechova, A. R. Kaul, N. A. Babushkina, and L. M. Belova, *Transverse kerr effect in the plcmo ceramics*, Journal of Physics: Condensed Matter **12**, 2857 (2000).

[144] E. Ganshina, N. Loshkareva, Y. Sukhorukov, E. Mostovshchikova, A. Vinogradov, and L. Nomerovannaya, *Optical and magneto-optical spectroscopy of manganites*, Journal of Magnetism and Magnetic Materials **300**, 62 (2006), the third Moscow International Symposium on Magnetism 2005.

[145] E. A. Ganshina, I. K. Rodin, O. Y. Gorbenko, and A. R. Kaul, *Magneto-optical properties of manganites lmo with different oxide non-stoichiometry*, Journal of Magnetism and Magnetic Materials **239**, 537 (2002).

[146] Y. P. Sukhorukov, E. A. Ganshina, B. I. Belevtsev, N. N. Loshkareva, A. N. Vinogradov, K. D. D. Rathnayaka, A. Parasiris, and D. G. Naugle, *Giant change in infrared light transmission in lcmo film near the curie temperature*, Journal of Applied Physics **91**, 4403 (2002).

[147] R. V. Pisarev, I. G. Siny, and G. A. Smolensky, *The origin and the magnitude of magneto-optical effects in ferri- and antiferromagnets*, Solid State Communications **7**, 23 (1969).

[148] J. M. Caicedo, M. C. Dekker, K. Dorr, J. Fontcuberta, and G. Herranz, *Strong magnetorefractive and quadratic magneto-optical effects in* $(pr_{0.4}la_{0.6})_{0.7}ca_{0.3}mno_3$, Phys. Rev. B **82**, 140410 (2010).

[149] T. Moriya, *Theory of light scattering by magnetic crystals*, Journal of the Physical Society of Japan **23**, 490 (1967).

[150] J. Ferre and G. A. Gehring, *Linear optical birefringence of magnetic crystals*, Reports on Progress in Physics **47**, 513 (1984).

[151] I. C. Infante, J. O. Osso, F. Sanchez, and J. Fontcuberta, *Tuning in-plane magnetic anisotropy in lcmo films by anisotropic strain relaxation*, Applied Physics Letters **92**, 012508 (2008).

[152] M. Freiser, *A survey of magnetooptic effects*, Magnetics, IEEE Transactions on **4**, 152 (1968).

[153] D. Pesquera, X. Marti, V. Holy, R. Bachelet, G. Herranz, and J. Fontcuberta, *X-ray interference effects on the determination of structural data in ultrathin lsmo epitaxial thin films*, Applied Physics Letters **99**, 221901 (2011).

[154] H. L. Liu, M. X. Kuo, J. L. Her, K. S. Lu, S. M. Weng, L. M. Wang, S. L. Cheng, and J. G. Lin, *Thickness-dependent optical properties of thin films*, Journal of Applied Physics **97**, 113528 (2005).

[155] M. Bibes, B. Martinez, J. Fontcuberta, V. Trtik, F. Benitez, C. Ferrater, F. Sanchez, and M. Varela, *Magnetoresistance at artificial interfaces in the itinerant srruo*3 *ferromagnet*, Phys. Rev. B **60**, 9579 (1999).

[156] Y. P. Sukhorukov, A. V. Telegin, A. B. Granovsky, E. A. Ganshina, A. Zhukov, J. Gonzalez, G. Herranz, J. M. Caicedo, A. N. Yurasov, V. D. Bessonov, A. R. Kaul, O. Y. Gorbenko, and I. E. Korsakov, *Magnetorefractive effect in manganites with a colssal magnetoresistance in the visible spectral region*, Journal of Experimental and Theoretical Physics **114**, 141 (2012).

[157] O. R. Mercier, *Optical Conductivity of Colossal Magnetoresistance Mangauites*, Ph.D. thesis, Victoria University of Wellington (2002).

[158] A. V. Boris, N. N. Kovaleva, A. V. Bazhenov, A. V. Samoilov, N. Yeh, and R. P. Vasquez, *Infrared optical properties of lcmo epitaxial films*, Journal of Applied Physics **81**, 5756 (1997).

[159] Y. Okimoto, Y. Tomioka, Y. Onose, Y. Otsuka, and Y. Tokura, *Charge ordering and disordering transitions in pcmo as investigated by optical spectroscopy*, Phys. Rev. B **57**, R9377 (1998).

[160] S. Yamaguchi, Y. Okimoto, K. Ishibashi, and Y. Tokura, *Magneto-optical kerr effects in perovskite-type transition-metal oxides:*, Phys. Rev. B **58**, 6862 (1998).

[161] S. K. Arora, R. G. S. Sofin, and I. V. Shvets, *Magnetoresistance enhancement in epitaxial magnetite films grown on vicinal substrates*, Phys. Rev. B **72**, 134404 (2005).

[162] S. Arora, H.-C. Wu, H. Yao, W. Ching, R. Choudhary, I. Shvets, and O. Mryasov, *Magnetic properties of ultrathin magnetite films grown by molecular beam epitaxy*, Magnetics, IEEE Transactions on **44**, 2628 (2008).

[163] R. Ramos, S. K. Arora, and I. V. Shvets, *Anomalous anisotropic magnetoresistance in epitaxial magnetite thin films on mgo(001)*, Phys. Rev. B **78**, 214402 (2008).

[164] T. Hibma, F. C. Voogt, L. Niesen, P. A. A. van der Heijden, W. J. M. de Jonge, J. J. T. M. Donkers, and P. J. van der Zaag, *Anti-phase domains and magnetism in epitaxial magnetite layers*, Journal of Applied Physics **85**, 5291 (1999).

[165] S. Matsumoto, T. Goto, Y. Syono, and Y. Nakagawa, *Magneto-optical study of low-temperature phase transition in magnetite*, Journal of the Physical Society of Japan **44**, 162 (1978).

[166] Z. Simsa, P. S. P., J. Kolacek, and V. Brabers, *Optical and magneto-optical properties of magnetite and manganese ferrites*, Journal of Magnetism and Magnetic Materials **15-18**, 775 (1980).

[167] J. Neal, A. Behan, A. Mokhtari, M. Ahmed, H. Blythe, A. Fox, and G. Gehring, *Magneto-optical study of the verwey transition in magnetite*, Journal of Magnetism and Magnetic Materials **310**, e246 (2007), proceedings of the 17th International Conference on Magnetism, The International Conference on Magnetism.

[168] J. Cheng, G. Sterbinsky, and B. Wessels, *Magnetic and magneto-optical properties of heteroepitaxial magnetite thin films*, Journal of Crystal Growth **310**, 3730 (2008).

[169] M. Ziese, *Spontaneous resistivity anisotropy and band structure of lcmo and magnetite films*, Phys. Rev. B **62**, 1044 (2000).

[170] I. V. Shvets, G. Mariotto, K. Jordan, N. Berdunov, R. Kantor, and S. Murphy, *Long-range charge order on the $fe3o4(001)$ surface*, Phys. Rev. B **70**, 155406 (2004).

[171] O. Pascu, J. Caicedo, J. Fontcuberta, G. Herranz, and A. Roig, *Magneto-optical characterization of colloidal dispersions. application to nickel nanoparticles*, Langmuir **26**, 12548 (2010), cited By (since 1996) 0.

[172] G. A. van Ewijk, *Phase behavior of mixtures of magnetic colloids and non-adsorbing*

polymer, Ph.D. thesis, Faculteit Scheikunde van de Universiteit Utrecht (1971).

[173] T. A. Taton, *Nanotechnology: Boning up on biology*, Nature **412**, 491 (2001).

[174] W. J. Parak, D. Gerion, T. Pellegrino, D. Zanchet, C. Micheel, S. C. Williams, R. Boudreau, M. A. L. Gros, C. A. Larabell, and A. P. Alivisatos, *Biological applications of colloidal nanocrystals*, Nanotechnology **14**, R15 (2003).

[175] X. Xu, G. Friedman, K. D. Humfeld, S. A. Majetich, and S. A. Asher, *Synthesis and utilization of monodisperse superparamagnetic colloidal particles for magnetically controllable photonic crystals*, Chemistry of Materials **14**, 1249 (2002), http://pubs.acs.org/doi/pdf/10.1021/cm010811h .

[176] J. Ge, L. He, J. Goebl, and Y. Yin, *Assembly of magnetically tunable photonic crystals in nonpolar solvents*, Journal of the American Chemical Society **131**, 3484 (2009), pMID: 19236050, http://pubs.acs.org/doi/pdf/10.1021/ja809772v .

[177] J. Ge, Y. Hu, and Y. Yin, *Highly tunable superparamagnetic colloidal photonic crystals*, Angewandte Chemie International Edition **46**, 7428 (2007).

[178] Y. Chen, D.-L. Peng, D. Lin, and X. Luo, *Preparation and magnetic properties of nickel nanoparticles via the thermal decomposition of nickel organometallic precursor in alkylamines*, Nanotechnology **18**, 505703 (2007).

[179] C. B. Murray, S. Sun, W. Gaschler, H. Doyle, T. A. Betley, and C. R. Kagan, *Colloidal synthesis of nanocrystals and nanocrystal superlattices*, Ibm Journal of Research and Development **45**, 47 (2001).

[180] O. Pascu, *Magneto-Photonic Crystal*, Ph.D. thesis, Universitat Autonoma de Barcelona (2012).

[181] P. Crespo, R. Litran, T. C. Rojas, M. Multigner, J. M. de la Fuente, J. C. Sanchez-Lopez, M. A. Garcia, A. Hernando, S. Penades, and A. Fernandez, *Permanent magnetism, magnetic anisotropy, and hysteresis of thiol-capped gold nanoparticles*, Phys. Rev. Lett. **93**, 087204 (2004).

[182] M. Inoue, K. Arai, T. Fujii, and M. Abe, *Magneto-optical properties of one-dimensional photonic crystals composed of magnetic and dielectric layers*, Journal of Applied Physics **83**, 6768 (1998).

[183] M. Inoue, K. Arai, T. Fujii, and M. Abe, *One-dimensional magnetophotonic crystals*, Journal of Applied Physics **85**, 5768 (1999).

[184] A. Levy, H. Yang, M. Steel, and J. Fujita, *Flat-top response in one-dimensional magnetic photonic bandgap structures with faraday rotation enhancement*, Lightwave Technology, Journal of **19**, 1964 (2001).

[185] A. Zvezdin and V. Belotelov, *Magnetooptical properties of two dimensional photonic crystals*, The European Physical Journal B - Condensed Matter and Complex Systems **37**, 479 (2004).

[186] E. Yablonovitch, *Inhibited spontaneous emission in solid-state physics and electronics*, Phys. Rev. Lett. **58**, 2059 (1987).

[187] S. John, *Strong localization of photons in certain disordered dielectric superlattices*, Phys. Rev. Lett. **58**, 2486 (1987).

[188] A. Mekis, J. C. Chen, I. Kurland, S. Fan, P. R. Villeneuve, and J. D. Joannopoulos, *High transmission through sharp bends in photonic crystal waveguides*, Phys. Rev. Lett. **77**, 3787 (1996).

[189] J. D. Joannopoulos, P. R. Villeneuve, and S. Fan, *Photonic crystals: putting a new twist*

on light, Nature **386**, 143 (1997).

[190] H. Miguez, C. Lopez, F. Meseguer, A. Blanco, L. Vazquez, R. Mayoral, M. Ocana, V. Fornes, and A. Mifsud, *Photonic crystal properties of packed submicrometric sio spheres*, Applied Physics Letters **71**, 1148 (1997).

[191] S. G. Johnson and J. D. Joannopoulos, *Introduction to photonic crystals: Blochs theorem, band diagrams, and gaps but no defects*, MIT **1**, 1 (2003).

[192] J. D. Joannopoulos, S. G. Johnson, J. N. Winn, and R. D. Meade, *Photonic Crystals: Molding the Flow of Light*, 2nd ed. (Princeton University Press, 2008).

[193] J. Wagner, *Book review: Optical properties of photonic crystals. by kazuaki sakoda*, Crystal Research and Technology **40**, 1107 (2005).

[194] E. Yablonovitch, *Photonics: One-way road for light*, Nature **461**, 744 (2009).

[195] J. F. GalisteoLopez, M. Ibisate, R. Sapienza, L. S. Froufe-Perez, A. Blanco, and C. Lopez, *Self-assembled photonic structures*, Advanced Materials **23**, 30 (2011).

[196] Z. Wang, Y. Chong, J. D. Joannopoulos, and M. Soljacic, *Observation of unidirectional backscattering-immune topological electromagnetic states*, Nature **461**, 772 (2009).

[197] A. Fedyanin, O. Aktsipetrov, D. Kobayashi, K. Nishimura, H. Uchida, and M. Inoue, *Enhanced faraday and nonlinear magneto-optical kerr effects in magnetophotonic crystals*, Journal of Magnetism and Magnetic Materials **282**, 256 (2004).

[198] H. Kato, T. Matsushita, A. Takayama, M. Egawa, K. Nishimura, and M. Inoue, *Properties of one-dimensional magnetophotonic crystals for use in optical isolator devices*, Magnetics, IEEE Transactions on **38**, 3246 (2002).

[199] I. L. Lyubchanskii, N. N. Dadoenkova, M. I. Lyubchanskii, E. A. Shapovalov, and T. Rasing, *Magnetic photonic crystals*, Journal of Physics D: Applied Physics **36**, R277 (2003).

[200] I. L. Lyubchanskii, N. N. Dadoenkova, M. I. Lyubchanskii, E. A. Shapovalov, A. Lakhtakia, and T. Rasing, *Spectra of bigyrotropic magnetic photonic crystals*, phys. stat. sol. (a) **201**, 3338 (2004).

[201] K. Takahashi, F. Kawanishi, S. Mito, H. Takagi, K. H. Shin, J. Kim, P. B. Lim, H. Uchida, and M. Inoue, *Study on magnetophotonic crystals for use in reflection-type magneto-optical spatial light modulators*, Journal of Applied Physics **103**, 07B331 (2008).

[202] A. Merzlikin, A. Vinogradov, M. Inoue, A. Khanikaev, and A. Granovsky, *The faraday effect in two-dimensional magneto-photonic crystals*, Journal of Magnetism and Magnetic Materials **300**, 108 (2006).

[203] V. I. Belotelov and A. K. Zvezdin, *Magneto-optical properties of photonic crystals*, J. Opt. Soc. Am. B **22**, 286 (2005).

[204] V. I. Belotelov, V. A. Kotov, and A. K. Zvezdin, *New magnetooptical materials on a nanoscale*, Phase Transitions: A Multinational Journal **79**, 1135 (2006).

[205] M. Inoue, R. Fujikawa, A. Baryshev, A. Khanikaev, P. B. Lim, H. Uchida, O. Aktsipetrov, A. Fedyanin, T. Murzina, and A. Granovsky, *Magnetophotonic crystals*, Journal of Physics D: Applied Physics **39**, R151 (2006).

[206] S. Noda, K. Tomoda, N. Yamamoto, and A. Chutinan, *Full three-dimensional photonic bandgap crystals at near-infrared wavelengths*, Science **289**, 604 (2000), http://www.sciencemag.org/content/289/5479/604.full.pdf .

[207] X. Yu, Y. Lee, R. Furstenberg, J. White, and P. Braun, *Filling fraction dependent properties of inverse opal metallic photonic crystals*, Advanced Materials **19**, 1689 (2007).

[208] V. Pavlov, P. Usachev, R. Pisarev, D. Kurdyukov, S. Kaplan, A. Kimel, A. Kirilyuk, and

T. Rasing, *Optical study of three-dimensional magnetic photonic crystals opal/magnetite*, Journal of Magnetism and Magnetic Materials **321**, 840 (2009), proceedings of the Forth Moscow International Symposium on Magnetism.

[209] V. V. Pavlov, P. A. Usachev, R. V. Pisarev, D. A. Kurdyukov, S. F. Kaplan, A. V. Kimel, A. Kirilyuk, and T. Rasing, *Enhancement of optical and magneto-optical effects in three-dimensional opal magnetite magnetic photonic crystals*, Applied Physics Letters **93**, 072502 (2008).

[210] V. V. Pavlov, P. A. Usachev, R. V. Pisarev, D. A. Kurdyukov, S. F. Kaplan, A. V. Kimel, A. Kirilyuk, and T. Rasing, *Erratum: Enhancement of optical and magneto-optical effects in three-dimensional opal magnetite magnetic photonic crystals*, Applied Physics Letters **93**, 209901 (2008).

[211] N. Liu, H. Guo, L. Fu, S. Kaiser, H. Schweizer, and H. Giessen, *Three-dimensional photonic metamaterials at optical frequencies*, Nat Mater **7**, 31 (2008).

[212] M. Fang, T. T. Volotinen, S. K. Kulkarni, L. Belova, and K. V. Rao, *Effect of embedding magnetite nanoparticles in silica spheres on the optical transmission properties of three-dimensional magnetic photonic crystals*, Journal of Applied Physics **108**, 103501 (2010).

[213] J. Caicedo, E. Taboada, D. D. Hrabovsky, M. Lopez-Garcia, G. Herranz, A. Roig, A. Blanco, C. Lopez, and J. Fontcuberta, *Facile route to magnetophotonic crystals by infiltration of 3d inverse opals with magnetic nanoparticles*, Journal of Magnetism and Magnetic Materials **322**, 1494 (2010), proceedings of the Joint European Magnetic Symposia.

[214] J. M. Caicedo, O. Pascu, M. Lopez-Garcia, V. Canalejas, A. Blanco, C. Lopez, J. Fontcuberta, A. Roig, and G. Herranz, *Magnetophotonic response of three-dimensional opals*, ACS Nano **1**, 1 (2011), http://pubs.acs.org/doi/pdf/10.1021/nn1035872 .

[215] J. F. G. Lopez, *An optical study of opal based photonic crystals*, Ph.D. thesis, Universidad Autónoma de Madrid (2005).

[216] M. Allard, E. H. Sargent, E. Kumacheva, and O. Kalinina, *Characterization of internal order of colloidal crystals by optical diffraction*, Optical and Quantum Electronics **34**, 27 (2002), 10.1023/A:1013397721552.

[217] M. S. Thijssen, R. Sprik, J. E. G. J. Wijnhoven, M. Megens, T. Narayanan, A. Lagendijk, and W. L. Vos, *Inhibited light propagation and broadband reflection in photonic air-sphere crystals*, Phys. Rev. Lett. **83**, 2730 (1999).

[218] J. F. Galisteo Lopez and W. L. Vos, *Angle-resolved reflectivity of single-domain photonic crystals: Effects of disorder*, Phys. Rev. E **66**, 036616 (2002).

[219] Y. A. Vlasov, V. N. Astratov, A. V. Baryshev, A. A. Kaplyanskii, O. Z. Karimov, and M. F. Limonov, *Manifestation of intrinsic defects in optical properties of self-organized opal photonic crystals*, Phys. Rev. E **61**, 5784 (2000).

[220] Y. A. Vlasov, V. N. Astratov, O. Z. Karimov, A. A. Kaplyanskii, V. N. Bogomolov, and A. V. Prokofiev, *Existence of a photonic pseudogap for visible light in synthetic opals*, Phys. Rev. B **55**, R13357 (1997).

[221] Y. A. Vlasov, M. A. Kaliteevski, and V. V. Nikolaev, *Different regimes of light localization in a disordered photonic crystal*, Phys. Rev. B **60**, 1555 (1999).

[222] K. W. K. Shung and Y. C. Tsai, *Surface effects and band measurements in photonic crystals*, Phys. Rev. B **48**, 11265 (1993).

[223] G. B. Scott, D. E. Lacklison, H. I. Ralph, and J. L. Page, *Magnetic circular dichroism and faraday rotation spectra of yfo*, Phys. Rev. B **12**, 2562 (1975).

[224] S. Gottardo, M. Burresi, F. Geobaldo, L. Pallavidino, F. Giorgis, and D. S. Wiersma, *Self-alignment of liquid crystals in three-dimensional photonic crystals*, Phys. Rev. E **74**, 040702 (2006).

[225] A. Reza, I. Simkiene, R. Vaisnoras, C. Lopez, D. Golmayo, and J. Babonas, *Optical anisotropy of synthetic opals*, Photonics and Nanostructures - Fundamentals and Applications **9**, 82 (2011).

[226] J. F. GalisteoLopez, M. Galli, M. Patrini, A. Balestreri, L. C. Andreani, and C. Lopez, *Effective refractive index and group velocity determination of three-dimensional photonic crystals by means of white light interferometry*, Phys. Rev. B **73**, 125103 (2006).

[227] I. H. MALITSON, *Interspecimen comparison of the refractive index of fused silica*, J. Opt. Soc. Am. **55**, 1205 (1965).

[228] O. Pascu, J. M. Caicedo, M. Lopez-Garcia, V. Canalejas, A. Blanco, C. Lopez, J. Arbiol, J. Fontcuberta, A. Roig, and G. Herranz, *Ultrathin conformal coating for complex magneto-photonic structures*, Nanoscale **1**, 1 (2011).